

THE UNIVERSITY OF HULL

**A novel method to develop nanoporous polymeric membranes using self-assembled magnetic nanoparticles as templates**

being a Thesis submitted for the Degree of Doctor of Philosophy

in the University of Hull

by

Mr. Jarryd Keng Gene, Ng, BEng

December 2013

# Abstract

---

Nanoporous membrane systems have received attention within the scientific community due to their potential in micro-fluidic devices and bio-medical applications over the past decades. The increasing interest in applications drives the development of manufacturing methods of the nanoporous membranes. This thesis describes the development of a novel method of procuring free-standing nanoporous polymeric membranes in a cost-effective and reproducible manner.

The novelty of the technique hinges on the exploitation of self-assembling magnetic nanoparticles in colloidal suspensions. The self-assembly technique is accomplished through application of an external magnetic field causing the nanoparticles to form columnar structures that span across the membrane thickness. These columnar structures form the pore templates which when selectively etched away results in the array of nanopores.

The research details the initial concept, describes the fabrication techniques used and highlights the characterisation methods employed.

# Acknowledgements

---

I would like express my sincerest gratitude to supervisors Dr. Sergei Lukaschuk and Dr. Sergey Rybchenko for their expert advice, guidance and in-depth knowledge of the field. They have provided me with the opportunity to undertake the research project and have invested a large amount of effort and time.

I would also like to acknowledge the efforts of the staff of the microscopy suite and mechanical workshop here in the University of Hull. Special thanks go to Mr. Garry Robinson for his dedication, advice and patience.

Finally, I would like to thank my family and friends who have provided me with moral support, counseling and technical help during the research. My gratitude goes to those who have taken their time to proof read the thesis.

# Table of Contents

---

ABSTRACT .....	I
ACKNOWLEDGEMENTS .....	II
TABLE OF CONTENTS .....	III
LIST OF FIGURES .....	VI
LIST OF TABLES .....	XI
LIST OF EQUATIONS.....	XIII
<i>Chapter 1: General Introduction</i> .....	1
1.1. Aims and Objectives .....	1
1.2. Thesis Organisation .....	2
<i>Chapter 2: Literature Review</i> .....	3
2.1. Membrane Definition.....	4
2.2. Applications of Nanoporous Membranes .....	4
2.2.1. Synthetic Nanoporous Membranes as Bio-sensing and Molecular Detection .....	5
2.2.2. Synthetic Nanoporous Membranes as Filtration Units .....	6
2.2.3. Fabrication Strategies or Approaches.....	6
2.2.4. Organic Nanopore Membrane System.....	7
2.2.5. Synthetic Nanopore Membrane System .....	8
2.2.5.1. Micro Fabricated Solid-State Membranes .....	8
2.2.5.2. Polymeric Membranes.....	9
2.2.5.3. Anodic Alumina Membranes.....	10
2.3. Proposed Manufacturing Approach.....	11
2.3.1. Design Merits and Limitations of Previous Works.....	11
2.3.2. Bottom-Up Element of Our Approach.....	12
2.3.3. Top-Down Element of Our Approach.....	12
2.4. Summary of Approach.....	13
<i>Chapter 3: Colloidal Solution of Magnetic Nanoparticles: Magnetic Interactions</i> .....	14
3.1. Magnetic Nanoparticles: A Brief Review.....	15
3.2. Magnetic Interactions.....	16
3.2.1. Structural Transition of Ferrofluids .....	16
3.2.2. Average Complexity Transition Point between Structural Modes.....	19
3.2.3. Inter-Columnar Spacing.....	20
3.3. Physical Morphology of Structures .....	20
3.4. Template of Nanopore .....	22
3.5. Chapter Summary .....	26
<i>Chapter 4: Colloidal Solution of Magnetic Nanoparticles: Synthesis</i> .....	27
4.1. Synthesis of Fe <sub>3</sub> O <sub>4</sub> Magnetite Nanoparticles .....	28
4.1.1. Surface Modification of Magnetic Nanoparticles.....	29
4.1.2. Managing the Volume of Extraction .....	32

4.1.3. TEM Characterisation of Magnetic Nanoparticles .....	32
4.2. Chapter Summary .....	35
<i>Chapter 5: Device Design</i> .....	36
5.1. Establishing a Fabrication Technique .....	37
5.1.1. Fabrication of Thin Films: Bubble Membrane Generation.....	38
5.1.2. Fabrication of Thin Films: Confinement between Two Substrates.....	41
5.1.2.1. Glass substrate Selection and Treatment .....	45
5.2. Helmholtz Coil Pair System.....	47
5.2.1. Design Considerations .....	47
5.2.2. Theoretical Computations .....	48
5.2.3. Theoretical Estimates of Magnetic Field Strength .....	49
5.2.4. Magnetic Field Homogeneity .....	51
5.2.5. Design Outline: Fabrication and Winding .....	52
5.2.6. Device Testing and Results Obtained .....	54
5.3. Direct Current Power Supply .....	57
5.4. Control System: LabVIEW programming scheme .....	58
5.4.1. Control System: Testing the Program .....	58
5.5. Chapter summary.....	59
<i>Chapter 6: Experimental Processes</i> .....	60
6.1. Initial Experimental Setup.....	61
6.1.1. Experimental Results: Helmholtz Coil Pair System.....	66
6.2. Alternative Sources of Magnetic Fields .....	68
6.2.1. Experimental Results: Permanent Magnet Type .....	69
6.3. Chapter Summary .....	70
<i>Chapter 7: Image Analysis and Characterisation of Membranes</i> .....	71
7.1. Optical Microscopy Analysis: Introduction.....	72
7.1.1. Image Processing Software: ImageJ .....	72
7.2. Structure of Optical Microscopy Analysis .....	73
7.2.1. Optical Microscopy Analysis: Array Density .....	73
7.2.2. Optical Microscopy Analysis: Inter-Array Spacing .....	78
7.2.3. Optical Microscopy Analysis: Pre-Etching and Post-Etching.....	80
7.3. SEM and TEM Analysis: Introduction .....	86
7.4. Structure of SEM and TEM analysis .....	86
7.4.1. Validating the Optical Images via Chemical Element Analysis.....	87
7.4.2. Physical Morphology of the Columnar Structures .....	98
7.4.3. Membrane Surface Morphology Investigation .....	103
7.4.4. Cross-sectional View of Membrane through Ion Milling Technique.....	114
7.5. Chapter Summary .....	118
<i>Chapter 8: Ionic Conductance Characterisation of Membranes</i> .....	119
8.1. Ionic Conductance Characterisation .....	120
8.1.1. Ionic Conductivity Methods and Concepts from Previous Works .....	121
8.1.2. Experimental Setup, Design and Schematics .....	123
8.1.2.1. Membrane Platform Diaphragm Preparation.....	124

8.1.2.2. Flow Cell Design.....	126
8.1.2.3. The Silver/Silver Chloride (Ag/AgCl) Electrode.....	128
8.1.2.4. Chlorinating Silver Wire .....	130
8.1.2.5. Ag/AgCl Electrode Fabrication.....	131
8.1.2.6. LabVIEW™ Programming .....	132
8.2. Preliminary Calibrations: The Open Circuit Test.....	135
8.3. Preliminary Calibrations: Cyclic Sweep Range Identification .....	138
8.4. Preliminary Calibrations: Shifting Current Response to Different Scan Delays .....	141
8.5. Experimentation: Ionic Conductance Characterisation.....	146
8.5.1. Benchmark Characterisation: Track-Etched Membranes .....	146
8.5.2. Analysis of Results: Track-Etched Membranes.....	147
8.5.3. Ionic Characterisation: Fabricated Membrane Platforms .....	157
8.5.3.1. Investigating Discrepancy: Mrampstest 2 (O6102013).....	158
8.5.4. Analysis of Results: Fabricated Membrane Platforms .....	159
8.6. Chapter Summary.....	173
<i>Chapter 9: Summary and Conclusions.....</i>	<i>175</i>
9.1. Final Summary .....	175
9.2. Future work.....	178
9.3. Conclusions .....	179
Appendix: Chapter 5 .....	180
Appendix: Chapter 7 .....	196
Appendix: Chapter 8.....	201
References .....	216

# List of Figures

---

FIGURE 3.2.A: STRUCTURAL TRANSITIONS OF MAGNETICALLY INDUCED FERROFLUIDS. (IMAGE TAKEN FROM IVEY AND CO-WORKERS (IVEY, LIU, ZHU, & CUTILLAS, 2000)) .....	18
FIGURE 3.3.A: TOP VIEW OF THE STRUCTURAL CONFIGURATION FORMED USING $Fe_3O_4$ MAGNETITE PARTICLES MAGNETIC FIELD IS PARALLEL WITH VIEWING ANGLE (IMAGE TAKEN FROM (HONG, JANG, HORNG, HSU, YAO, & YANG, 1997)).....	21
FIGURE 3.3.B: A CROSS-SECTIONAL VIEW OF THE STRUCTURAL CONFIGURATION FORMED USING $Fe_3O_4$ MAGNETITE PARTICLES MAGNETIC FIELD IS PERPENDICULAR TO VIEWING ANGLE (IMAGE TAKEN FROM (G.FLORES, J.LIU, MOHEBI, & JAMASBI, 1999)).....	21
FIGURE 3.4.A: DIAGRAM ILLUSTRATING OF SPECULATED SHAPE OR SINGLE NANOPORE (DENSE COLUMN)	23
FIGURE 3.4.B: DIAGRAM ILLUSTRATING OF SPECULATED SHAPE OR SINGLE NANOPORE (SEMI DENSE COLUMN).....	24
FIGURE 3.4.C: DIAGRAM ILLUSTRATING OF SPECULATED SHAPE OR SINGLE NANOPORE (SEMI DENSE COLUMN WITH SPLIT ENDS) .....	25
FIGURE 4.1.A: VISUAL COMPARISON OF SAMPLE 8 AND 9 AFTER 24 HOUR WAITING PERIOD .....	31
FIGURE 4.1.B: IMAGE ANALYSIS CONDUCTED ON THE EMBEDDED $Fe_3O_4$ CONSTITUENTS WITHIN THE POLYMER FILM AT 158000X MAGNIFICATION .....	33
FIGURE 5.1.A: DEVICE TO GENERATE A PRESSURE GRADIENT TO GENERATE A BUBBLE MEMBRANE.....	39
FIGURE 5.1.B: STAGE FABRICATED FOR BUBBLE MEMBRANE FABRICATION .....	40
FIGURE 5.1.C: (A.) EARLY STAGE OF THE BUBBLE MEMBRANE FORMATION; ENTRAPPED AIR FORMS THE INITIAL SHAPE OF THE BUBBLE (B.) ACTUAL FORMATION OF THE BUBBLE MEMBRANE WHEN ENTRAPPED AIR APPROACHES SURFACE OF SOLUTION .....	40
FIGURE 5.1.D: PROPAGATION OF THE NEWTON BLACK FILM INDICATED WITH THE WHITE ARROW .....	41
FIGURE 5.1.E: DEVICE SCHEMATICS PROCURED BY S. RYBCHENKO ET. AL. ILLUSTRATING THE THIN POLYMER FILM FABRICATION TECHNIQUE (RYBCHENKO, DYAB, HAYWOOD, ITSKEVICH, & PAUNOV, 2009) .....	42
FIGURE 5.1.F: FINAL ASSEMBLY OF THE SPECIMEN HOUSING.....	43
FIGURE 5.1.G: CROSS-SECTIONAL VIEW OF THE DESIGN TO HOUSE THE SPECIMEN CONTAINMENT UNIT ....	44
FIGURE 5.2.A: CROSS-SECTIONAL VIEW OF FINITE HELMHOLTZ COIL PAIR SYSTEM .....	48
FIGURE 5.2.B: A CROSS-SECTIONAL VIEW OF THE HELMHOLTZ COIL PAIR DEPICTING ALL LOCATIONS RELEVANT TO SUBSEQUENT DISCUSSION .....	50
FIGURE 5.2.C: A PLOT DEPICTING THE MAGNETIC FIELD ALONG THE CENTRAL AXIS FOR 50 MM AT 1 MM INTERVALS AT 100 W .....	52
FIGURE 5.2.D: AN EXPLODED VIEW OF THE INITIAL DESIGN OF THE HELMHOLTZ COIL PAIR PROTOTYPE.....	53
FIGURE 5.2.E: FINALISED DESIGN OF THE HELMHOLTZ COIL PAIR PROTOTYPE.....	54
FIGURE 6.1.A: IMAGE DEPICTING THE APPLICATION METHOD OF THE O-RING.....	62

FIGURE 6.1.B: CROSS-SECTIONAL VIEW OF THE SPECIMEN CONFIGURATION DURING EXPERIMENTATION ..	63
FIGURE 6.1.C: EXPERIMENTAL SCHEMATIC DEPICTING ALL DEVICES USED FOR THE WORK.....	64
FIGURE 6.1.D: EXAMPLE OF COMPLETED SAMPLES AFTER THE PHOTO-POLYMERISATION PROCESS.....	65
FIGURE 6.1.E: ILLUSTRATION DETAILING THE ETCHING PROCEDURE USING HCL ACID.....	66
FIGURE 6.1.F: A DEMONSTRATIVE SAMPLE DEPICTING THE COLUMNAR STRUCTURES PRODUCED USING THE HELMHOLTZ COIL PAIR SYSTEM .....	67
FIGURE 6.2.A: A CROSS-SECTIONAL VIEW OF THE CONFIGURATION USED IN THE EXPERIMENTATION .....	68
FIGURE 6.2.B: A DEMONSTRATIVE SAMPLE DEPICTING THE COLUMNAR STRUCTURES PRODUCED USING THE NEODYMIUM PERMANENT MAGNETS .....	70
FIGURE 7.2.A: SAMPLE OF A GREYSCALE IMAGE BEFORE IMAGE THRESHOLDING .....	74
FIGURE 7.2.B: SAMPLE OF IMAGE AFTER IMAGE THRESHOLD CONVERSION .....	74
FIGURE 7.2.C: HISTOGRAM DEPICTING THE ARRAY SIZE DISTRIBUTION AT RANGES OF 5 PIXELS TO 100 PIXELS RANGE .....	77
FIGURE 7.2.D: HISTOGRAM DEPICTING THE ARRAY SIZE DISTRIBUTION AT RANGES OF 0 PIXELS TO 20 PIXELS RANGE.....	77
FIGURE 7.2.E: EXAMPLE OF THE IMAGED LOCATIONS OF THE FILM ACCOMPANIED WITH A CORRESPONDING IMAGE FILM SECTIONS PRIOR TO ETCHING .....	80
FIGURE 7.2.F: EXEMPLAR IMAGE OF A SAMPLE BEFORE AND AFTER SELECTIVE ETCHING.....	81
FIGURE 7.2.G: SCENARIOS OF ARRAY PROPAGATION DUE TO PARTICLE DEPLETION EFFECT .....	82
FIGURE 7.2.H: ILLUSTRATION OF THE EFFECT OF ETCHING FROM A SINGLE SIDE OF THE FILM SUBTRACTING Fe <sub>3</sub> O <sub>4</sub> CONSTITUENTS.....	83
FIGURE 7.2.I: ORIGINAL IMAGE OF SAMPLE AREA BEFORE ETCHING PROCESS TAKES PLACE.....	84
FIGURE 7.2.J: IMAGE OF SAMPLE AREA DEPICTING 16 MINUTES AFTER ETCHING PROCESS HAS TAKEN PLACE .....	84
FIGURE 7.2.K: IMAGE OF SAMPLE AREA DEPICTING 32 MINUTES AFTER ETCHING PROCESS HAS TAKEN PLACE .....	85
FIGURE 7.4.A: TYPICAL SAMPLE WITH A DESIGNATED SITE FOR BE IMAGING ANALYSIS .....	88
FIGURE 7.4.B: A 500 X 500 PIXEL IMAGE OF DESIGNATED SITE WITH DISTINGUISHABLE MARK .....	88
FIGURE 7.4.C: SEM EQUIVALENT IMAGE RELEVANT TO FIGURE 7.4.A.....	89
FIGURE 7.4.D: SEM IMAGE OF AFOREMENTIONED SITE ACCOMPANIED WITH VISUAL REFERENCE MARKERS. SEM IMAGING PARAMETERS: 353.52 PA AT 15 kV.....	90
FIGURE 7.4.E: BE IMAGE OF AFOREMENTIONED SITE ACCOMPANIED WITH VISUAL REFERENCE MARKERS. BE IMAGING PARAMETERS: 1 nA AT 15 kV.....	91
FIGURE 7.4.F: VISUAL EVIDENCE DEPICTING SAMPLE VIEWED IN SE MODE.....	92
FIGURE 7.4.G: VISUAL EVIDENCE DEPICTING SAMPLE VIEWED IN BE MODE .....	92
FIGURE 7.4.H: A 500 X 500 PIXEL IMAGE OF THE DESIGNATED SITE WITH ANNOTATIONS OF THREE COLONIES PRESENT IN THE FILM REGION .....	93
FIGURE 7.4.I: A 500X MAGNIFICATION OF CORRESPONDING BE IMAGE WITH ANNOTATIONS OF THREE COLONIES PRESENT IN THE FILM REGION BE IMAGING PARAMETERS: 1 nA AT 15 kV.....	94

FIGURE 7.4.J: OM IMAGE TAKEN DEMONSTRATING LARGE CLUSTER OF ARRAYS SITUATED IN THE FILM.....	95
FIGURE 7.4.K: SE IMAGE TAKEN DEMONSTRATING A FEATURELESS SURFACE ACROSS THE FILM .....	95
FIGURE 7.4.L: BE IMAGE TAKEN DEMONSTRATING LARGE CLUSTER OF ARRAYS EMBEDDED WITHIN THE FILM AT THE SAME LOCATION AS FIGURE 7.4.K.....	96
FIGURE 7.4.M: BACKGROUND SCAN DETAILING NO TRACES OF FE VIA X-RAY ELEMENT ANALYSIS .....	97
FIGURE 7.4.N: RESULTS FROM THE X-RAY ELEMENT ANALYSIS ON THE BRIGHT SPOTS ACROSS THE BE IMAGES.....	98
FIGURE 7.4.O: A TEM IMAGE OF THE EMBEDDED $Fe_3O_4$ CONSTITUENTS WITHIN THE POLYMER FILM AT 53000X MAGNIFICATION .....	99
FIGURE 7.4.P: TEM IMAGE DEPICTING THE COLUMNAR STRUCTURE WITH THEIR SIGNATURE TAPERED ENDS .....	101
FIGURE 7.4.Q: TEM IMAGE DEPICTING THE COLUMNAR STRUCTURES WITH DIFFERENT LENGTHS .....	102
FIGURE 7.4.R: SEM IMAGE DEPICTING THE ASSEMBLE FROM A THREE DIMENSIONAL POINT OF VIEW .....	103
FIGURE 7.4.S: (TOP LEFT) OM IMAGE OF THE FILM LOCATION IN THE PRE-ETCH STAGE (BOTTOM RIGHT) OM IMAGE OF THE FILM LOCATION IN THE POST-ETCH STAGE.....	104
FIGURE 7.4.T: (LEFT) OM IMAGE OF THE FILM CONSTITUENT IN THE PRE-ETCH STAGE (RIGHT) OM IMAGE OF THE FILM CONSTITUENT IN THE POST-ETCH STAGE .....	104
FIGURE 7.4.U: SE MICROGRAPH OF THE SURFACE MORPHOLOGY OF FIRST ITERATION SAMPLES (1000X MAGNIFICATION) .....	105
FIGURE 7.4.V: SE MICROGRAPH OF THE SURFACE MORPHOLOGY OF FIRST ITERATION SAMPLES (500X MAGNIFICATION) .....	106
FIGURE 7.4.W: OM ILLUSTRATION OF FILM SHRINKAGE SUBSEQUENT TO ETCHING PROCESS AND SITES OF MEASUREMENT CORRESPONDING TO ARRAY POSITION .....	107
FIGURE 7.4.X: SE MICROGRAPH OF THE SURFACE MORPHOLOGY OF SECOND ITERATION SAMPLES (500X MAGNIFICATION) .....	109
FIGURE 7.4.Y: SE MICROGRAPH OF THE SURFACE MORPHOLOGY OF SECOND ITERATION SAMPLES (1500X MAGNIFICATION) .....	110
FIGURE 7.4.Z: SE MICROGRAPH OF THE SURFACE MORPHOLOGY OF THIRD ITERATION SAMPLES (10000X MAGNIFICATION) .....	111
FIGURE 7.4.AA: SE MICROGRAPH OF THE SURFACE MORPHOLOGY OF THIRD ITERATION SAMPLES (20000X MAGNIFICATION) FROM FIGURE 7.4.Z.....	112
FIGURE 7.4.BB: SE MICROGRAPH OF THE SURFACE MORPHOLOGY OF THIRD ITERATION SAMPLES (40000X MAGNIFICATION) FROM FIGURE 7.4.Z.....	112
FIGURE 7.4.CC: SE MICROGRAPH OF THE SURFACE MORPHOLOGY OF THIRD ITERATION SAMPLES (20000X MAGNIFICATION) .....	113
FIGURE 7.4.DD: SE MICROGRAPH OF THE SURFACE MORPHOLOGY OF THIRD ITERATION SAMPLES (20000X MAGNIFICATION) FROM FIGURE 7.4.CC.....	113
FIGURE 7.4.EE: ILLUSTRATION OF A SECTION OF A MEMBRANE UNDER THE MILLING CONDITION PREVIOUSLY DESCRIBED .....	115

FIGURE 7.4.FF: SE MICROGRAPH OF A CROSS SECTION OF THE SAMPLE (30000X MAGNIFICATION) .....	116
FIGURE 7.4.GG: SE MICROGRAPH OF A CROSS SECTION OF THE SAMPLE AT A DIFFERENT LOCATION (30000X MAGNIFICATION) .....	116
FIGURE 8.1.A: SCHEMATIC DIAGRAM OF A SCANNING ION CONDUCTANCE MICROSCOPY SYSTEM PIONEERED BY (CHEN, DERLYO, & BAKER, 2009).....	122
FIGURE 8.1.B: (A) SCHEMATIC OF A FLOW CELL (B) CROSS-SECTION OF A NANO CHANNEL (C) TRANSMISSION ELECTRON MICROSCOPY IMAGE OF NANO CHANNEL. IMAGE TAKEN FROM (LEE, JOLY, SIRIA, BIANE, & BOCQUET, 2012) .....	122
FIGURE 8.1.C: A CROSS-SECTIONAL VIEW OF THE FILM POSITIONING DEVICE .....	125
FIGURE 8.1.D: (LEFT TO RIGHT) IMAGE OF THE RESERVOIR DEVICE FROM A SIDE AND TOP VIEW .....	126
FIGURE 8.1.E: SEALING SOLUTION USED FOR CONDUCTIVITY EXPERIMENTATION.....	127
FIGURE 8.1.F: (TOP) SOLIDWORKS MODEL OF CONDUCTIVITY CELL (BOTTOM) EXPLODED VIEW OF CONDUCTIVITY CELL .....	128
FIGURE 8.1.G: ILLUSTRATION OF A STANDARD CONSTRUCTION OF A AG/AGCL ELECTRODE.....	129
FIGURE 8.1.H: SCHEMATIC OF THE CHLORINATION PROCESS OF SILVER WIRE .....	131
FIGURE 8.1.I: EXAMPLE OF DESCRIBED SWEEP FUNCTION RELEVANT TO MODE 1 .....	133
FIGURE 8.1.J: DESCRIBED SWEEP FUNCTION RELEVANT TO MODE 2 .....	134
FIGURE 8.1.K: DESCRIBED SWEEP FUNCTION RELEVANT TO MODE 3.....	134
FIGURE 8.2.A: I-V CHARACTERISTIC PLOT OF LDPE SPECIMEN AT 0.1 M KCL CONCENTRATION .....	136
FIGURE 8.2.B: I-V PLOT OF A BLANK HDDA SAMPLE AT VARIOUS KCL CONCENTRATIONS.....	137
FIGURE 8.2.C: I-V CHARACTERISTIC PLOT OF SILICONE RTV 630 AT 0.1 M KCL CONCENTRATION .....	137
FIGURE 8.3.A: RECORDED CYCLIC VOLTAMMOGRAM FOR 8 $\mu$ M (0.1 SECOND SCAN DELAY) .....	140
FIGURE 8.3.B: PLOT OF CURRENT RESPONSE OF THE NUCLEPORE 8 $\mu$ M DIAMETER PORES AT -0.1 V TO + 0.1 V RANGE.....	141
FIGURE 8.4.A : A PLOT OF DESCENDING SCAN GRADIENTS COMPARISON. PARAMETERS OF SCAN LISTED IN TABLE 8.4.A .....	143
FIGURE 8.4.B: A PLOT OF ASCENDING SCAN GRADIENTS COMPARISON. PARAMETERS OF SCAN LISTED IN TABLE 8.4.A .....	144
FIGURE 8.5.A: IMAGE REPRESENTATION OF THE ACCESS RESISTANCE THEORY AND CORRESPONDING SUM OF RESISTANCE AT BOTH SIDES OF THE CHANNEL. IMAGE TAKEN FROM (VODYANOV & BEZRUKOV, 1992) .....	148
FIGURE 8.5.B: EXEMPLAR PLOT OF AN 8 $\mu$ M DIAMETER PORE USING 0.001 M KCL CONCENTRATION .....	151
FIGURE 8.5.C: EXEMPLAR PLOT OF AN 8 $\mu$ M DIAMETER PORE USING 0.01 M KCL CONCENTRATION .....	152
FIGURE 8.5.D: EXEMPLAR PLOT OF AN 8 $\mu$ M DIAMETER PORE USING 0.1 M KCL CONCENTRATION .....	153
FIGURE 8.5.E: EXEMPLAR PLOT OF AN 8 $\mu$ M DIAMETER PORE USING 1 M KCL CONCENTRATION.....	154
FIGURE 8.5.F: PLOT DEPICTING THE CHANGE IN THEORETICAL CONDUCTANCE VERSUS PORE DIAMETER AT 0.1 M KCL CONCENTRATION .....	162
FIGURE 8.5.G: ILLUSTRATION DEMONSTRATING A CUT-OUT VIEW OF DENSE TAPERED COLUMN AS A TEMPLATE EMBEDDED IN A MEMBRANE .....	164

FIGURE 8.5.H: IMAGE ILLUSTRATING THE GEOMETRY OF A SINGLE PARTICLE BREACHING THE MEMBRANE SURFACE.....	165
FIGURE 8.5.I: PLOT DEPICTING THE <i>D<sub>central</sub></i> AS A FUNCTION OF CONDUCTANCE .....	166
FIGURE 8.5.J: AN EXEMPLAR ILLUSTRATION OF A CUT-OUT VIEW OF PORE TEMPLATES DETAILING A SEMI-DENSE STRUCTURE WITH AND WITHOUT SPLIT-ENDS .....	167
FIGURE 8.5.K: A 3D AND 2D VISUAL INTERPRETATION OF THE DISCUSSION REGARDING THE THIRD THEORETICAL MODEL .....	169
FIGURE 8.5.L: A REPRESENTATIVE CIRCUIT DIAGRAM DETAILING A SINGULAR NANOPORE STRUCTURE .....	170
FIGURE 8.5.M: PLOT OF CONDUCTANCE AS A FUNCTION OF <i>D<sub>access2</sub></i> .....	172

# List of Tables

---

TABLE 4.1.A: SURFACE MODIFICATION TECHNIQUE FOR REGIME 1 .....	30
TABLE 4.1.B: SURFACE MODIFICATION TECHNIQUE FOR REGIME 2 .....	30
TABLE 5.2.A: TABULATED THEORETICAL RESULTS OF OPTIMISED DESIGN PARAMETERS FOR HELMHOLTZ COIL PAIR SYSTEM USED IN EXPERIMENTATION.....	51
TABLE 5.2.B: TABULATED RESULTS COMPARING MAGNETIC FIELD STRENGTH OF BOTH COILS WITH THEORETICAL COMPUTATIONS.....	56
TABLE 6.1.A: CONTROL PARAMETERS USED TO DETERMINE $\langle C \rangle$ .....	64
TABLE 7.2.A: TABULATED SUMMARY OF ANALYSED ARRAY DENSITY OF PERMANENT MAGNET SAMPLES .....	75
TABLE 7.2.B: TABULATED SUMMARY OF ANALYSED ARRAY DENSITY OF HELMHOLTZ COIL PAIR SAMPLES....	75
TABLE 7.2.C: TABULATED POST-PROCESSED RESULTS RELEVANT TO ARRAY SIZE (PERMANENT MAGNET) ...	76
TABLE 7.2.D: TABULATED POST PROCESSED RESULTS RELEVANT TO ARRAY SIZE (HELMHOLTZ COIL PAIR).	76
TABLE 7.4.A: TABULATED COMPUTATIONS OF FILM SHRINKAGE AS AN EFFECT OF ETCHING .....	108
TABLE 8.3.A: PARAMETERS USED FOR INITIAL REDOX REACTION LIMIT IDENTIFICATION.....	139
TABLE 8.4.A: TEST PARAMETERS INITIAL TEST FOR CHANGE IN CURRENT RESPONSE UNDER DIFFERENT SCAN RATE .....	142
TABLE 8.4.B: TABULATED GRADIENT VALUES FOR BOTH FIRST DESCENDING AND SECOND ASCENDING SWEEP AT DIFFERENT SCAN DELAYS. ....	145
TABLE 8.5.A: PROGRAMMING PARAMETERS CONDUCTED FOR BENCHMARK TESTS MEASUREMENTS .....	147
TABLE 8.5.B: TABULATE SUMMARY OF GRADIENT VALUES FOR TWO TRACK-ETCH MEMBRANE USING FOUR KCL CONCENTRATION VALUES .....	150
TABLE 8.5.C: TABULATED SUMMARY OF THEORETICAL CONDUCTANCE VALUES FOR TWO TRACK-ETCHED MEMBRANES USING FOUR KCL CONCENTRATIONS.....	155
TABLE 8.5.D: TABLE OF RESULTS DETAILING THE RESISTANCE RECTIFICATION OF ACTUAL MEASUREMENTS .....	156
TABLE 8.5.E: SUMMARISED CONDUCTANCE MEASUREMENTS FROM FABRICATED MEMBRANES AT VARIOUS KCL CONCENTRATION .....	157
TABLE 8.5.F: AVERAGED APPARENT PORE SIZES FOR ALL SAMPLES.....	158
TABLE 8.5.G: TABULATED VALUES OF $N_{PORE}$ .....	160
TABLE 8.5.H: COMPUTED THEORETICAL CONDUCTANCE OF MEMBRANE AT THE MINIMUM LIMIT OF PORES USING 1 M KCL CONCENTRATION .....	160
TABLE 8.5.I: COMPUTED THEORETICAL CONDUCTANCE OF MEMBRANE AT THE AVERAGE LIMIT OF PORES USING 1 M KCL CONCENTRATION .....	161
TABLE 8.5.J: COMPUTED THEORETICAL CONDUCTANCE OF MEMBRANE AT THE MAXIMUM LIMIT OF PORES USING 1 M KCL CONCENTRATION .....	161

TABLE 8.5.K: TABULATED SUMMARY OF PORE SIZE APPROXIMATION BASED ON MEASUREMENT OBTAINED .....162

TABLE 8.5.L: TABULATED RESULTS BASED ON THE THEORETICAL MODEL DISCUSSED.....166

TABLE 8.5.M: TABULATED COMPUTATIONS BASED ON EQUATION 8.5.8 TO DETERMINE *Daccess2* ..... 172

# List of Equations

---

EQUATION 3.2.1: THE RATIO OF THE DIPOLE INTERACTION ENERGY TO THERMAL ENERGY.....	17
EQUATION 3.2.2: THE MAGNETIC SUSCEPTIBILITY OF A SINGULAR PARTICLE .....	17
EQUATION 3.2.3: EQUATION WHICH DETERMINES THE POINT OF TRANSITION BETWEEN EQUILIBRIUM AND NON-EQUILIBRIUM STRUCTURES .....	19
EQUATION 3.2.4: EQUATION TO DETERMINE THE INTER-ARRAY DISTANCE FOR EQUILIBRIUM STRUCTURES .....	20
EQUATION 4.1.1: CHEMICAL REACTION OF CO-PRECIPIATION OF AQUEOUS FERROUS AND FERRIC SALTS WITH AN ALKALINISING AGENT .....	28
EQUATION 5.2.1: DERIVED SOLUTION FOR ON-AXIS FIELD STRENGTH AT ANY POINT ALONG THE CONCENTRIC AXIS FOR FINITE HELMHOLTZ COIL PAIR SYSTEM (E.DENNISON, 2005) & (D.B. MONTGOMERY, 1961) .....	48
EQUATION 5.2.2: EQUATION TO DETERMINE THE G-FACTOR OF THE HELMHOLTZ COIL PAIR SYSTEM .....	49
EQUATION 7.2.1: EQUATION GOVERNING THE INTER-ARRAY SPACING FOR CELL THICKNESS OF $3 \leq L \leq 800$ $\mu\text{M}$ .....	79
EQUATION 8.5.1: EQUATION TO COMPUTE THE CONDUCTIVITY OF A SINGLE EMBEDDED PORE WITHIN A MEMBRANE .....	147
EQUATION 8.5.2: EQUATION OF THE TOTAL RESISTANCE OF A SINGLE EMBEDDED PORE WITH ACCESS RESISTANCE TAKEN INTO ACCOUNT.....	148
EQUATION 8.5.3: EQUATION OF THE TOTAL CONDUCTANCE FOR A SINGLE EMBEDDED PORE COMPLETE WITH ACCESS RESISTANCE CONSIDERATION .....	149
EQUATION 8.5.4: THEORETICAL MODEL TO OBTAIN PORE GEOMETRY ESTIMATES ASCERTAINED FOR MULTI PORE SYSTEMS.....	149
EQUATION 8.5.5: MODIFIED EQUATION FOR SECOND THEORETICAL PORE MODEL .....	163
EQUATION 8.5.6: GEOMETRIC EQUATION TO DETERMINE THE <i>Daccess</i> OF FIGURE 8.5.H .....	165
EQUATION 8.5.7: EQUATION OF THE SUMMATION OF <i>Raccess</i> FOR A SINGULAR PORE.....	171
EQUATION 8.5.8: EQUATION DETAILING THE TOTAL CONDUCTANCE OF THE MEMBRANE .....	171

# Chapter 1: General Introduction

---

The advent of nanoporous membrane systems has been receiving numerous interests predominantly in the medical and biological applications. For these systems, various methods of fabrication have been researched to fulfil the specific demands of existing applications and to stimulate the development of novel ones. The main goal of the research presented in this thesis is a development of a new manufacturing method of polymeric nanoporous membranes. The originality of the method is based on making use of the self assembly of magnetic nanoparticles.

## 1.1. Aims and Objectives

The main aim of the project was to conduct exploratory work into developing a novel method of producing a polymeric nanoporous membrane. The new method was also aimed to be cost effective and competitive with current membrane preparation approaches.

The identified aims were to be achieved by incorporating the design merits of past works by employing a robust and repeatable method to fabricate these membranes. This was accomplished by the merger of two main design strategies which are the capitalisation of the self-assembly method of the magnetic nanoparticles to create embedded structures that form templates from which can then be selectively removed via chemical etching leaving behind the polymeric material effectively creating a free standing nanoporous platform or film.

## 1.2. Thesis Organisation

The thesis is systematically organised in the following manner; Chapter 2 introduces the reader to several nanoporous membrane systems and their applications with a focus on design limitations and merits. Consequently a research methodology was formulated to develop our technology.

Chapter 3 describes the magnetic interaction in colloidal solutions of the self-assembly phenomena and its mechanics.

Chapter 4 the synthesis method of nanoparticles, particle characterisation and techniques of dispersing them in monomer were also discussed.

Chapter 5 and Chapter 6 detail the technique to fabricate a thin polymeric film out of the colloidal dispersions of magnetic nanoparticles and its subsequent transformation into a nanoporous membrane. The description of the experimental setup used for fabrication is also presented here.

Chapter 7 presents the results of the morphological characteristics of the produced films and membranes by methods of optical microscopy and scanning electron microscopy.

Chapter 8 analyses from the previous chapter received supporting evidence from which presents the results of the ionic conductivity studies via the produced membranes.

Chapter 9 summarises the research work, posing ideas for future work and ultimately concludes the entire project.

## Chapter 2: Literature Review

---

The chapter is organised by establishing the significance of synthetic nanopore membrane technologies and basis of their design strategies. These are primarily divided into two distinctive approaches; the top-down and bottom-up strategies. Additionally they can be split further into sub-groups addressing the different materials used, quantity of nanopores fabricated, pore size customisation and the arrangement of pores. These groups are represented and exemplified accordingly. Furthermore, the description also expands into their applications which are predominantly centred on medical and biological applications. This forms the background knowledge acquired relevant to the field of work.

Next is the introduction to the research methodology by addressing the design merits and limitations of previous works. From here, a solution is formulated by adopting key design elements from past works combined with modifications of others. The research methodology serves as a precursor that outlines the entire mode of research and our resultant conclusions.

## 2.1. Membrane Definition

Membranes are defined as a medium that separates two adjacent environments which allow particles or molecules to traverse through them. These barriers are unique in a sense that traversing matter is done selectively in accordance to particle size or chemical composition. When referring to biological systems, an close example are the cellular membranes consist of a protein channels embedded in lipid bi-layers which allow molecules to pass through them. Similarly, synthetic nanoporous membranes serve to act as barrier that regulates particle or molecular transport between two mediums with no additive requirements and operating at low energy and temperature conditions (Ulbricht, 2006).

The standard classification of porous materials presented by the international union of pure and applied chemistry (IUPAC) clearly states the three division of nanoporous materials which are; Macroporous (pore diameter widths  $>50$  nm), Mesoporous (pore diameter widths between 2 nm to 50 nm) and finally Microporous (pore diameter widths  $< 2$  nm) (Polarz & Smarsly, 2002). Additionally, it was also recommended that nanoporous membrane systems be classified in four elements; membrane materials, membrane cross-section, preparation method and membrane shape (Ulbricht, 2006). For the current work however, membranes fabricated will be termed nanoporous to avoid confusion.

## 2.2. Applications of Nanoporous Membranes

There are various fields in which nanoporous membrane technologies can be applied. Nanopore membranes are typically employed in segregation of molecules (Gaborski, et al., 2010), molecular sensing (Kasianowicz, Robertson, Chan, Reiner, & Stanford, 2008)(Collins, et al., 2008) or releasing chemical components as a means of drug delivery (Desai, Chu, Tu, Beattie, Hayek, & Ferrari, 1998). One such example proposed by Fissell and co-workers (Fissell, Humes, Fleischman, & Roy, 2007) was incorporation of nanoporous membranes as high performance filters in renal replacement procedure for dialysis. Other example of nanoscale systems

replacing their microscale counterparts are integration of nanoscale devices in microfluidics devices (Wang, J.Xu, Chen, & Xia, 2012).

Through frequent research efforts, many scientists have developed several novel fabrication methods of these membrane systems (Adiga, Jin, Curtiss, Monteiro-Riviere, & Narayan, 2009)(Rhee & Burns, 2007). A frequent occurrence of this technology is the production of polymeric nanoporous membranes. Polymeric materials are relatively cheap to produce, highly malleable and chemically stable to oxidising agents such as acids which makes it a very good choice as building materials for this application. In response to the rising interest, our research focused on developing an alternative method to fabricate a polymeric nanoporous membrane. Furthermore the research efforts detail numerous applications and impractical to cover all of them in the description. However there are three consistent trends to which these technologies were applied.

### 2.2.1. Synthetic Nanoporous Membranes as Bio-sensing and Molecular Detection

Bio-sensing and molecular detection systems operate by detecting biological components such as nucleic acids (DNA), microorganisms, viruses, proteins or enzymes. The compositions of these sensors typically involve a nanoporous membrane to segregate the intended components from the bulk to analyse and a transducer to record physiochemical related data (Mo & Fei, 2012). For this type of application, membrane systems typically feature a single pore and rely on precise pore sizes for accurate measurement. The original intention to create one of the first nanopore membrane systems was for bio-sensing and molecular detection. First pioneered by Kasianowicz and co-workers (Kasianowicz, Robertson, Chan, Reiner, & Stanford, 2008); the transmembrane  $\alpha$ -hemolysin protein embedded into a lipid bi-layer to allow single strands of DNA and RNA to traverse through the membrane to be sequenced. However due to particular limitations, synthetic nanopore systems have been procured to rival the capabilities of their organic counterparts (Collins, et al., 2008). Other examples of potential bio-sensing applications include the detection of harmful substances such as 2,4,6-

Trinitrotoluene (TNT), liquid explosives, organophosphorus nerve agents and organic arsenicals and mustard gas (Guan, Liu, & Zhao, 2010).

### 2.2.2. Synthetic Nanoporous Membranes as Filtration Units

Nanoporous membrane systems used in filtration applications typically feature multi-pore configurations. They are fabricated as such to provide quick separation of complex biological samples. These systems can be divided into two sub-types of pore assemblies which are the disordered and the regular patterned porous media.

Disordered nanoporous media rely on complex structures of intertwined materials to conduct filtration. These configuration features high internal surface area which in effect lead to high flow resistance, sample loss (in the molecular scale) and clogging or fouling (Gaborski, et al., 2010). An example of a disordered nanoporous media are the block copolymer membrane systems (Li, Szewczykowski, Clausen, Hansen, Jonsson, & Ndoni, 2011).

Conversely, regular patterned porous media feature ordered cylindrical or close to cylindrical nanopore systems which spans through the membrane thickness. Additionally, pore sizes can be customised to accommodate a wide resolution of filtration sizes. An example of a regular patterned nanopore membrane system is the anodised alumina membranes (Zhang, Liu, Pan, & Zhu, 2007).

Consequently, nanoporous membranes systems as filtration units could be applied in blood purification simulating functions of the kidneys in renal replacements (Fissell, Humes, Fleischman, & Roy, 2007).

### 2.2.3. Fabrication Strategies or Approaches

There are two distinctive fabrication strategies when procuring nanoporous polymeric membranes or nanoscale devices. These said-strategies are termed the top-down approach and the bottom-up approach (Shong, Haur, & Wee, 2010). The top-down approach begins with a bulk material which is patterned onto. For example removal of material using focused electron beam milling (Collins, et al.,

2008) or subtraction of material as a result of selective etching (Dinesh & Pradeep, 2011). The bottom-up approach relies on actual manipulation of molecular components to construct desired structures. For example layer-by-layer assembly techniques which integrates assemblies of predefined architectures into active nanostructures (Jiang & Tsukruk, 2006) or membranes procured by block copolymers (Abetz, et al., 2013).

Nanoporous membranes can be divided into two main types which are organic and the synthetic nanopore systems. Intuitively, this classification entails the materials used in fabrication. For example, the organic nanoporous membranes utilises a trans-membrane protein as an ionic channel that allows macromolecules to traverse through (Kasianowicz, Robertson, Chan, Reiner, & Stanford, 2008). These membrane systems feature only a single pore. On the other hand, the synthetic nanopore membrane systems that exhibit high degree of customisation such as the ability to fabricate a system with multiple pores of a uniform size as well as reproduce single pore systems which are thermally and chemically stable under various environments (Rhee & Burns, 2006) & (Rhee & Burns, 2007).

#### 2.2.4. Organic Nanopore Membrane System

A well established organic nanopore-based system is the biological trans-membrane protein ion channel,  $\alpha$ -hemolysin. Self-assembling monomers secreted from the human pathogen *Staphylococcus aureus* is reconstituted onto a synthetic lipid bi-layers forming an aqueous channel through the membrane (Kasianowicz, Robertson, Chan, Reiner, & Stanford, 2008). This membrane type pioneered the usage of nanopores for DNA detection (Rhee & Burns, 2006). However these membrane systems are typically fragile and susceptible to high operating temperatures or denaturants that disrupt the  $\alpha$ -hemolysin trans-membrane assembly (Branton, Chen, Gu, Brandin, Kim, & Wang, 2004) & (Guan, Liu, & Zhao, 2010)

## 2.2.5. Synthetic Nanopore Membrane System

The advent of synthetic membranes provides opportunities to overcome the limitations of organic nanopore membranes as they could be fabricated through various means, material choice and easily customisable to suit its intended application (Rhee & Burns, 2007). These systems have been the subject matter of nanopore membrane systems for past decades due to their design flexibility, chemical stability, capability to operate at extreme conditions, operational voltages, temperature and solvent variations (Guan, Liu, & Zhao, 2010). There are various novel synthetic nanopore fabrication techniques specific to medical and biological applications that have been produced over the last decade which have been extensively reviewed by Duan and co-workers (Duan, Wang, & Xie, 2013) and Adiga and co-workers (Adiga, Jin, Curtiss, Monteiro-Riviere, & Narayan, 2009). Most notable techniques encompass electron- and ion-beam formed solid-state membranes, subtracting material from fast-ion tracks through chemical etching and procurement of highly ordered honeycomb like structures through non-equilibrium electrochemical etching.

### 2.2.5.1. Micro Fabricated Solid-State Membranes

These membranes are typically made by depositing a combination of silicon (Si) and silicon nitride ( $\text{Si}_3\text{N}_4$ ) layers onto a metallic support. Subsequently a focused electron beam accelerates electrons to impact the Si and  $\text{Si}_3\text{N}_4$  thus gradually removing the material at an atomic level to create a cylindrical pore (Collins, et al., 2008). This process is classified as the electron beam milling technique utilising a field-emission transmission electron microscope.

Another example of micro fabricated solid-state membranes is the ion beam sculpting technique pioneered by Li and co-workers (Li, Stein, McMullan, Branton, Aziz, & Golovchenko, 2001). A bowl shaped cavity embedded on the underside of a  $\text{Si}_3\text{N}_4$  substrate; then material was gradually removed from the top surface through erosion using an ion sputtering system. The entire process was controlled by a feedback controlled loop system that monitors the ion transmission through the

opening and then stopping the erosion process accordingly (Li, Stein, McMullan, Branton, Aziz, & Golovchenko, 2001).

These fabrication techniques typically offer a high degree of pore size selection (1.8 nm to 7 nm) and material customisability which is a key feature. In addition to a single pore system, these membranes are also capable in replicating the pores across the  $\text{Si}_3\text{N}_4$  substrate thus creating a multi-pore system as demonstrated by (Meller, Kim, Wanunu, & Bell, 2006). This fabrication method has an inherent limitation for their low-throughput and requires specialised equipment and skill set to operate. Furthermore the material and material preparation methods can be costly relative to other methods which were discussed.

#### 2.2.5.2. Polymeric Membranes

Polymeric membranes are typically designed through the top-down approach through subjecting a predefined template across a polymer matrix then subsequently selectively etched to remove the desired parts. The most common and widely commercialised technology is the track-etch technique. This fabrication technique employs high-energy nuclear fission fragments to bombard thin polycarbonate films. This in effect damages the material leaving parallel intermittent trails descending along the thickness of the material. Then the material is subjected to a time controlled etch using a chemical etchant which is specific to the polymeric material in effect creating cylindrical pores following the damaged tracks. With regards to pore size customisability, the etching time, pH, temperature and concentration of the etchant defines the size of the fabricated nanopores (Chen, Derlyo, & Baker, 2009). These tracks-etch systems were reported to have a minimum pore diameter of 2 nm (Rhee & Burns, 2007).

Another example of fabricating polymeric membrane systems is by employing thermoplastic nano-imprint lithography. This technique is accomplished by replicating a pattern from a silicon dioxide ( $\text{SiO}_2$ ) mould (made using electron beam lithography and appropriately etched to reveal mould shape) on to a Poly methyl methacrylate (PMMA) resist layer then subsequently polymerised. As PMMA material has poor adhesive qualities with  $\text{SiO}_2$ . The mould could be easily

removed thus revealing a negative imprint of the mould. To create nanopores the mould is patterned to have cylindrical feature; once removed the material is subsequently chemically etched to reveal the pores similarly to the track-etched pores. The reported pore size achievable from this fabrication technique was down to 25 nm (Chou, Krauss, & Renstrom, 1996).

These are low cost techniques relative to the micro machined membrane systems which make them an attractive element to adopt. Although they lack the precision to fine tune the pore sizes, their easy and straightforward fabrication technique are typically sought after. However there have not been innovations to fabricate highly ordered embedded nanopores in polymeric systems with the exception to the thermoplastic nano-imprint lithography.

#### 2.2.5.3. Anodic Alumina Membranes

Anodic alumina membranes are known for their highly ordered hexagonal pore structure resembling honeycomb-like shapes. This process is possible through electrochemical etching of aluminium as the anode to using a specific strong acid; sulphuric acid ( $H_2SO_4$ ). This electrochemical etching process causes the material to erode in that particular honeycomb configuration; this is called the self-organising formation (Jessensky, Muller, & Gosele, 1998). In other words, the process is a highly controlled erosion process which is dependent on control parameters such as the anode potential and selection of acids. Several works have experimented on various setups using acids such as perchloric acid ( $HClO_4$ ) (Lira & Paterson, 2002) or a combination of acids (Zhang, Liu, Pan, & Zhu, 2007) both yielding minimum nanopore diameter sizes of 5 nm to 6 nm.

## 2.3. Proposed Manufacturing Approach

From the discussion above, it is imperative that the next generation of synthetic nanopore membrane systems must incorporate all design merits of current membrane systems whilst circumventing their limitations. Next was to formulate a fabrication technique which capitalises on these design merits and employing characterisation methods to validate the proof of concept.

### 2.3.1. Design Merits and Limitations of Previous Works

The design merits of the micro fabricated membrane systems offer a high degree of precision in terms of pore size selection. However, such systems are not viable for mass-production as they require specialised equipment and materials.

Next was the polymeric systems such as the track-etch nanopores membranes; while they offer a low cost fabrication method suitable for mass production, the resolution of pore dimensions are limited as there are too many factors that dictate the resultant pore parameters. Additionally, there is little control of pore placement across the surface. However a solution was presented in thermoplastic nano-imprint lithography. This technique can be mass produced and can fabricate highly ordered arrangement of nanoparticles. Nevertheless the design was limited by the minimum pore size that technique could produce.

Next technology to be considered was anodised alumina membranes; they offered highly ordered pore locations and the pore sizes were customisable to a certain degree. However the materials used to procure these membrane systems may suffer biocompatibility issues or erosion when in contact with oxidising agents whereas polymeric materials are ideal due to being chemically inert to most oxidising agents.

Consequently, our research attempts to formulate a technique to fabricate a polymeric nanoporous membrane which feature ordered nanopore arrays. Have a decent amount control over pore sizes selection which can rival micro fabrication techniques whilst maintaining a low production cost permitting potential of mass

production similar to track-etch membranes. Subsequently the membrane system must feature the potential of nanopore array patterning similar to the hexagonal structure of anodised alumina membranes but remaining chemically inert from oxidising agents. The design strategy and fabrication method was a combination of the top-down and the bottom-up approaches.

### 2.3.2. Bottom-Up Element of Our Approach

The bottom-up element entails the self-assembly method of a colloidal suspension of magnetite nanoparticles to form columnar structures that arrange themselves or self assemble into weakly ordered two-dimensional arrays. These columnar structures are formed by inducing an external magnetic field and as a result the magnetite nanoparticles aggregate to form chains that coalesce into cylindrical columnar structures that propagate thorough both adjacent membrane surfaces. These nanostructures are tune-able by introducing control parameters such as membrane thickness, particle volume fraction and induced magnetic field strength.

Therefore research work was done to investigate the self-assembly phenomena of these colloidal solutions by exploring their magnetic interactions and relevant devices required that facilitate the assembly and magnetite nanoparticles synthesis.

### 2.3.3. Top-Down Element of Our Approach

The top-down element entails the exploitation of the self-assembly process to produce templates that form the physical shape of the nanopores. This is accomplished by inducing an external magnetic field to start formation of the columnar assemblies. Then while in its liquid state, the monomer solution then subsequently photo-polymerised while the external magnetic field is still on. Consequently immobilising these columnar structures embedded in the polymeric matrix. To create nanopores, the film was then subjected to chemical etching that subtracts the magnetite constituents whilst leaving the polymeric film intact. The resultant product is a template of nanoparticle arrays embedded inside the polymeric film.

Consequently, an investigation to establish a consistent and robust technique to fabricate thin polymer films was achieved adopting film fabrication methods from past efforts from Rybchenko and co-workers (Rybchenko, Dyab, Haywood, Itskevich, & Paunov, 2009) with some modifications.

## 2.4. Summary of Approach

The bottom-up and top-down approaches carried out in this particular sequence stated below:

- Investigation of magnetic dipole interactions of magnetisable nanoparticles in columnar formation. Synthesis of particles and dispersal as a colloidal suspension in a 1,6 – Hexanediol Diacrylate (HDDA) monomer.
- Establishing a robust and reliable method to fabricate thin polymeric films through the incorporating of past works with modifications.
- The application of knowledge acquired from magnetic interaction investigation and producing the relevant devices to procure the self-assembly process.
- Systematic morphological characterisation through optical, scanning electron microscopy with supporting evidence from electrochemical characterisation.

## Chapter 3: Colloidal Solution of Magnetic Nanoparticles: Magnetic Interactions

---

This chapter investigates magnetic interactions and mechanics of colloidal solution of magnetite nanoparticles induced by an external magnetic field. It is imperative to understand the mechanics of the magnetic interactions as the structural outcome of these assemblies directly affect the shape and size of our pores since these columnar structures form the initial pore template.

The chapter begins by providing a brief overview of other applications of these magnetic nanoparticles in the biomedical field and a brief description of the composition and synthesis of nanoparticles. Next was exploring the magnetic interactions that dictate the structural configuration, the transitional phases from gaseous to solid, the transitional point between columnar and more complex structures and inter-columnar spacing. Finally the physical morphology is

discussed as to how the self-assembly technique phenomena occur and generating a speculative outcome shape of a single nanopore template.

### 3.1. Magnetic Nanoparticles: A Brief Review

In past decades, magnetic nanoparticles have been extensively researched for their seemingly limitless modes of application. These applications can be found in various scientific disciplines which have been covered in past scientific reviews (Schüth, Lui, & Salabas, 2007)(Gupta & Gupta, 2005). The sizes of these particles are typically in the ranges of 10 nm – 20 nm. Since its discovery, various types of magnetic nanoparticles have been procured. However, the most ubiquitous type was the iron oxide,  $\text{Fe}_3\text{O}_4$  magnetite nanoparticles chosen to its biocompatibility (Sun, et al., 2006)(Bloemen, Brullot, Luong, Geukens, Gils, & Verbiest, 2012).

This particle type is typically synthesised using wet chemistry where large quantities can be produced. This is accomplished by the co-precipitation of aqueous ferric and ferrous salts by an alkalising agent (Kim, Y.Zhang, Voit, Rao, & Muhammed, 2001). The resultant product of this chemical reaction is a black precipitate suspended in the mixture. The advantage of this method is that the synthesis procedure could be conducted under normal ambient temperature. However the method is has limitation in the fact that these magnetite particles are prone to oxidation if no form of surface modification takes place. Hence these particles are usually treated with an oleic acid surfactant which forms a protective shell around it.

The dispersal of these magnetic nanoparticles into a solvent or carrier to form a colloidal suspension are called magnetorheological fluids or in this case ferrofluids due to its chemical composition of magnetisable iron oxide,  $\text{Fe}_3\text{O}_4$ . The physical interactions of ferrofluids have been a subject of extensive research by various scientists over the past decades (G.Flores, J.Liu, Mohebi, & Jamasbi, 1999), (Liu, et al., 1995), (Ivey, Liu, Zhu, & Cutillas, 2000), (Mohebi & Jamasbi, 1996), (Ricardi & Weis, 2011) & (Ytreberg & McKay, 2000).

## 3.2. Magnetic Interactions

Magnetorheological or ferrofluids are substances which undergo a phase transition from liquid to solid via the influence of an external magnetic field (Liu, et al., 1995). These are colloidal suspensions of nano-sized iron oxide,  $\text{Fe}_3\text{O}_4$  magnetite particles dispersed in oil or solvent based carriers (Mohebi & Jamasbi, 1996) which have a permanent magnetic dipole moment. Inversely, with the absence of a magnetic field, they disperse and undergo a Brownian motion due to a zero net magnetic dipole moment (Ivey, Liu, Zhu, & Cutillas, 2000).

These experiments are typically conducted by inducing an external magnetic field to a colloidal solution of magnetite nanoparticles confined between two parallel plates or substrates; the particles aggregate to form chains that coalesce to form specific structures. These assemblies typically come in two modes which are the columnar and worm- or labyrinth-type structures. This process is termed the self-assembly technique.

Though they present different modes, they share a common factor which is they must span across the entire distance between the two parallel plates. The columnar assemblies have another unique ability where they arrange themselves into hexagonal lattice pattern due to magnetic monopole repulsion. This phenomenon has been extensively researched by scientists but only a handful of applications exploit this capability.

### 3.2.1. Structural Transition of Ferrofluids

Experimentation typically begins with ferrofluids confined between two parallel plates. Structures are formed when the external magnetic field perpendicular to the parallel plates are introduced in gradual ascending increments. Phase transition takes place when the external magnetic field induces a net magnetic dipole moment causing each magnetic nano-particle to interact with it and other particles (Mohebi & Jamasbi, 1996). This in effect causes an alteration from a gaseous or liquid state into solid aggregates of particles (Hong, Jang, Horng, Hsu, Yao, & Yang, 1997)(G.Flores, J.Liu, Mohebi, & Jamasbi, 1999). This is possible to the dipole

interaction energy between two particles,  $E_d$  overcoming the thermal energy,  $k_b T$ . The equation for this ratio can be derived as:

$$\lambda = \frac{E_d}{k_b T} = \frac{\pi \mu_0 a^3 \chi^2 H^2}{9 k_B T}$$

**Equation 3.2.1: The ratio of the dipole interaction energy to thermal energy**

Where  $k_B$  is the Boltzmann constant,  $T$  is the temperature in Kelvins,  $\mu_0$  is the magnetic permeability constant,  $a$  is the radius of the particle (it is assumed that the particles are spherical in shape),  $H$  is applied magnetic field strength in Tesla,  $\chi$  is the magnetic susceptibility of a singular particle:

$$\chi = \frac{\chi_b}{[1 + (\chi_b/3)]}$$

**Equation 3.2.2: The magnetic susceptibility of a singular particle**

$\chi_b$  is the bulk ferrofluid susceptibility. Intuitively, to stimulate dipole interaction between two particles require the ratio  $\lambda$  to be more than 1. To understand the effect of the external magnetic field, Ivey and co-workers have (Ivey, Liu, Zhu, & Cutillas, 2000) have defined four different transitional stages which magnetic induced ferrofluids undergo at different magnitudes of magnetic fields. Figure 3.2.a below are images taken from their work aiding explanation.

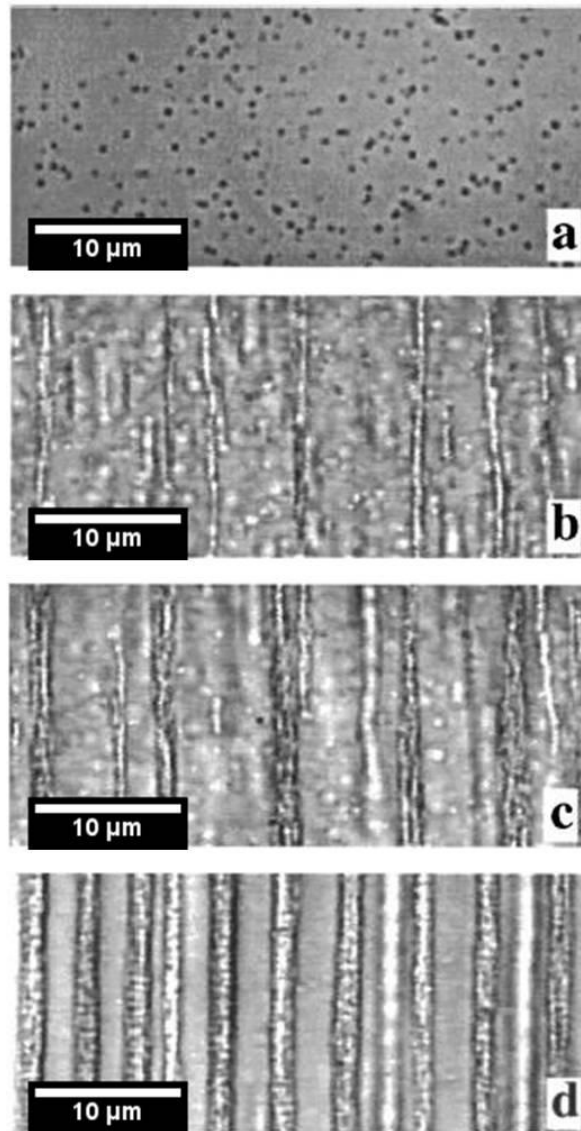


**Figure 3.2.a: Structural transitions of magnetically induced ferrofluids.**  
 (Image taken from Ivey and co-workers (Ivey, Liu, Zhu, & Cutillas, 2000))

They highlighted the phase transition progressions as:

- Randomly dispersed particles (when  $\lambda$  is less than 1) depicted in image A,
- Formation of short chains coexisting with lone particles (nematic-liquid-crystal-like) depicted in image B,
- Formation of longer chains coexisting with shorter chain and lone particles (nematic-liquid-crystal-like) depicted in image C
- Formation of tightly packed columns with no chains or lone particles present (length of longer chains are equal to the distance between parallel plates) depicted in image D.

### 3.2.2. Average Complexity Transition Point between Structural Modes

As discussed before it is imperative that structures obtained from the self-assembly process were columnar structures that were aligned in patterned arrays. Therefore it is important to understand the physical characteristics to these structures.

Magnetically induced columnar structures are formations of magnetite particles that had ample time to find their lowest-energy configuration. This entails controlling the rate at which the external magnetic field is applied deemed as parameter  $R$  (mT/s). The distance of the between the two parallel plates,  $L$  also plays an important role because the average chain separation is dependent on their inherent length (Mohebi & Jamasbi, 1996). Narrower parallel plates allow shorter chains to develop which repel each other better than longer chains which tend to aggregate to form more complex structures. Another factor to consider is the particle volume fraction  $\phi$ . This is important because the increasing the volume fraction decreases the inter-particle distance and increases the dipole interaction between them (G.Flores, J.Liu, Mohebi, & Jamasbi, 1999).

Understanding these parameters, Flores and co-workers through experimentation have derived an equation to define the transitional point between equilibrium (columnar) and non-equilibrium (worm- or labyrinth-type) structures:

$$\langle C \rangle = 1.8\phi^{3.11}L + 0.141 \log_{10} R + 0.83$$

**Equation 3.2.3: Equation which determines the point of transition between equilibrium and non-equilibrium structures**

The variable  $\langle C \rangle$  is the average complexity of the aggregates. They computed that average complexity valued above 1.5 will feature worm- or labyrinth-type structures it is these transitional modes that allow scientists to manipulate these parameters to form two primary modes which are hexagonal ordered array patterned columnar structures or disordered worm- or labyrinth-like structures as seen from past works. With regards to our experimental work, Equation 3.2.3 was used to determine the balance between the control parameters to obtain the desired columnar structures.

### 3.2.3. Inter-Columnar Spacing

Another magnetic interaction to consider is the arrangement of columnar structures once they have past the structural transition (mentioned in Section 3.2.1) of the formation of columns with no chains or lone particles present. Since they align themselves in hexagonal patterned arrays, the inter-array spacing can be considered. Liu and co-workers (Liu, et al., 1995) have determined the correlation between the inter-array spacing  $d$  and the spacing between the two parallel plates  $L$ . The equation for this correlation can be derived as:

$$d = 1.33L^{0.37}$$

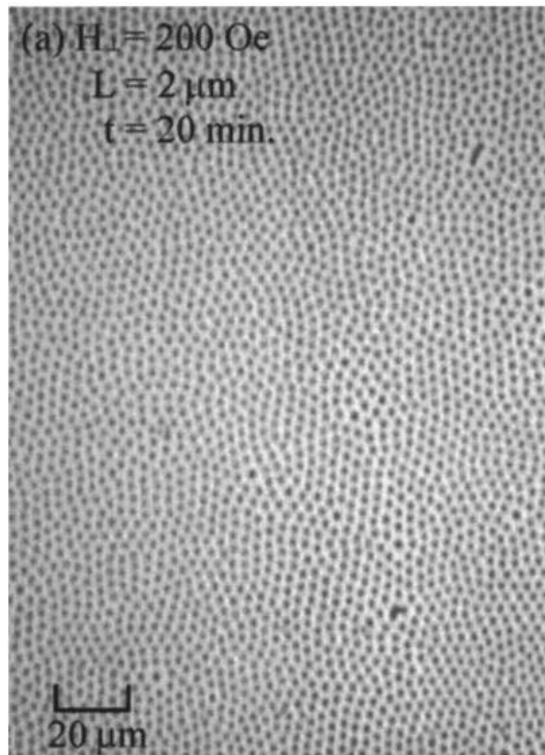
**Equation 3.2.4: Equation to determine the inter-array distance for equilibrium structures**

They have also determined that this correlation only holds true when the spacing is at  $3 \mu\text{m} \leq L \leq 800 \mu\text{m}$  and a volume fraction of  $0.04 \leq \phi \leq 0.2$ . It was also reported that increasing  $\phi$  forms thicker columns instead increasing the number of columns formed. Equation 3.2.4 was used comparatively with the results obtained in our experimentation.

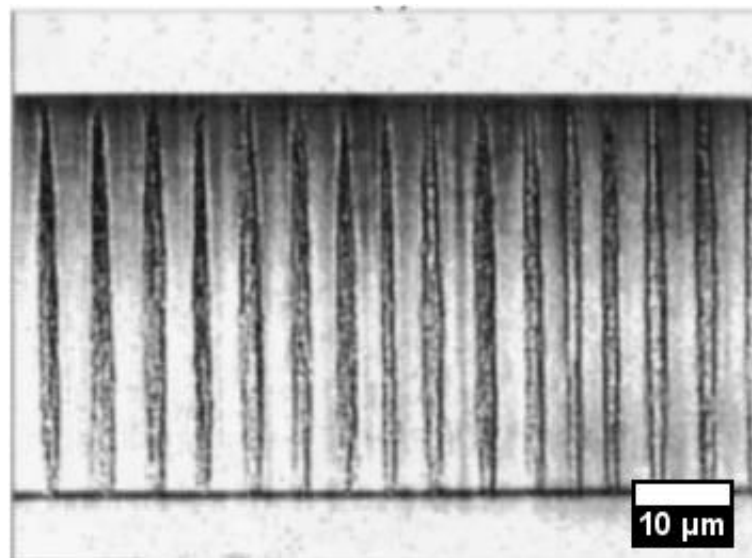
## 3.3. Physical Morphology of Structures

For this research, we are only interested in columnar structures. Therefore understanding their physical morphology is important as it dictates the final form of the nanopore produced.

These columnar structures retain hexagonal pattern arrangement is due to the monopole repulsive forces. Fully formed columns have the same polarity on the top ends and likewise at the bottom i.e. the top ends of all columns will carry a northern polarity and vice versa at the bottom ends. Hence by the law of magnetism, each column ends will in effect repel each other neighbouring chain. As a result fully formed columns are situated equidistant from each other neighbouring column and is said to be in equilibrium state as seen in Figure 3.3.a.



**Figure 3.3.a: Top view of the structural configuration formed using  $\text{Fe}_3\text{O}_4$  magnetite particles magnetic field is parallel with viewing angle (Image taken from (Hong, Jang, Horng, Hsu, Yao, & Yang, 1997))**



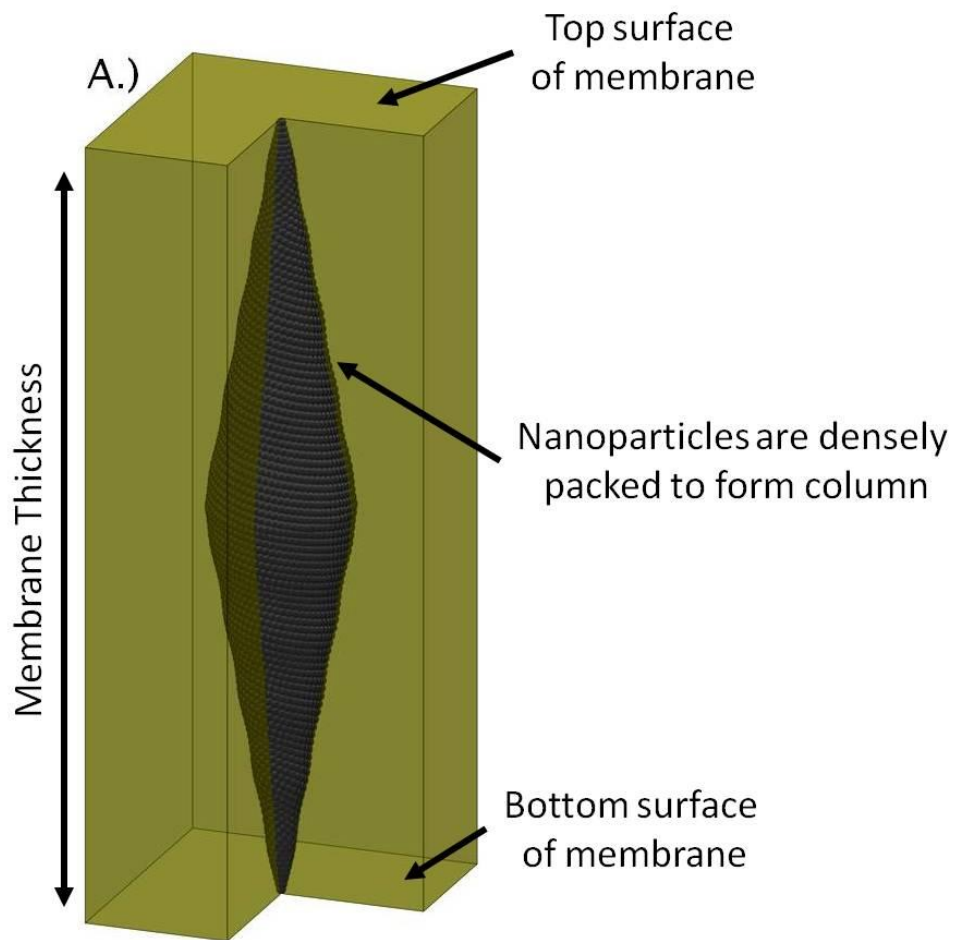
**Figure 3.3.b: A cross-sectional view of the structural configuration formed using  $\text{Fe}_3\text{O}_4$  magnetite particles magnetic field is perpendicular to viewing angle (image taken from (G.Flores, J.Liu, Mohebi, & Jamasbi, 1999))**

Figure 3.3.b demonstrates a typical structural configuration of columnar structures from a cross-sectional view. It is understood that the tip of the two opposite ends have a stronger magnetic field strength as compared to the middle of the column

hence the tips typically converge to a concentric point demonstrated in Figure 3.3.b. This meant that there is clear descending gradient of magnetic field strength. Therefore the repulsive energy progressively decreases as one move toward the centre from either side of the tips; thus causing the columns to have the signature tapered ends. However no specific references were found to characterise the physical dimension of the columnar shapes. Additionally, Liu and co-workers (Liu, et al., 1995) and Ivey and co-workers (Ivey, Liu, Zhu, & Cutillas, 2000) have shown that these tips do not necessarily converge into a single concentric point but have been known to fray in which they have defined as split-ends. This is due to the formation of thicker neighbouring short chains among a larger chain ends causing them to shift along laterally with respect the central axis of the column.

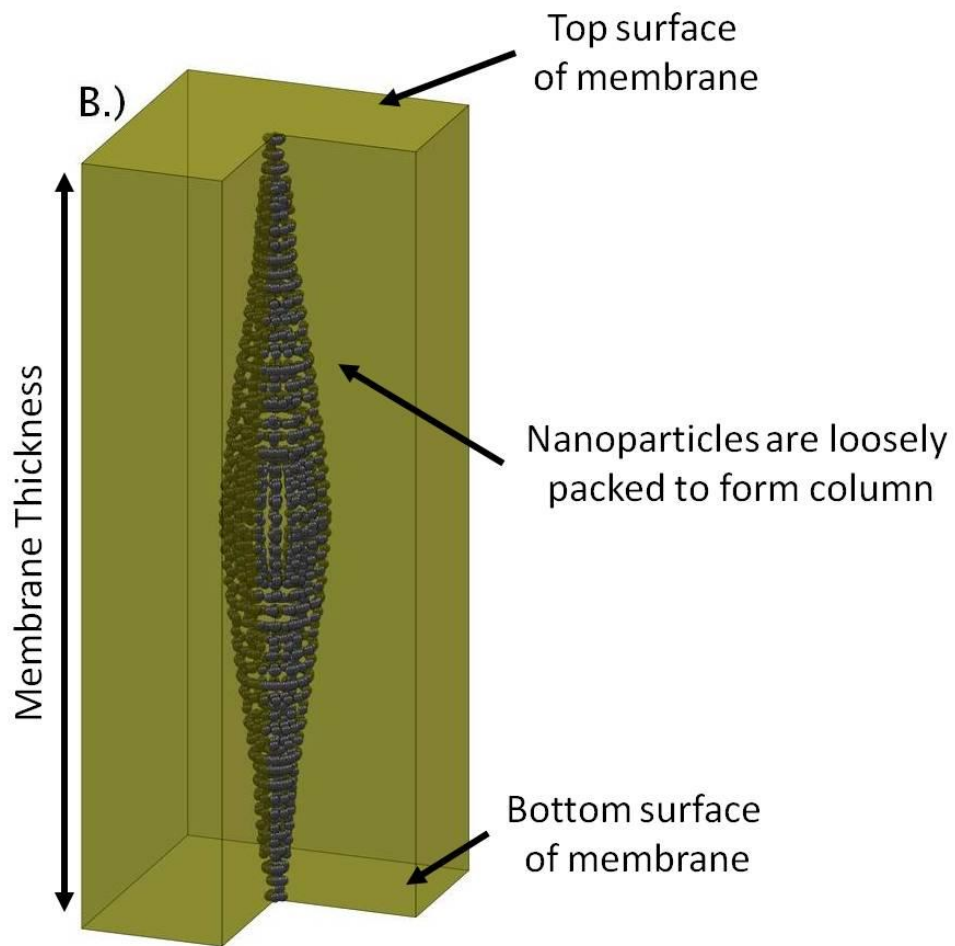
### 3.4. Template of Nanopore

Taking these theories and past experimentation in to consideration, it is possible make an intuitive speculation of morphologies of a singular nanopore template. Firstly the general shape of a singular columnar structure must feature its signature tapered ends due to the aforementioned monopole repulsive forces at both ends. Subsequently it is also possible to speculate the density of the column assembly. The ideal column will feature a tightly packed column of nanoparticles of homogenous diameters and sizes however in practice irregularities in particle size are always present hence a separate speculative model must considered featuring a lesser dense column. Finally, the phenomena of split ends must be taken into account as well hence a third speculative model was considered featuring a lesser dense column with split-ends. Illustrated in Figure 3.4.a through Figure 3.4.c are three speculative artistic renditions of single nanopore template which are represented in the form of a cut-out view.



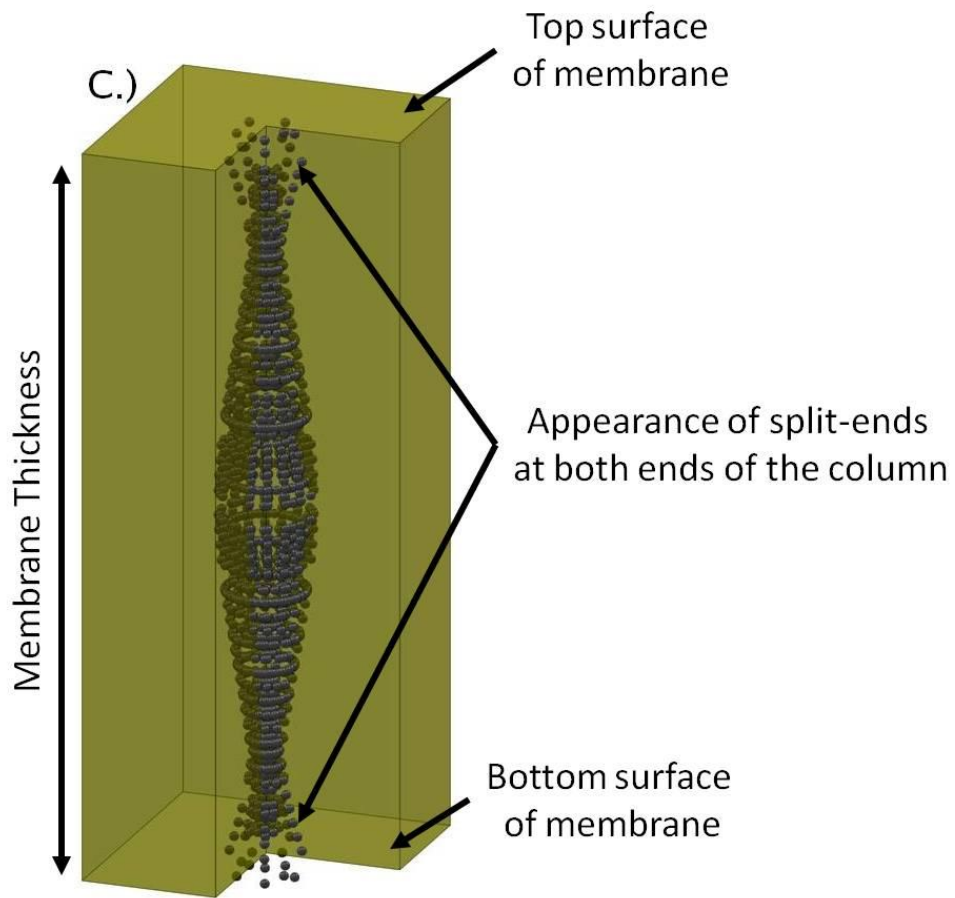
**Figure 3.4.a: Diagram illustrating of speculated shape or single nanopore (Dense column)**

Image A represents the ideal pore shape which was previously discussed; a well packed structure with pin-point tapered ends which most importantly spans thorough then entirety of the membrane thickness. The transparent yellow material is physical representation of the membrane layers.



**Figure 3.4.b: Diagram illustrating of speculated shape of single nanopore (Semi dense column)**

It is also important to note that Like A, image B has pin-point tapered ends but does not feature tight packing of nanoparticles. This is to compensate for possible size irregularities or partial pre-aggregation of  $\text{Fe}_3\text{O}_4$  particles. Although these templates feature a semi-dense structure, the particles are inter-connected through the top and bottom surface regardless.



**Figure 3.4.c: Diagram illustrating of speculated shape or single nanopore (Semi dense column with split ends)**

Finally image C is a nanopore template that features split-ends as discussed previously. This column configuration should generate pores with multiple small openings across the surface of the membrane but also must be inter-connected through the entirety of the thickness.

## 3.5. Chapter Summary

This chapter has described the importance and potential of magnetic nanoparticles and understanding their magnetic interactions of magnetically induced structures in ferrofluid form. This was covered in Section 3.1.

Furthermore various magnetic interactions and structural transitions of these magnetic nanoparticles have been explored in Section 3.2.1 detailing the assembly sequence of the self-assembly process which is utilised the current research.

Finally, the physical morphology of equilibrium structures was described in Section 3.3 which enabled the speculation of expected columnar placement configuration and shape of the nanopore template demonstrated in Section 3.4. These speculative configurations are important as it aid in the identification of the embedded structures during qualitative inspections.

## Chapter 4: Colloidal Solution of Magnetic Nanoparticles: Synthesis

---

This chapter describes the methods used to synthesise and characterise the iron oxide,  $\text{Fe}_3\text{O}_4$  magnetite nanoparticles which were subsequently dispersed in a 1,6-Hexanediol Diacrylate (HDDA) monomer.

The techniques used here are an amalgamation of several synthesis methods from previous works (Argawal & Maity, 2006) & (Dyab, Ozmen, Ersoz, & Paunov, 2009) which all were incorporated into one. The synthesis of the iron oxide,  $\text{Fe}_3\text{O}_4$  magnetite nanoparticles in used our experimental work was described here. The synthesis method of choice was the co-precipitation via wet chemistry method as a quick method to procure these iron oxide,  $\text{Fe}_3\text{O}_4$  nanoparticles. These methods are well established methods which are have been widely used.

Subsequent to synthesis the particles were coated with a layer of oleic acid surfactant disallowing the particles to agglomerate due to Van der Waals attractive

forces. Some exploratory work was conducted here to obtain the best dispersal of particle within its carrier solution.

Next was to establish a method to determine the ratio of volume of particles per the bulk HDDA solution. Finally the average sizes of these synthesised particles were determined via transmission electron microscopy (TEM) image characterisation.

## 4.1. Synthesis of $Fe_3O_4$ Magnetite Nanoparticles

The  $Fe_3O_4$  magnetite nanoparticles were produced by means of co-precipitating an aqueous mixture 5.406g ferric chloride hexahydrate ( $FeCl_3 \cdot 6H_2O$ ) and 1.988g ferrous chloride tetrahydrate ( $FeCl_2 \cdot 4H_2O$ ) using ammonium hydroxide ( $NH_4OH$ ). The chemical reaction was conducted under a nitrogen atmosphere. Chemicals used were procured by Fisher Scientific.

The synthesis begins with de-oxygenising deionised water in attempt to remove as much oxygen in the solution as it is an oxidising agent. This was accomplished by bubbling nitrogen gas ( $N_2$ ) into the volume of water. Then the ferric and ferrous salts were dissolved in the deionised water in a 1.75:1 ratio<sup>1</sup> in moles. The mixture was then transferred into a tri-neck flask with a mechanical stirrer attachment. The mixture was stirred constantly and while also bubbled with  $N_2$  through the entirety of the chemical reaction.  $NH_4OH$  was introduced into the mixture to start the precipitation reaction. The final precipitate should appear as a black suspension. Using a simple litmus test, the pH level of the solution should register above 12. The corresponding reaction can be written as (Gupta & Gupta, 2005):



**Equation 4.1.1: Chemical reaction of co-precipitation of aqueous ferrous and ferric salts with an alkalising agent**

Then the particles were collected by magnetic decantation and subsequently rinsed with the de-oxygenated deionised water repeatedly. This process usually takes 4

---

<sup>1</sup> Argawal and co-worker (Argawal & Maity, 2006) reported that to maintain the 2:1 ratio was not as straightforward as the  $Fe^{2+}$  is oxidised to back to  $Fe^{3+}$  under oxidising environment. Therefore a smaller molar ratio <2:1 was introduced as compensation.

washes or until the pH level of the solution has dropped to neutral. This completes the magnetite nanoparticle synthesis.

#### 4.1.1. Surface Modification of Magnetic Nanoparticles

An investigation of the coating methods were conducted to find the best dispersity in the carrier monomer solution HDDA sensitized with photo initiator Diphenyl (2,4,6- trimethylbezoyl) phosphine oxide to facilitate photo-polymerisation. Particles synthesised from metals are prone to oxidation which affects their magnetisation capabilities and the final outcome of their size (Schüth, Lui, & Salabas, 2007). Therefore the newly synthesised magnetite nanoparticles require a protective shell to inhibit any oxidising agents from entering its surface and to aid the dispersion HDDA monomer. Various techniques (Argawal & Maity, 2006)(Schüth, Lui, & Salabas, 2007) have been introduced to modify the surface of these nanoparticles. Oleic acid was found to be a compatible surface modification agent for  $\text{Fe}_3\text{O}_4$  particles. However the compatibility of the surface modification agent or surfactant with a monomer carrier solution such as HDDA has not been fully explored.

Therefore a series of experimental trails was conducted to explore the best surface modification method for particle dispersion in HDDA. Uncoated newly synthesised particles were subjected to various oleic acid coating regimes before and after the final rinsing and during synthesis. For simplicity sake, the trails were tabulated and explained.

Sample	Surface Modification Technique: Regime 1					
	Added Hydrogen Peroxide	Rinse and stir at room temperature (DI)	Rinse and stir at 70° -80° (DI)	First Isopropanol Rinse	Second Isopropanol Rinse	Warm Isopropanol
1		✓		✓		
2		✓		✓	✓	
3		✓		✓		✓
4		✓		✓	✓	✓
5			✓	✓		
6			✓	✓	✓	
7			✓	✓		✓
8			✓	✓	✓	✓
9	✓	✓		✓		

**Table 4.1.a: Surface modification technique for regime 1**

The techniques are carried out in sequence that is interpreted from left to right. The ✓ symbol represents that the technique has been carried out. The warm isopropanol column stated in the table represents the temperature at which the first and second rinse was carried out (40 °C – 50 °C). The abbreviation DI represents deionised water. This regime starts by collecting the particles via magnetic decantation and draining the deionised water. Next, the oleic acid was added ( $\approx 1$  mL) after rinsing with DI water at a neutral pH.

Sample	Surface Modification Technique : Regime 2	
	First Isopropanol Rinse	Second Isopropanol Rinse
10	✓	
11	✓	✓

**Table 4.1.b: Surface modification technique for Regime 2**

For regime 2, the oleic acid was added prior to the repeated rinsing to neutralise the solution pH level. Upon obtaining a neutral pH the solution was heated to 80°C for 30 minutes. Only then the magnetic decantation, draining and isopropanol rinsing began. These samples were then dispersed in a HDDA monomer solution subjected to ultrasonic agitation for 30 minutes.

Regime 3 was an amalgamation of the first and second where small volumes of oleic acid (0.2 ml) were added to the particles at each deionised water rinse interval. Upon obtaining a neutral pH, the sample (Sample 12) was only rinsed once in isopropanol at room temperature. Next, the particles were dispersed in a mixture of 1 part styrene followed by a 10 part HDDA solution then the photo

initiator was introduced (0.5 wt %). This was followed by ultrasonic agitation for 30 minutes.

Finally samples 1 through 12 were stored overnight to allow the particles to sediment. Consequently they were characterised visually by accessing their dispersity and observing signs of sedimentation after a period of 24 hours. Figure 4.1.a below demonstrates sample 8 and 9 after the 24 hour waiting period.

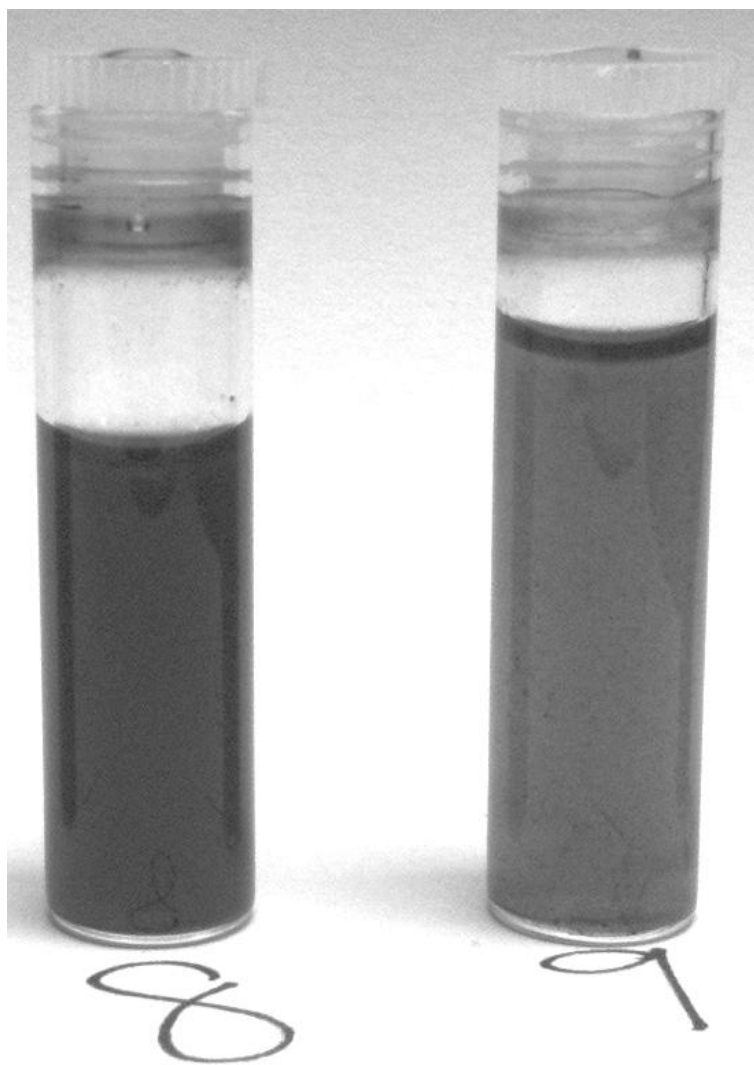


**Figure 4.1.a: Visual comparison of sample 8 and 9 after 24 hour waiting period**

To determine that a sample was indeed colloidal, there should not be any signs of sedimentation or floating aggregates after the 24 hour waiting period. For example Figure 4.1.a, sample 8 on the left was found to be better dispersed as compared to sample 9 where signs of sedimentation were found collected at the bottom of the

vial. Through these experimental trails, Sample 12 from Regime 3 was found to have the most stable colloidal suspension in the HDDA monomer solution. Therefore, the all subsequent samples used for experimentation were synthesised and coated using Regime 3 unless stated otherwise.

#### 4.1.2. Managing the Volume of Extraction

Intuitively before dispersing of  $\text{Fe}_3\text{O}_4$  magnetite nanoparticles in the HDDA monomer carrier solution, a simple quantitative study was conducted to obtain an approximated value of the bulk volume of nanoparticles when extracting the colloidal particles in the isopropanol mixture.

A designated volume was extracted from the colloidal particles in the isopropanol mixture using a micropipette and deposited into another container and weighed. The sample was then dried completely to remove the remaining isopropanol and weighed again to obtain the effective weight of nanoparticles after drying. Density of  $\text{Fe}_3\text{O}_4$  was determined as  $5 \text{ g/cm}^3$ , therefore the effective nanoparticle volume can be derived.

Therefore a ratio between the effective volumes of nanoparticles to volume of HDDA monomer  $\phi^2$  could be established. This test regime allowed subsequent experimentations to operate at consistent concentrations.

#### 4.1.3. TEM Characterisation of Magnetic Nanoparticles

TEM characterisation was conducted to determine the effective particle size. This was achieved by embedding multiple stacks<sup>3</sup>  $\text{Fe}_3\text{O}_4$  embedded polymer film platforms sandwiched on top of each other in to resin. The preparation technique was similar method used in previous works (Ward, Chun, Queenan, Calabro, Morales, & Becker, 2010).

---

<sup>2</sup> Variable  $\phi$  was defined as the particle volume fraction previously discussed in Chapter 3:

<sup>3</sup> The  $\text{Fe}_3\text{O}_4$  magnetite nanoparticles embedded polymer films were fabricated in accordance to our developed technique. Description technique these films is covered in Chapter 5: Section 5.1.2.

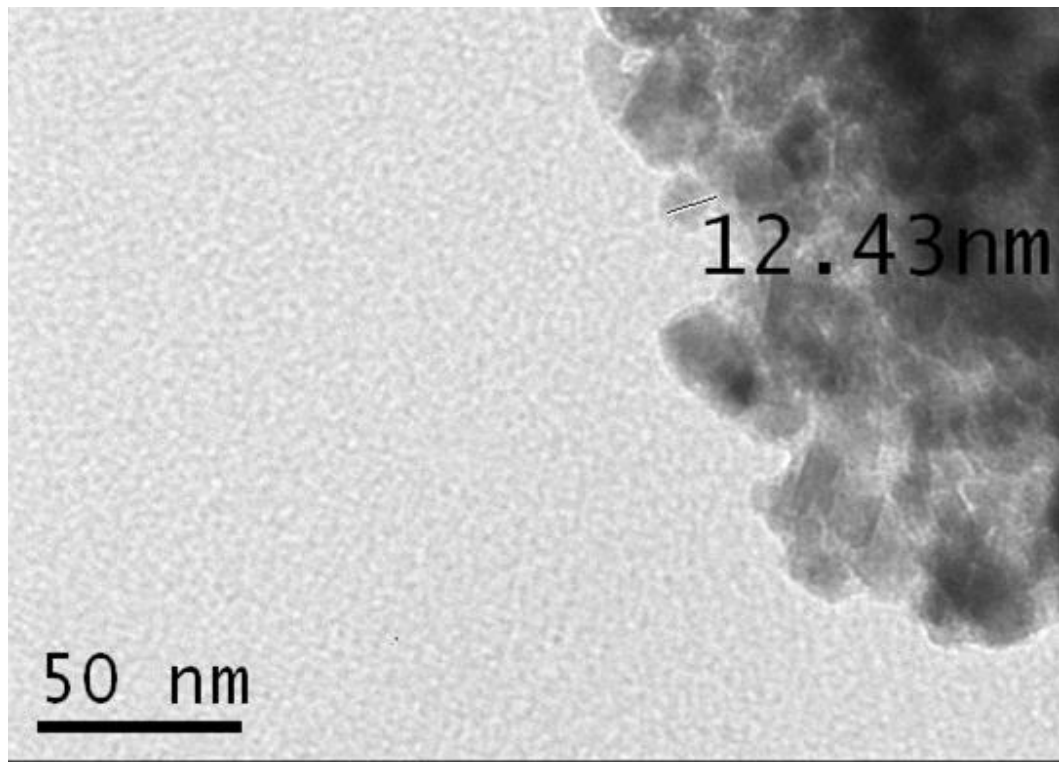


**Figure 4.1.b: Image analysis conducted on the embedded Fe<sub>3</sub>O<sub>4</sub> constituents within the polymer film at 158000x magnification**

Figure 4.1.b demonstrates a colony of Fe<sub>3</sub>O<sub>4</sub> constituents. Energy dispersive X-ray spectroscopy (EDX) was conducted as supporting evidence for element identification and analysis confirms that the colonies were indeed iron based. Upon closer inspection, the effective diameter of a singular magnetite nanoparticle was measured (indicated by the straight line on the top right of the image). The image analysis indicates that the effective size of the magnetite particle to be approximately 12 nm.

This result confirms the synthesised magnetic nanoparticle were within the critical value of 10 nm – 20 nm range (Schüth, Lui, & Salabas, 2007). For confirmation, the effective sizes of the particle were compared with the data obtained from Dyab and co-workers (Dyab, Ozmen, Ersoz, & Paunov, 2009) and Lee and co-workers (Lee, Isobe, & Senna, 1996) which they have claimed the critical particle size to be 25 nm where they switch from ferromagnetic to superparamagnetic. This was possible because any causation for thermal fluctuations can alter the magnetisation direction of a singular particle.

This meant that the particles should exude a zero dipole moment upon the absence of magnetic excitation. This was imperative as any remnants of magnetic interactions will cause the particles to agglomerate into larger assemblies even without magnetic excitation compromising their effective size. Based on the resultant diameter of our magnetite particles, they should demonstrate similar magnetisation curves obtained by Dyab and co-workers (Dyab, Ozmen, Ersoz, & Paunov, 2009) since the both share similar synthesis methods and particle size.

## 4.2. Chapter Summary

This chapter has covered the aspects of the application and potential of magnetite nanoparticles and subsequently their synthesis. Particle synthesis procedures were detailed utilising wet chemistry covered in Section 4.1 and instilled surface modifications to inhibit oxidation and aid the dispersal of particle in HDDA solution then sensitise with a photo initiator described. This was described in Section 4.1.1. From this, a robust and repeatable method of synthesizing and coating method has been established ensuring a consistent quality of nanoparticles which in turn translate into consistent quality of assembly of columnar structures.

The extracted volume of synthesised particles was quantitatively characterised. These allowed subsequent samples to be have a consistent nanoparticle concentration when dispersed the HDDA monomer solution covered in Section 4.1.2. This method ensures all subsequent samples procured from the membrane fabrication process have a quantifiable volume fraction,  $\phi$  as it is an important variable that governs final configuration of the self-assembly process.

Finally, the effective size of the procured magnetic nanoparticles was established through TEM analysis and was found to be in agreement within the critical range suggested from past works and data covered in Section 4.1.3.

## Chapter 5: Device Design

---

This chapter highlights the fabrication of devices to aid the experimental process. A total of three relevant design elements were identified for successful experimentation: establishing a reliable method to fabricate thin polymeric films, the fabrication of an external source of magnetic field which simulate field conditions similar to past works (Liu, et al., 1995) & (Ivey, Liu, Zhu, & Cutillas, 2000), the appropriate power source and the development of a control system for the corresponding magnetic field source. Once identified, the elements were addressed individually by adopting design concepts and acquiring quantitative data which was comparable with previous experiments.

The chapter begins by identifying the first design element which was the establishment of a reliable method to fabricate thin polymeric film. The rationale behind this was to fabricate a stable free-standing polymeric platform. To address this, two fabrication methods were developed but only one was chosen of which details were covered. The main goal was to contain a photo-polymerisable colloidal dispersion of magnetic nanoparticles to a specific area at which the magnetic flux

can intersect the solution inducing the self-assembly process. Equally important was that the specimen required a source of ultra-violet (UV) radiation under a nitrogen atmosphere. Finally this method must be straightforward to operate and cost effective to facilitate the potential of mass production.

The second design element to address was the development of a magnetic field source. For this, several conditions were put forward; the magnetic field source constructed must produce homogenous fields because these columnar assemblies rely on chains of nanoparticles to coalesce concurrently to the invisible flux lines that intersect it. A good example of an electromagnetic device that fits the description is the Helmholtz coil pair system. As the name suggests, the system uses two electromagnet coils with equal radii separated by the length of their radius. It creates a relatively homogeneous field in the space between the two coils along the central axis of the coils but only to a certain extent.

Once these devices were in place, a suitable electrical power source was required which allowed incorporation of a programming infrastructure. This was imperative as these nanoparticle assemblies require sufficient time to aggregate into the desired columnar array assembly under magnetic dipole excitation. Therefore a control system was produced. These elements addressed present all findings and relevant design data.

## 5.1 . Establishing a Fabrication Technique

It was imperative to understand all the important factors to incorporate into a successful design as it dictates the following devices and apparatuses needed. Experimental trails have led into two methods of fabrication but only one of which was chosen for the task at hand. Nevertheless the design data for two methods investigated will be detailed in the following section.

For this, two fabrication methods were developed:

- The creation of a thin bubble membrane through the application of small controllable increments of air pressure gradients.
- The confinement of the polymer solution between two glass substrates creating a sandwich effect.

Both techniques were researched to take advantage of the inherent characteristic of producing a thin polymer film and coupled with the possibility of instant curing capabilities via photo-polymerization. These methods were put through rigorous experimentation and it was finally determined that the fabrication method of choice for this work is a similar iteration of the previous works accomplished by (Rybchenko, Dyab, Haywood, Itskevich, & Paunov, 2009).

#### 5.1.1. Fabrication of Thin Films: Bubble Membrane Generation

The following discussion attempts to present findings based on a fabrication technique that exploits the method of generating bubble membranes by establishing an understanding of the thinning or draining mechanism undergone by a bubble membrane. Factors that cause this draining mechanism entail convection, evaporation or suction produced by pressure gradients (Isenberg, 1992).

Utilising pressure gradients, a bubble generation device based on the manometer principle was conceptualized which aimed to produce a stable bubble membrane across a predefined sized channel outlet. The aim was to polymerise the membrane whilst in its pressurised state. The pressure was applied by incremental translation of the opened end of the tube whilst the other remains stationary creating a pressure difference in the tube as the solution within the tube traverses towards the stationary end. This setup enables the user to apply and control the pressure at the other end at small and precise increments. An illustration of the experimental setup is depicted in Figure 5.1.a.

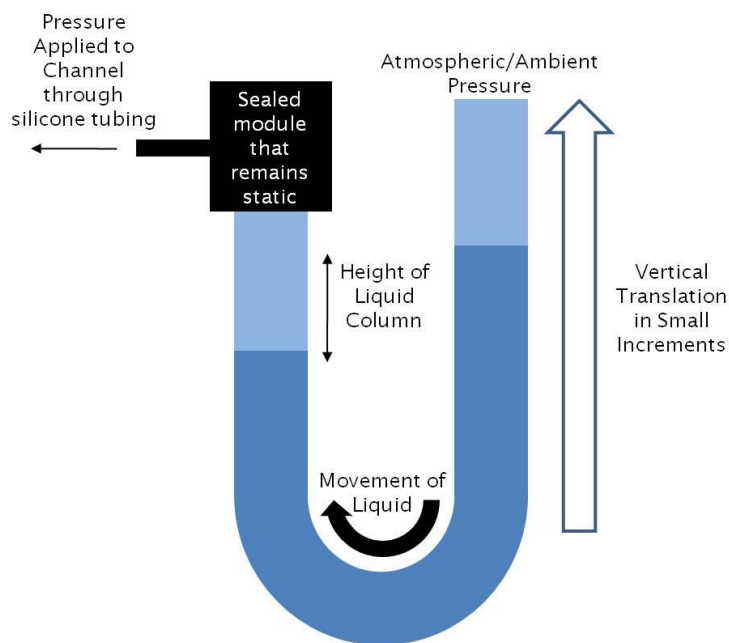


**Figure 5.1.a: Device to generate a pressure gradient to generate a bubble membrane**

The static part of the device incorporates the bubble membrane holder illustrated in Figure 5.1.b. The holder comprises of a copper foil with a tiny perforation connected to rigid plastic tubing. A series of liquid samples in this case the iron oxide,  $\text{Fe}_3\text{O}_4$  particles dispersed in HDDA were extracted and swabbed across the copper foil surface. This wets the entire perforation and creates a suspended liquid membrane. The tubing system in its position of origin does not exhibit pressure gradients. The experiment begins by moving the open end of the U-tube upward in known vertical translations whilst keeping the sealed module in a static position in effect causing a pressure gradient which pushes the solution upward generating the draining mechanism.

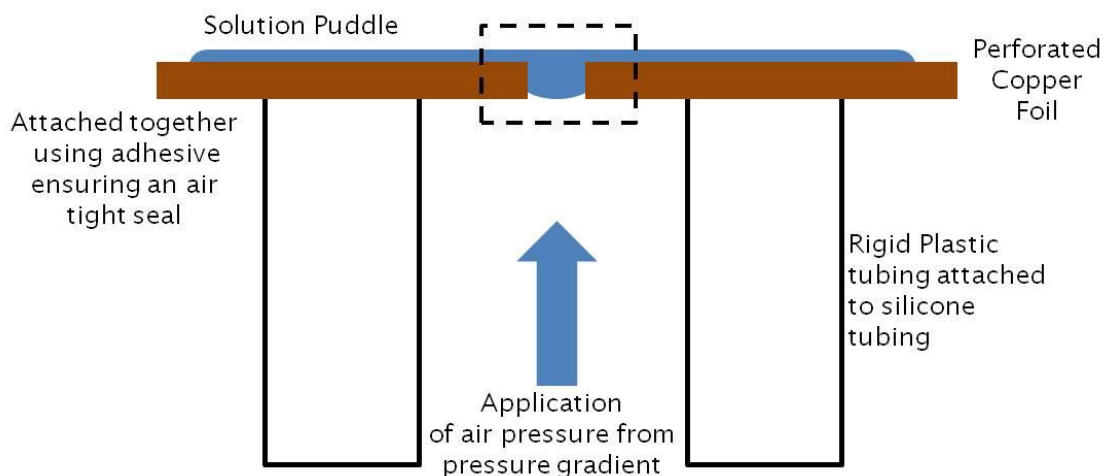


**Figure 5.1.b: Stage fabricated for bubble membrane fabrication**

The schematic in Figure 5.1.c illustrates the bubble formation process from the manipulation of pressure gradient causing the entrapped air bubble to form a thin membrane as it approaches the surface of the solution.

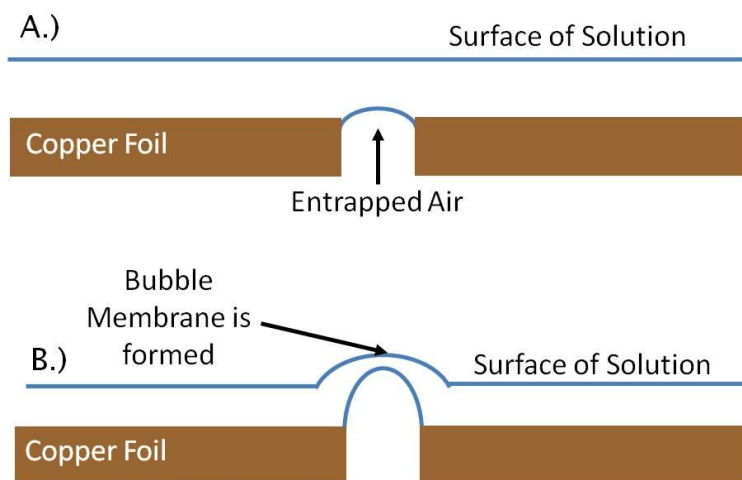


**Figure 5.1.c: (A.) Early stage of the bubble membrane formation; Entrapped air forms the initial shape of the bubble (B.) Actual formation of the bubble membrane when entrapped air approaches surface of solution**

Attempts to create these thin films using this technique have produced some interesting results as it was possible to create liquid thin films which were in the nanometer scale range. This is confirmed by the sighting of the Newton black film (Isenberg, 1992). These films are typically are 30 – 35 Å in thickness (3 – 3.5 nm). The series of images below is a demonstration of the propagation of the Newton black film annotated by the arrows. The progression of the experimentation came

to a halt when the photo-polymerisation process took place as it caused instabilities on the bubble surface causing it to rupture.

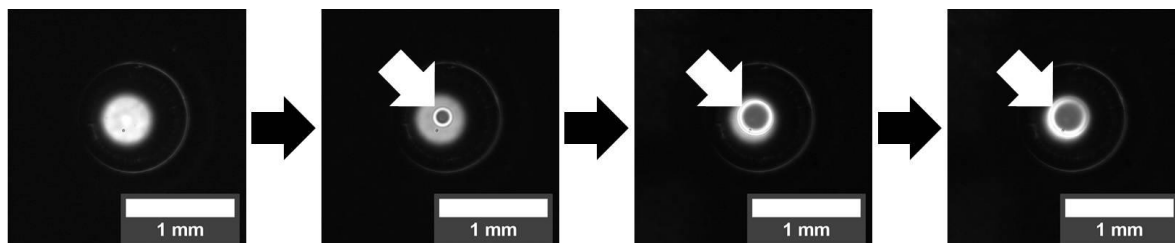


**Figure 5.1.d: Propagation of the Newton black film indicated with the white arrow**

Figure 5.1.d is sequence of events (viewed from left to right) taken from our optical microscopy images perpendicular to the surface of the perforated copper foil. The images demonstrate the propagation of the Newton black film annotated as the emerging dark spot from the centre. Through our efforts, the film was stable for about 5 minutes before rupture occurs.

### 5.1.2. Fabrication of Thin Films: Confinement between Two Substrates

This film fabrication procedure is an adaptation of the past works of Rybchenko and co-workers (Rybchenko, Dyab, Haywood, Itskevich, & Paunov, 2009) which feature additional modifications. The fabrication technique they employed utilised two indium tin oxide coated glass substrates that constrain a colloidal solution of magnetite nanoparticles. These substrates were separated by small silica spheres which provided sufficient spacing for the nanoparticles to conduct Brownian motion (particle size  $\ll$  silica sphere size). This technique was reminiscent of liquid crystal display technology where a similar configuration was employed (Soref, 1974). Figure 5.1.e is demonstrated to compliment the description.

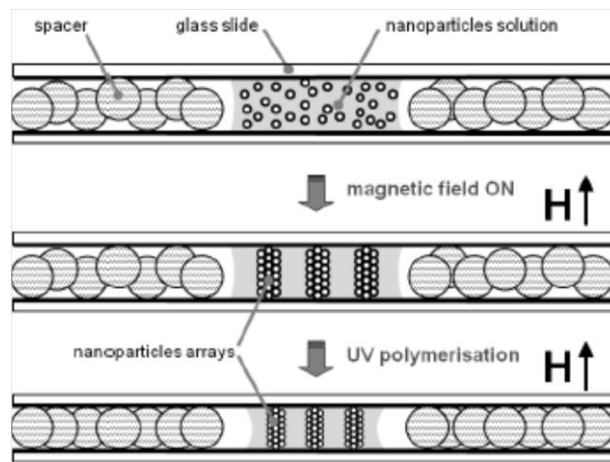


**Figure 5.1.e: Device schematics procured by S. Rybchenko et. al. Illustrating the thin polymer film fabrication technique (Rybchenko, Dyab, Haywood, Itskevich, & Paunov, 2009)**

Next, an external magnetic field perpendicular to the substrate ( $H\uparrow$  denotes the field direction) was induced to facilitate the self-assembly process. Then the samples were photo-polymerised via UV radiation from a high-pressure mercury lamp while the magnetic field is still on. This effectively immobilises the embedded constituent inside the HDDA matrix which was reported to be sensitized with 0.5 wt % of Diphenyl (2,4,6 –trimethylbenzoyl) phosphine oxide. The resultant product reported was an array of immobilised columnar structures embedded in a thin polymeric film.

This method was chosen for its potential as a low cost fabrication technique that utilises basic materials additionally its capability to polymerize under UV radiation with no risk of rupture demonstrates the system’s robustness as exclaimed in Section 5.1.1.

In our fabrication method, the spherical silica spacers were substituted with low density polyethylene (LDPE) film as the spacers for the parallel substrates. This modification effectively abolishes the difficulty of obtaining an even distribution of spherical silica spacers around the substrate borders whilst still maintaining constant thicknesses. This was important as irregularities in spacer thicknesses causes unwanted travelling of the solution across the substrates surface. As a result of capillary forces; additionally, there was no need for coating the glass substrates.

HDDA solution used for the experimentation is prone to oxygen contamination that inhibits photo-polymerisation. Thus specimens were kept in an oxygen free environment during fabrication via the introduction of nitrogen gas into a sealable containment unit.

It was also imperative that the specimen containment unit could fit inside the space between the Helmholtz coil pair system where the homogenous flux lines intersect the specimen perpendicularly. The configuration of the containment unit is illustrated in an exploded view below.

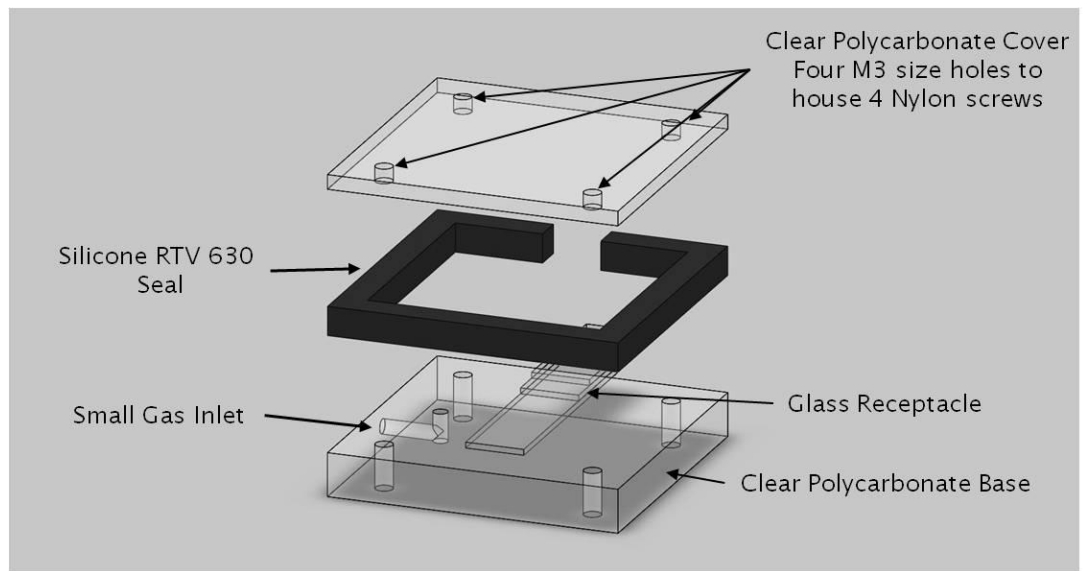


**Figure 5.1.f: Final assembly of the specimen housing**

The black segment labelled as silicone RTV 630 seal from Techsil acts as an air tight seal that surrounds the sample whilst nitrogen enters through the small channel within the polycarbonate base. It is imperative that the base and the top cover should be optically clear to allow sample viewing during the experiment. The entire cell was secured together by four M3 nylon screws secured into the tapped polycarbonate base. The small gas inlet on the side of the base is connected by silicone tubing of the appropriate size.

Intuitively the materials chosen for this housing had to be fabricated out of non-magnetic materials to prevent any magnetic flux interference. Any form of magnetic interference could affect the flux lines generated from the source and in effect causing irregularities of the magnetite assembly.

Another feature to acknowledge was to construct a non-obstructive method that irradiates the sample using UV light. This predicament was solved by using vertically stack glass slides which protruded out from the housing to create a small window that allowed light to enter for photo-polymerization. This was accomplished by optical transmission of the UV light source from the side of the glass stack; additionally, this configuration also forms the glass substrate receptacle that holds the specimen in place. To provide a clearer description of the arrangement, Figure 5.1.g is provided below. High pressure mercury lamp was procured from LOT-Oriel & Co.

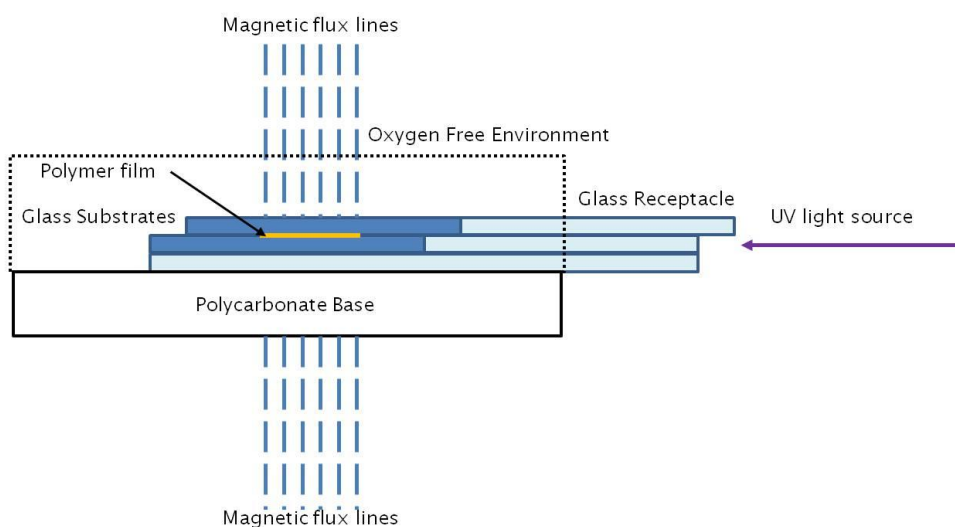


**Figure 5.1.g: Cross-sectional view of the design to house the specimen containment unit**

It is important to note that the two glass substrates were placed in an offset configuration (highlighted in darker shade of blue in Figure 5.1.g). This was to ease the removal of the top or bottom slide to expose the polymer film for inspection.

The glass receptacles (highlighted in lighter shade of blue Figure 5.1.g) were made of two 26 mm × 10 mm × 1 mm and one 50 mm × 10 mm × 1 mm glass pieces which were stacked on top of each other. The base piece which is the longest glass piece (50 mm × 10 mm × 1 mm) was used to provide a solid base which disallowed any material flexing as the top cover was secured. The pieces were assembled together using 5 minute curing epoxy from RS instruments.

The dimensions of the polycarbonate base used also influences where the specimen will rest relative to the spacing between the coil pair. This is because the generated homogenous flux line by the Helmholtz coil system only holds true within a designated region relative to a point which is equidistant between the pair. Therefore dimensions of the specimen housing plays an important role as the specimen must sit inside this region to allow the homogenous fields to intersect it. The height of the polycarbonate base chosen was 6 mm thick and thickness of the glass base piece with the glass substrate would equate approximately 8mm in total taking into account material tolerances. All relevant design drawings containing the specimen housing unit can be found in the Appendix: Chapter 5.

Conversely, it was important to impose a quality control on the samples fabricated using this procedure. Therefore the glass substrates that constrain the ferrofluid had to be sufficiently clean from any form of contamination (dirt, dust and oily residues), a stringent cleaning regime was formulated to handle this. Details of the cleaning procedure presented accordingly in Section 5.1.2.1. The following step of the fabrication process was to find an appropriate external magnetic field source. This concludes the first element addressing the need to find a reliable and robust method to fabricate polymeric thin films.

#### 5.1.2.1. Glass substrate Selection and Treatment

To ensure consistent sample quality, the glass substrates of the specimen holder needed to be cleaned to avoid sample contamination. Therefore, the 26 mm by 10 mm soda lime glass substrates underwent a special cleaning procedure to remove any contamination (oil and dust). The cleaning process was prepared as such:

- Substrates were cleaned initially using standard detergent (Soap Bath). The substrates were soaked in a bath of warm soapy water for 15 minutes. They are removed and rinsed with deionised water then wiped dry with lint-free tissues to remove all dirt and residues.

- The substrates were then cleaned using acetone for 10 minutes (Solvent Bath 1). This method removes all oils and organic residues adhered to the surface. They are then removed and dried thoroughly using nitrogen gas.
- The substrates were then soaked in methanol for 5 minutes (Solvent Bath 2). This removes any residues that are left from the previous solvent as they dissolve well in methanol. They are then removed and dried thoroughly using nitrogen gas.
- The substrates were soaked in warm deionised water (DI water) for 15 minutes to dissolve any residues left from the methanol bath. They are then removed and dried thoroughly using nitrogen gas.
- Finally the glass substrates underwent an acid bath using hydrochloric acid for 30 minutes. This removes all remaining organic residues. Again, they are rinsed with deionised water and dried thoroughly using nitrogen gas and finally stored in a clean container.
- A qualitative microscopy examination of the sample from that batch was conducted to assure quality is maintained after every wash.

In later stages of the experimentation, the samples which underwent the hydrochloric acid etching process suffered heavy contamination even after ample rinsing using deionised water. It was hypothesised that the cause was the hydrochloric acid was reacting to constituents of the soda lime glass facilitating the removal of additional unwanted material. Consequently, a more stable borosilicate glass was used as its replacement and subsequent samples have not shown signs of contamination since.

## 5.2. Helmholtz Coil Pair System

First developed by German scientist Hermann von Helmholtz, the electromagnet comprises of two circular coils each with an equal number of turns separated by a distance equivalent to the radius of the coils itself. This system was unique due to its inherent capability to produce homogeneous magnetic fields between the two coils along its concentric axis.

The first design step was to ascertain the design considerations. This was important as it influences the entire coil dimensions based on the maximum allowable working space for the specimen housing. Then theoretical calculations were made based on the allowable working space.

Next suitable materials were sourced and only then the electromagnets were designed accordingly. These findings are presented in the subsequent sections of the chapter.

### 5.2.1. Design Considerations

Prior to construction, a series of design considerations were made. This was based on the space constraints available when assembling the entire experimental setup as one. The goal was to achieve a workable Helmholtz coil pair that could be retrofitted into an Olympus CX41 optical microscope where the microscope objective could fit inside the inner radius of the coils without obstructions. This allowed the user to view the array propagation through the optically clear polycarbonate cover in real time permitting image capture. Approximated allowable working space was found to be 150 mm × 150 mm × 80 mm.

These spatial constraints limited the performance of the electromagnets. Additionally, the distance between the coils had to be large enough to accommodate the specimen housing discussed in Section 5.1.2. In order to maximise the allowable working space, it was crucial to acquire background knowledge pertaining to the Helmholtz coil pair system. For this, theoretical calculations were established to acquire an understanding of an operating

Helmholtz Coil system and subsequent computation to obtain an optimal design. The electromagnet needed to be situated on a base that permitted vertical translations to aid image focusing. Material selection was again straight forward, only non-magnetic materials were chosen ensuring no magnetic field interferences were present.

### 5.2.2. Theoretical Computations

The equations for the Helmholtz pair were duly sourced from equations derived by Dennison (E.Dennison, 2005). The rationale behind this was to formulate a simple and elegant solution in order to provide a close estimate of the magnetic field strength without the use of complex commercially available Finite Element Analysis (FEA) software. The equations and visual reference provided below was to compute the on-axis field for a finite Helmholtz coil pair.

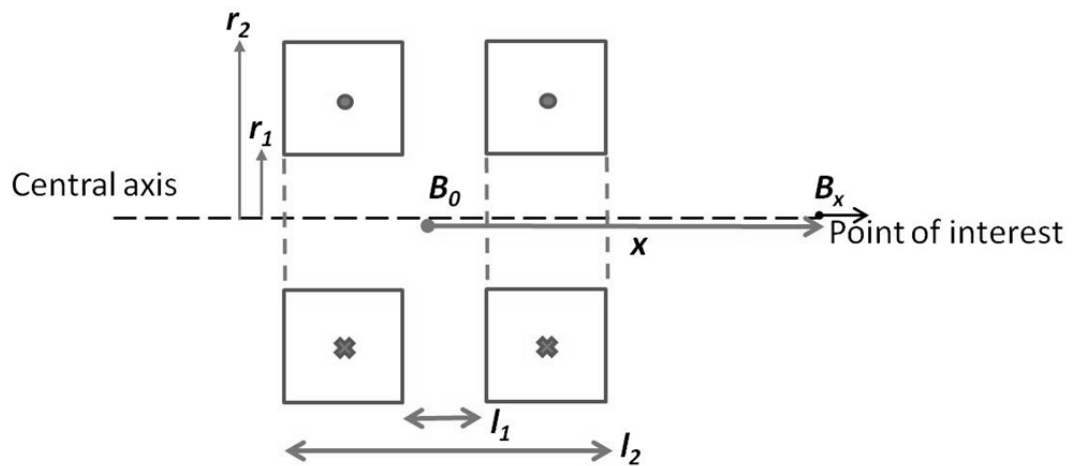


Figure 5.2.a: Cross-sectional view of finite Helmholtz coil pair system

$$B_x = \mu_0 \sqrt{\frac{P\lambda}{r_1\rho}} G$$

**Equation 5.2.1: Derived solution for on-axis field strength at any point along the concentric axis for finite Helmholtz coil pair system (E.Dennison, 2005) & (D.B. Montgomery, 1961)**

<sup>4</sup> Theoretical understanding of the sourced equation can be found in Appendix: Chapter 5.

The variables:  $l_1$  and  $l_2$  respectively are the distances between the inner- and outer-most distance coil winding of the system,  $P$  is the total power consumed,  $\rho$  is the conductor resistivity,  $\lambda$  is the ratio between the total conductor cross-section area and the total coil cross-section area and finally  $G$  is the unit-less geometric factor of the system. The G-factor is determined by shape and size of the coils. The G-factor equations were derived and compiled by Montgomery et al. (D.B. Montgomery, 1961) and can be found in their work. In his work, Dennison (E.Dennison, 2005) has simplified and derived illustrated below.

$$G = \sqrt{\frac{1}{8\pi(\alpha^2 - 1)(\beta_2 - \beta_1)}} \left[ \begin{array}{l} +(\gamma + \beta_2) \ln \frac{\alpha + \sqrt{\alpha^2 + (\gamma + \beta_2)^2}}{1 + \sqrt{1 + (\gamma + \beta_2)^2}} \\ -(\gamma + \beta_1) \ln \frac{\alpha + \sqrt{\alpha^2 + (\gamma + \beta_1)^2}}{1 + \sqrt{1 + (\gamma + \beta_1)^2}} \\ +(\gamma - \beta_1) \ln \frac{\alpha + \sqrt{\alpha^2 + (\gamma - \beta_1)^2}}{1 + \sqrt{1 + (\gamma - \beta_1)^2}} \\ -(\gamma - \beta_2) \ln \frac{\alpha + \sqrt{\alpha^2 + (\gamma - \beta_2)^2}}{1 + \sqrt{1 + (\gamma - \beta_2)^2}} \end{array} \right]$$

$$\text{The variables: } \gamma = \frac{x}{r_1} \quad \alpha = \frac{r_2}{r_1} \quad \beta_1 = \frac{l_1}{2r_1} \quad \beta_2 = \frac{l_2}{2r_1}$$

**Equation 5.2.2: Equation to determine the G-factor of the Helmholtz coil pair system**

Consequently, the Helmholtz coil system can now be computed and adapted into the design. Based on the theoretical derivation an optimum design was then electronically drawn using commercially available software.

### 5.2.3. Theoretical Estimates of Magnetic Field Strength

Based on the space constraints discussed in the Section 5.2.1 the coil design and dimensions were optimised. To simplify the discussion, coil geometries were termed accordingly using the schematic presented in Figure 5.2.a and visual aid Figure 5.2.b was provided below to assist the following descriptions.

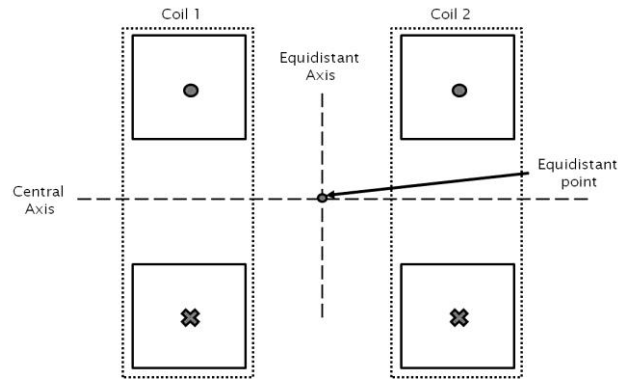


**Figure 5.2.b: A cross-sectional view of the Helmholtz coil pair depicting all locations relevant to subsequent discussion**

Figure 5.2.b depicts the locations of the geometric terminology used to aid subsequent discussions regarding the Helmholtz coil pair system. The control parameters which dictate the magnetic field strength of the electromagnets are as follows:

- the geometric dimensions  $l_1$ ,  $l_2$ ,  $r_1$  and  $r_2$  (refer to Figure 5.2.a)
- Wire diameter  $D_{wire}$  (1 mm diameter copper wire was chosen)
- Wire resistivity  $\rho_{copper}$  (the material of the wire)
- Number of wire windings  ${}^5N_{turns}$
- Estimated total resistance for both coils  $R_{total}$  determined from

$${}^6R_{total} = \frac{L_{wire} \times \rho_{copper}}{A_{wire}}.$$

These parameters had to be determined in order to exhibit magnetic fields that could either match or surpass the field strength rating used by Liu and co-workers (Liu, et al., 1995) in their experiments which they reported was 38 mT. Preliminary conditions were set where the magnetic field strength should surpass an optimistic 50 mT. Consequently optimised parameters were found and tabulated in Table 5.2.a below

---

<sup>5</sup> Data for this parameter was taken from the works of the Rational Wire Tables by C.R. Cosen (Cosen, 1937). Data assumes that the windings are bedded; meaning the cross-sectional packing of wires is fully optimised.

<sup>6</sup>  $L_{wire}$  is the total length of the wire,  $\rho_{copper}$  is the density of copper and  $A_{wire}$  is the cross-sectional area of the corresponding wire.

<b>Parameter</b>	$l_1$	$l_2$	$r_1$	$r_2$	$D_{wire}$	$\rho_{copper}$	$N_{turns}$
<b>Unit</b>	mm	mm	mm	mm	mm	$\Omega m$	turns
<b>Value</b>	20	50	20	50	1	$1.68 \times 10^{-8}$	397

**Table 5.2.a: Tabulated theoretical results of optimised design parameters for Helmholtz coil pair system used in experimentation**

To satisfy the preliminary conditions, the theoretical computations using Equation 5.2.1 indicate that a minimum of 88 W was required. It should be noted that the computations were accomplished relative to the equidistant point between the two coil pairs where the specimen will be situated. Therefore, the power supply must be capable of similar or more wattage rating based on the empirical data.

#### 5.2.4. Magnetic Field Homogeneity

The Helmholtz coil system was chosen for its ability to produce homogenous fields along the central axis. However the homogeneity holds true only to a certain extent. Therefore this section defines the extent of homogeneity as a function distance between the coil pairs. Theoretical calculations were made based on to compute the field strength along the central axis.

Let's consider the equidistant point at geometric coordinates x:0 y:0 in Figure 5.2.b as the point of origin, the central axis is the horizontal X-axis and coordinate displacements to the left with respect to the equidistant point is considered negative and the vice versa for the right. Now let's establish that at each coordinate displacement along the central axis has a specific G-factor (since the value of  $\gamma$  changes). Next, was to designate 51 coordinate points along the central axis with respect to the equidistant point as x: 0 y: 0. Hence we would have 25 points on either side of the equidistant point and now we designate that each point has a 1 mm distance apart from each other. For each point designated point, the magnitude of the magnetic field strength can be computed accordingly and the data is presented in Figure 5.2.c.

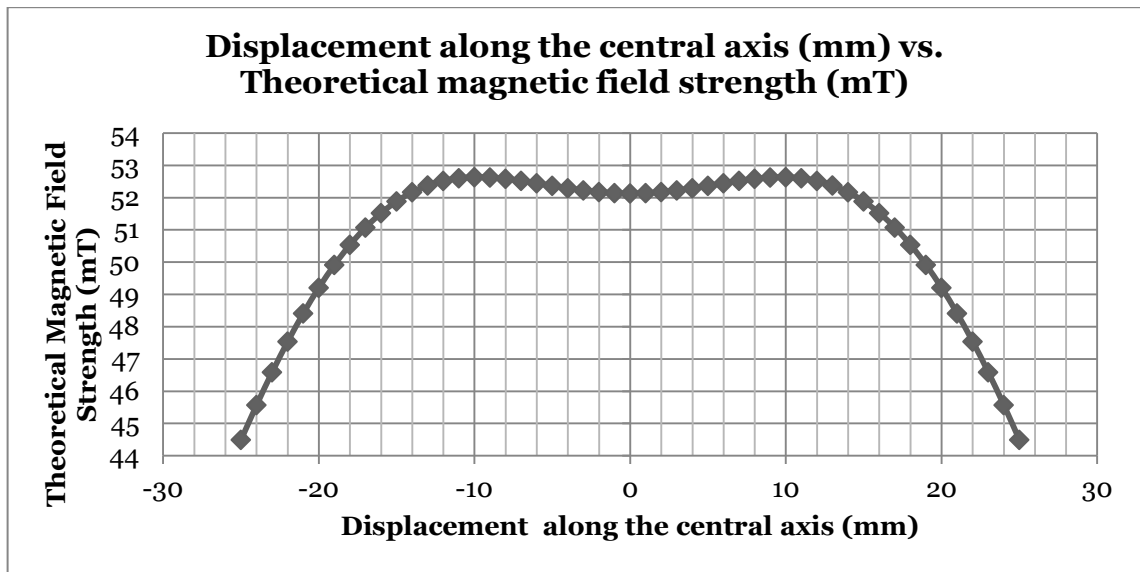


**Figure 5.2.c: A plot depicting the magnetic field along the central axis for 50 mm at 1 mm intervals at 100 W**

Figure 5.2.c is a plot depicting the change in magnetic field strength along the central axis. The power consumption parameter for this plot was set at whilst retaining the physical data of the coil pairs presented in Table 5.2.a. Note that the magnetic field at -6 m to + 6 mm region does not fluctuate as much relative to the regions surpassing the  $\pm 10$  mm regions. This particular range was chosen for analysis as it is where the specimen would be situated at. These small deviations were found to be in the range of  $\pm 0.1$  mT which is a consistent with respect to the -25 mm to -10 mm region and their inverse.

### 5.2.5. Design Outline: Fabrication and Winding

Consequently, factoring the design considerations and allowable dimension parameters, a final blueprint was produced using a computer aided design software package; SolidWorks. An additional safety feature incorporated was coating the inner walls of the coil plates with clear acrylic paint to insulate the coil windings from the aluminium walls. The designed receptacle attachment resembles a U-shaped prong fabricated to fit the coil size. This enabled the coil to be securely held in place using screws. Illustrated below is an exploded view of the initial prototype to provide a clearer description of the design.

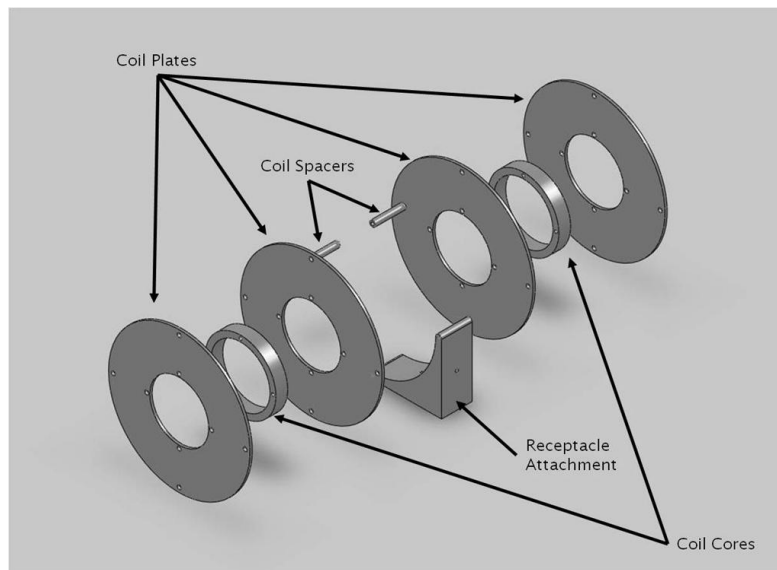


**Figure 5.2.d: An exploded view of the initial design of the Helmholtz coil pair prototype**

Other key features of the design included were the multi-piece design to ease any maintenance or adjustment should it become necessary. The coil plates were 120 mm in diameter and had 2 mm thickness. The coil cores were 40 mm in diameter and 15 mm in thickness. Finally, the spacers had a thickness of 16 mm. When assembled the total dimensions amount to a 120 mm diameter coil with an effective thickness of 54 mm which is within maximum allowable working space. All detailed blue prints of the multi-piece design and receptacle will be included in Appendix: Chapter 5 for scrutiny.

It is important to note that Figure 5.2.d illustrates the initial design and this was not used for actual experimentation. This was due to complications during the fabrication process of the round spacers and U-shaped spacer illustrated was unpractical. The resulting solution was to simplify the spacers into rectangular blocks with same height. Figure 5.2.e illustrates the final assembled design with modified spacers.

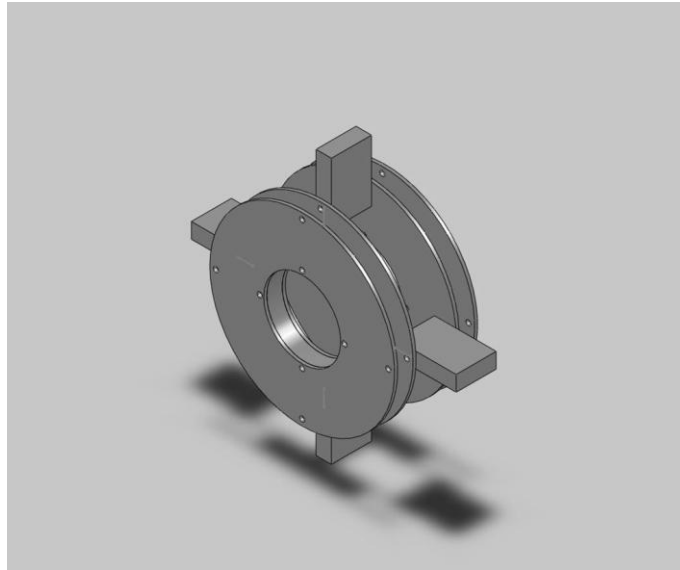


**Figure 5.2.e: Finalised design of the Helmholtz coil pair prototype**

Figure 5.2.e illustrates the finalised design of the Helmholtz coil pair prototype. The two electromagnetic coils were separated with a 16 mm spacer depicted in the four rectangular blocks protruding from the coils. The circular coil plates are cores were the same dimensions as the initial design as previously mentioned above.

Aluminium was the material of choice for the design for its non-magnetic attributes. 1 mm thick enamelled copper wire was used to wound the coils. It should be noted that the coils were wound manually which caused the coil windings to be inefficiently packed which effects the coils overall performance. To circumvent this, the total number of wire wounds for both coils were made equally. A total of 390 windings were made for each coil as oppose to the 397 windings from the theoretical calculation of the optimised design from Section 5.2.3. Additionally, the coil pairs were electrically connected in series. Furthermore, all screws and fittings had to be made from non-magnetic materials i.e. brass.

### 5.2.6. Device Testing and Results Obtained

The coils were tested to assess their magnetic field strength output capabilities. This step was imperative to determine the Helmholtz coil system produced featured a homogenous field in between the two coils. Additionally, the system must have sufficient output to stimulate a magnetic dipole moment in order to

facilitate the self assembly process of the magnetite particles. This factor is limited to the electrical output of the power supply therefore the tests were operated within these limits.

These assessments were achieved by simple measurement of the field strength of the coils and comparing them to the theoretical computations. This was accomplished by using a Hall Effect probe from Phillip Harris to measure the field strength between the two coils. The probe has a measurement range of -70 mT to +70 mT giving an output voltage of -4 V to +4 V.

In an ideal situation, to assess the homogenous field quality of a Helmholtz coil pair system would require placing the probe at the equidistant point along the central axis between the coil pairs. Measurements should be taken starting with the equidistant point and subsequently moving along the central axis at designated displacements. Realistically, obtaining measurements at these displacements were unpractical due to the limited spacing between the coil pairs.

The solution for this predicament was to obtain measurements from a single coil system which now resembles a finite thick solenoid where theoretical calculations were also possible. Additionally, the elimination of spatial constraints facilitated the ease of measurements. The test here was to present a correlation between the deteriorating magnetic field strength as a function of the increasing distance from the coils. Since both coils were created identically in terms of the number of wire windings and coil dimension, therefore they must share the same deterioration characteristics.

Two specific points of measurement were chosen for this test; both points had <sup>7</sup>geometric coordinates  $x_i$  of which were 20 mm and 30 mm plus 2 mm taking into account the thickness of the coil plate. The tests ran at a 5 A current draw at 10V. Tabulated results and comparative theoretical computations are demonstrated below.

---

<sup>7</sup> The geometric coordinates mentioned here correspond to the diagram illustrated in for a thick finite solenoid. Diagram and sourced equations can be found in Appendix: Chapter 5.

Distance of $x_i$ relative to point of origin (mm)	Measurement for Coil 1(mT)	Measurement for Coil 2 (mT)	Theoretical Computations (mT)
20	13.6	14.0	15.16
30	7.79	8.3	10.19

**Table 5.2.b: Tabulated results comparing magnetic field strength of both coils with theoretical computations**

The drop in magnetic field strength demonstrated by the two coil measurements above confirms the initial statement of the deterioration characteristics. However there was a small deviation between the two measurements. This can be explained by the manual wire winding method causing the deviations of wire length in which effected coil performance. Additionally, the measurement probe is highly sensitive to slight angle changes relative to the magnetic fields that intersect it and effective distances to relative to the field source. These factors are unavoidable but they demonstrate field strengths in similar ranges. However with respect to the theoretical data, the result ranges were reasonable.

This test confirms the coil pairs have similar electromagnetic characteristics. Hence it can be concluded when both coils assembled in Helmholtz coil configuration; they must exude similar flux patterns exhibiting homogenous characteristics.

The next step was to determine the maximum power output that the coil pair. For this, a simplified approach of measuring the current response from the Helmholtz coil system in series as a function of voltage. The current-voltage (I-V) characteristic of the Helmholtz coil system was identified to be a linear relationship of  $y = 0.19x$ .

The bench top DC power supply used to run the Helmholtz coil system has a 65 V output with a 5 A maximum current draw. Therefore to conduct the test at a safe operational limit, current draw was capped at 4.7 A. As the linear relationship suggest, substituting the current value into the linear equation will compute a voltage of 25.6V. This meant to operate the Helmholtz coil system safely, the output voltage must not breach the 25 V limit.

As a result, the Helmholtz coil system was connected in series that ran at a 25 V maximum output voltage and magnetic field strength was measured at the equidistant point. The resultant magnetic field generated was measured at 49.2 mT. The theoretical computations presented a field output of 56.8 mT, which is rated more than the measured output.

There are several reasons to explain this;

- The theoretical model assumes that the Helmholtz system is an ideal system. This meant that there are no losses of energy due to the dissipation of heat that would add additional resistance to the system.
- Coils were wound manually; the  $\lambda$  ratio from Equation 5.2.1 was severely skewed and deteriorates the field output performance.
- The sensitivity of the measurement probe to the magnetic fields that intersect it. It was imperative that the intersecting fields had to be perpendicular with the probe surface to obtain accurate results. Therefore the probe had to be exactly at the equidistant point between the coils which was un-realistically to situate.

Nevertheless, with these factors taken into consideration the maximum field strength was in a comparable range with the theoretical data and when compared to past works (Liu, et al., 1995), (Mohebi & Jamasbi, 1996) & (Ivey, J.Liu, Zhu, & Cutillas, 2000) they have operated at similar or less field strengths. This confirms that the Helmholtz system was suitable to excite magnetic dipole moment for the self-assembly process of columnar structure. Finally, this concludes the section addressing the vital elements of design, fabrication and experimental testing the Helmholtz coil pair system. Next on the agenda was the introduction of the power supply and development of a control system to accommodate the devices.

### 5.3. Direct Current Power Supply

The bench-top DC power supply series from Elektro-Automatik was chosen to run the designed Helmholtz system. The power supply has an output voltage of 65 V at maximum current draw of 5 A equating to a 325 W power consumption which is suitable in accordance the discussion in Section 5.2.3. An additional feature available in the equipment was the remote control capability which was

advantageous with a Universal Serial Bus (USB) interface. Additional information regarding the power supply can be found in the Elektro-Automatik database (Elektro-Automatik, 2000).

## 5.4. Control System: LabVIEW programming scheme

A control system was needed to operate the power supply that runs the Helmholtz system as the goal was to achieve equilibrium structures that resemble columnar configuration which were spaced in a hexagonal lattice order. Past works (Liu, et al., 1995) and (Mohebi & Jamasbi, 1996) have explained that a slow gradual field allowed the particles to explore the lowest energy configuration which resembled a system of chains and columns. To achieve this; the application of the magnetic field had to be introduced in a gradual ascending manner. This meant the programming parameters had to encompass the ability to offer the user to select a feasible range of step-up voltage and choosing delay time for each step (volts/second). The program was written using the commercially available software, LabVIEW. A detailed flow diagram and programming schematic of the entire program infrastructure is included in Appendix: Chapter 5.

### 5.4.1. Control System: Testing the Program

The control system was tested by ramping the output voltage from 0 V to 25 V by 1 V increments and a 1 second time delay (1 Volt/second). This effect increases the magnetic field in a gradual ascending manner. Measurement was again taken using whilst the voltage ramp took place. Similarly a linear relationship of  $y = 1.98x - 0.24$  was obtained when plotting the change in magnetic field strength as a function of the voltage applied.

Since the voltage applied axis can also be seen as the time axis as the step size was set to 1 Volt/second. Therefore slope of the linear trend indicates the magnetic field ramp rate registering a value of  $\approx 2$  mT/second. Understandably, the process is

entirely flexible and to obtain a milder slope the time delay can be increased. This concludes the description for every single element identified to be used in the experimental setup.

## 5.5. Chapter summary

This chapter has detailed and identified all design elements in which were incorporated in experimental setup. The first element was to establish a robust and reliable method to fabricate thin polymer films. This technique was proven to satisfy the element requirements as demonstrated in Section 5.1.

The next element addressed was the incorporation of a magnetic field source which features a homogenous field and had sufficient field strength to stimulate the dipole interaction of the magnetite particles. Consequently the Helmholtz coil system was introduced, designed, fabricated and subsequently tested. The outcome of the design proved successful as it satisfied requirements of the corresponding element as presented in Section 5.2.

Next on the agenda was to introduce a power supply accompanied with a remote control system. For this task the PS3000B power supply series from Elektro-Automatik was chosen for its USB compatible interface. Additionally, a bespoke control system was designed to allow the user to subject a voltage ramp to power the Helmholtz system. Similarly these were covered in Section 5.3.

## Chapter 6: Experimental Processes

---

This chapter highlights the experimental processes incorporating all experimental devices described in the previous chapter. The description covers the fabrication process of the magnetic  $\text{Fe}_3\text{O}_4$  nanoparticle arrays to construct columnar structures via an external magnetic source. Once the predetermined field is achieved; UV light photo-polymerises the HDDA monomer immobilising its embedded constituents. Finally a discussion regarding the hydrochloric acid (HCl) etching process that removes  $\text{Fe}_3\text{O}_4$  constituents embedded in the polymeric film to reveal the nanopore array template.

Alternative methods magnetic field inductions were also employed. Neodymium permanent magnets were utilised to investigate the outcome of instantaneous application of magnetic field and possibilities to assemble columnar structures under conditions specific to our experimental setup.

## 6.1. Initial Experimental Setup

The fabrication procedure begins with applying a small amount of isopropanol onto the surface-cleaned borosilicate glass substrate using a foam swab. This serves as the final cleaning process to remove any contaminants that may have settled after the extensive cleaning process covered in Chapter 5: Section 5.1.2.1. Remaining solvent residues were then dried using a lint free tissue subsequently.

A sheet of LDPE was stretched (to remove any creases) and placed onto the glass substrate. The spacer borders for the specimen were made by scoring a smaller rectangular pattern within the LDPE/glass surface. This pattern was then carefully removed. This forms a spacer of an approximated thickness  $L$  of 10  $\mu\text{m}$ . The corresponding substrate was then transferred onto the bottom half of the glass receptacle described in Section 5.1.2 with the LDPE spacer facing upwards.

A small volume of magnetic  $\text{Fe}_3\text{O}_4$  nanoparticles dispersed in the HDDA monomer solution using a volume fraction  $\phi$  of 0.05 was extracted from the bulk solution and transferred onto the corresponding glass substrate then another glass substrate was carefully placed on top in the offset position. This confines the solution between the two glass substrates. Finally a small O-ring was gently place in a <sup>8</sup>central location on top of the two substrates and the top cover was fastened with four M3 nylon screws simultaneously applying pressure to the O-ring which holds the two glass substrates securely while squeezing the solution. This is demonstrated in Figure 6.1.a

---

<sup>8</sup> The central location was found just by visual estimation where the concentric point of the O-ring matches the concentric point of the constrained specimen between the two substrates which is typically has a close to circular outline.

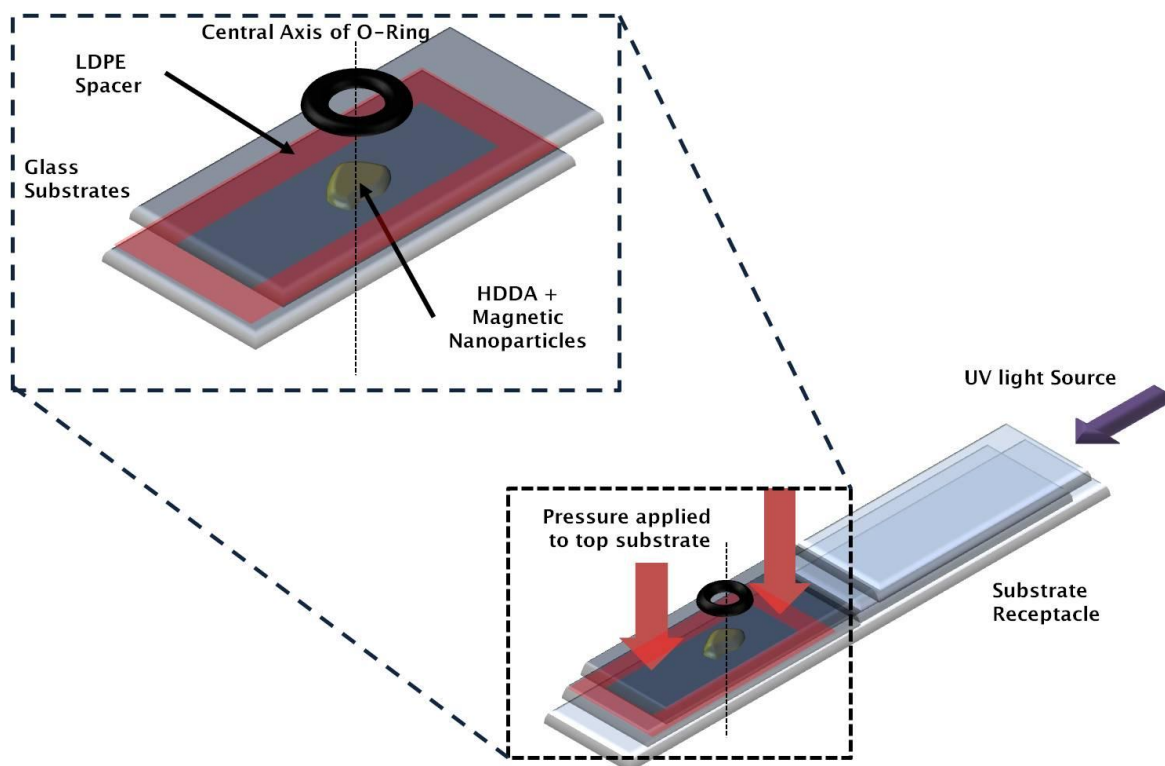


**Figure 6.1.a: Image depicting the application method of the O-ring**

Figure 6.1.a illustrates the location to place the O-ring with respect to the location of the HDDA and the magnetic nanoparticle solution. Glass substrates are placed together in an offset position illustrated by the plates which are in a darker shade of blue. As soon as the O-ring was placed onto the glass substrates the cover must be immediately be placed securing the two substrates, HDDA solution and the O-ring in place.

This process drastically decreases the thickness of the resultant polymer film. Figure 6.1.b illustrated below demonstrates the configuration from a cross-sectional view. It also depicts the fabrication process in two separate steps observing the specimen without the presence of a magnetic field and with the presence of a magnetic with.

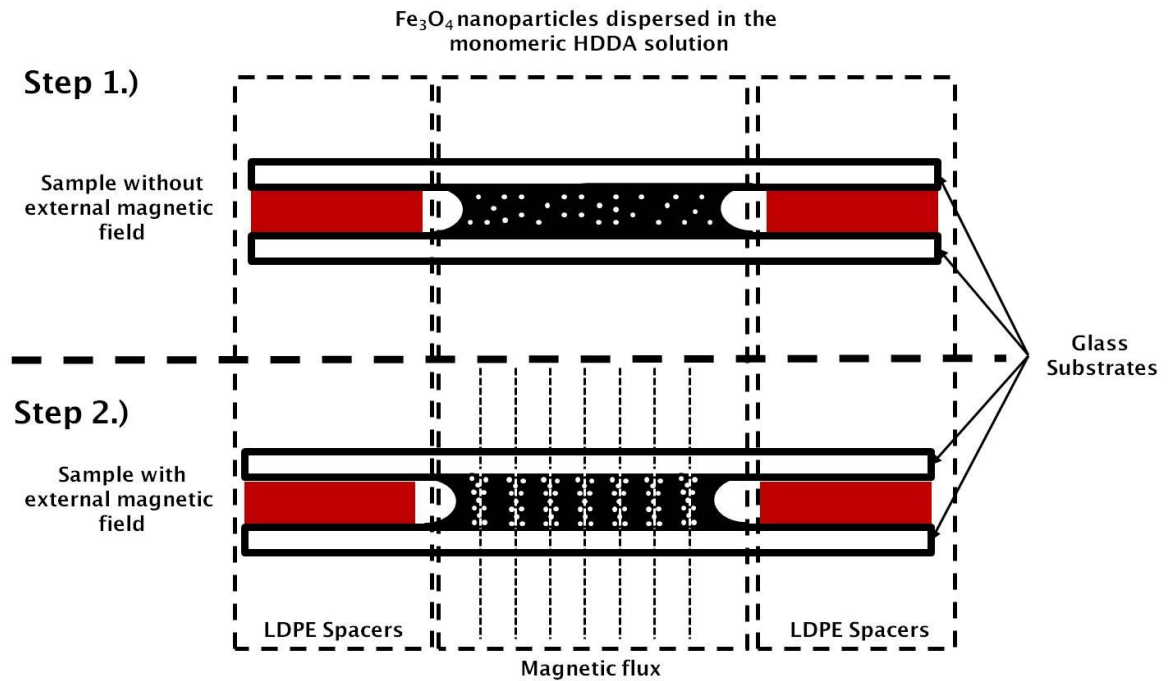


**Figure 6.1.b: Cross-sectional view of the specimen configuration during experimentation**

Similar to the past works of Rybchenko and co-workers (Rybchenko, Dyab, Haywood, Itskevich, & Paunov, 2009) the monomer containing the magnetic nanoparticles were constrained between two borosilicate glass substrates. The substrates were separated via the LDPE spacers discussed. As the external magnetic field was applied, the self-assembly process takes place when the external magnetic field was applied. These structures span the across the entirety of the thickness of the LDPE spacers.

The entire specimen containment unit was then place in between the two coils. Since the coils were specifically designed to accommodate the microscope objective, it could be place concentric along the central axis of the coils; this made it possible to designate an accurate location to place the specimen thusly. Specimen was also kept parallel to the equidistant axis between two coils with the help of the flat polycarbonate base. This was important due to the inherent characteristic of the Helmholtz coil pair system which was known to exude homogenous magnetic field in within the central vicinity between the coil pair. The summation of the above description is depicted in Figure 6.1.c.

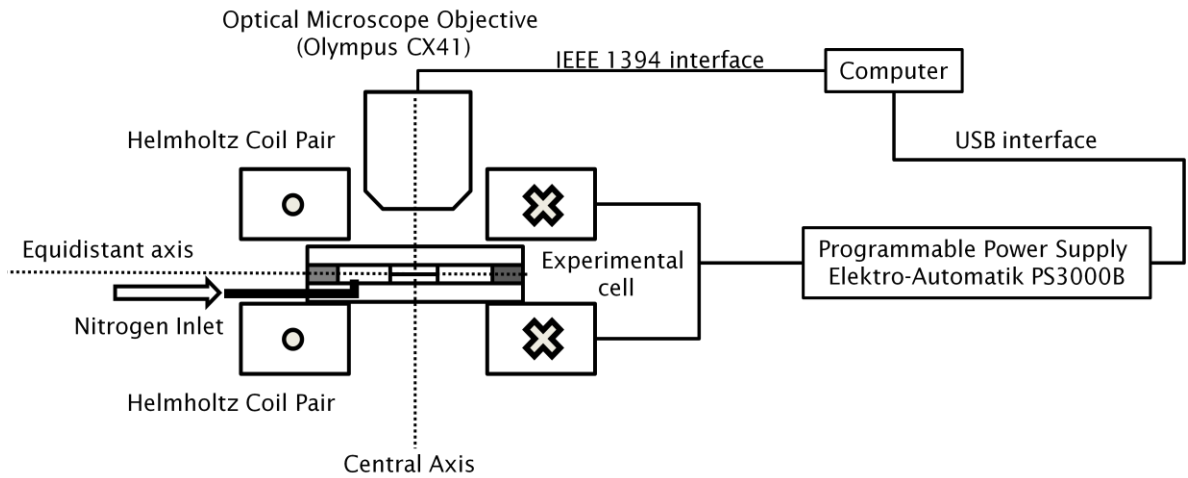


**Figure 6.1.c: Experimental schematic depicting all devices used for the work**

The • and × symbols inside the Helmholtz pair is to demonstrate that the direction of current flow within the coil and also indicating they were connected in series and using the right-hand rule determine polarity direction. The small nitrogen inlet (represented by the black “L” shaped figure) was connected to an external nitrogen source for oxygen purging purposes via silicone tubing. Subsequently, the internals were left to purge for 10 minutes expelling any traces of oxygen during the photopolymerisation process. The nitrogen source was left to flow throughout the entirety of the experiment.

Once the initial purging period was over, the external magnetic field was applied in small increments to start the self-assembly process. The direction of the field was perpendicular to the specimen surface. This process was controlled remotely using the control system written in LabVIEW covered in Chapter 5: Section 5.4. The magnetic field ramp rate  $R$  was set at 2 mT/second using parameters explained in Chapter 5: Section 5.4.1. For clarity, all three control parameters which dictate the resultant structural configuration were summarised in Figure 6.1.a.

Control Parameter	Volume Fraction $\phi$	Specimen Thickness $L$	Magnetic Field $R$
Unit	N/A	$\mu\text{m}$	$\text{mT/s}$
Value	0.05	10 approx.	2

**Table 6.1.a: Control Parameters used to determine <C>**

Using Equation 3.2.3 from Chapter 3: Section 3.2.2, the average complexity  $\langle C \rangle$  transition point was found to be 0.873, which was less than 1.5 this implies the resultant expected structural configuration was columnar.

As soon as the predetermined maximum magnetic field strength was achieved at 49.5 mT, the specimen was appropriately irradiated with a high-pressure mercury lamp facilitating photo-polymerisation. This process was allotted 15 minutes while the magnetic field was held at maximum strength which immobilised the embedded columnar arrays. Once the photo-polymerisation process was complete, both the nitrogen and magnetic field source were discontinued. Finally, the specimen can be extracted from the housing characterised using OM. The characterisation technique is explained on Chapter 7 Section 7.2.

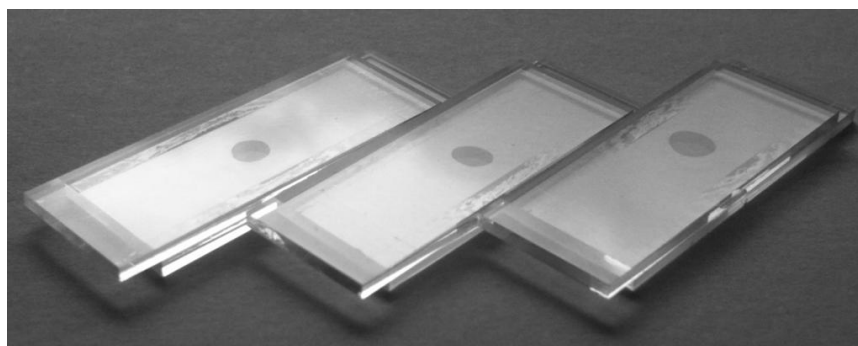


**Figure 6.1.d: Example of completed samples after the photo-polymerisation process**

Figure 6.1.d details examples of fully polymerised specimens still confined between their corresponding glass substrates. The substrates were situated in an offset position for reasons discussed in Section 5.1.2. The top substrates were removed to reveal the film still adhering to the bottom substrates which were ready for image analysis and characterisation described in Chapter 7.

Pre-selected samples were subjected to selective etching using HCl acid. This process selectively removes the  $\text{Fe}_3\text{O}_4$  constituents embedded inside the polymer films whilst keeping the polymeric material intact. This was accomplished by pipetting small droplets of HCl acid diluted with deionised water (50% volume) onto the film surface demonstrated in Figure 6.1.e below.

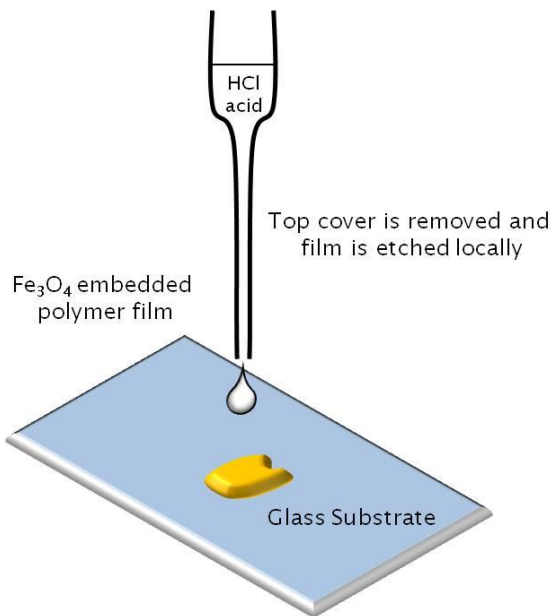


**Figure 6.1.e: Illustration detailing the etching procedure using HCl acid**

They were left to etch for 24 hours to ensure complete removal of the Fe<sub>3</sub>O<sub>4</sub> constituents to create channels which resemble the imprints left by the columnar structures and was subsequently rinsed with deionised water. This was confirmed by a later analysis covered in Chapter 7 Section 7.2.3.

### 6.1.1. Experimental Results: Helmholtz Coil Pair System

The results of the experimental processes utilising the Helmholtz coil was successful in terms of producing columnar structures. Although the procured arrays did not resemble exactly the hexagonal lattice patterns; the concept of the transitional point  $< C >$  between columnar and labyrinth-like structures still hold true. A representative image of this series is demonstrated below.

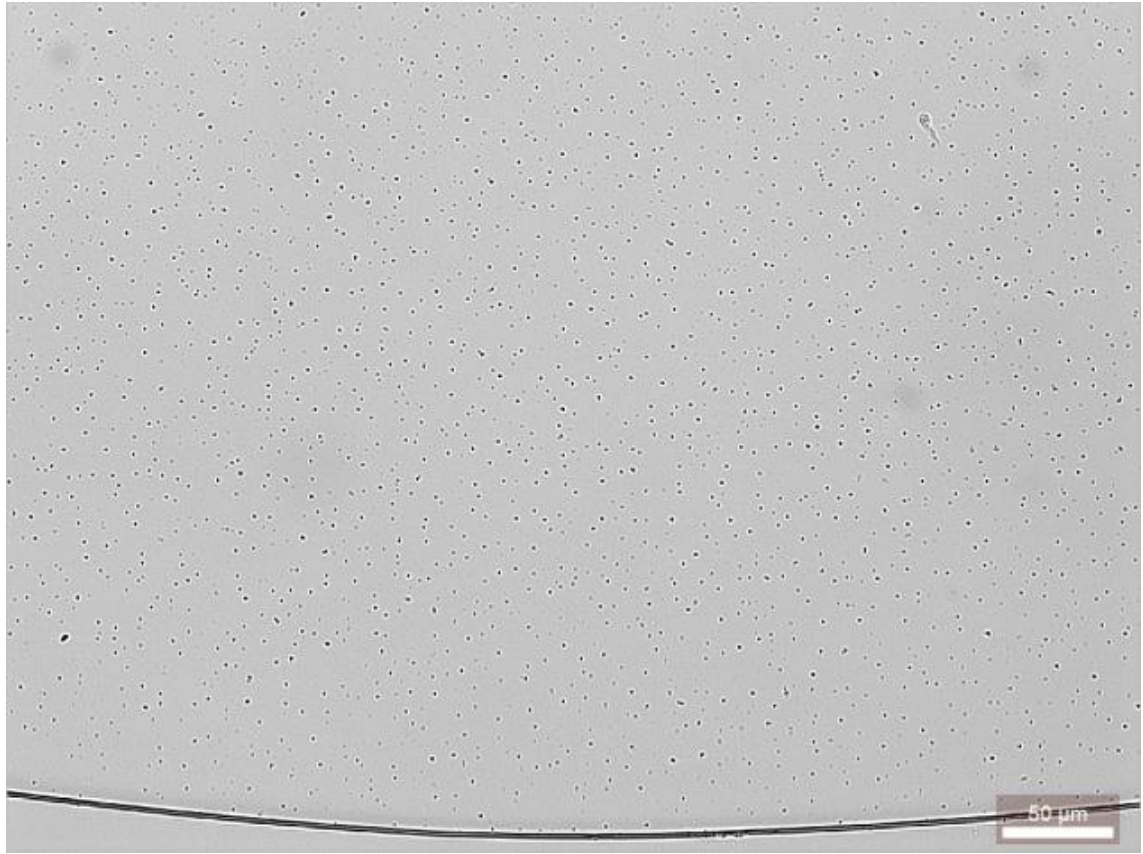


**Figure 6.1.f: A demonstrative sample depicting the columnar structures produced using the Helmholtz coil pair system**

Figure 6.1.f is an example of the specimen produced using the Helmholtz coil pair system. The black observable dots are the aforementioned columnar structures assembled using the external magnetic field. Initial observations indicate that the sizes of the observable arrays appear to be large ( $\approx 1 \mu\text{m}$  in diameter). This is due to the configuration of the columns are structured; it is understood that the column has a wider diameter in the middle as it tapers to both ends hence causing a distortion when trying to obtain the right the focal depth during microscopy.

## 6.2. Alternative Sources of Magnetic Fields

Alternative experimental trials incorporating the instantaneous excitation of a magnetic field instead of a gradual climb was introduced. The rationale for this experimentation was to explore simpler and less specialised methods of membrane preparation with the intention to reduce production cost.

This experimental procedure has been attempted and studied before in past works (Mohebi & Jamasbi, 1996) & (G.Flores, J.Liu, Mohebi, & Jamasbi, 1999). Their experimental works typically employ an electromagnet to induce the self-assembly process. However, no corresponding works have been found which utilises a pair of permanent magnets of similar rated magnetic strength.

Similarly, the experimentation begins in nitrogen atmosphere with 10 minutes initial purging. Then a pair of permanent neodymium ring magnets was placed in a similar configuration of the Helmholtz system onto specimen containment unit where they hold themselves together through magnetic attraction. For simplicity sake this will be termed the north-south-north-south (NSNS) configuration. The specimen was left for another 10 minutes before UV irradiation took place. Figure 6.2.a is provided below as a visual aid.

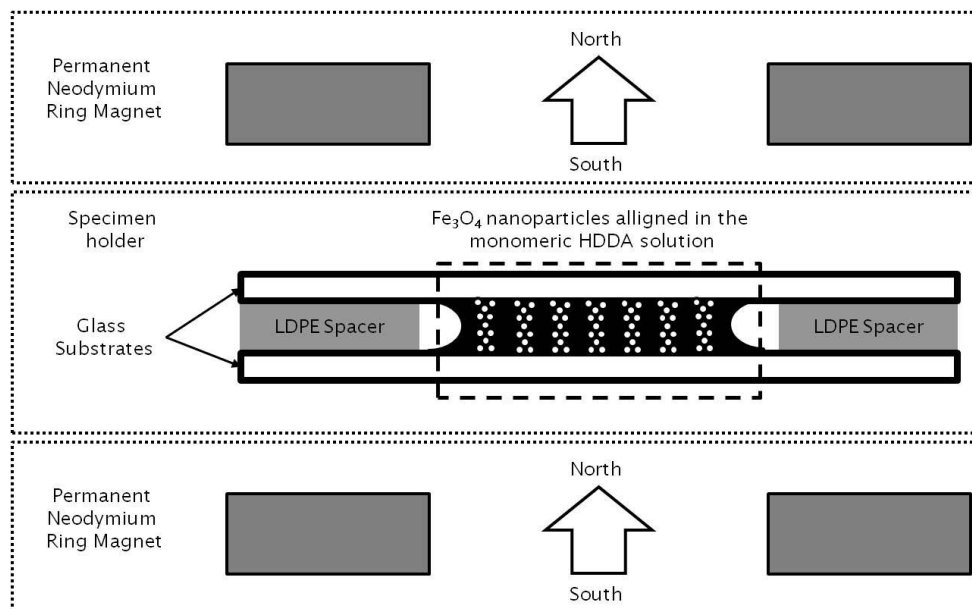


**Figure 6.2.a: A cross-sectional view of the configuration used in the experimentation**

The arrows depicted above demonstrate the NSNS configuration previously discussed. Understandably, it was important to measure the field strength of the permanent neodymium magnets in this NSNS configuration with the measurement probe in between the two magnets. The induced field strength of 43.6 mT was recorded. When compared to our corresponding Helmholtz system of 2 mT/second which was a significant increase of approximately 22 times. Nevertheless, resultant generated assemblies from this test were similarly columnar arrays and those samples have too been extensively discussed in Chapter 3 Section 3.3.

The rationale behind these tests was to observe if it was viable to use permanent magnets as an alternate external magnetic source. Additionally, this thought process is also in line with the initial objective to construct low cost devices as specialised equipment such as the Helmholtz system and the power supply was no longer needed here.

### 6.2.1. Experimental Results: Permanent Magnet Type

Similar to the specimens procured from the previous experiment, the columnar structures were too observed. It was deduced that this was possible due to the inherent small film thickness  $L$  which was dictated by the thickness of the LDPE spacers. A small  $L$  causes short chains to coalesce into columnar structures which by the accounts of Mohebi and co-workers (Mohebi & Jamasbi, 1996) thinner cells (small parallel plate separation) only allow short chain to form which repel each other and form separated singles chains. For argument sake, we took  $R$  as 43.8 mT and remaining two parameters  $\phi$  as 0.2 and  $L$  as 10  $\mu\text{m}$ ; the average complexity  $\langle C \rangle$  equates to 1.182 and therefore still consistent with the previous statement. For further confirmation, we observed the previous experiments from Flores and co-workers (G.Flores, J.Liu, Mohebi, & Jamasbi, 1999) which have used more extreme control parameters which they reported to be  $L = 50 \mu\text{m}$ ,  $\phi = 0.03$  and  $R = 400 \text{ mT/s}$  and still manage to produce a columnar configuration. Additionally the inter-array distance  $d$  has shown that it is consistent with the film thickness. To demonstrate the result from our experimentation (shown in a later chapter), Figure 6.2.b is provided below.

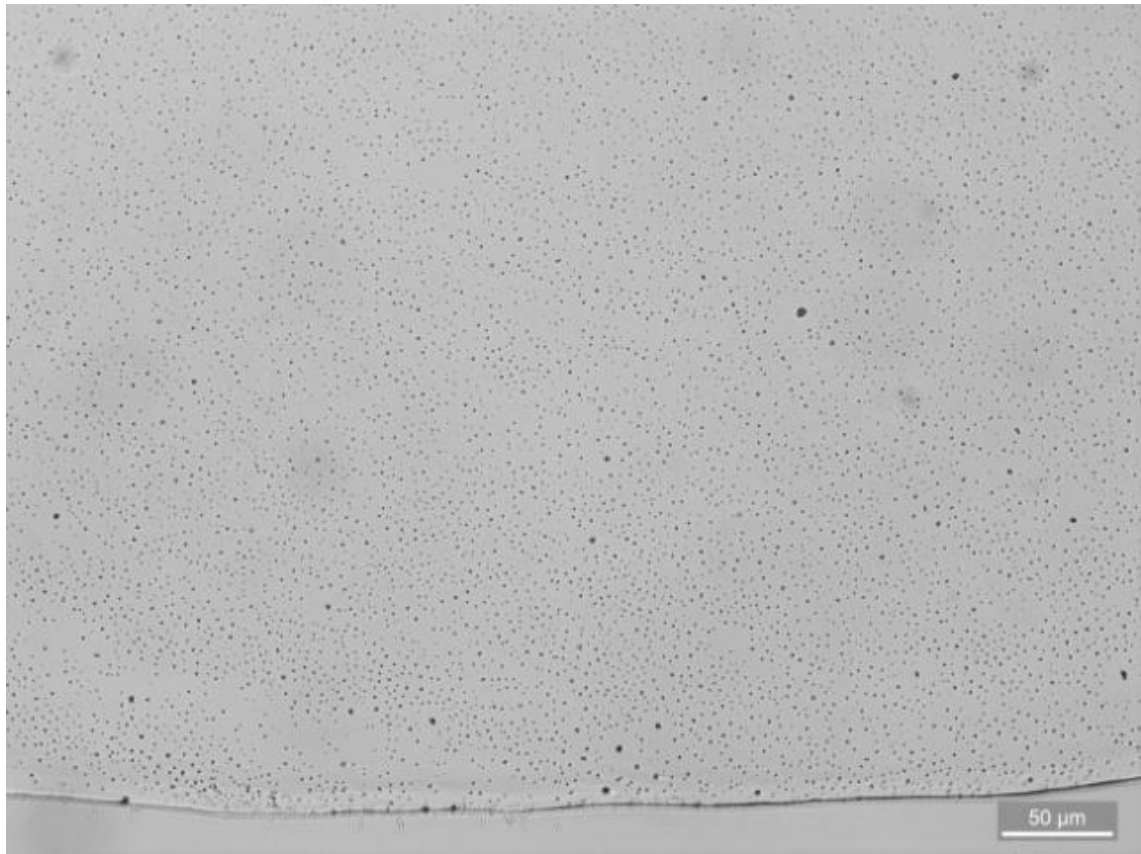


**Figure 6.2.b: A demonstrative sample depicting the columnar structures produced using the neodymium permanent magnets**

Sample procured from this method forms the bulk of OM analysis of the sample series in Chapter 7 Section 7.4.

### 6.3. Chapter Summary

This chapter has highlighted the two experimental processes which were utilised for the entirety of the research which were the Helmholtz coil pair system and the permanent neodymium ring magnets. The experimental processes were described accordingly in Section 6.1 and Section 6.2.

Control parameters of volume fraction  $\phi$ , rate of magnetic field application  $R$  and sample thickness  $L$  for both experiments were also disclosed with their respective average complexity  $\langle C \rangle$  computed to obtain the expected structural configuration which was in agreement with our actual results obtained. The results have also been compared to past works for consistency.

## Chapter 7: Image Analysis and Characterisation of Membranes

---

This chapter encompasses the extensive image analysis conducted subsequent to fabrication of the membranes. This presents the first supporting evidence regarding the presence of the embedded pores subsequent to the etching process in order to feature this technology. The methodology of analysis hinges on the images ascertained from a combination optical, scanning electron and transmission electron microscopy followed by additional aid from an open source image processing software.

The analysis begins with the examining OM images of samples prior and after the etching process to determine the quality and density of the embedded self assembled arrays. The results obtained through the investigation are grouped in accordance to their relevance to each other. Preselected OM images were then put through additional post-processing which yielded crucial parameters which included inter-array spacing and array density. The results were compared and found to be consistent with past works.

Consequently, secondary electron (SE) and backscattered electron (BE) microscopy techniques were also employed in the investigation to validate the OM images obtained.

Next a combination of TEM and scanning electron microscopy (SEM) analysis was conducted to observe the cross-sectional shape of a single array. This was accomplished using two techniques; sectioning the polymer film which the  $\text{Fe}_3\text{O}_4$  constituents was still embedded inside and flushing out freshly assembled columnar structures for scrutiny.

SEM analyses also provided a closer insight into morphological investigations. This meant that the exploratory work would encompass the understanding of surface morphology of these membranes from secondary electron images and the investigation of the cross-sectional regions of the membrane through alternative techniques.

## 7.1. Optical Microscopy Analysis: Introduction

OM analysis serves as the initial step towards the characterisation process. This was accomplished through establishing a visual characterisation system whereby the membrane was extensively imaged in sections and several image magnifications for each subsequent series. All images taken were accomplished using a Leica DM4000M series in transmission lighting mode which according to the manufacturer offers perfect illumination homogeneity which ensures image quality of the observable arrays although no prior tests to determine the degree of homogeneity.

### 7.1.1. Image Processing Software: ImageJ

An open source image processing software, ImageJ was used through the entirety of the microscopy analysis. The software features various plug-ins identified as macros which enables the user to conduct a variety of post-processing computations. These macros can be obtained from their database library complete with guides and straight-forward explanations (Ferreira & Rasband, 1997). As for

the task at hand, the particle analyser was utilised to compute the array density for all pre-selected samples and the radial averaged auto correlation macros was used to compute the inter-array distances as a benchmark to demonstrate consistency with past works(Liu, et al., 1995).

## 7.2. Structure of Optical Microscopy Analysis

The OM analysis incorporates three factors: identification of embedded array density in Section 7.2.1, the inter-array spacing computations in Section 7.2.2 and the after effects of the etching process in Section 7.2.3. This provides crucial information regarding the surface morphology of the membrane and forms the basis of the subsequent SEM in Section 7.4 and ionic conductance in Chapter 8 where the analysis would take place.

### 7.2.1. Optical Microscopy Analysis: Array Density

The importance of obtaining the pore density parameter was paramount in aiding the ionic conductance analysis as it enabled one to ascertain the theoretical number of pores contributing to conductance of the system. This was achieved through the identification of the array density as of number of pores per meter squared (Pores/m<sup>2</sup>). For this analysis the image processing software, ImageJ was exploited for the task. The Analyse Particle function (Ferreira & Rasband, 1997) enabled the user to quantify of number and dimensions of pores of an image given that the pixel to distance conversion is known. This calibration settings was obtained from the microscope settings accordingly. The techniques and methods to acquire the parameters are extensively covered in the website (Ferreira & Rasband, 1997). Therefore this section will only cover the results of the measurement.

Several 500 x 500 square pixel areas were selected and cropped from various series of images and were 'thesholed' prior to any image analyses. This is an image conversion technique that converts a greyscale image in to a binary image or a 1-bit monochrome image. This meant that images represented in binary colours black (colour scale: 0) or white (colour scale: 255) for the macro to function. Figure 7.2.a

illustrated below demonstrates the effects of image threshold conversion. Details regarding the image thresholding techniques can be found in Appendix: Chapter 7.

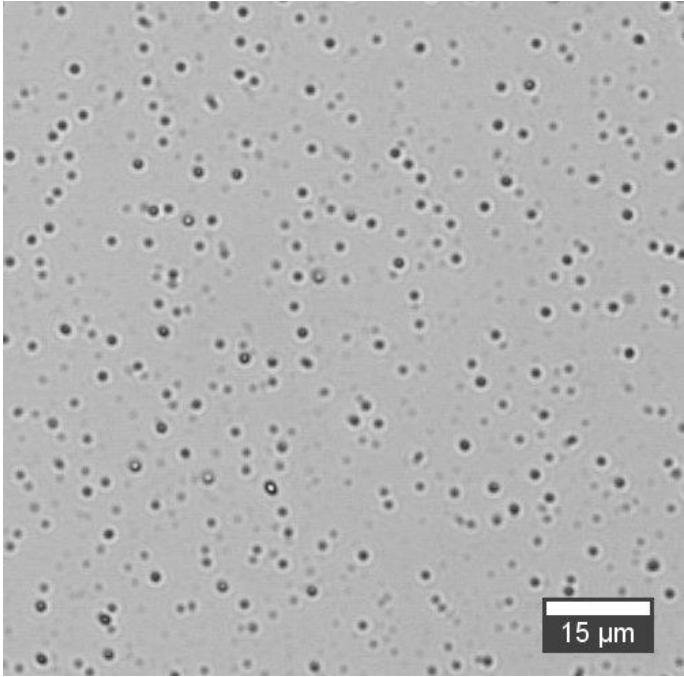


**Figure 7.2.a: Sample of a greyscale image before image thresholding**

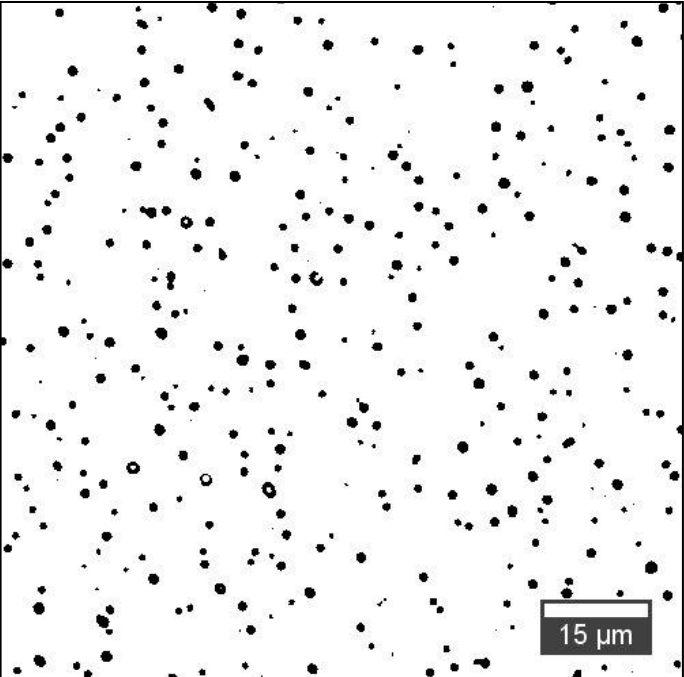


**Figure 7.2.b: Sample of image after image threshold conversion**

A total of 63 (53 permanent magnet samples 7 Helmholtz coil pair samples<sup>9</sup>) preselected sample sites were analysed to quantify the embedded array density. Furthermore, the raw images were processed via 500 x 500 pixels for the permanent magnets samples and Helmholtz coil pair samples at arbitrary locations of the membrane for the imaging software to analyse. The pixel to distance ratio for these images was found to be 5.1 pixels/ $\mu\text{m}$  and 2.0 pixels/ $\mu\text{m}$  respectively based on the micro scale provided by the microscope image grabbing software. A summary of the results was tabulated below.

<b>Resultant pore density for Permanent Magnet Samples</b>		
Particle count	Number of particles within area of analysis	Particle density (Pores/ $\text{m}^2$ )
Minimum	140	$1.45 \times 10^{10}$
Average	258	$2.66 \times 10^{10}$
Maximum	461	$4.76 \times 10^{10}$

**Table 7.2.a: Tabulated summary of analysed array density of permanent magnet samples**

<b>Resultant pore density for Helmholtz Coil Pair Samples</b>		
Particle count	Number of particles within are of analysis	Particle density (Pores/ $\text{m}^2$ )
Minimum	110	$1.77 \times 10^9$
Average	590	$9.48 \times 10^9$
Maximum	1020	$1.64 \times 10^{10}$

**Table 7.2.b: Tabulated summary of analysed array density of Helmholtz coil pair samples**

Table 7.2.a and Table 7.2.b encompass the information regarding quantity of arrays in the area of analysis. Additional post processing was conducted to compute the minimum, maximum and average embedded array density (Pores/ $\text{m}^2$ ). This information proved vital when recalled in Chapter 8 to aid in the ionic conductance analysis of the fabricated membranes.

It is also possible to conduct a comparative analysis to determine the apparent size of the arrays. The term ‘apparent size’ was used is because the optical images are

<sup>9</sup> Since the exploratory work is based on viability of using simpler and less specialised equipment as a method of fabrication thus reducing cost.

very sensitive with respect to the focal depth and does not reflect on the true assembled pore opening size across the membrane surface.

Additionally when considering sub-micron arrays, there is a strong diffraction distortion hence these estimates can be several times smaller than its real size. However this information is useful for quick comparative tests. Table 7.2.c and Table 7.2.d demonstrated below are the quantified apparent sizes of the arrays.

<b>Average Size in pixel units for permanent magnet samples</b>	
Size (pixel <sup>2</sup> )	Standard Deviation (pixels)
31.14	5.08

**Table 7.2.c: Tabulated post-processed results relevant to array size (Permanent magnet)**

<b>Average Size in pixel units for Helmholtz coil pair samples</b>	
Size (pixel <sup>2</sup> )	Standard Deviation (pixels)
5.37	2.68

**Table 7.2.d: Tabulated post processed results relevant to array size (Helmholtz Coil pair)**

Table 7.2.c and Table 7.2.d present the post processed results obtained relevant to the apparent array size represented in pixel units. Furthermore the data can be presented in histogram form to demonstrate the apparent size distribution in pixel units. To demonstrate the computation from this investigation, a histogram is presented below to demonstrate array size distribution across the specific range. Figure 7.2.c and Figure 7.2.d exhibited below accompanies the aforementioned description.

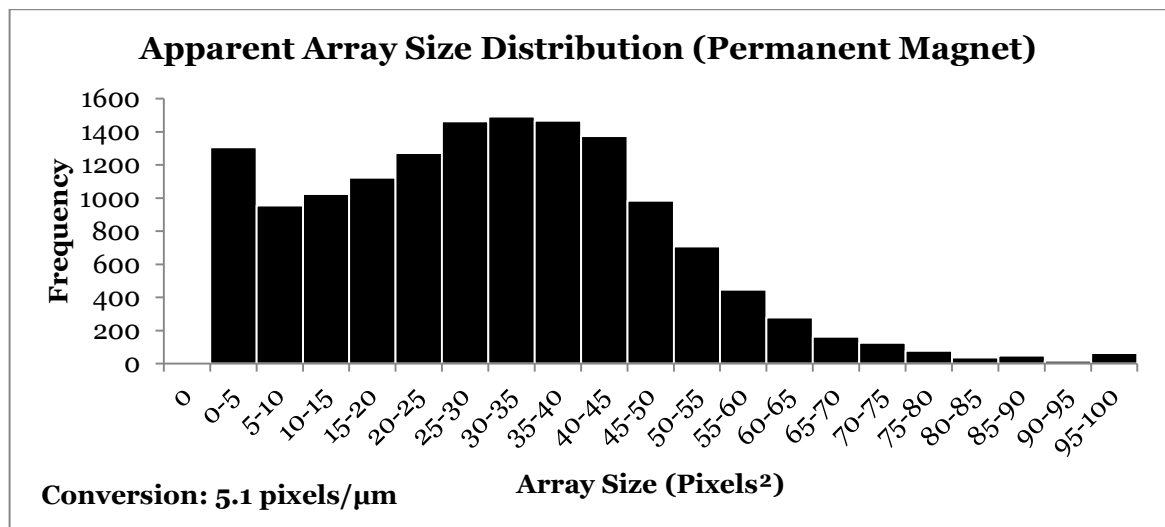


**Figure 7.2.c: Histogram depicting the array size distribution at ranges of 5 pixels to 100 pixels range**

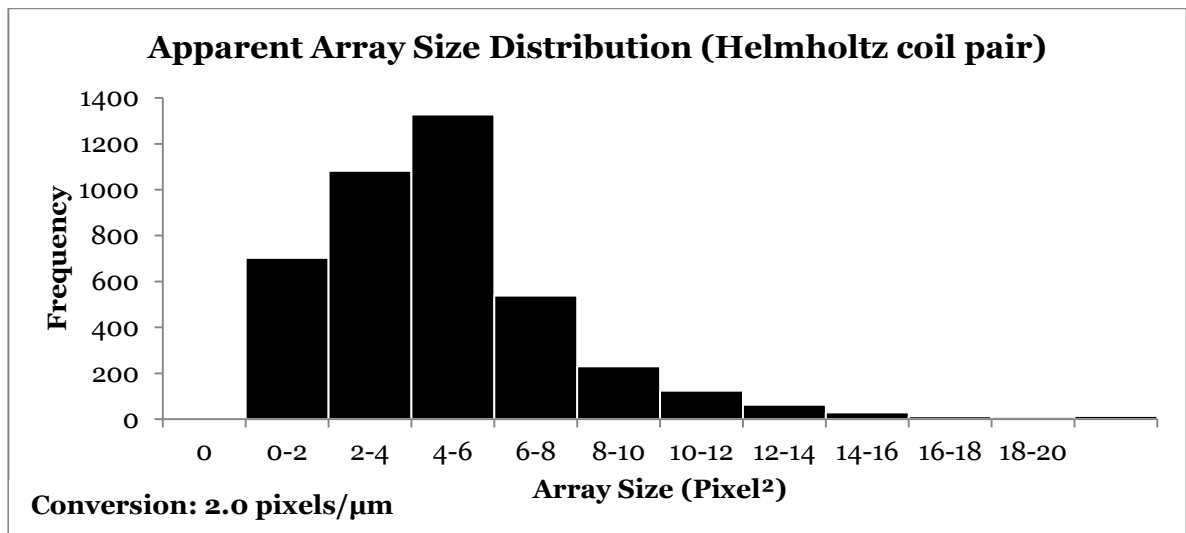


**Figure 7.2.d: Histogram depicting the array size distribution at ranges of 0 pixels to 20 pixels range**

Figure 7.2.c and Figure 7.2.d depicts the apparent size distribution of preselected sample sites for both types of fabrication methods. A quick observation demonstrates the 0 – 5 pixel category has a large frequency of arrays for the permanent magnet samples. This is due to the inherent effect of image noise<sup>10</sup> generated from the image thresholding method become apparent when interpreting the data. As for the Helmholtz coil pair samples, the arrays appear to have a clear contrast with the background as compared to the permanent magnet

<sup>10</sup> The image noise effect was found when increasing the spot detection sensitivity which was detailed in Appendix: Chapter 7.

counter-parts. The causation for this effect is due to the inherent fabrication method that these type fabrication methods entail. The instantaneous application of an external magnetic field causes the particles to abruptly form chains that align themselves to the perpendicular flux that intersects them. Therefore these chains have not sufficient time to assemble into fully formed columns due to the instantaneous introduction of the external magnetic field and thus producing loosely packed structures. Conversely, the Helmholtz coil pair samples were gradually assembled into well-defined close-packed columnar structures since the particle has sufficient time to assemble into tightly packed structures which forms the fully propagated pores. Additionally, the Helmholtz coil samples exhibited a smaller pixel<sup>2</sup> size was due to the small volume concentration  $\phi$  used to procure the samples which was highlighted in Chapter 6. The information compiled regarding the size distribution was later utilised in later Chapter 8 aiding the ionic conductance analysis.

### 7.2.2. Optical Microscopy Analysis: Inter-Array Spacing

Exploratory analyses were conducted regarding the inter-array spacing of the fabricated membranes. The inter-array spacing was taken into consideration as it highlights the interaction between the nanoparticles with various parameters which governs it. This analysis was based on past works (Liu, et al., 1995) & (G.Flores, J.Liu, Mohebi, & Jamasbi, 1999) where a magnetorheological fluid or ferrofluid emulsion constrained between two parallel plates then subjected to an external magnetic field and extensively analysing particle interactions at various parameters.

Furthermore, the analysis was accomplished by using the Radial Average Autocorrelation macro<sup>11</sup> provided by ImageJ complete with results calibration and validation. Additionally, manual measurements were also conducted for confirmation. This was vital as it demonstrated customisable capabilities the simple manipulation of thickness of the constrained fluid,  $L$  the particle volume fraction,  $\phi$  and the ramp speed of the external magnetic field.

---

<sup>11</sup> Details regarding the usage of the radial averaged autocorrelation macro from ImageJ can be found in Appendix: Chapter 7.

The analysis method was accomplished by gathering a series of pre-selected samples which feature homogenous array propagation. A series of 66 images were analysed using the macro. The outcome of this analysis yields an average inter-array spacing of  $3.2 \mu\text{m} \pm 0.6 \mu\text{m}$  for permanent magnet samples and  $2.7 \mu\text{m} \pm 0.7 \mu\text{m}$  for Helmholtz coils pair samples. In comparison to past works in relation to inter array spacing (Liu, et al., 1995) the respective parameter is govern by

$$d = 1.33L^{0.37}$$

**Equation 7.2.1: Equation governing the inter-array spacing for cell thickness of  $3 \leq L \leq 800 \mu\text{m}$**

Where notations  $d$  is the averaged distance between two columnar structures and  $L$  is the thickness of the solution when constraint between the two parallel plates. Liu and co-workers(Liu, et al., 1995), through experimentation have found that the average inter-array spacing was not entirely dependent from volume fraction  $\phi$  at ranges  $0.04 \leq \phi \leq 0.2$  and the inherent effects was an increase in column width but maintaining constant inter-array distance  $d$ .

With regards to our samples; the sample thickness  $L$  was defined by the thickness of the LDPE spacer used during fabrication which was initially approximated to be  $10\mu\text{m}$ . By rearranging Equation 7.2.1 it was now possible to verify that the initial approximations were correct. Based on inter-array spacing obtained, the computed membrane thickness for permanent magnet and Helmholtz coil pair was found to be  $10.7 \mu\text{m}$  and  $6.7 \mu\text{m}$  respectively which were in an acceptable range from initial estimation.

### 7.2.3. Optical Microscopy Analysis: Pre-Etching and Post-Etching

The pre-etching and post-etching analysis was accomplished by constructing a meticulous imaging regime that categorised each distinguishable section of the film before the etching process and then later identified and categorised again after the etching process was completed. This meant that each section of the membranes could be easily identified subsequent to the etching process; a similar location of the film could then be approximated and imaged hence offering better clarity. Figure 7.2.e illustrated below is an exemplar of the locations of the aforementioned imaged sections.

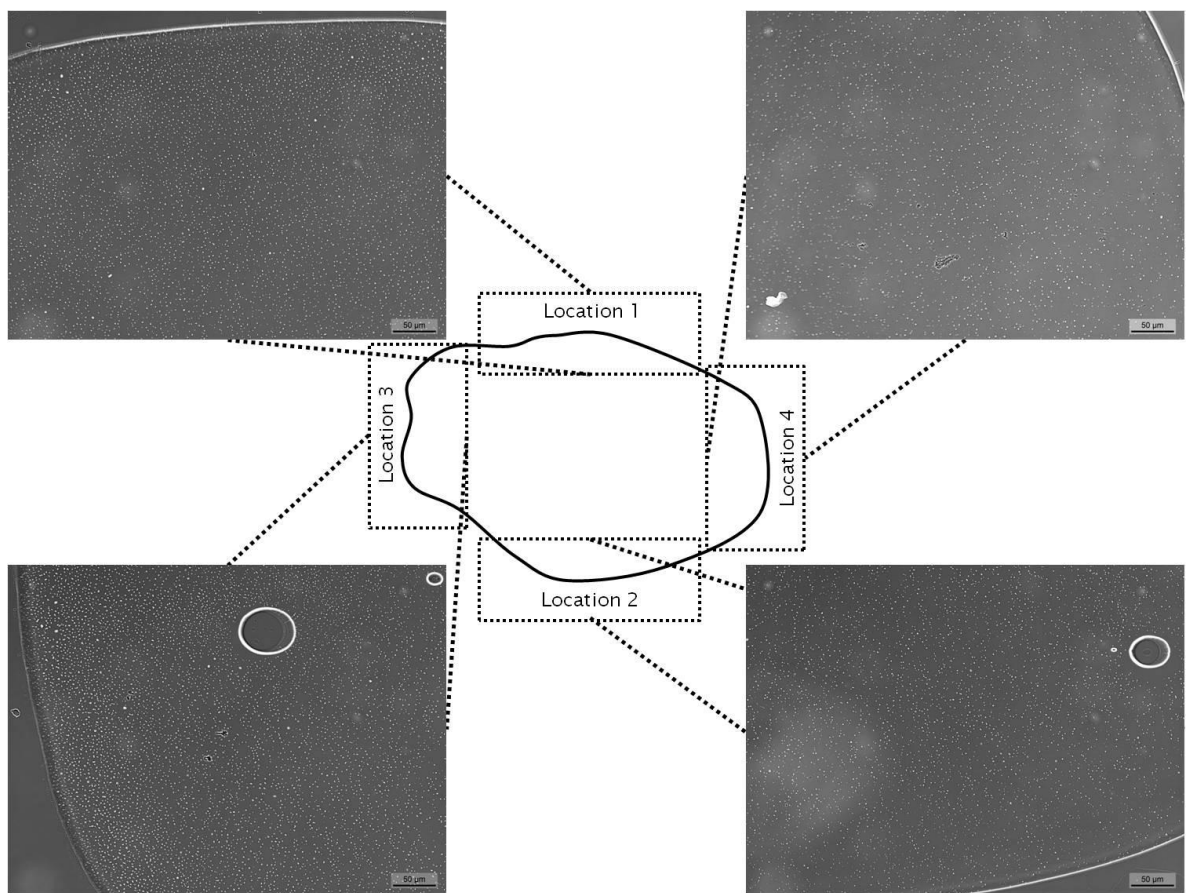


**Figure 7.2.e: Example of the imaged locations of the film accompanied with a corresponding image film sections prior to etching**

It should be noted that subsequent SEM analysis also benefitted from this regime in terms of navigation through the samples during the microscopy sessions. On closer inspection the difference between etched and un-etched samples becomes very apparent. Figure 7.2.f demonstrated below is a visual comparison of an

un-etched and etched site of the fabricated film. The image colours were converted into a negative format to better highlight the embedded arrays inside the film region.

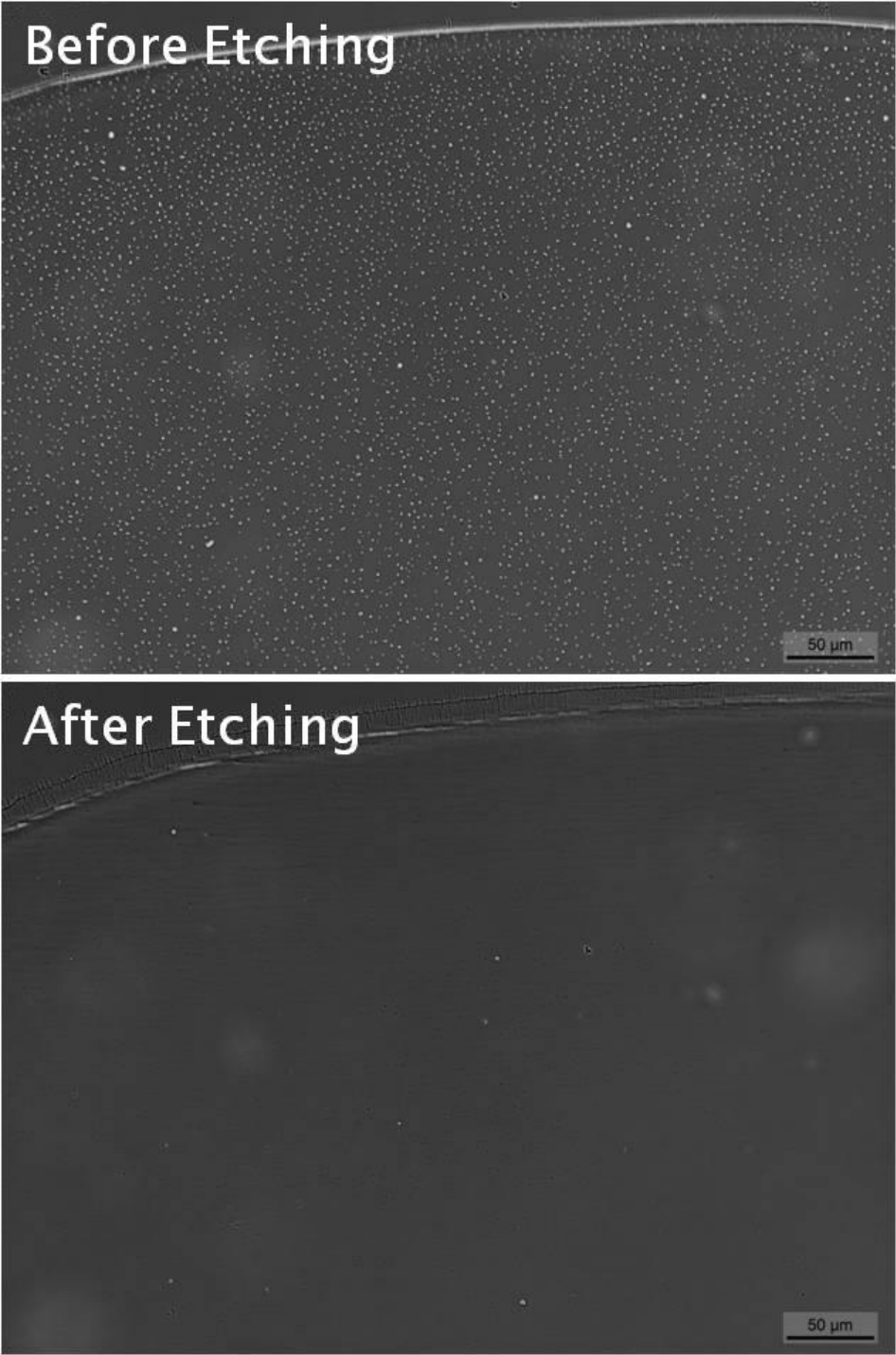


**Figure 7.2.f: Exemplar image of a sample before and after selective etching**

It was advantageous to obtain an understanding of the film condition during different time intervals of the etching process as it provides a small window to observe the reaction of the etchant in contact with the  $\text{Fe}_3\text{O}_4$  constituents but only from one side of the film.

The rationale behind this method was due to the method of fabrication of these membranes when a droplet with dispersed nanoparticles was first extracted from the bulk solution and placed onto the glass substrate. Generally, the bottom substrate will on average spend more time in contact with the solution hence would generate a particle depletion effect due to sedimentation. It was hypothesised that due to this depletion effect the shape of the arrays formed would be feature a slight offset towards the bottom half of the arrays as compared to a dual-sided tapered cylinder (G.Flores, J.Liu, Mohebi, & Jamasbi, 1999) or a cylindrical shape with two frayed ends described from past works (Liu, et al., 1995) & (Ivey, Liu, Zhu, & Cutillas, 2000) & (Ricardi & Weis, 2011). This suggests that the arrays formed could have an in-average higher concentration of particles at the bottom half of the cell and taper off towards the top or the possibility of frayed ends. Additionally, this effect could inhibit array propagation from the top to the bottom substrate therefore forming an incomplete pore. Figure 7.2.g illustrates the above scenarios.

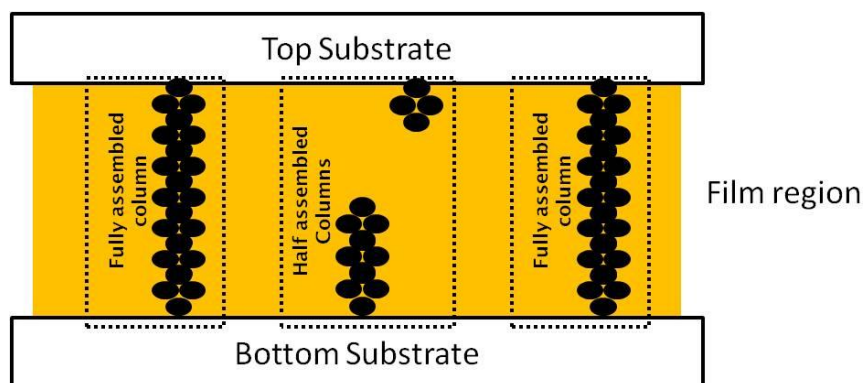


**Figure 7.2.g: Scenarios of array propagation due to particle depletion effect**

Hence an experiment was devised to observe the effect of etching from a single side of the film at designated periods of time whilst imaging the corresponding sample during each time interval. This in turn should offer a rough estimation regarding the percentage of the columnar structures which are fully propagated. Figure 7.2.h is illustrated below accompany the aforementioned description. The rationale

behind this experimentation was to observe the subtraction of  $\text{Fe}_3\text{O}_4$  constituents whereby the etchant could only affect one side of the film at the time.

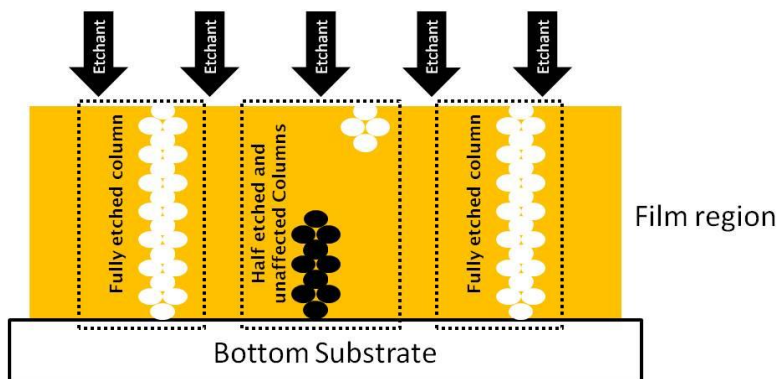


**Figure 7.2.h: Illustration of the effect of etching from a single side of the film subtracting  $\text{Fe}_3\text{O}_4$  constituents**

As a result, the percentage of the arrays etched-off (the etchant here is HCl) from the top side can be estimated to be fully propagated columns. It should be noted that this method is only a simple approximation and does not provide an exact number of fully propagated pores. Consequently a sample was chosen for this experiment where the etching time intervals were 30 seconds, and 1, 2, 4, 8, 16 and 32 minutes. Figure 7.2.i through to Figure 7.2.k provided below are three exemplar images of the same location of the film during the etching intervals. Again the colours of the images have been converted into the negative format to highlight the arrays.

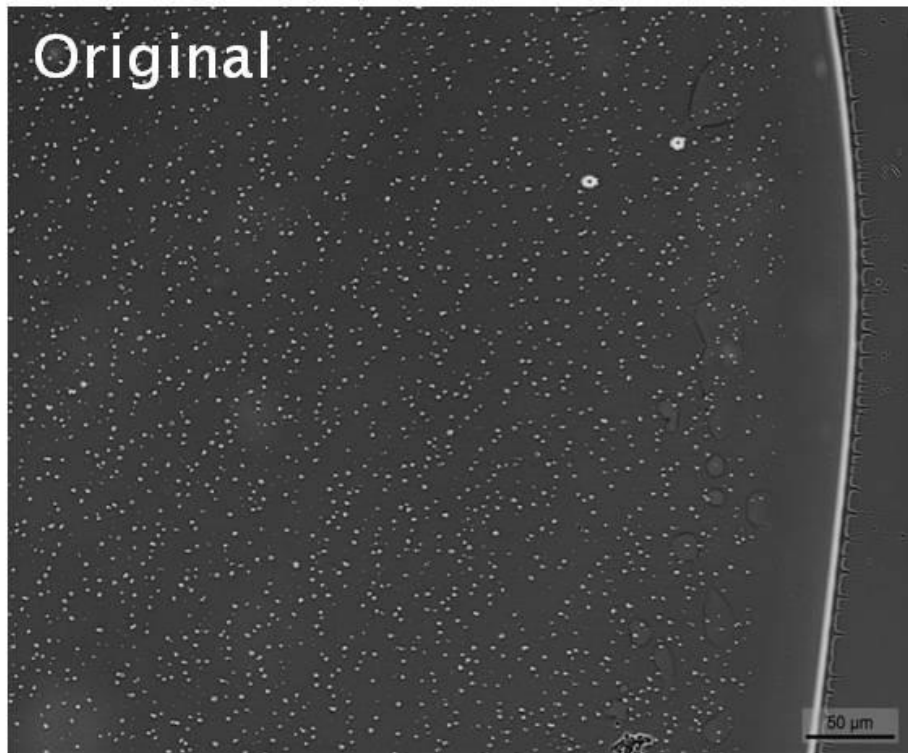


**Figure 7.2.i: Original image of sample area before etching process takes place**

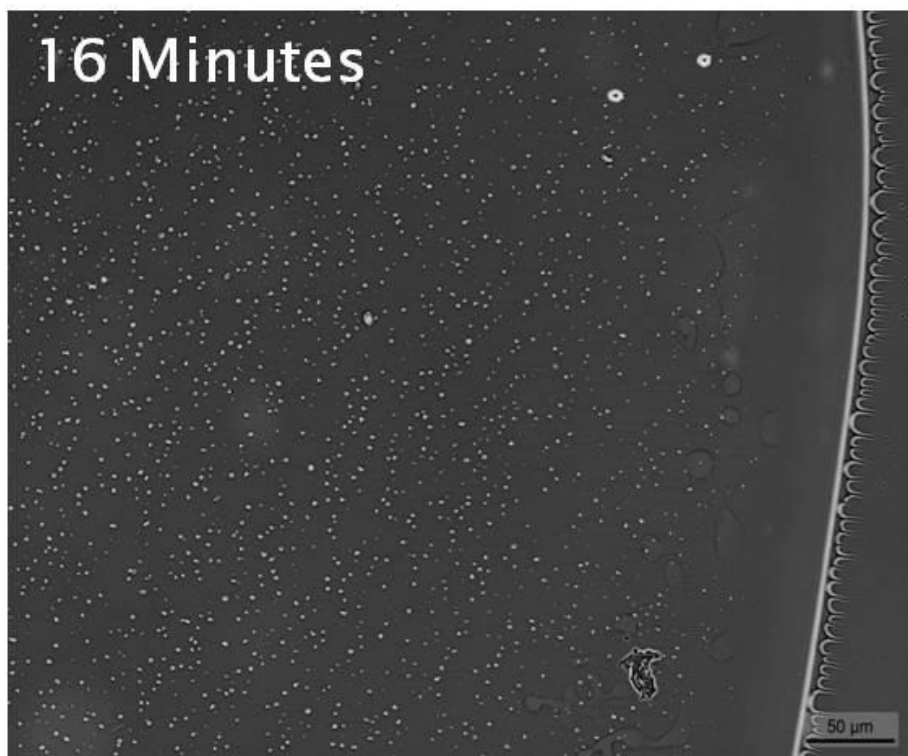


**Figure 7.2.j: Image of sample area depicting 16 minutes after etching process has taken place**

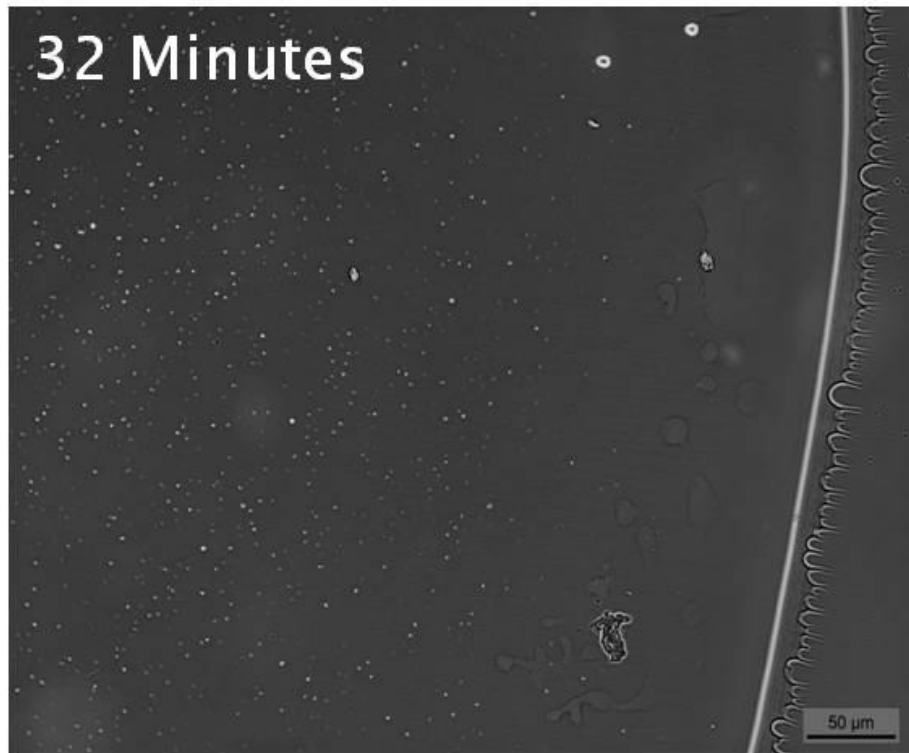


**Figure 7.2.k: Image of sample area depicting 32 minutes after etching process has taken place**

These three images of a series of 8 demonstrate a clear decrease of the embedded  $\text{Fe}_3\text{O}_4$  constituents via HCl etching over a time span of 32 minutes. The time span chosen based on the qualitative comparison between the original image and the current one. This was accomplished through a trial and error basis where the effective etching time to clear a  $500 \times 500$  pixel area of the etched samples. We have found that 32 minute was sufficient to observe this effect as seen in Figure 7.2.k.

The analysis was accomplished based on a similar principle to the array density analysis completed in Section 7.2.2 but accompanied with a passing time interval. The results were ascertained from computing only from the original number of arrays and the total number of arrays left after the 32 minute mark with three specific  $500 \times 500$  pixel area locations. The rationale behind this was due to the slight changes in the imaging position causing some arrays to enter the field of view in the area of interest causing errors. These errors are unavoidable as it is unfeasible to obtain an image which is exact position and at the same rotation each time the sample was imaged. Based on the results obtained the percentage of array

subtraction after etching for were computed to be an optimistic 81.5%, and a minimum of 60.4%. Nevertheless, the minimum percentage of 60.4% was used as it was found through iterative experiments that the percentage did not decrease any further. The information generated here was later used in Chapter 8 to approximate the pore size via ionic conductance analysis. This concludes the OM analysis the effects of Pre-etch and Post-etch samples.

### 7.3. SEM and TEM Analysis: Introduction

SEM analyses were conducted in order to ascertain the information regarding the surface morphology of the samples subsequent to etching utilising secondary electron imaging and the investigating the internal constituents of the film prior to etching via back-scattered electron imaging. A majority of the secondary electron images were acquired using a Cambridge Instruments Stereoscan 360 while the subsequent back-scattered images were acquired using a combination of the Stereoscan 360 and Zeiss EVO60. The analyses provided here represent the secondary step of providing visual evidence towards the viability of the technology.

Whilst the TEM in combination with SEM aims determine the general shape of a single array embedded in the polymeric film.

### 7.4. Structure of SEM and TEM analysis

As mentioned previously, the SEM analysis was structured validate the findings obtained from the aforementioned OM analysis. For simplicity sake, the entirety of the following investigation was divided into sub-sections which highlight the different aspects that were to be investigated. Brief description of the sample preparation method accompanies in their respective investigative sections.

Additionally, different sample preparation methods were employed to suit the subject of scrutiny. For example, samples that were prepared for BE imaging were left un-etched and carbon coated as the embedded arrays were required to be intact for imaging while samples prepared for surface morphology studies using SE

imaging work were etched accordingly and gold coated. Furthermore, two methods of magnetic field manipulation were too incorporated into the fabrication procedures which are:

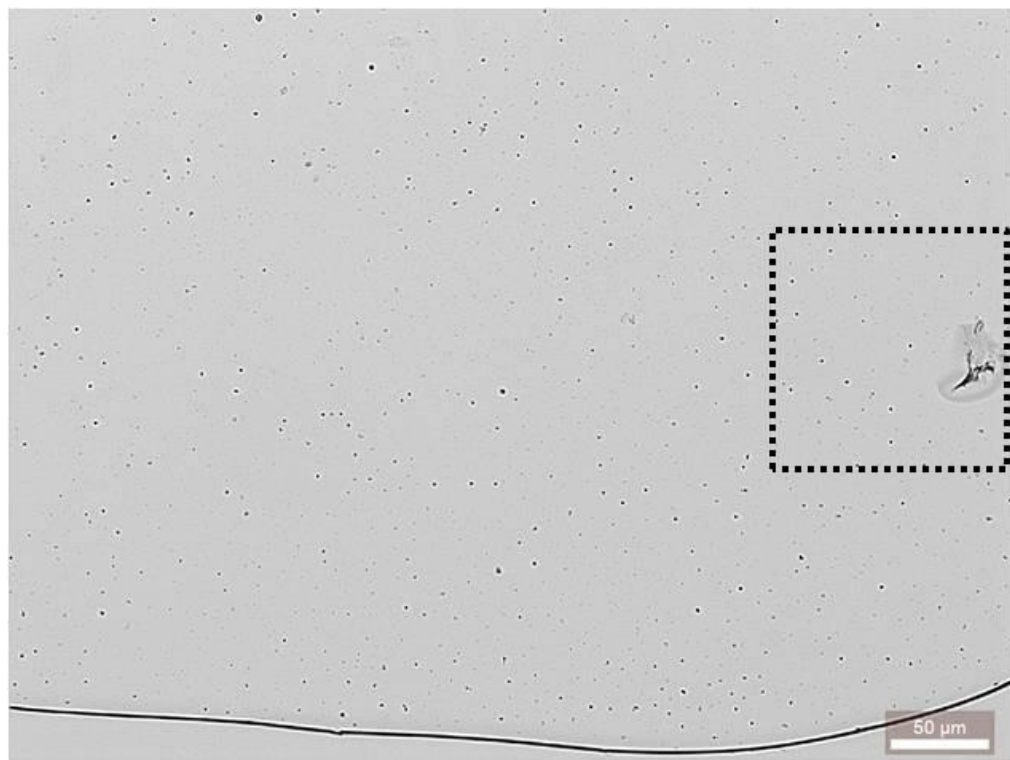
- The instantaneous application of a magnetic field via the pair of neodymium magnets and;
- The gradual introduction of the magnetic field via the Helmholtz coil system.

#### 7.4.1. Validating the Optical Images via Chemical Element Analysis

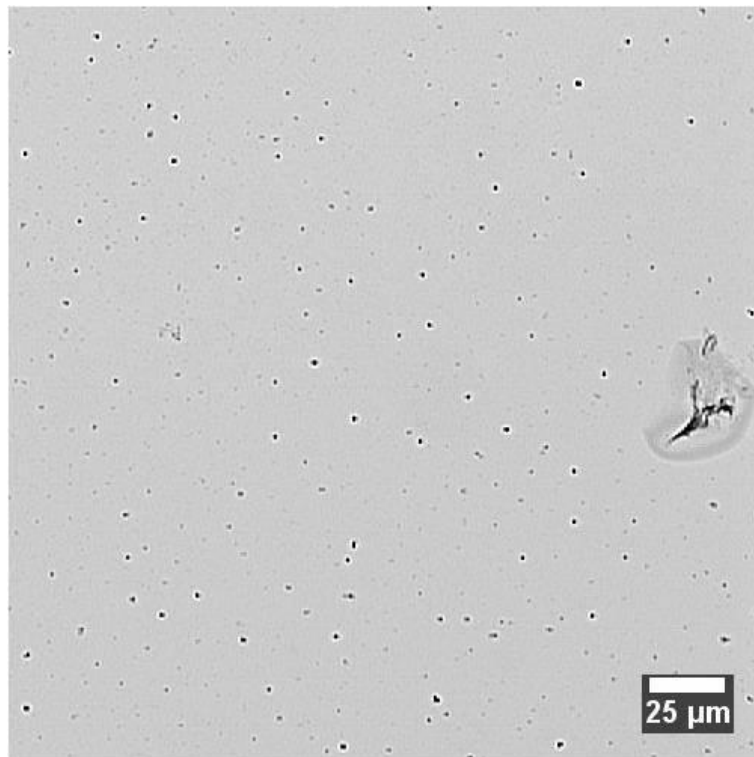
This investigative series incorporates the backscattered electron imaging via the combination of the Stereoscan 360 and Zeiss EVO60. The objectives of this series of tests were to confirm the presence of embedded  $\text{Fe}_3\text{O}_4$  constituents correspond to the dark spots observed in the OM analysis coupled with EDX as supporting evidence for elemental identification thus validating the initial findings.

This analysis is accomplished by combining three types of imaging techniques; the OM, SEM imaging via SE and BE imaging. Back scattered electron imaging techniques provide an elemental ‘map’ detailing different chemical composition of materials at different contrasts. For example, heavier elements such as iron, nickel and cobalt will be represented strongly as brighter regions as they backscatter the electron better with respect to lighter materials such as carbon, aluminium and silicon. Since our samples contain iron elements inside the polymeric matrix, the iron constituents will in effect be projected as brighter spots.

Figure 7.4.a exemplifies the above description by demonstrating a direct correlation with each other providing visual evidence. The analysis begins with a typical sample which has been optically characterised detailing the observable arrays prior to carbon coating.

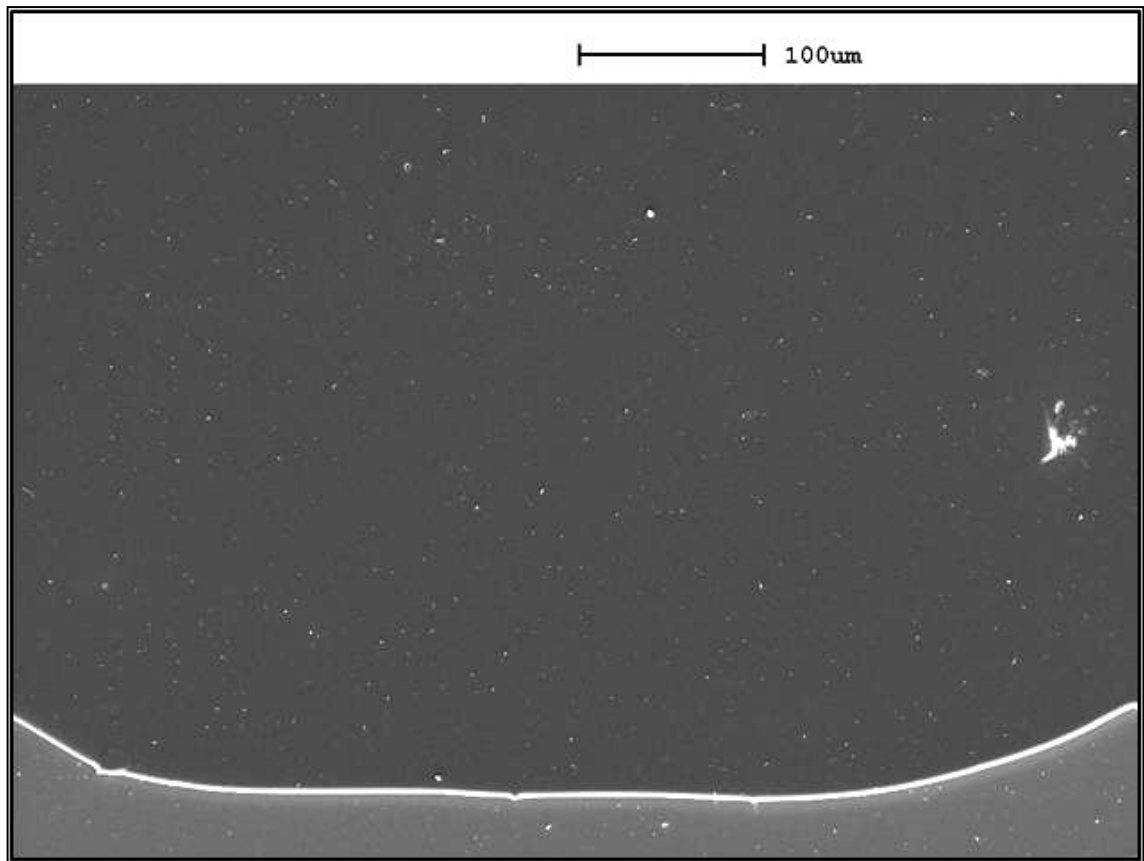


**Figure 7.4.a: Typical sample with a designated site for BE imaging analysis**



**Figure 7.4.b: A 500 x 500 pixel image of designated site with distinguishable mark**

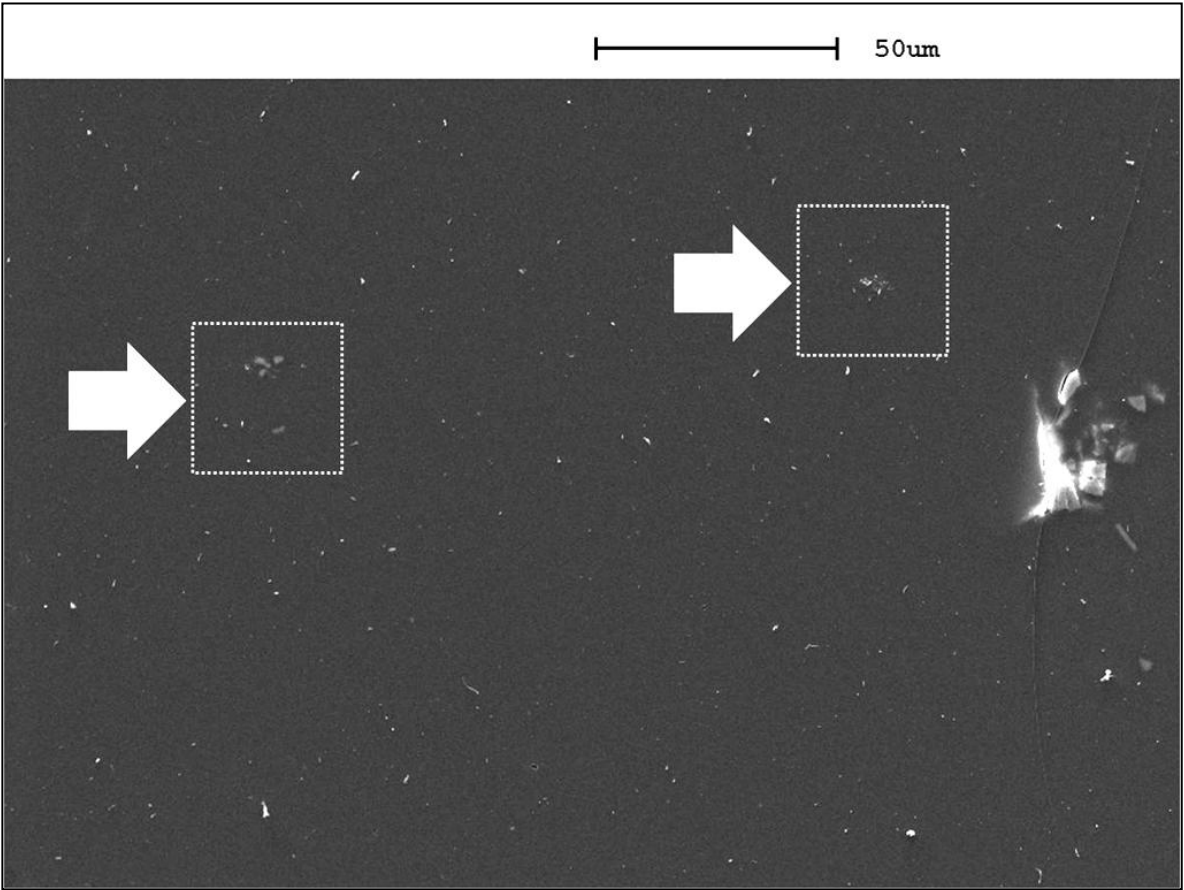
Figure 7.4.a demonstrates a preselected sample for BE analysis with a highlighted region of interest constrained to a  $500 \times 500$  pixel region demonstrated in Figure 7.4.b. The site was chosen for its easily distinguishable mark on the film. This facilitates straightforward navigation through the sample during SEM and BE imaging. The following figure below demonstrates the corresponding equivalent SEM image to compare with the OM image presented in Figure 7.4.a.



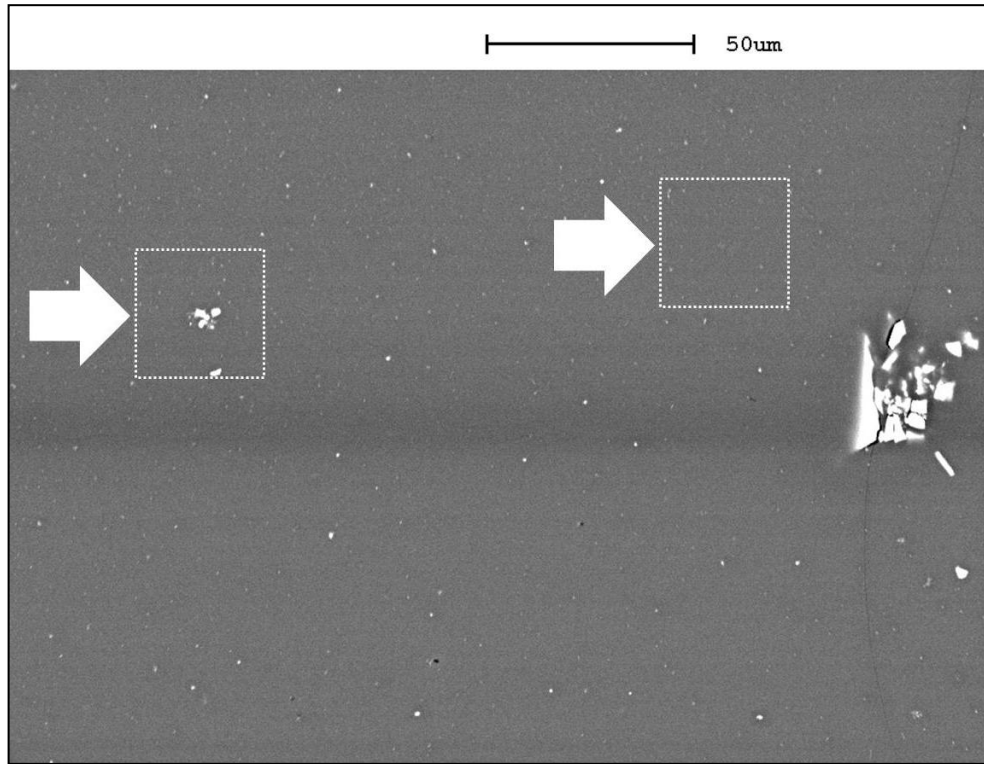
**Figure 7.4.c: SEM equivalent image relevant to Figure 7.4.a**

Figure 7.4.c demonstrates the SEM micrograph equivalent of Figure 7.4.a after the carbon coating process. The purpose of this demonstration serves as visual reference when all three OM, SE and BE micrographs are compared with each other. The rationale here is to obtain a point of reference based on the imaging regime via the OM analysis and intuitively the same site was imaged via SE and BE mode for comparison. The following step was to obtain a BE image at the designated site similar location relative to Figure 7.4.a. A visual comparison is provided Figure 7.4.d and Figure 7.4.e to detail the direct correspondence of density and location of the embedded iron (Fe) constituents.

To obtain the best imaging conditions, the  $\text{Fe}_3\text{O}_4$  constituents within the film were exaggerated by increasing the SEM probe current. It was found that a 1 nA probe current at 15 kV acceleration voltage gave the best results using the Stereoscan 360.

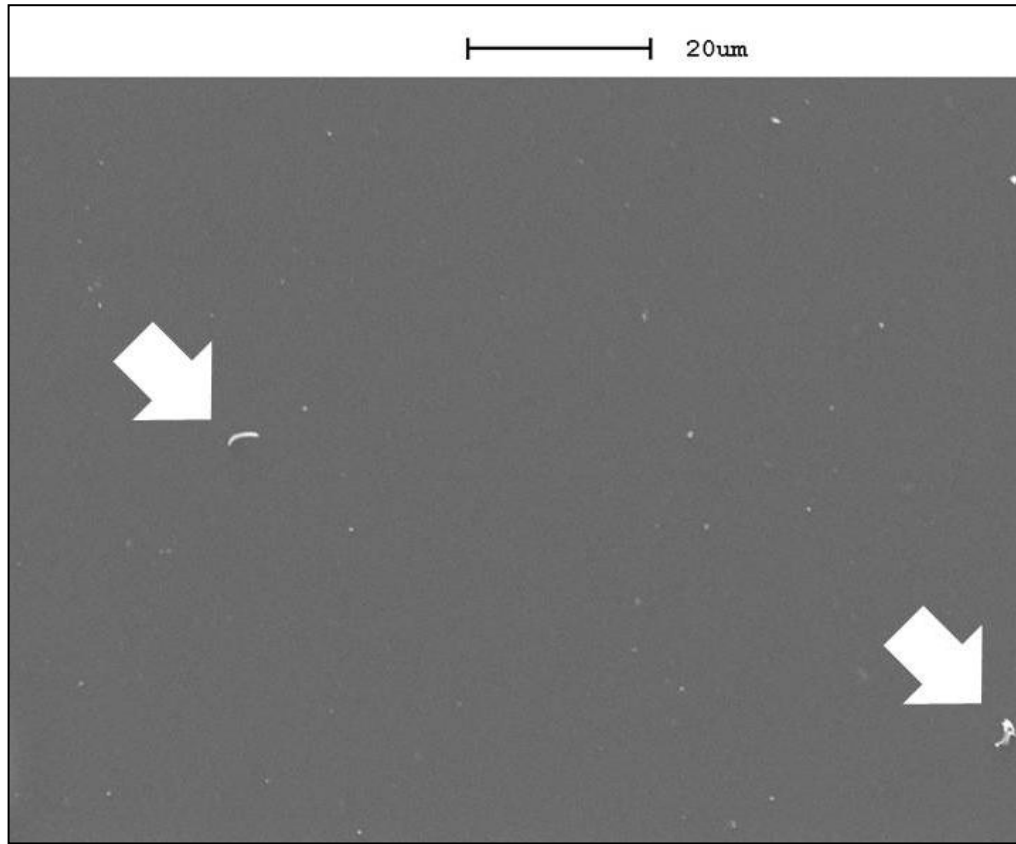


**Figure 7.4.d: SEM Image of aforementioned site accompanied with visual reference markers.  
SEM imaging parameters: 353.52 pA at 15 kV**

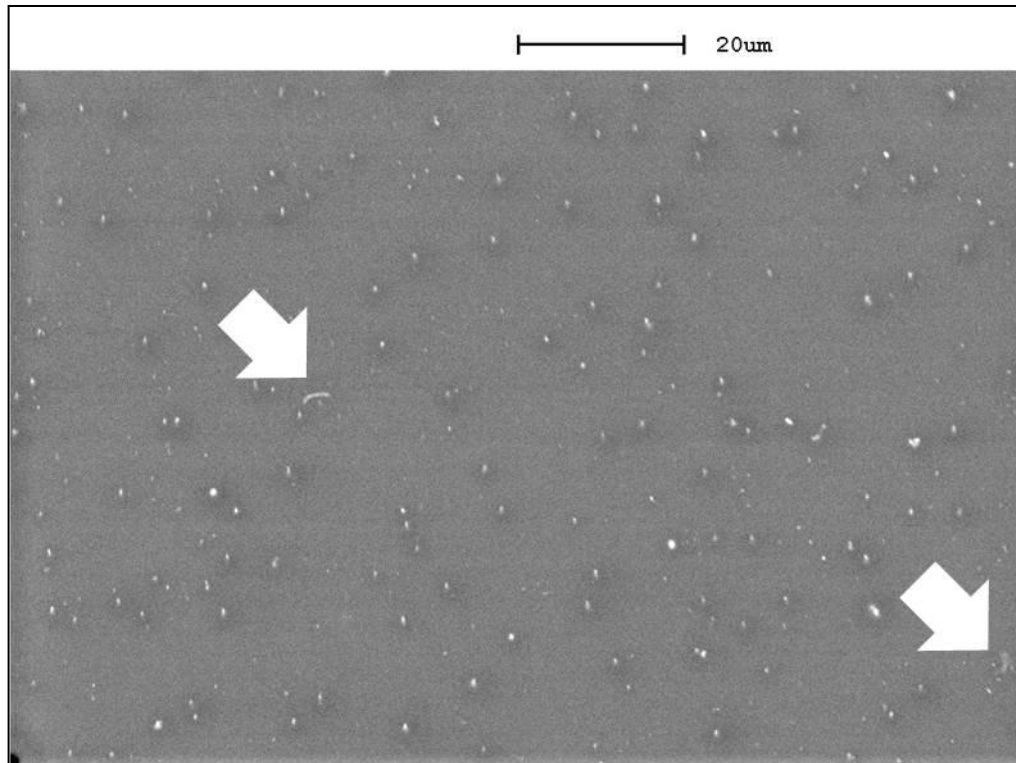


**Figure 7.4.e: BE Image of aforementioned site accompanied with visual reference markers. BE imaging parameters: 1 nA at 15 kV**

The annotations in Figure 7.4.d and Figure 7.4.e provide visual evidence of the difference between the SE imaging and the BE imaging. As a rule of thumb, denser elements tend to exude a brighter contrast in comparison to the background. As additional evidence Figure 7.4.f and Figure 7.4.g demonstrate below are SE and BE micrographs of another of our samples depicting a clear effect between the two modes.



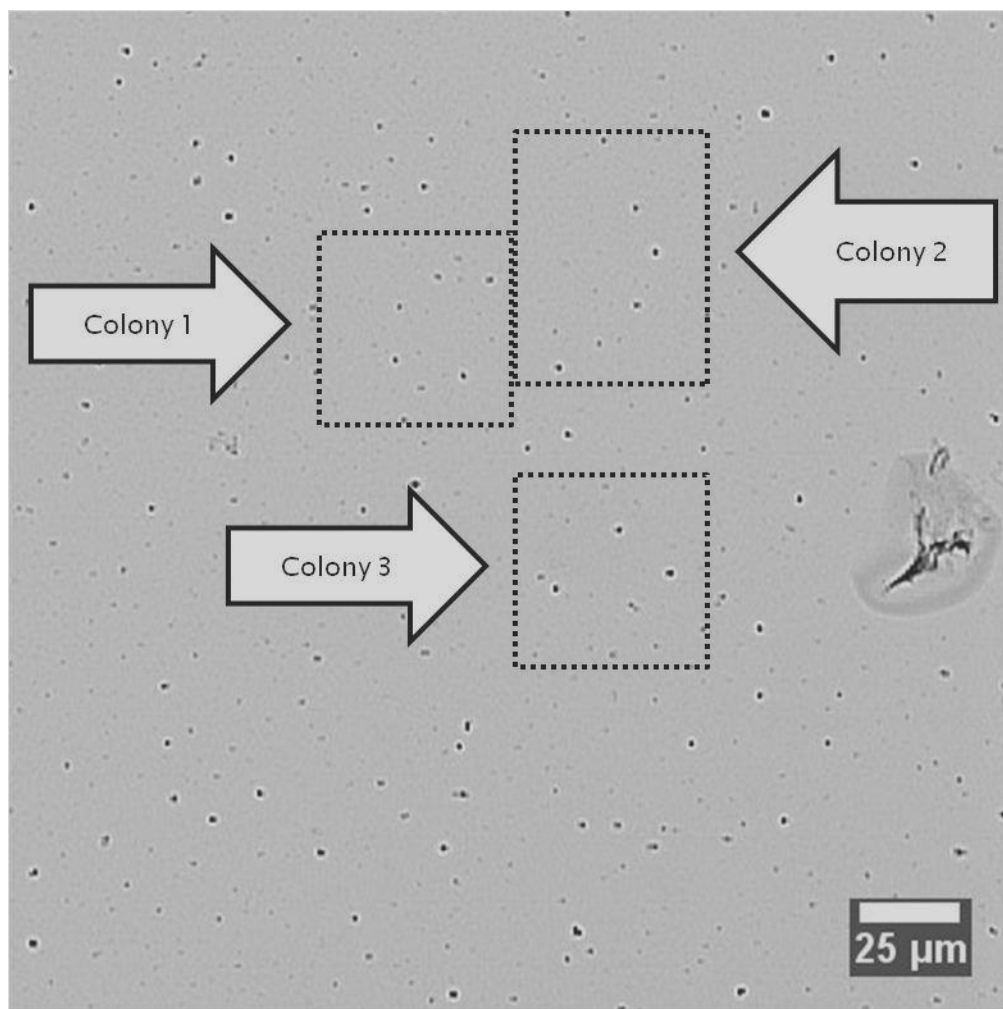
**Figure 7.4.f: Visual evidence depicting sample viewed in SE mode**



**Figure 7.4.g: Visual evidence depicting sample viewed in BE mode**

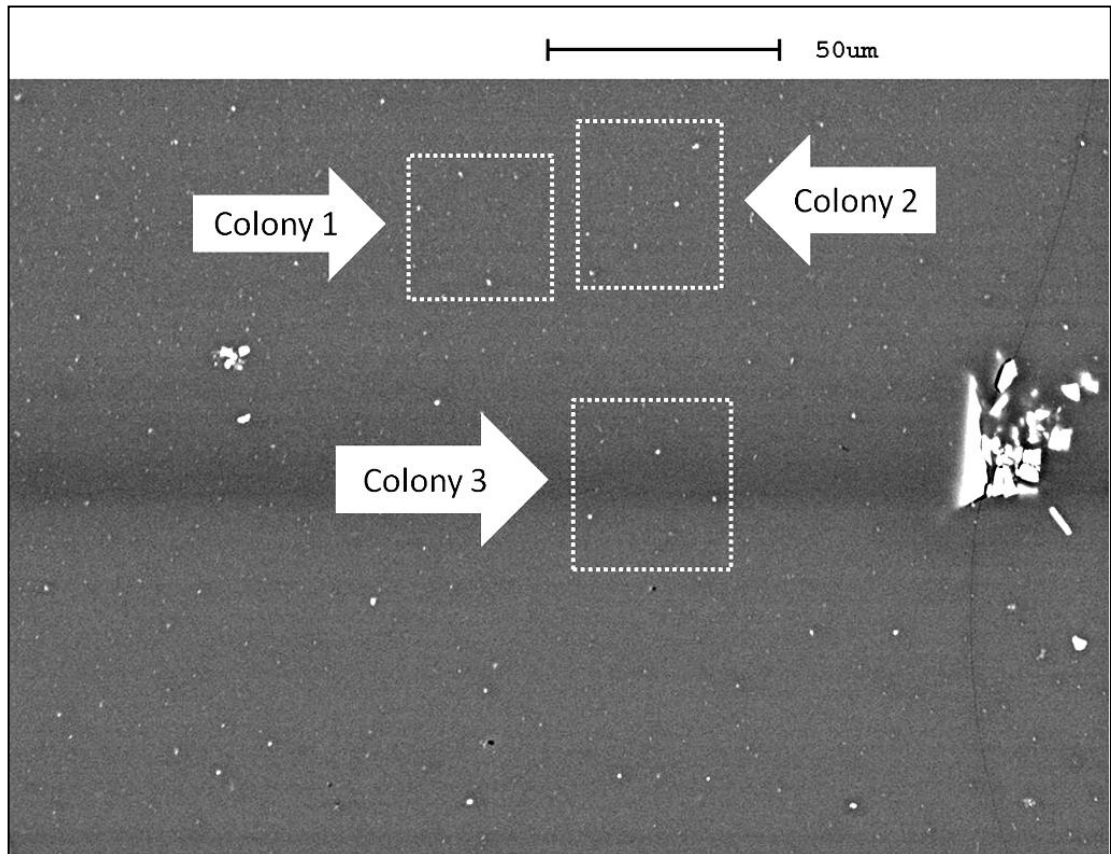
The Figure 7.4.f depicts the sample in SE electron mode. Note the annotation indicating the debris that was situated on the sample surface. Inspection in BE mode illustrated in Figure 7.4.g the debris shows a lighter contrast (annotated by the white arrows) in comparison with the bright spots that surround it. Closer scrutiny reveals the bright spots on the BE image (Figure 7.4.g) which do not correspond to the surface features of the SE image (Figure 7.4.f).

The presences of these bright spots indicate the  $\text{Fe}_3\text{O}_4$  constituents embedded in the polymer material it is also possible to observe the correlation between the bright spots highlighted by BE and OM imagery.



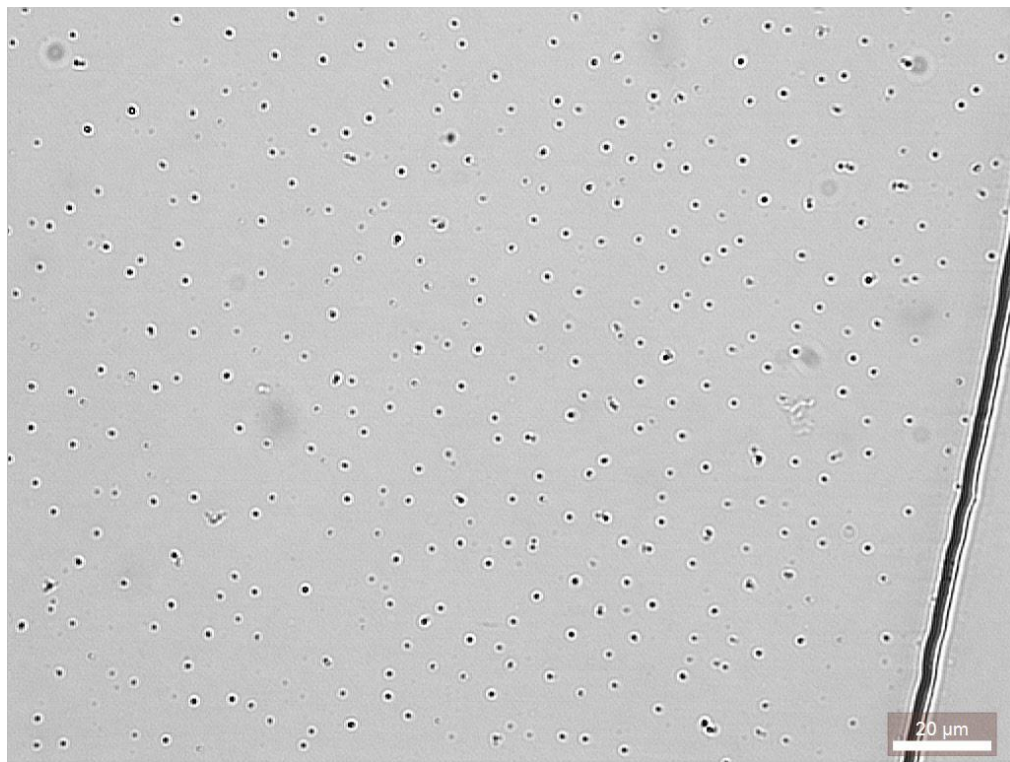
**Figure 7.4.h: A 500 x 500 Pixel image of the designated site with annotations of three colonies present in the film region**

Figure 7.4.h demonstrates an example of two clusters or colonies of arrays situated above the distinguishable mark that resemble two crescent shapes and the third colony which resembles a triangle. To demonstrate that the bright spots from the BE image correspond to the colonies presented in Figure 7.4.h, Figure 7.4.i is presented below for scrutiny.



**Figure 7.4.i: A 500x magnification of corresponding BE image with annotations of three colonies present in the film region BE imaging parameters: 1 nA at 15 kV**

Now that some basis has been established regarding the bright spots in the BE images representing the  $\text{Fe}_3\text{O}_4$  constituents in the film, it is then possible to demonstrate two corresponding images of a large cluster of arrays in a single frame. Figure 7.4.j through to Figure 7.4.l features the OM image, SE image and the BE respectively all imaged at similar magnifications summarising the entire process.



**Figure 7.4.j: OM image taken demonstrating large cluster of arrays situated in the film**

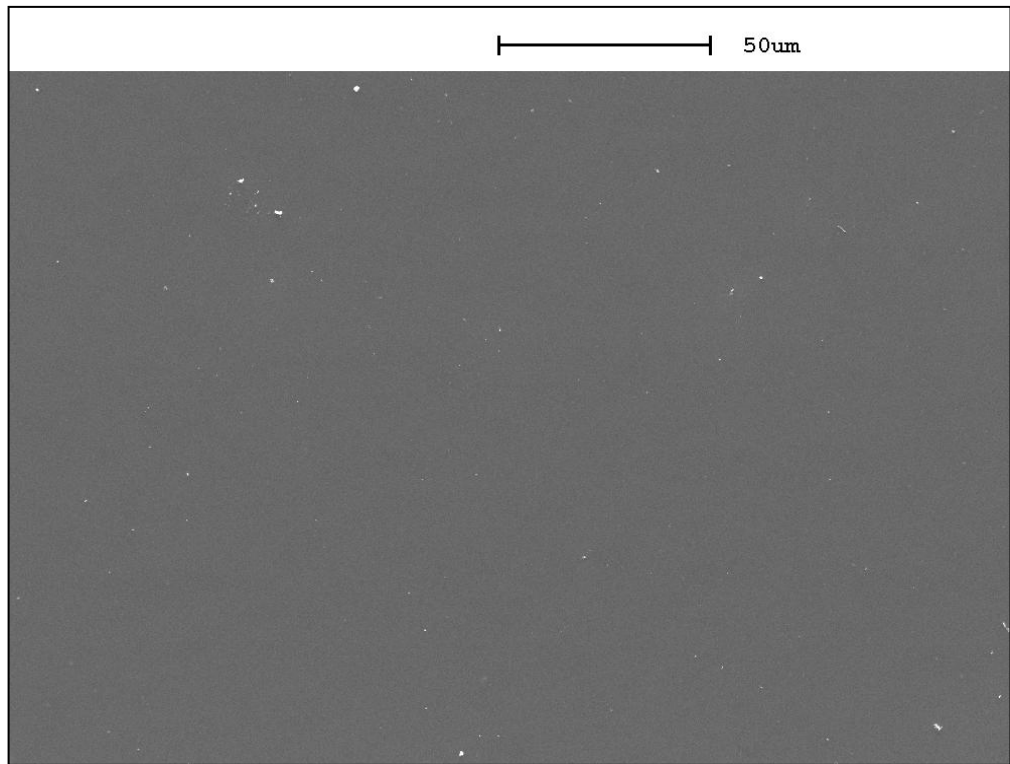


**Figure 7.4.k: SE image taken demonstrating a featureless surface across the film**

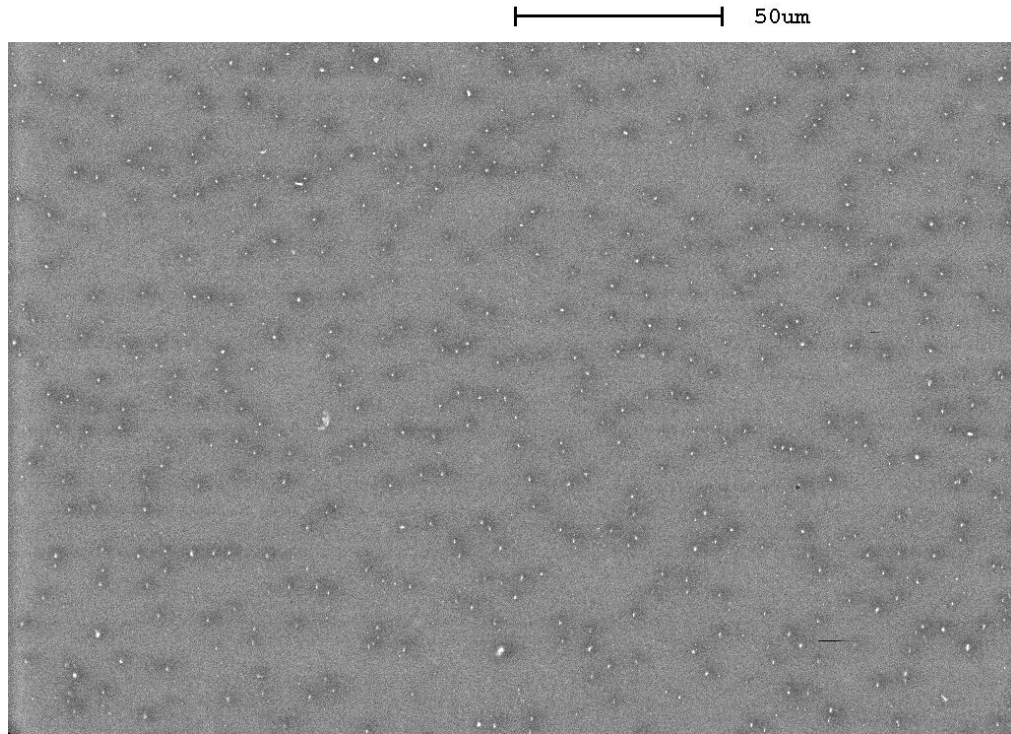


**Figure 7.4.l: BE image taken demonstrating large cluster of arrays embedded within the film at the same location as Figure 7.4.k**

To support claims that the Fe<sub>3</sub>O<sub>4</sub> constituents are represented by the bright spots exhibited in the BE images, X-ray elemental analysis was conducted on the corresponding samples. Consequently, the readings of the analysis had to detect traces of iron. For this elemental analysis, the Zeiss EVO60 was used accompanied with the INCA EDX elemental spectroscopy system. Results of the analysis are presented Figure 7.4.n. For this analysis, two tests were conducted whereby one analysis was conducted on the background surface away from the bright spot presented in BE images and vice versa. Figure 7.4.m and Figure 7.4.n presented below exemplifies this first criterion.

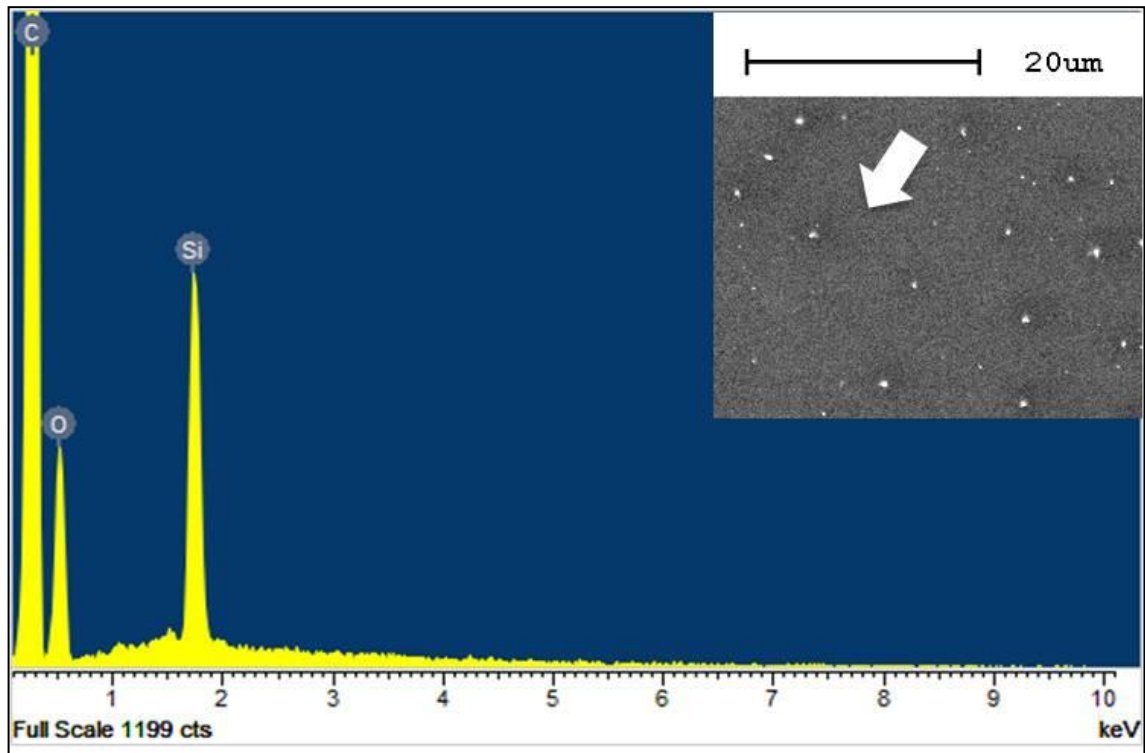


**Figure 7.4.m: Background scan detailing no traces of Fe via X-ray element analysis**

Figure 7.4.m illustrates the result for the background spectroscopy analysis should present no traces of Iron, Fe element in range. The in-set and annotation of demonstrates a typical location to conduct the aforementioned chemical element analysis.

The results obtained here are in agreement with premise of it should bear no traces of iron and only the polymer and glass substrate are detected. This causes the high traces of carbon, C from the polymer itself and silicon, Si from the glass substrate. Alternatively when placing the scanning point across the bright spots, small traces of iron, Fe were detected. The results are presented in Figure 7.4.n.

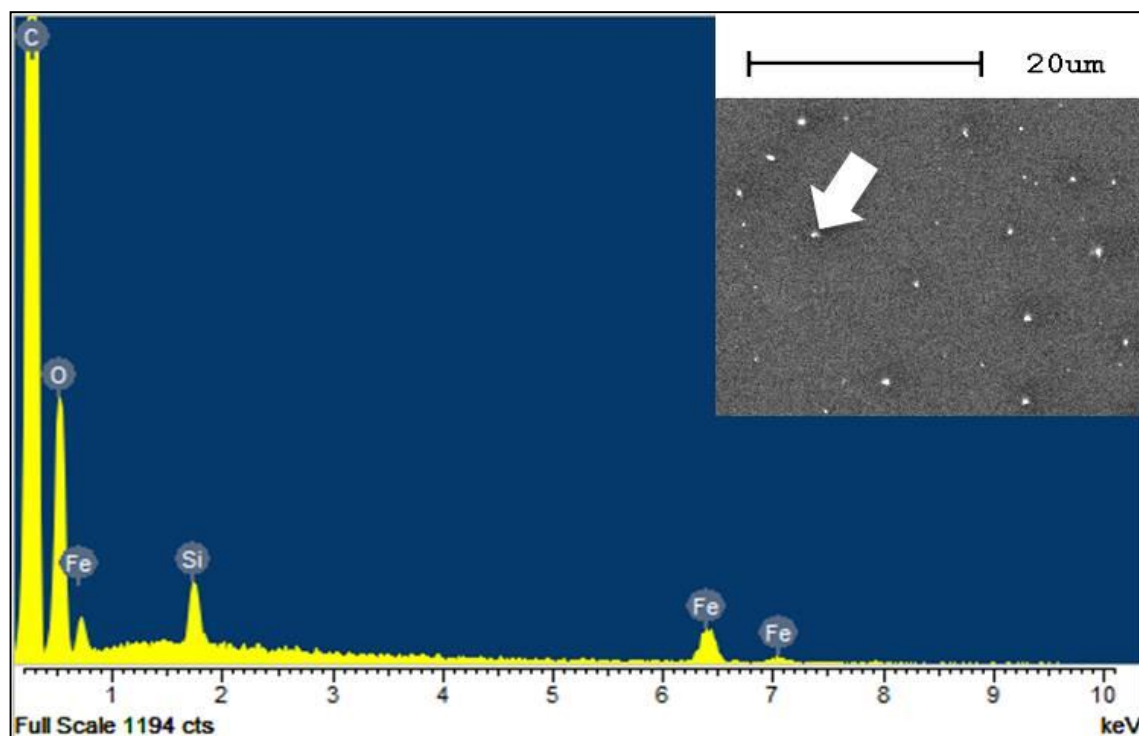


**Figure 7.4.n: Results from the X-ray element analysis on the bright spots across the BE images**

In Figure 7.4.n some traces of iron, Fe is visible within the spectrum due to the  $\text{Fe}_3\text{O}_4$  constituents embedded in the film. Again, the in-set and annotation of demonstrates a typical location to conduct the aforementioned chemical element analysis of the observable bright spots. The reason for the low concentrations presented here is because the sampling volume is much larger than the array diameter (it typically has few microns in radius). Nevertheless, the analyses does highlight the initial hypothesis and confirms a direct correspondence from OM and BE analysis.

#### 7.4.2. Physical Morphology of the Columnar Structures

TEM characterisation was conducted to determine the effective single array shape embedded in the polymeric film. This was achieved by embedding multiple stacks  $\text{Fe}_3\text{O}_4$  embedded polymer film platforms sandwiched on top of each other in to resin. The preparation techniques were a similar method used in previous works (Ward, Chun, Queenan, Calabro, Morales, & Becker, 2010)

The specimen was then cured for 48 hours in a vacuum oven to remove unwanted air bubbles. Then the resin block was sliced perpendicular via ultramicrotomy using a Leica EM UC6 and finally sent for TEM analysis using the JEOL 2010 High Resolution TEM. The rationale behind this method was to capture a cross-sectional image of the immobilised  $\text{Fe}_3\text{O}_4$  columnar structures inside the polymer films so that image analysis could take place. The preparation technique a similar method used in previous works (Ward, Chun, Queenan, Calabro, Morales, & Becker, 2010). An overall image and image analysis from the TEM work are demonstrated in Figure 7.4.0.

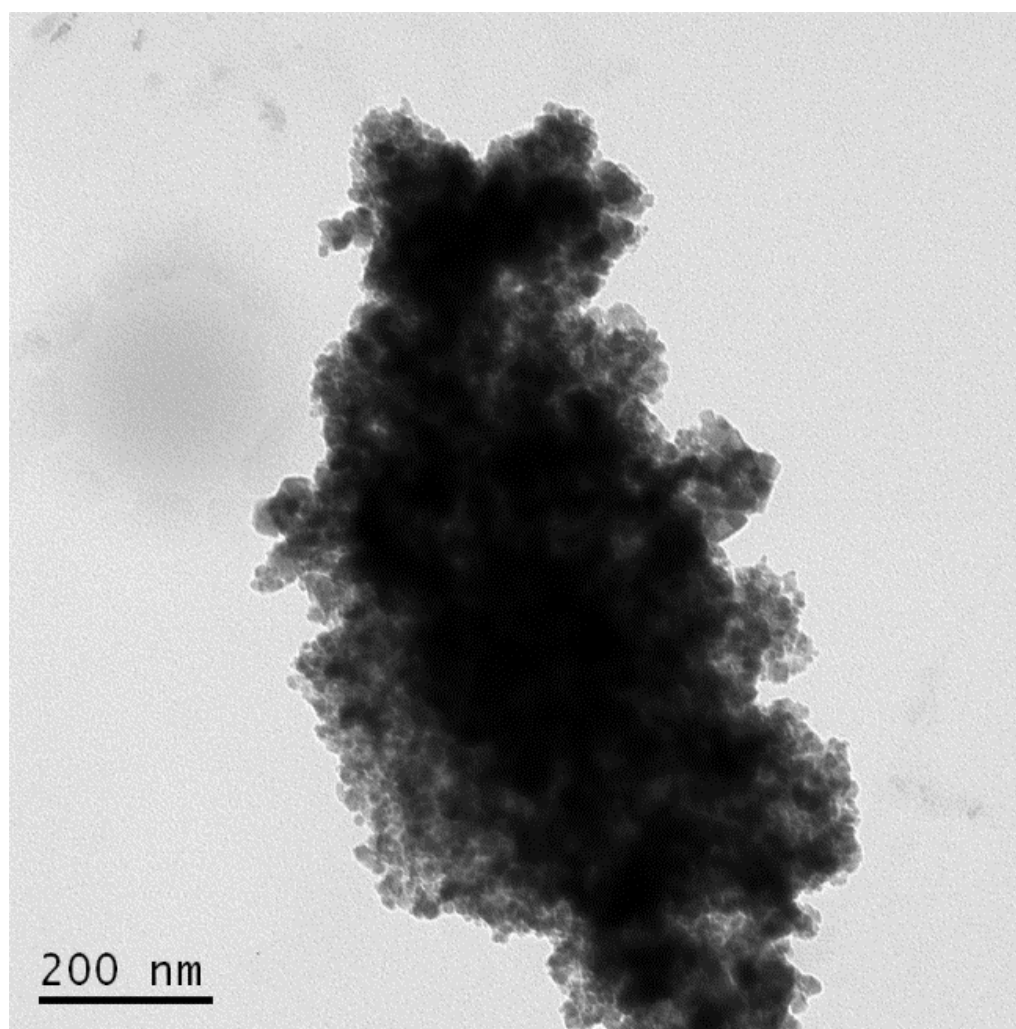
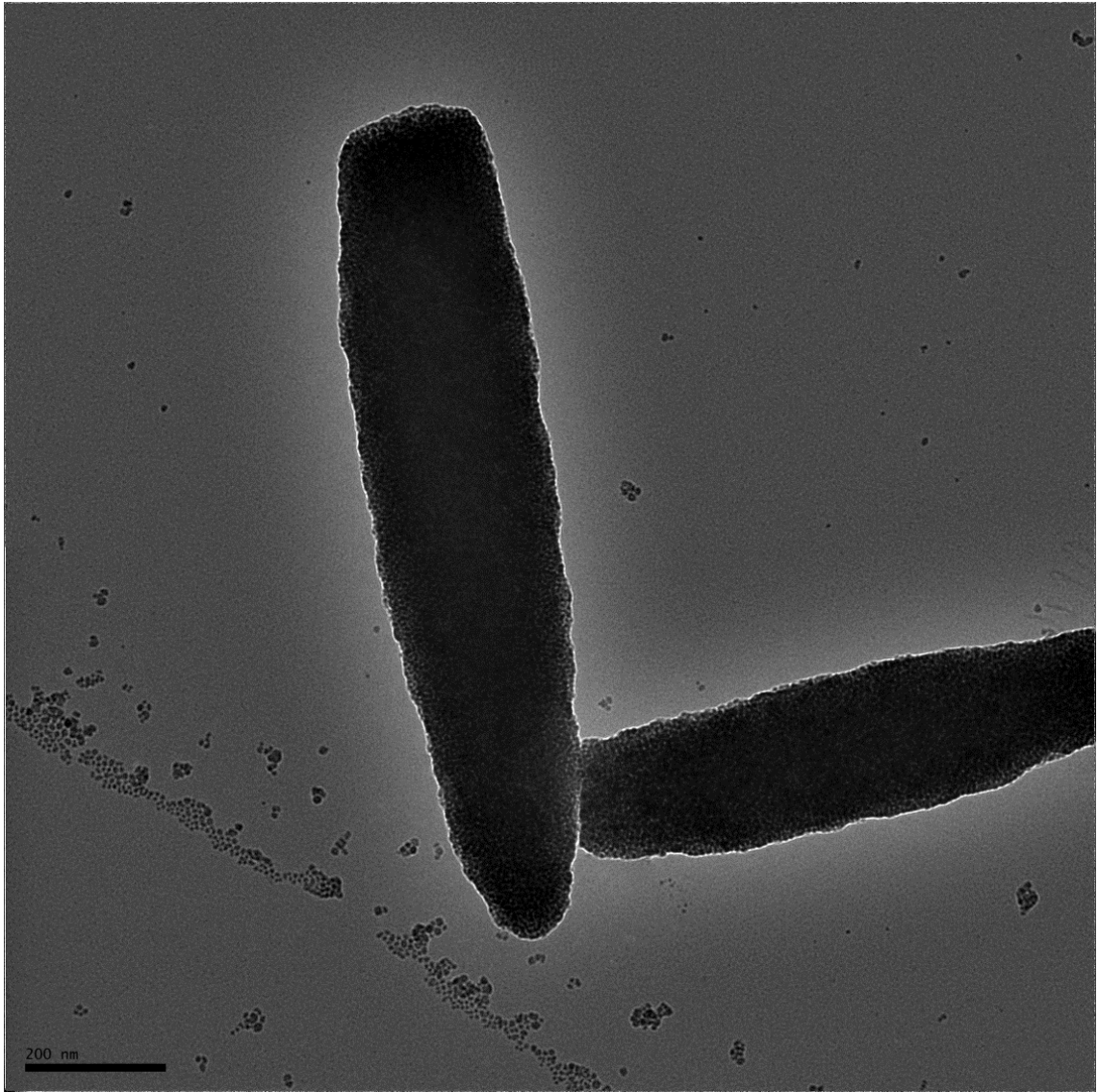


**Figure 7.4.0: A TEM image of the embedded  $\text{Fe}_3\text{O}_4$  constituents within the polymer film at 53000x magnification**

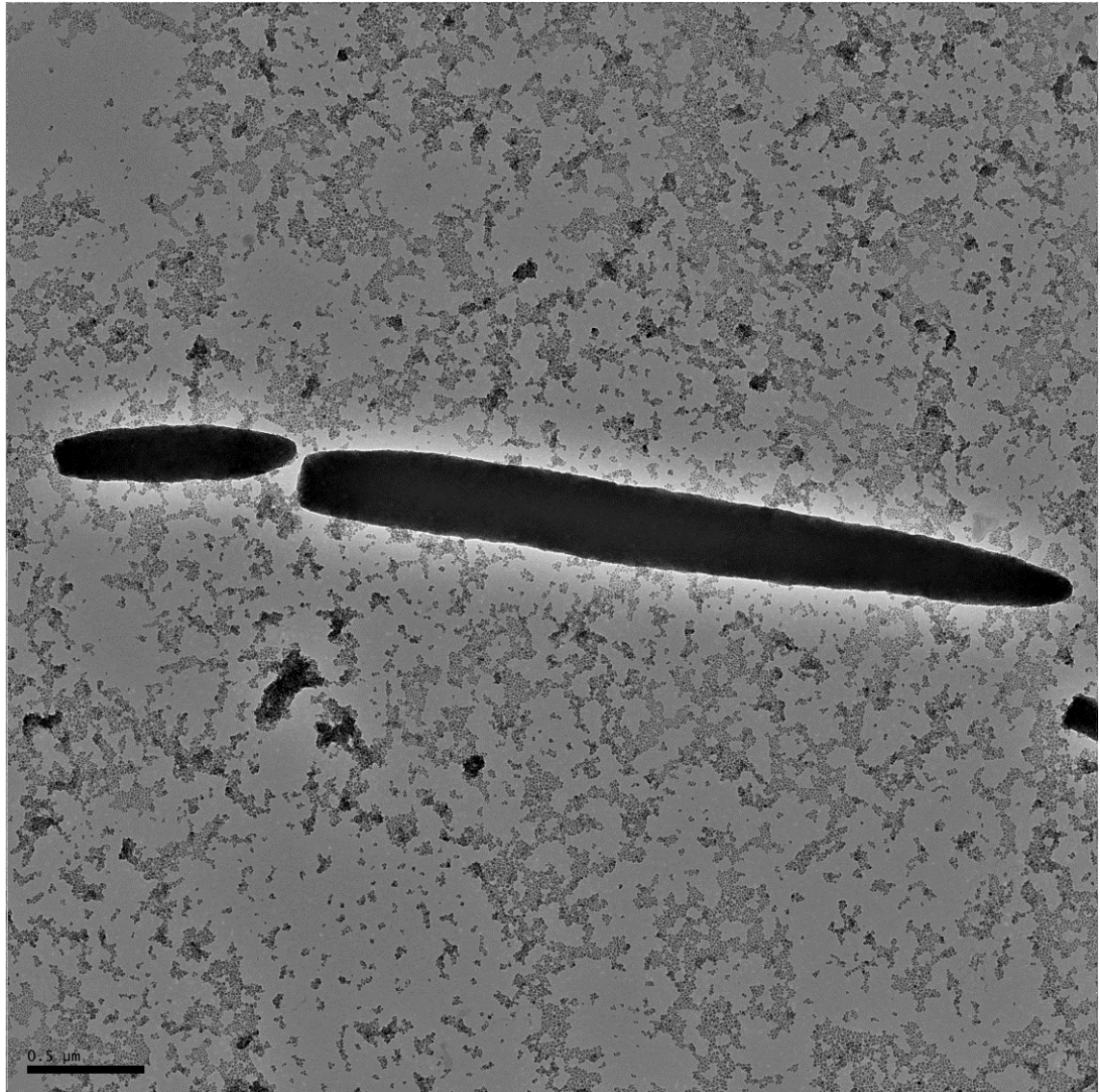
Figure 7.4.o demonstrates a colony of  $\text{Fe}_3\text{O}_4$  constituents resembling a formation similar to the aforementioned columnar structures in Chapter 3 Section 3.3. However, column appears to be strongly deformed; this could be due to the perpendicular cleaving effects from the ultramicrotomy causing some  $\text{Fe}_3\text{O}_4$  constituents to become dislodged from the overall structure. An X-ray spectroscopy was conducted as supporting evidence for element identification. The analysis confirms that the colonies were indeed iron based. The results confirm the theory of the magnetic field induced columnar structures.

To clearly observe the growth of singular columnar structure that feature tapered ends; experimentation similar to the works of Rybchenko and co-workers (Rybchenko, Dyab, Haywood, Itskevich, & Paunov, 2009) were repeated where they have successfully represented a fully assembled columnar structure via TEM and SEM imagery. This was accomplished depositing a small volume of the colloidal dispersed nanoparticles in HDDA onto a carbon-coated TEM grid situated on a glass substrate which was then subjected to the external magnetic field provided by the Helmholtz coil system to facilitate the self-assembly process. Intuitively the droplet containing magnetic nanoparticles deposited onto the glass substrate had its own inherent thickness which allows the structures to self-assemble spanning the entirety of the puddle thickness.

Upon reaching the desired magnetic field strength, the electromagnets were powered down and the specimen was abruptly rinsed with acetone. Consequently the HDDA monomer was dissolved and carried away along with the acetone leaving behind a deposit of fully formed structures on the substrate surface. The specimens prepared this way were analysed via TEM which revealed the columnar structures resembling the dense columnar assembly. The subsequent figures (Figure 7.4.p and Figure 7.4.q) demonstrated below exemplify the analysis.

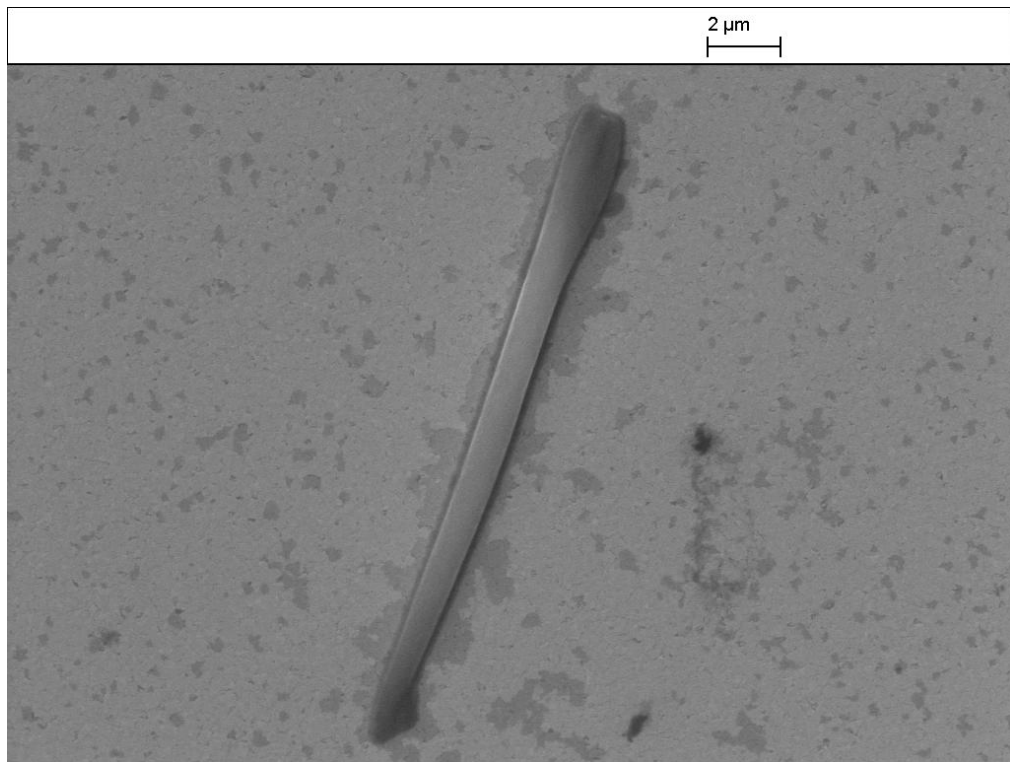


**Figure 7.4.p: TEM image depicting the columnar structure with their signature tapered ends**



**Figure 7.4.q: TEM image depicting the columnar structures with different lengths**

Figure 7.4.p and Figure 7.4.q exhibits results obtained from TEM analysis which confirms the expected tapered end shapes discussed in Chapter 3:Section 3.3. It is important to notice tapering of the assembly was well defined only on one side of the columns. The causation for the offset was due to gravitational forces upon the acetone rinsing which obscures the final column shape. This effect was also discussed in Section 7.2.1. Furthermore, a SEM imagery techniques were also employed to provide a three dimensional image of these assemblies which is presented accordingly:



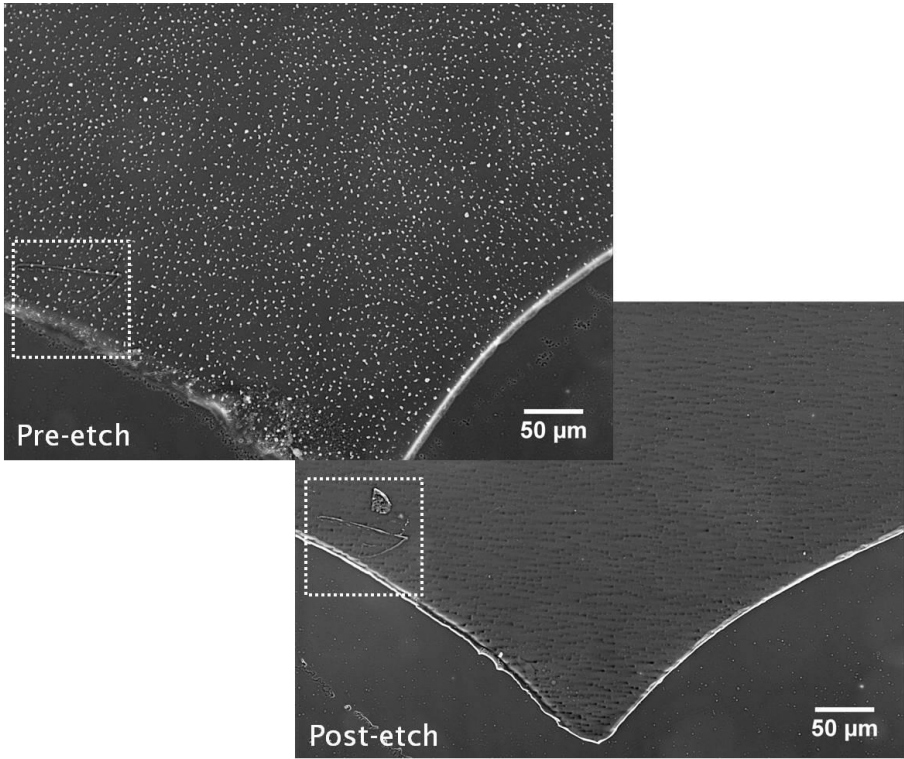
**Figure 7.4.r: SEM image depicting the assemble from a three dimensional point of view**

Figure 7.4.r is a three dimensional representation of the columnar assemble which was procured the same method and again the noticing the inherent offset towards the bottom of the assembly. The three dimensional image the columns verifies the initial densely pack columns from the previous discussion. Understandably the evidence of split-ends cannot be demonstrated here as there is no supporting matrix to retain their shape. Nevertheless this experiment confirms the previous inference concerning the expected structural configuration.

### 7.4.3. Membrane Surface Morphology Investigation

This section details initial exploratory work to investigate the surface morphology of the membrane after subjected to localised etching utilising Hydrochloric Acid from Fisher Scientific for a 24 hour period. Consequently, it was found that the analytical grade HCl removed the iron oxide,  $\text{Fe}_3\text{O}_4$  constituents embedded in the film leaving behind a porous membrane platform. Demonstrated below is an image comparison of a fabricated film in the pre-etch stage and post-etch stage adapted

from Figure 7.4.s for demonstrative purposes. Again the colours of the images have been inverted in to the negative format to highlight the embedded arrays.



**Figure 7.4.s: (Top Left) OM Image of the film location in the Pre-etch stage  
(Bottom Right) OM Image of the film location in the Post-etch stage**

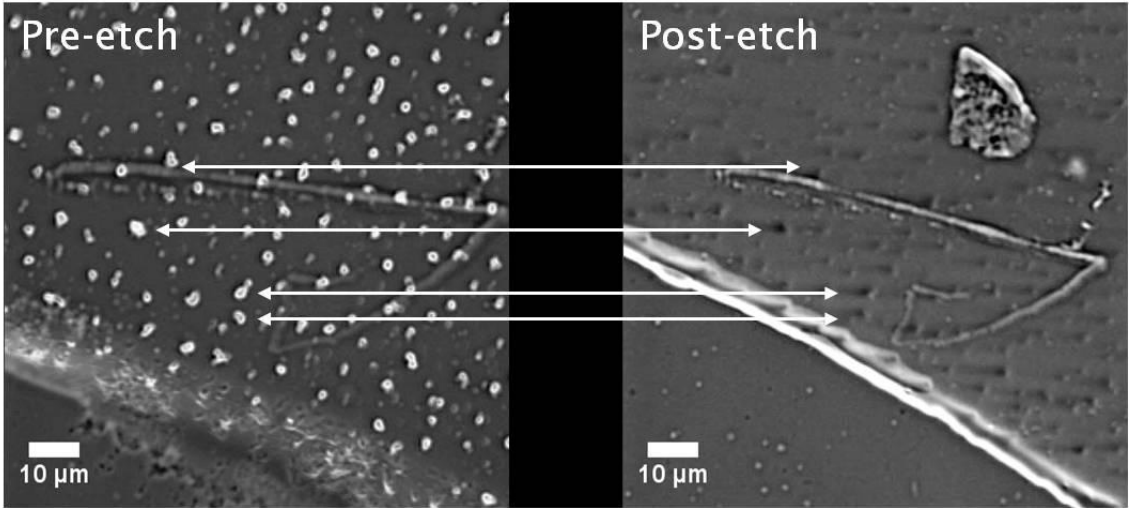


**Figure 7.4.t: (Left) OM Image of the film constituent in the Pre-etch stage  
(Right) OM Image of the film constituent in the Post-etch stage**

Figure 7.4.t are images which have been cropped to a 500 x 500 pixel image and scaled accordingly from Figure 7.4.s provides a clear indication of the total subtraction of arrays of  $\text{Fe}_3\text{O}_4$  constituents embedded in the film demonstrating the effectiveness of the etching process. The annotations between the images are there to highlight remaining artefacts as a product of etching. Progressing on, these samples were coated with gold via a gold evaporation via the Edwards vacuum coating Unit E306A at a thickness of 15 nm (this was confirmed by the thickness monitor attachment available to the evaporator). The specific gold thickness was chosen as it was the minimum coating thickness that could be achieved before surface charging occurs.

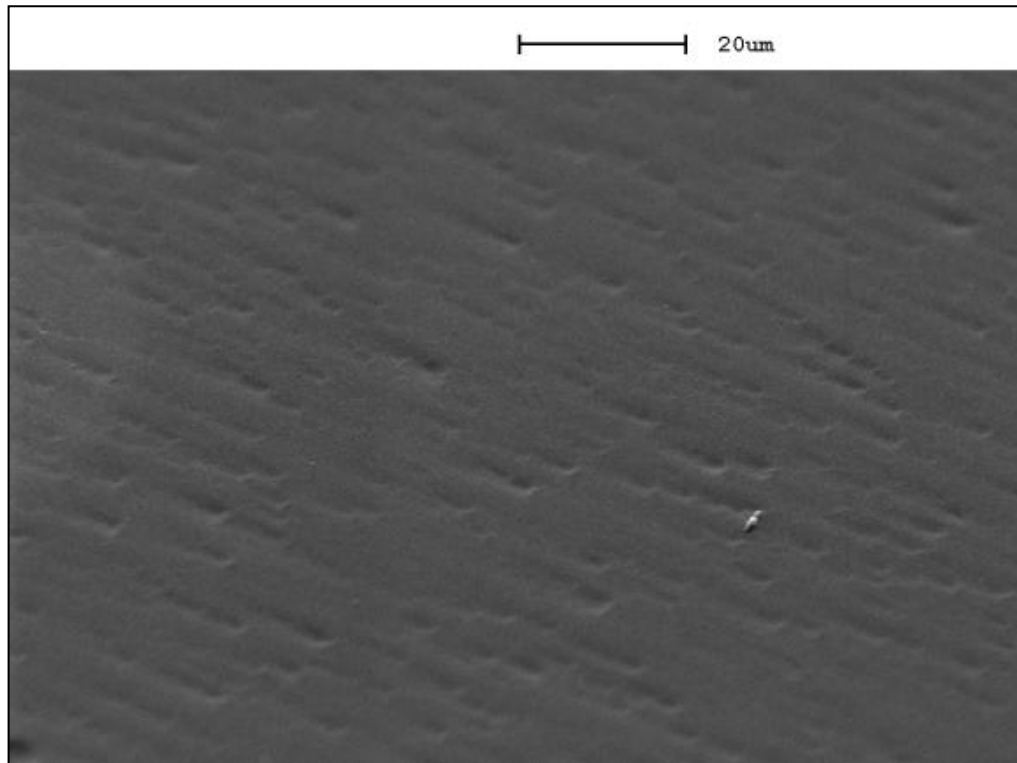


**Figure 7.4.u: SE micrograph of the surface morphology of first iteration samples (1000x Magnification)**

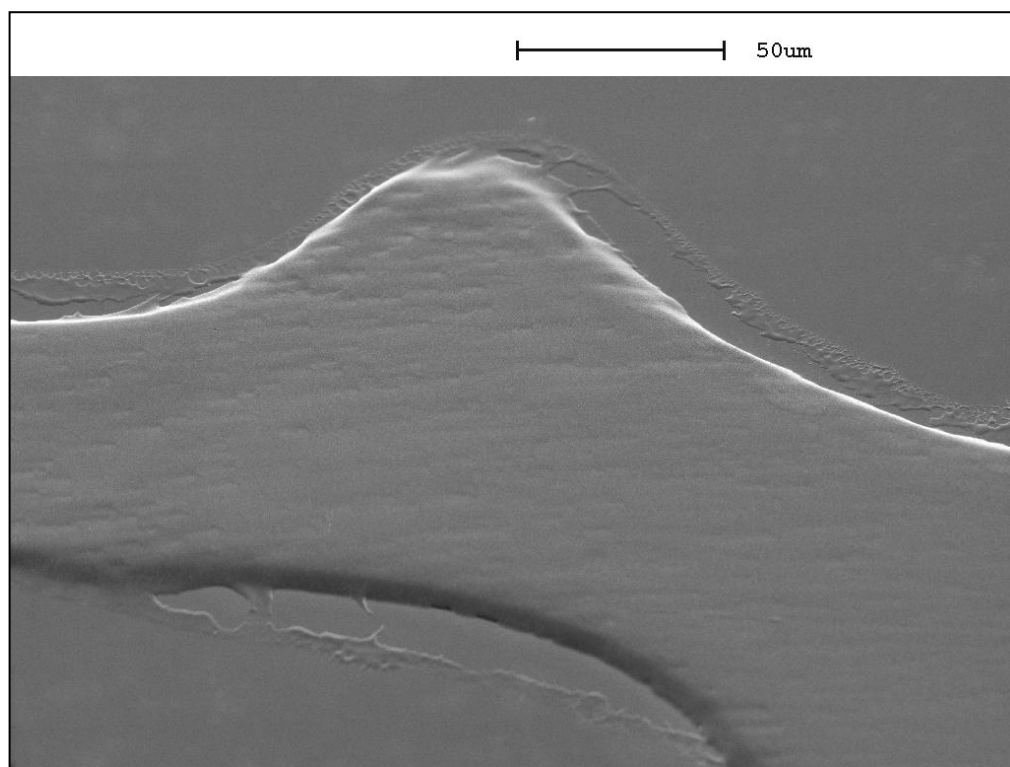


**Figure 7.4.v: SE micrograph of the surface morphology of first iteration samples (500x Magnification)**

From the results observed in Figure 7.4.u and Figure 7.4.v, SE micrograph images demonstrated a shadowing or a streaking effect running parallel with each other which suggest insufficient UV radiation time during the photo-polymerisation process. However at closer inspection at higher images magnifications did not reveal any signs of a pore opening.

Further investigation into the polymer film conditions also indicates a noticeable shrinkage after the etching process can be observed as well. The results of this scrutiny are demonstrated below.

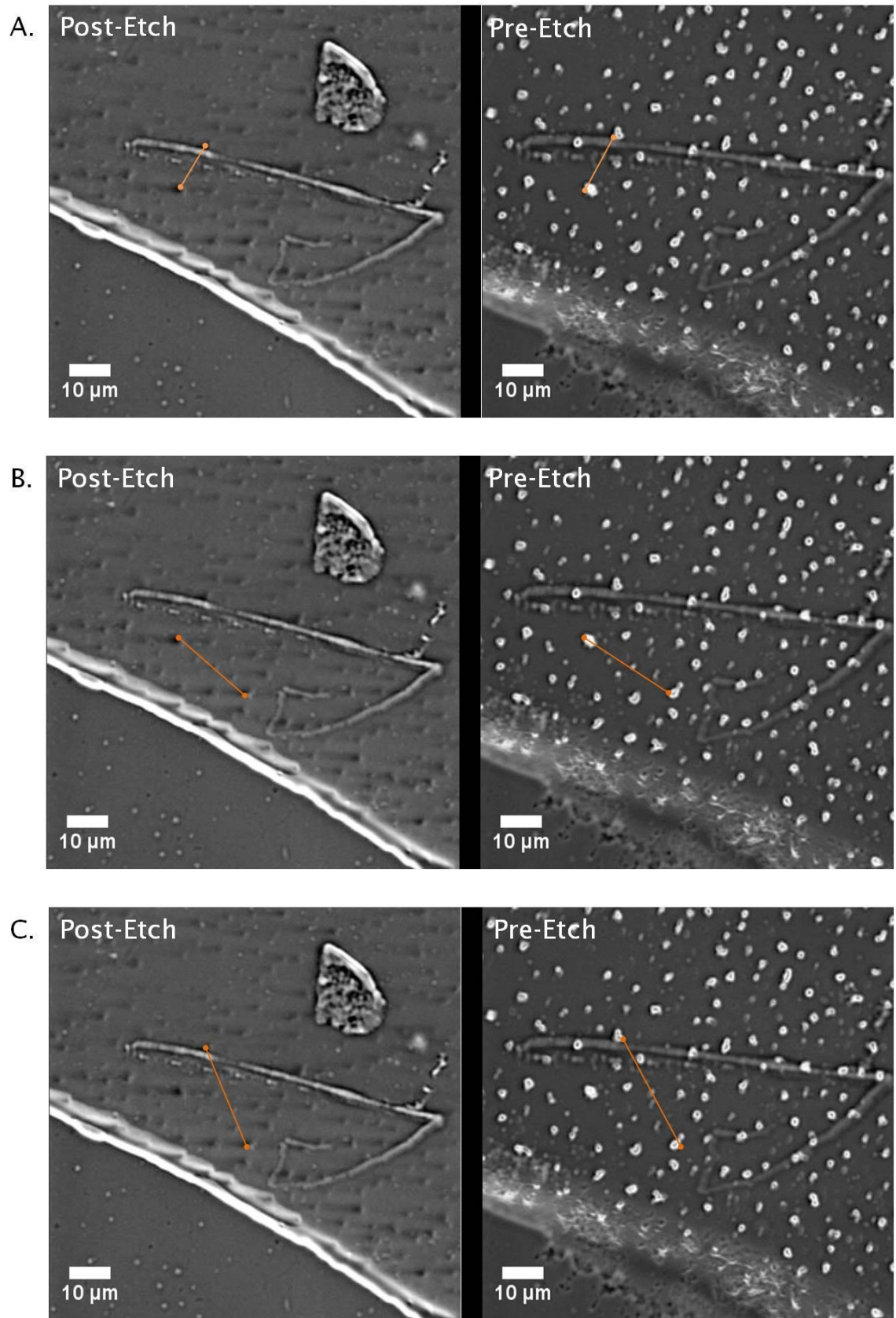


**Figure 7.4.w: OM illustration of film shrinkage subsequent to etching process and sites of measurement corresponding to array position**

Measuring the change of corresponding array sites should provide a clear indication of the percentage of shrinkage as an effect to etching. Once again measurement procedure was accomplished using ImageJ.

Array Site	Length ( $\mu\text{m}$ )		Shrinkage (%)
	Before Etching	After Etching	
A	15.2	12.4	18.5
B	23.9	20.8	12.9
C	29.3	24.7	15.7

**Table 7.4.a: Tabulated computations of film shrinkage as an effect of etching**

The data clearly demonstrates a significant decrease size relative to the change in distance between array sites. It is feasible to hypothesise the shrinkage film could be due to the relief from the polymerisation induced stresses as material is selectively removed from the bulk compromising the structural strength. This would in effect, cause a collapse at the pore openings across the surface.

The next series of specimens was an improvement from the first iteration of membrane platforms. The fabrication process featured longer curing times. This investigation yielded results which facilitated the understanding of the effects of the etching process as well as a better control over the photo-polymerisation time of these membrane platforms. Results from SEM analysis exhibited depressions that corresponded to dark patches on the surface of the film. The SE micrographs are exhibited below.

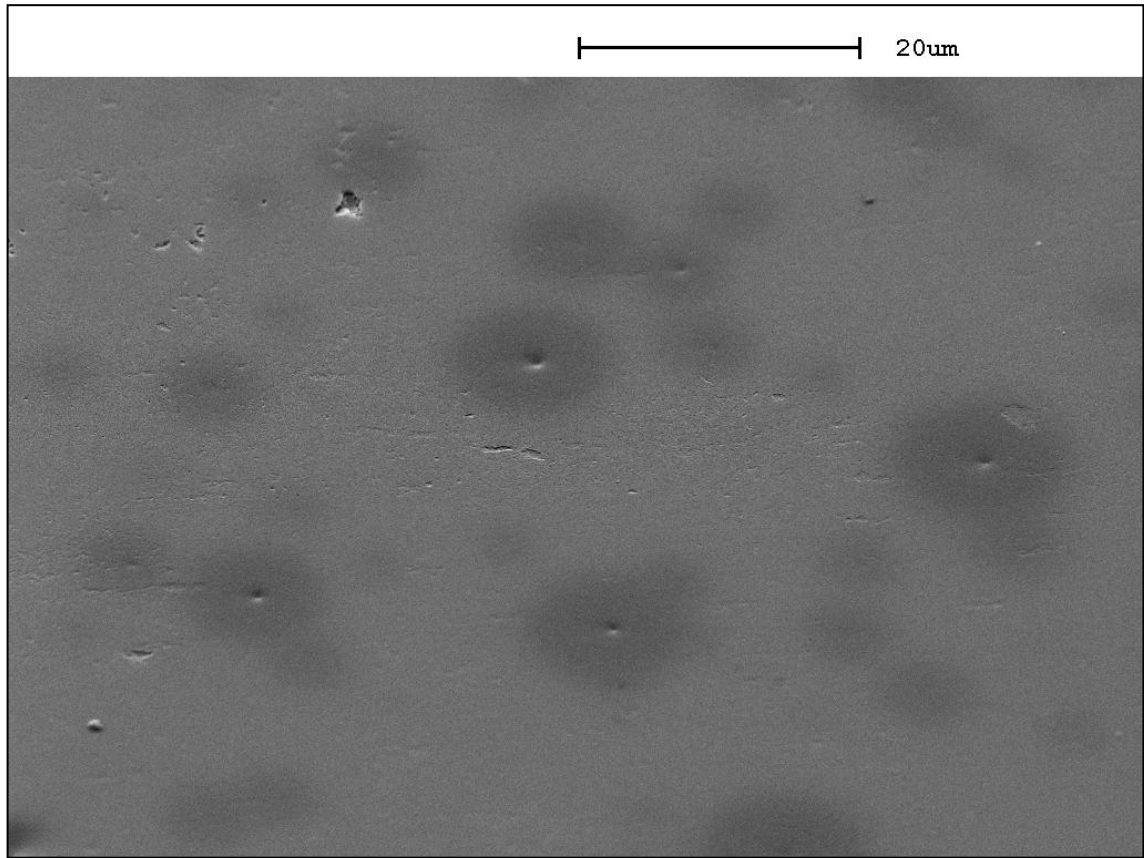


**Figure 7.4.x: SE micrograph of the surface morphology of second iteration samples (500x Magnification)**

Additionally the streaking or shadowing effect observed in the first iteration samples did not take place. This confirmed the initial hypothesis. However the surface morphology did not demonstrate any evidence porous configuration across the film surface.

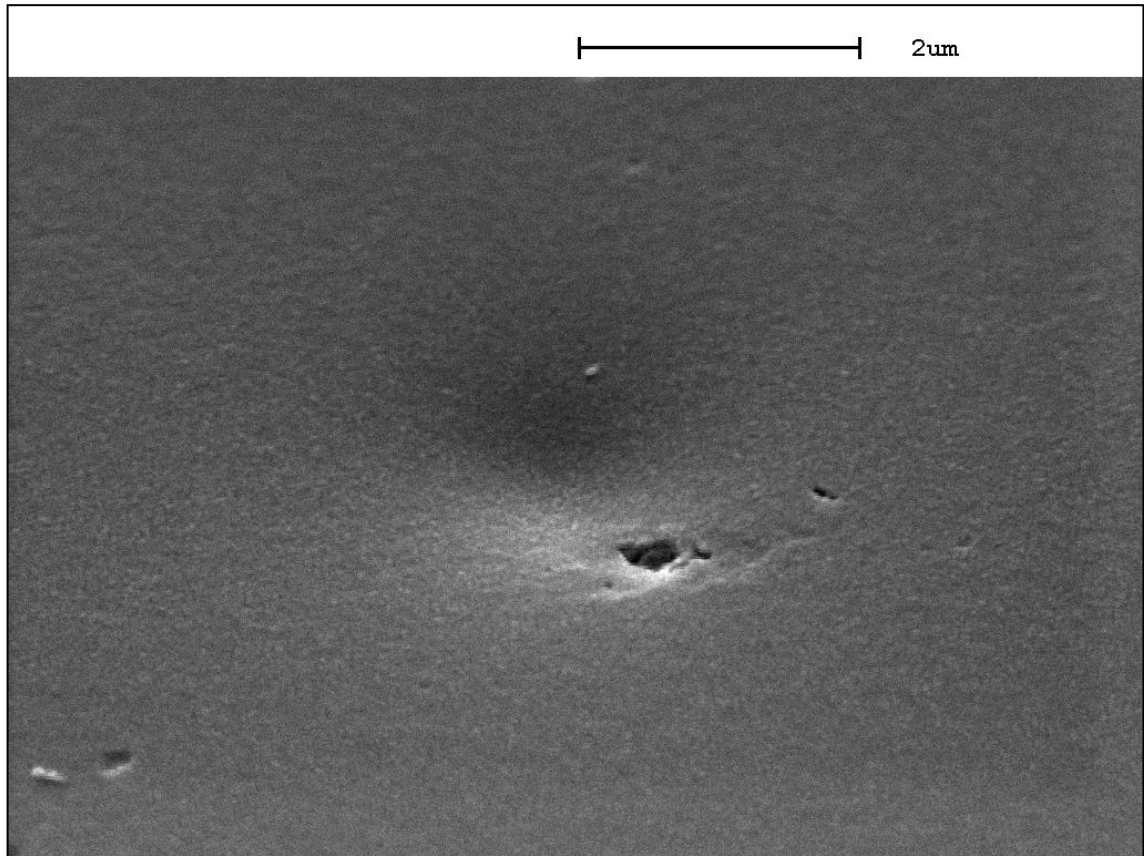


**Figure 7.4.y: SE micrograph of the surface morphology of second iteration samples (1500x Magnification)**

Furthermore the cavity across the surface presented in Figure 7.4.y suggest a presences of a pore opening however did not prove conclusive upon closer inspection as the depth was too shallow to be considered an opening. A possible justification for the elusiveness of pores openings could be the generation heat from the evaporation coating process causing the pores to collapse and alternatively the complete removal of the  $\text{Fe}_3\text{O}_4$  constituents could compromise the structural integrity of the pore opening as a causation of its eventual collapse.

Therefore to approach the predicament, an attempt to fabricate films which were partially etched was undertaken. Theoretically the pores should maintain a majority of its structural rigidity following the gold coating process. Furthermore an alternative to the gold evaporation coating technique with a low operating temperature was needed.

The third iteration of samples was the culmination of the predicament faced in the First and Second iterations. The first solution was to employ a controlled etched scheme between thirty seconds to an hour whereby would solve the problem of collapsing pores due to compromise in structural integrity of the pore openings. The second solution to follow was the use of an alternative sample coating technique whereby any effect of heat cause deformation was at a minimal. For this, a gold sputter coater Edwards Sputter Coater Unit S150B which offered low temperature coating conditions was utilised. These tests were employed in accordance to the previous hypothesis made during the second iteration test series. The results from the experimentation yielded interesting results as it revealed a network of pore openings on the surface. Recordings are exhibited in Figure 7.4.z through to Figure 7.4.cc.

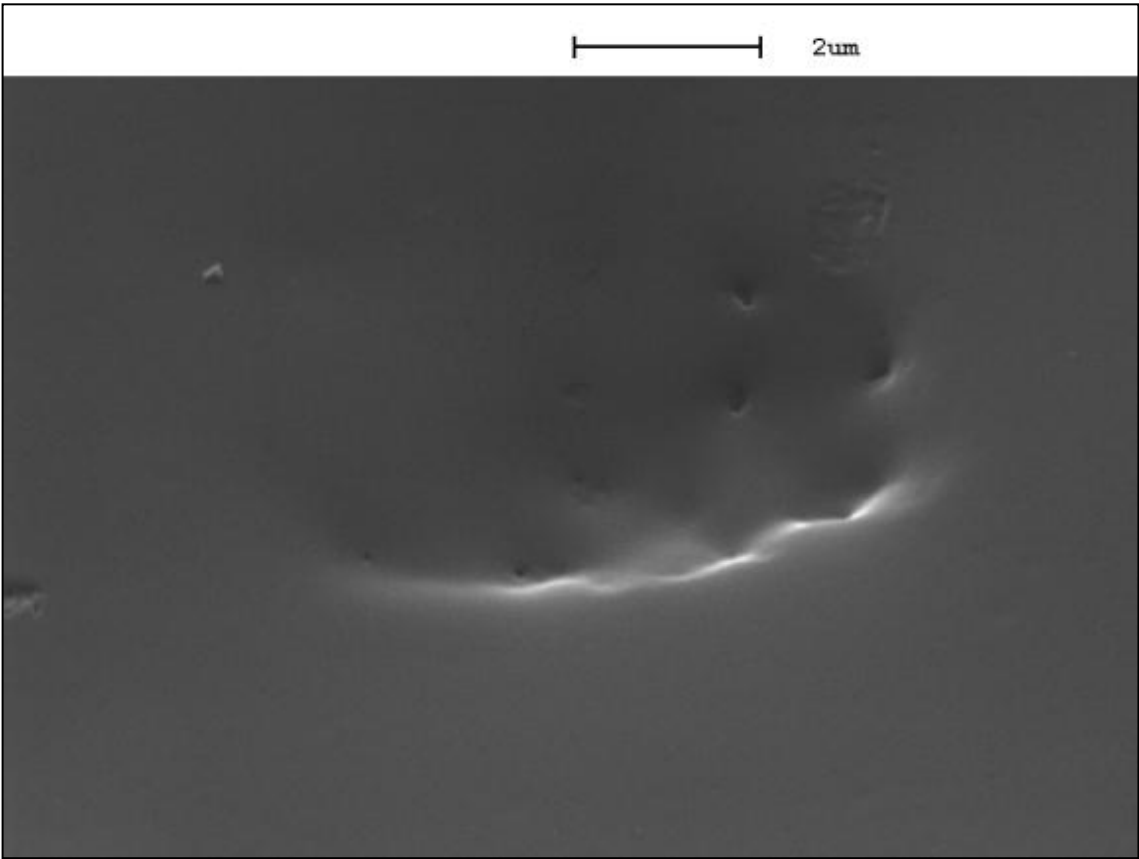


**Figure 7.4.z: SE micrograph of the surface morphology of third iteration samples (10000x Magnification)**

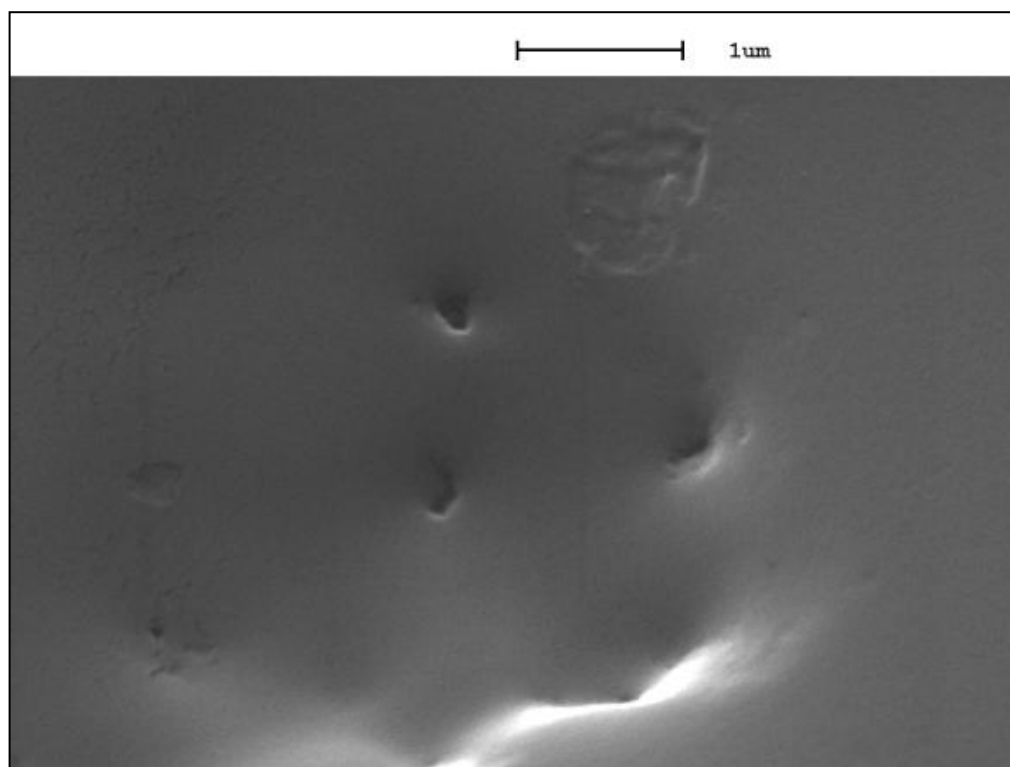


**Figure 7.4.aa: SE micrograph of the surface morphology of third iteration samples (20000x Magnification) from Figure 7.4.z**

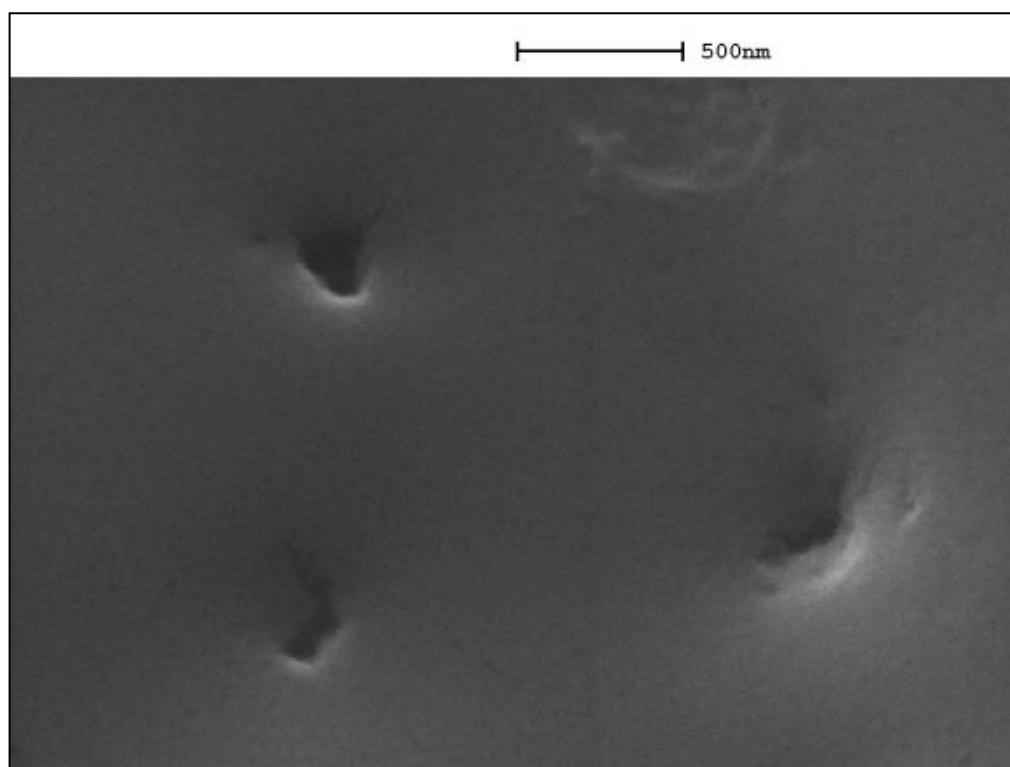


**Figure 7.4.bb: SE micrograph of the surface morphology of third iteration samples (40000x Magnification) from Figure 7.4.z**

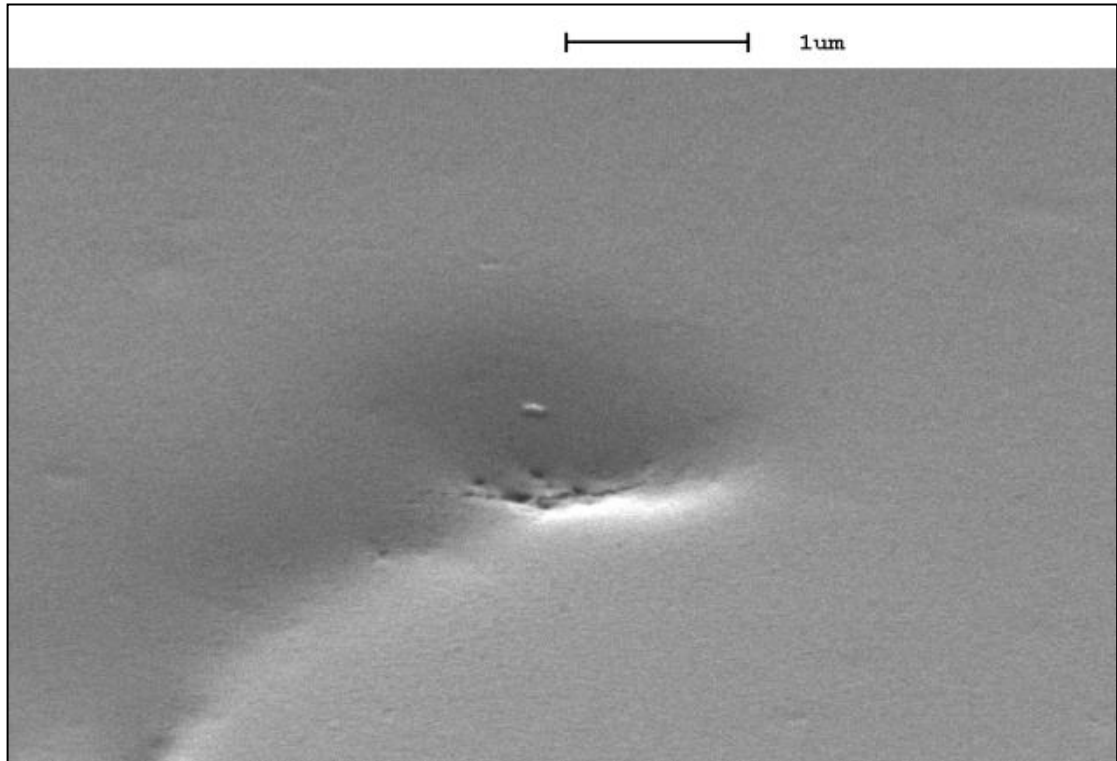


**Figure 7.4.cc: SE micrograph of the surface morphology of third iteration samples (20000x Magnification)**

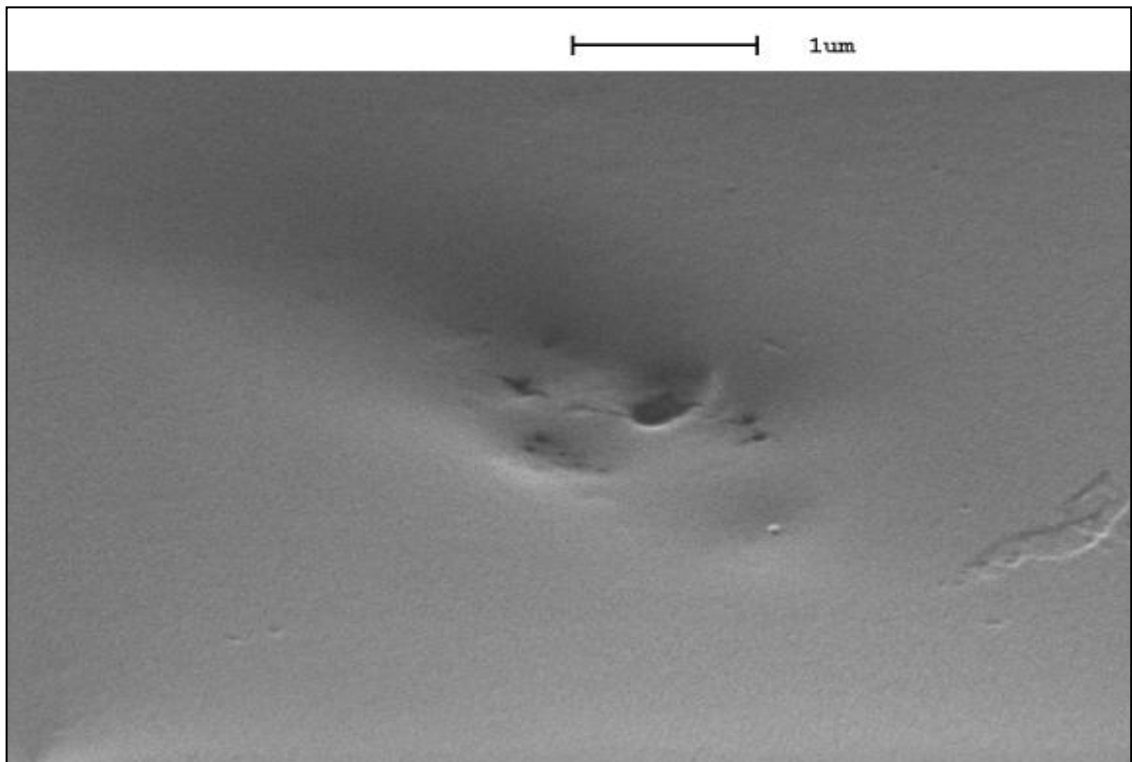


**Figure 7.4.dd: SE micrograph of the surface morphology of third iteration samples (20000x Magnification) from Figure 7.4.cc**

Consequently these were the first evidence of a porous configuration in the morphological analysis. This suggests that the previous hypothesis was to some extent accurate regarding the eventual collapse of the pore from either the etching process or during gold evaporation. However the density of these porous structures did not match their OM counter parts which exhibited a high density of the embedded arrays. Additionally, it was unclear if the length of these pores did equate to the entirety of the film thickness. Another predicament was the query regarding the effectiveness of the employed etching time which did not provide a clear indication whether the etchant would have affected most of the embedded  $\text{Fe}_3\text{O}_4$  constituents.

Based on the evidence obtained at this point, there were a few important issues that had to be addressed which were to achieve an effective removal of the embedded  $\text{Fe}_3\text{O}_4$  constituents; the etchant should be left over night.

To build a convincing argument regarding the embedded array height, attention was turned to an ion milling technique of a fully etched sample. The rationale behind this was to remove small incremental layers of the film which would expose the embedded pores within the film for analysis.

#### 7.4.4. Cross-sectional View of Membrane through Ion Milling Technique

This iterative series focused on the preparation samples which were sent for ion milling to obtain a cross-sectional view of the membrane. The procedure was conducted using the precision ion polishing system from Gatan Precision Ion Polishing System (PIPS™). The milling procedure was carried out at 2 KeV at 25  $\mu\text{A}$  and using a rotational speed of 6 revolutions per minute at a milling angle of  $10^\circ$ . The rationale behind the low output and high rotational speed due to the behaviour of polymers subjected to high temperatures as several past works have encountered a similar situation (Park, Ko, Yi, Petrov, & Kim, 2007) when dealing with ion milling and polymeric materials (Raczowska, et al., 2005). For the task at hand, the appropriate milling time was found through a trial and error basis to about one and half hours at the designated parameters. A termination point for the

milling process was determined by observing interference fringes occurring on the film surface. Similar to the concept of a soap bubble exhibiting interference fringes when its wall thickness is comparable to the wavelength of light. Once the samples are milled appropriately, they were sent for gold coating for SEM analysis. An illustration of the milling setup and the results of these samples are presented below.

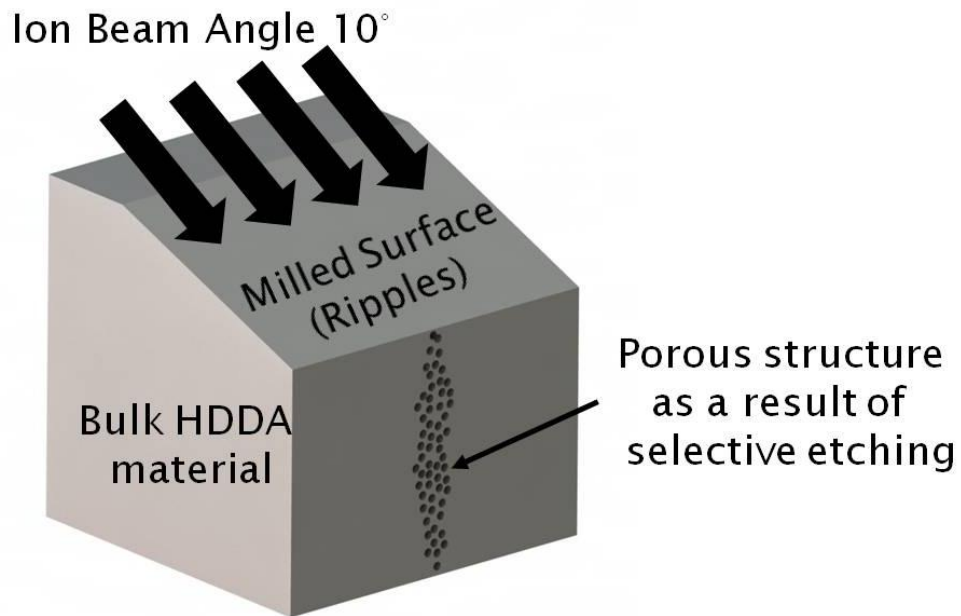


**Figure 7.4.ee: illustration of a section of a membrane under the milling condition previously described**

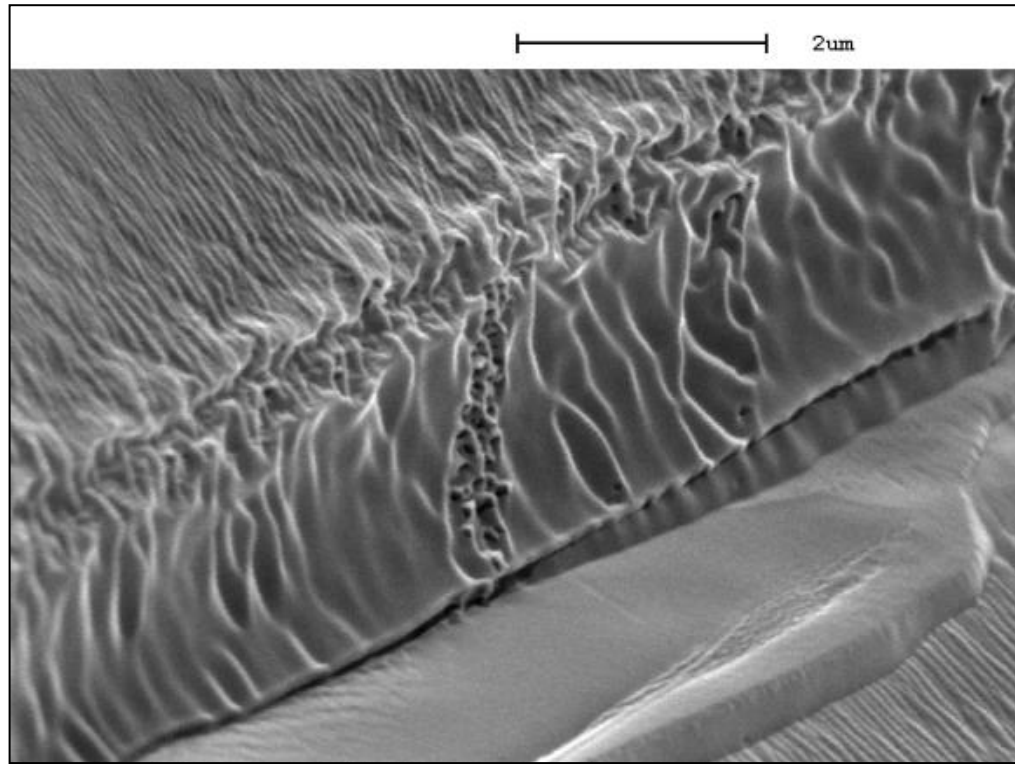


**Figure 7.4.ff: SE micrograph of a cross section of the sample (30000x Magnification)**

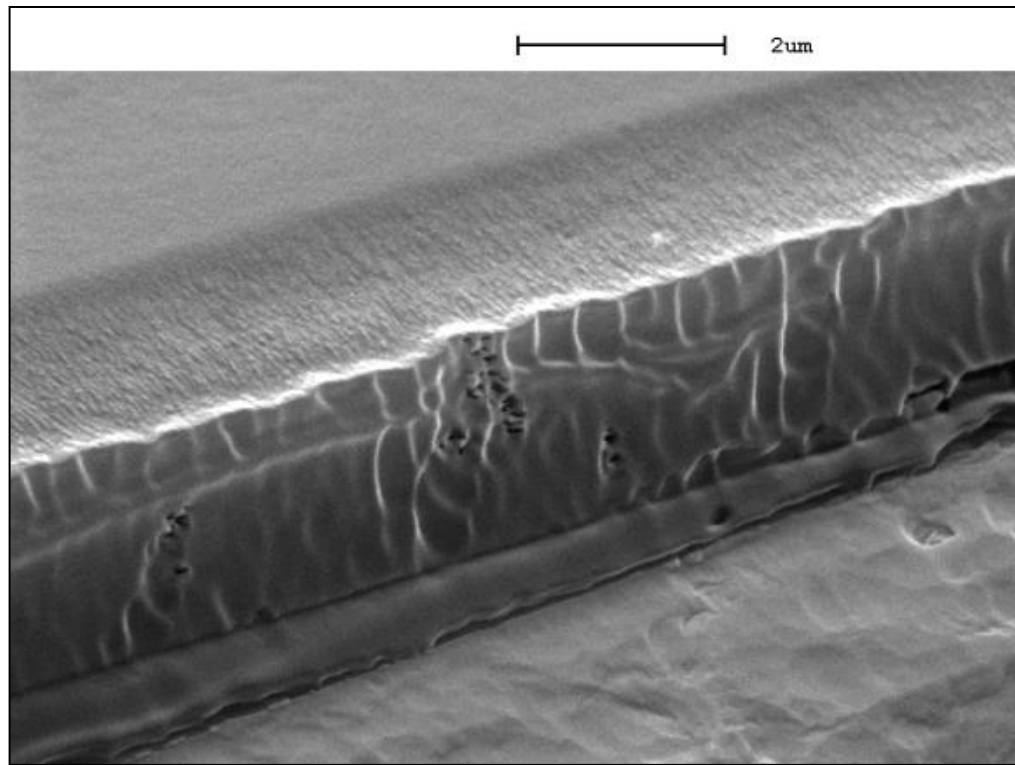


**Figure 7.4.gg: SE micrograph of a cross section of the sample at a different location (30000x Magnification)**

Figure 7.4.ff and Figure 7.4.gg demonstrate SE micrographs a cross-section of the ion milled sample. The small ripples on the top demonstrate the damaged effects of the ion milling.

The dark holes aligned in the form of a column illustrated in Figure 7.4.ff are the recesses where the magnetic nanoparticles used to be before the etching process took place. The shape and structure of the column resembles a network of interconnected cavities spanning across the entirety of the column which implies that  $\text{Fe}_3\text{O}_4$  arrays spanning through the entirety of the film thickness are not in a form a solid structure. Figure 7.4.gg demonstrates the network of cavities forming across the top surface of the film however does not span across the cross sectional thickness of the film. This would indicate that not all observable arrays were fully propagated columnar structures which span the respective film thickness.

Referring back to the expected columnar structure configuration discussed in Chapter 3 Section 3.4, the dark holes from Figure 7.4.ff resembles the semi-dense column configuration from the previous speculation. Additionally, the polymer template also demonstrates signs of tapering towards the top and the bottom which confirms the initial inference made in that particular chapter. Furthermore, this tapering effect was made more obvious in the subsequent TEM image analysis where another sectional view is provided.

The SEM images obtained revealed the cross-section of the membrane platforms which provides some validation to the initial hypothesis of etching embedded  $\text{Fe}_3\text{O}_4$  arrays in a polymer film would impart a pore which spans the entirety of the cross sectional thickness of the film. However it still does not provide sufficient evidence whereby these arrays are interconnected from both sides and would allow ionic transport. Therefore moving forward from this point was to determine the presence of the pore openings on both surfaces of the membrane which was to be determined from the ionic conductivity characterisation which will be covered in Chapter 8.

## 7.5. Chapter Summary

The chapter has highlighted the all the relevant OM works in efforts to characterise the specimens. Establishing an imaging regime to systematically optically characterise each specimen has made three post processing analysis possible which were the array density covered in Section 7.2.1, inter-array spacing covered in Section 7.2.2 and the effects the of both pre-etching and post-etching stages Section 7.2.3.

Next, SE and BE image analysis was conducted to obtain some initial validation of the correlation between the observable arrays or dark spots from the optical images and the assembled columnar structures. As a result it was established that the observable arrays did comprise of a heavier element in which was further confirmed using chemical element analysis where traces of iron element was present. Subsequently, the general shape of the singular columnar structure was identified through a combination of TEM and SEM analysis. The resultant shapes was found to be consistent with initial speculative shapes discussed in Chapter 3.

The surface morphology regarding the nanopores was too explored. Although the SEM analysis did not demonstrate a substantial amount of pores across the surface, however our efforts to obtain secondary information has brought in supporting evidence to maintain the claim of their existence.

This prompted employing alternative methods of analysis which was the cross-sectional view of the membrane where it provided clear indication of a template effect within the polymeric matrix. The effective shape and the internal morphology of the array assembly matches the initial inference made in Chapter 3Chapter 3: Section 3.3 of a semi dense porous structure. The investigation also exhibits the proof that the self-assembled nanoparticles indeed have propagated through the entirety of the membrane thickness. This was covered in Section 7.4.4.

Nevertheless alternative method of characterisation was needed to provide additional supporting evidence for this technology. Therefore, ionic conductivity characterisation was explored by which has a dedicated chapter due to the length of its content.

## Chapter 8: Ionic Conductance Characterisation of Membranes

---

The morphological investigations from Chapter 7 have provided initial confirmation of the presence of the nanopores. However to provide further verification of the full propagation of the arrays, we have employed electrochemical techniques. The rationale behind this was; should the membranes feature pores which are continuous throughout the entirety of the film thickness. Then they must facilitate ionic transport. Additionally, measurements ascertained from these experiments also assist the membrane characterisation.

Commonly employed by scientist in the field (Chen, Derlyo, & Baker, 2009)(Lee, Joly, Siria, Biane, & Bocquet, 2012)(Honda, Rao, Fujishima, Watanabe, Yasul, & Masuda, 2000)(Siwy, et al., 2003), ionic conductivity characterisation has become a common standard to determine important pore morphological characteristics as well as demonstrating the performance of porous membrane prototypes.

The chapter begins by highlighting a brief review regarding ionic conductivity methods and concepts from previous works to adopt. These experiments typically require the use of two silver/silver chloride (Ag/AgCl) electrodes submerged in electrolyte contained in separate reservoirs. For this application, a saturated solution of potassium chloride was chosen as the electrolyte of choice. These reservoirs were electronically isolated by the membrane of interest then a voltage potential was applied across the electrodes. Subsequently, the current-voltage (I-V) response of the system was monitored using a digital multi-meter connected to a computer with the appropriate interface for recording. The I-V response can be interpreted and analysed to provide characteristic information regarding the examined membrane such as the conductance of the system which indicates the presence of the nano-channels. Additionally, the measurement obtained here can then be compared with available theoretical models to ascertain the effective size of pores. This chapter illustrates the progression of the experimentation along with the background knowledge required to accomplish these tasks.

## 8.1. Ionic Conductance Characterisation

This section describes the ionic conductance characterisation of the free standing porous membrane platforms subsequent to their fabrication. The characterisation method serves as supporting evidence to reinforce the results obtained from the SEM image analysis with a quantitative approach. The experiment aims to obtain conductance measurements from the fabricated membranes adopting ionic conductivity methods and concepts discussed in later sections in this chapter. Furthermore, a series of control specimens were also introduced to provide reference conductivity measurements values which enabled us to compute approximations of pore size and density pertaining to the membrane platforms.

To provide a comparative analysis, commercially available track-etched polycarbonate membranes by Whatman plc were chosen as the control sample. The rationale behind the choice was the availability, costs, known physical attributes and access to the wide range of analysis conducted from previous works (Chen,

Derlyo, & Baker, 2009), (Crawford, Steele, Ondris-Crawford, & Iannacchione, 1992) & (John, Hering, Reischl, Sasaki, & Goren, 1983).

The following sections do also highlight several key factors that were addressed prior to experimentation. This encompasses the design considerations of the experimental setup, preparation of Ag/AgCl electrodes, the placement technique of the membrane platform onto the diaphragm and the bespoke LabVIEW programming suite.

### 8.1.1. Ionic Conductivity Methods and Concepts from Previous Works

*The Axon Guide for Electrophysiology and Biophysics Laboratory Techniques* from Axon Instruments Inc. (Axon Instruments, Inc., 1993) had addressed a few considerations for any ionic conductivity experimentations. One such factor is that the resulting current from the applied potential must carry at least two types of ions across which are one anion and one cation species to allow a chemical exchange or reaction to take place and thus completing its respective electrical circuit.

The current flow through in the bulk solution was to be considered proportional to the potential difference and if the ions are subjected to traverse through a membrane, only the two ionic species are considered to be carried across the solution.

When using the Ag/AgCl electrodes, the carrier salt solution of choice should contain chloride ions for the best results. Furthermore, the system must be completed as a closed circuit therefore two electrodes are required for the experiment. To provide a clearer picture, Figure 8.1.a & Figure 8.1.b is a representative experimental schematic for such trials from past works.

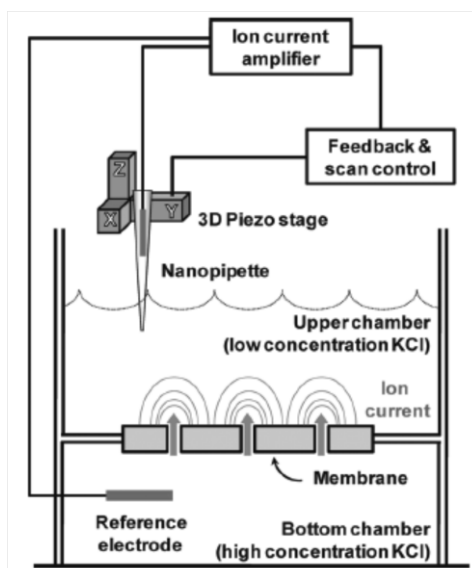


**Figure 8.1.a: Schematic diagram of a scanning ion conductance microscopy system pioneered by (Chen, Derlyo, & Baker, 2009)**

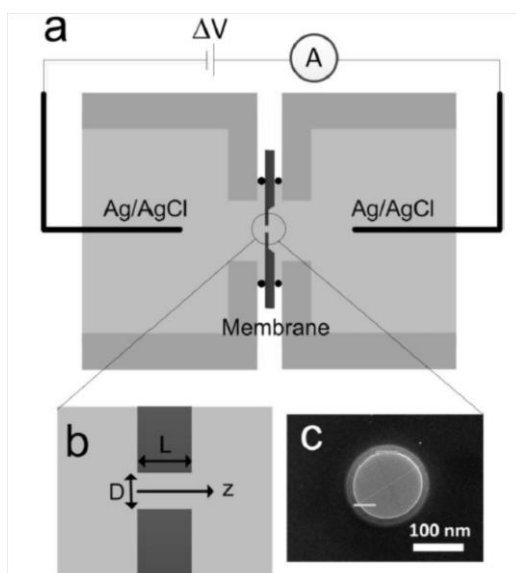


**Figure 8.1.b: (A) Schematic of a flow cell (B) Cross-section of a nano channel (C) Transmission electron microscopy image of nano channel. Image taken from (Lee, Joly, Siria, Biane, & Bocquet, 2012)**

Based on the figures illustrated Figure 8.1.a and Figure 8.1.b, there are several reoccurring design elements to identify. The first was these porous membranes were free standing and could be easily handled. Hence a reliable method to extract and handle the films was to be established.

The second element was porous membrane had to have a good seal from both sides to isolate the two bodies of electrolyte solution. This is because any leaks that occur will create an unwanted conductive pass across which will provide false measurements.

The third element to address was the electrical setup which was incorporated into the design. A pair of Ag/AgCl electrodes was required for experimentation work. Additionally, it is only the AgCl layer was exposed to the electrolyte solution.

The fourth element was devices required for ion excitation and current measurement. For this, a source meter was required that could simultaneously excite the ions to traverse through the pore whilst measuring the current responses that occur. Furthermore, these devices were computer controlled and could process readings simultaneously. Therefore the experimental setup for the work at hand had to incorporate these four design elements to obtain reliable results.

## 8.1.2. Experimental Setup, Design and Schematics

Several design considerations were made prior to experimentation. First to address was the extraction and preparation of our membranes. For this a reliable technique was established which incorporated the use of acetate diaphragms with a concentric perforation. Details regarding this technique are presented in Section 8.1.2.1.

Secondly adopting the experimental setup concept utilized by past works (Lee, Joly, Siria, Biane, & Bocquet, 2012), an electrolytic flow cell with two separate reservoirs complete with their respective embedded Ag/AgCl electrodes were needed in the finalised design. The emphasis was placed on the seal between two reservoirs. These reservoirs were filled with saturated KCl solution that exudes better electrical conductivity relative to deionised water. The membrane to be analysed must be the only junction that allows the ionic species to traverse through the system thus completing the circuit. Therefore, the seal that holds the membrane that separates both reservoirs must not only be water tight but must also inhibit ionic transport.

Thirdly was the fabrication of the Ag/AgCl electrodes utilising the electro-plating technique and subsequent tests to examine its reliability, voltage stability and performance.

The fourth element to address was the usage of the KEITHLEY 2400 SourceMeter incorporating a GPIB interface to the computer by Keithley Instruments Inc. A customised voltage sweep function program was written to suit the experimental test conditions.

With all four elements put forward in the previous section addressed, only then can actual experimentation take place. The following sections details the experimental setup, devices and schematics exemplify the work conducted for the research.

#### 8.1.2.1. Membrane Platform Diaphragm Preparation

One of the more challenging tasks of the experimental section was to transfer the membrane from their borosilicate glass substrates to the diaphragms. This is due to the strong adhesion forces of the polymerised membranes to their respective substrates. First identified by (Rybchenko, Dyab, Haywood, Itskevich, & Paunov, 2009) the adhesion forces of the membrane platform were exceptionally strong and due to the polymer shrinkage subsequent to polymerisation. To overcome this, a few droplets of isopropanol were deposited onto the membranes (droplet size enough to envelop the membrane platform) and left to soak in order to dislodge the film from the substrate. Then an eyelash tool was used to carefully retrieve the film from its substrate.

The next was to position the membrane roughly concentric with the perforated acetate diaphragm and secured with the epoxy. This vital procedure must take precedence because should the placement of the membrane have a slight offset, the possibility of a leak would be present. This in turn will provide the ionic conductivity tests with false measurements through the leakage of ionic current not flowing into the channels of the membranes. Furthermore, an unsupported free-standing membrane has the tendency to curl up when retrieving them from their substrates. This also presents another challenge when transferring the films onto the diaphragm.

Through several trials, a serviceable technique to solve both problems was to float the film on a water surface in order to unravel the film. This technique was possible due to the surface tension of water stretching them laterally from all directions while not exerting too much force to cause any tearing. Next, to position the film close to the concentric vicinity of the aperture, the water level lowered while the eyelash guides the film to the wanted position. To accomplish this, a device that could satisfy all these conditions was fashioned. The design includes a cylindrical reservoir with a draining outlet situated at the bottom which it attached to a syringe via silicone tubing. The syringe enabled the user to control the water level of in the reservoir. To provide a clearer description of this device, a schematic is provided below as a cross-sectional view of the setup.

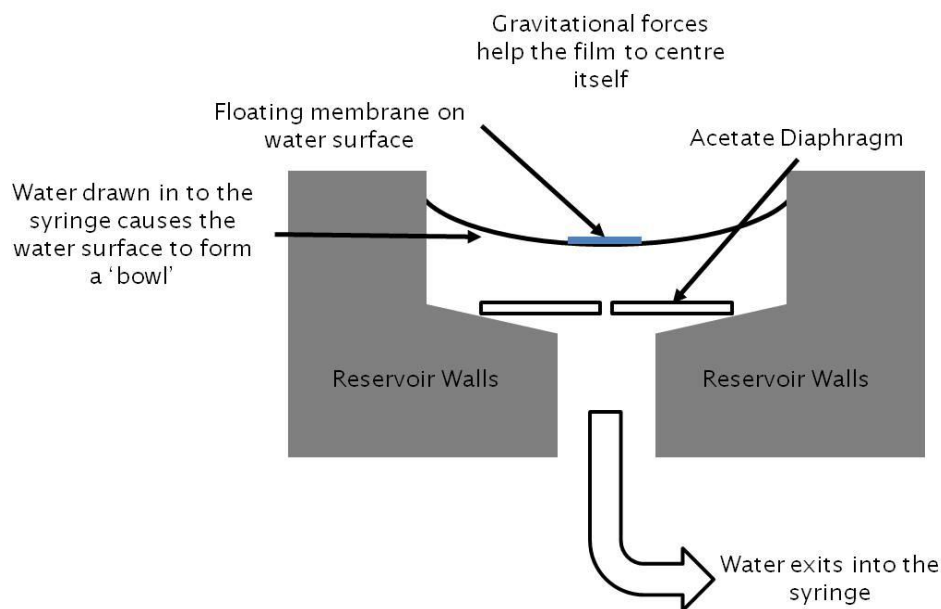


**Figure 8.1.c: A cross-sectional view of the film positioning device**

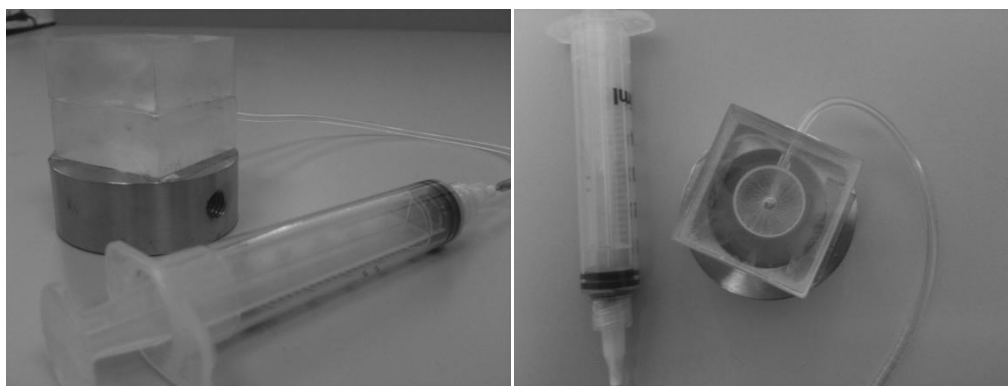


**Figure 8.1.d: (Left to Right) Image of the reservoir device from a side and top view**

A cylindrical bore was made into an acrylic block to form the main reservoir body it then tapers down to hold the diaphragm in place then followed by the outlet that ultimately goes into the syringe to control the water level. Due to the cylindrical shape of the reservoir, decreasing the water content causes the water level to form a concave shaped 'bowl'. Gravitational forces will then position the film in a concentric vicinity of the 'bowl'.

Prior to the placement of the membrane platform, the acetate diaphragm aperture was primed with a drop of Coat-Quick G adherent from Daido Sangyo Co., Ltd. This procedure was introduced to provide a semi-permanent bond between the membrane later and the acetate as they come into contact with each other. This was followed by an application of the adhesive epoxy which provided a more robust seal. This section concludes the mechanical design consideration portion for the ionic conductivity experiment.

#### 8.1.2.2. Flow Cell Design

The flow cell was constructed using two halves of acrylic vials attached to two acrylic bases which featured four screw 3mm holes with a concentric hole drilled in the middle of the base. These materials were chosen for their good electrical isolation properties which was a crucial factor for the design. All joints were joined together using epoxy. The vial caps were also used to house the Ag/AgCl electrodes. A 4 mm concentric hole was drilled in the caps to position the micro pipette tips that held the electrodes in place. Figure 8.1.e provided below demonstrates the

finalised design of the flow cell complete with a three dimensional image of the apparatuses.

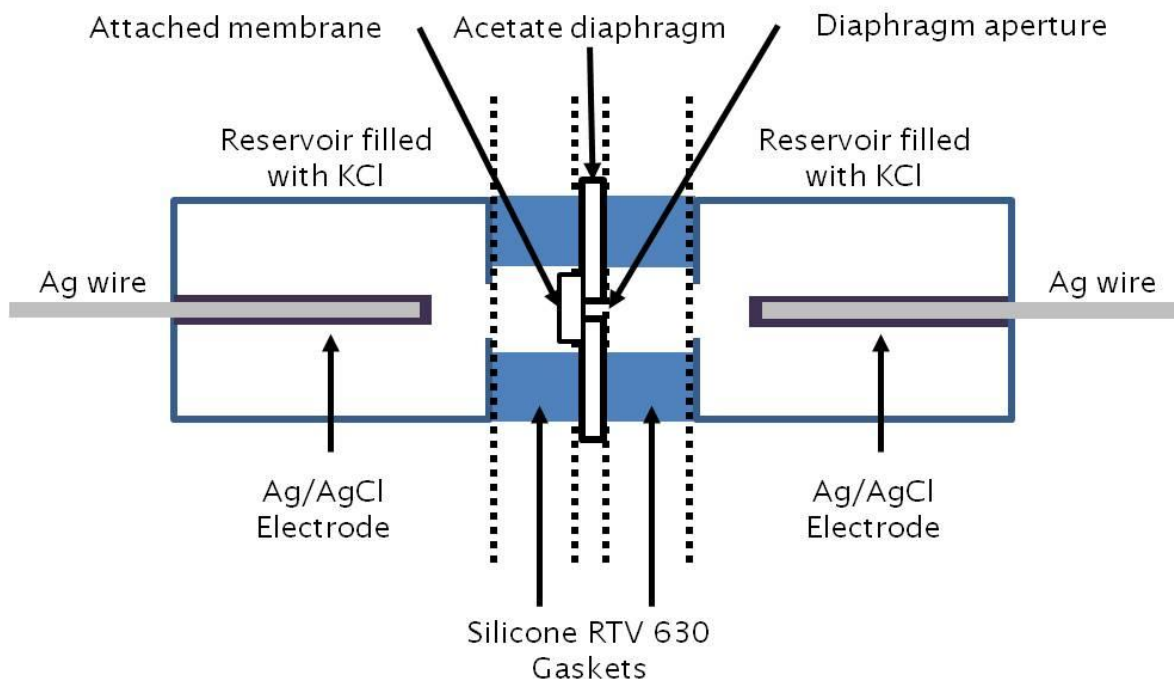


**Figure 8.1.e: Sealing solution used for conductivity experimentation**

Illustrated above, the room temperature vulcanising (RTV) silicone 630 gasket from Techsil was fashioned manually from a cured thin strip. The membrane is held and secured to the acetate diaphragm using LOCTITE 0151 Hysol® epoxy-patch adhesive from LOCTITE® the acetate diaphragm has a 1 mm concentric aperture to allow the KCl solution to wet both sides of the membrane. The entire sealing arrangement was held together by pressure applied by tightening the flow cell base using 4 M3 screws and nuts.

The exposed regions of the electrode within the electrolyte must be coated with a silver chloride layer. Any exposed bare silver that comes in contact to the solution will leak silver ions which can cause polarization. Polarization of the electrode facilitates the propensity an electrode of carrying a higher charge (slightly more electro-positive or electro negative) than the other. This causes initial readings to be skewed as the electrodes will retain a residual charge. To solve this predicament, initial tests should be carried out to verify the quality of the silver

chloride coating after the chlorination procedure which will be explained later in Section 8.1.2.5.

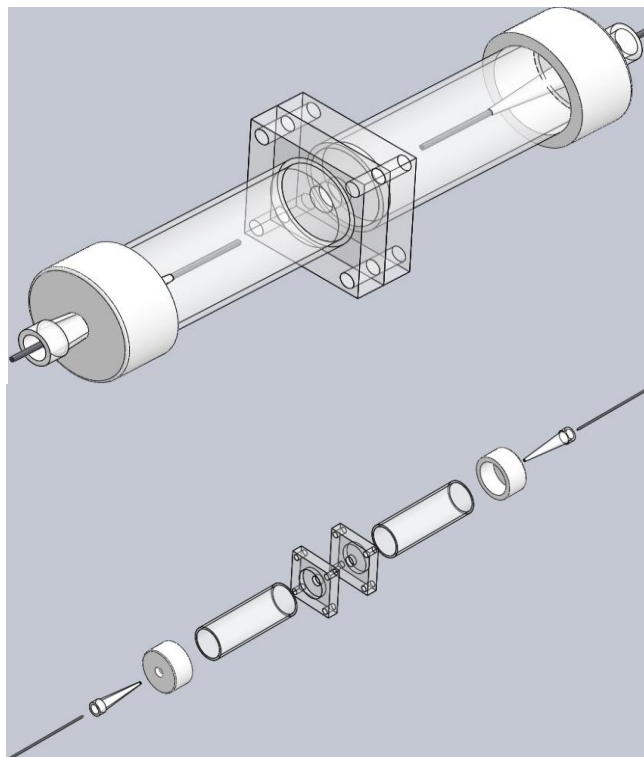


**Figure 8.1.f: (Top) Solidworks model of conductivity cell  
(Bottom) Exploded view of conductivity cell**

The silver wires were initially held in place by mechanical retention. However to secure it in place and seal the tip, some LOCTITE 0151 Hysol® epoxy-patch adhesive was used to coat the micro pipette tip immobilising the electrode. This concludes the flow cell design description.

### 8.1.2.3. The Silver/Silver Chloride (Ag/AgCl) Electrode

Owing its name to the silver/silver halide electrode category, the Ag/AgCl electrode can be classified as a reversible electrode of the *second kind*<sup>12</sup> (Ives & Janz, 1961). These electrode systems operate by conducting measuring the halide ion activity (in this case chloride ions) within a saturated aqueous chloride salt electrolyte. Queries regarding the standardisation and consistency regarding these electrode

---

<sup>12</sup> Electrodes of the second kind infers to an electrode system which operates in an equilibrium potential state via a soluble salt coated metal assembly immersed in a saturated solution of that particular salt in an electrode reaction. There are three types of electrodes available for electro-analytical chemistry. However for this work only second kind electrodes will be highlighted.

systems were extensively covered by Ives and Janz (Ives & Janz, 1961). Therefore the author will not delve into explicit details regarding these matters.

The electrode is made from a silver wire which then coated with a thin layer of silver chloride. This process is termed chlorinating. Commonly chosen for its stability and consistent measurement readings and robustness in various experimental conditions (Quilter & Surwillo, 1966) (Zhou, et al., 2010), the Ag/AgCl electrode is an ideal choice for the ionic conductivity tests at hand. Figure 8.1.g is provided below to complimenting the description.

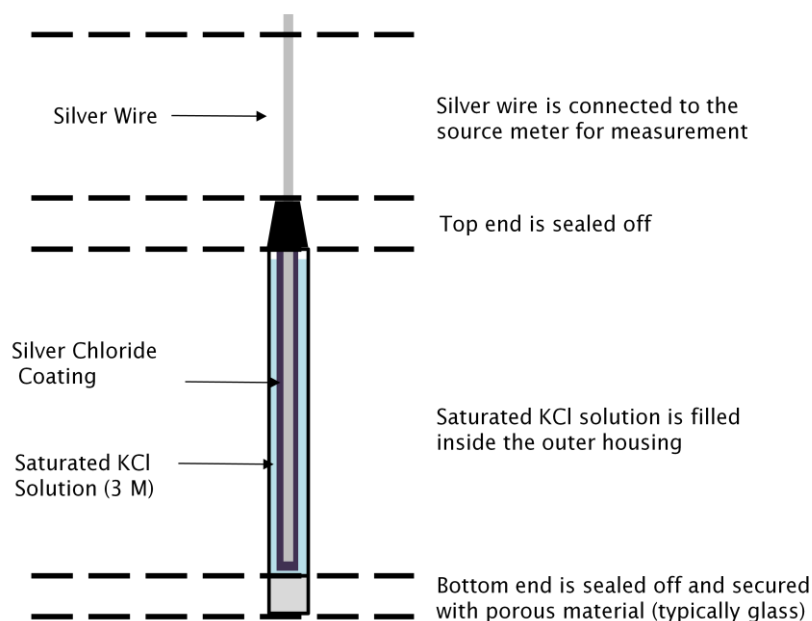


**Figure 8.1.g: Illustration of a standard construction of a Ag/AgCl electrode**

Illustrated Figure 8.1.g is a general shape and configuration of a typical construction of the Ag/AgCl electrode. The electrode construction comprises of a strand of chlorinated silver wire which is inserted into a containment reservoir (typically cylindrical in shape) containing a saturated salt solution or an electrolyte (typically potassium chloride). This reservoir is sealed in one end securing the chlorinated silver wire in place whilst a porous yet chemically inert material is situated in the other allowing diffusion of the analyte to reach the silver chloride layer. Design-wise, the electrode excels as it is cost-effective and features a straightforward method of fabrication.

#### 8.1.2.4. Chlorinating Silver Wire

A good coat of silver chloride onto a silver wire can pass an electrical current down to the micro-scale whilst remaining stable for an extended period of time (Warner Instruments, 2002). This statement will hold true as long as the preparation methods of these electrode systems are conducted accordingly. There are three common preparation techniques for chlorinating silver wires:

- A. Electrolytic type
- B. Thermal-electrolytic type
- C. Thermal type

The electrolytic type electrodes are prepared through a method described as electroplating whereby the silver wire is coated through the act of electrolytic hydrolysis. The anodised silver is immersed in a dilute chloride solution against a platinum wire as the cathode. Thermal electrode requires the decomposition of a predetermined chemical mixture of silver oxide, silver chlorate and water (Bates, 1954). Finally the thermal-electrolytic type electrodes are the combination of both above mentioned techniques of thermal and electrolytic methods. All these methods have their own individual attributes. For the experimentation at hand, the electrolytic preparation method was chosen for its simplicity and availability of materials.

The process requires a silver wire and an additional platinum wire to be immersed in a dilute halide solution of Hydrochloric Acid (0.1 M). An electrical current is then passed through the two wires at a rate of 10 mA/cm<sup>2</sup> (Ives & Janz, 1961) respectively for half an hour using the platinum wire as the cathode. The circuit configuration and schematic should resemble illustrated below.

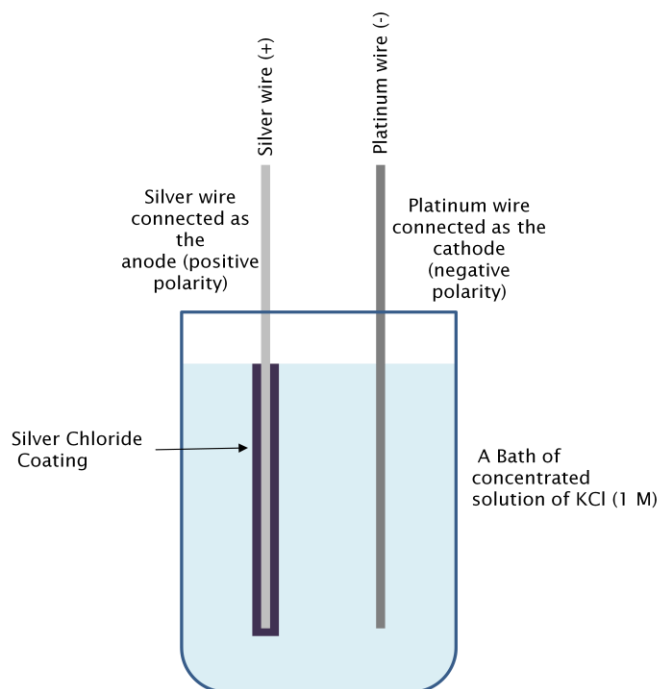


**Figure 8.1.h: Schematic of the chlorination process of silver wire**

The surface of the silver wire should turn in to a light gray then to a dark grey with a purplish hue signifying a successful coating process. This current is held for half hour to ensure a good coat. The newly coated electrode is then rinsed with deionised water and left to soak in a 3 M KCl solution overnight to allow the potential to stabilise.

Alternatively chlorination can also be achieved by immersing the silver wire in commercial grade cleaning bleach for a given period of time. Understandably, the longer the wires are soaked in the solution, the thicker the coating will be on the wire itself. The recommended soaking time defers between various manufacturers and experimenters.

#### 8.1.2.5. Ag/AgCl Electrode Fabrication

Extra care was taken to produce Ag/AgCl electrode for the experiment. Since the experiment requires two Ag/AgCl electrodes, two silver wires were coated simultaneously. The rationale behind this was to coat both wires at the same conditions therefore they should exhibit identical qualities. The silver wire chosen

has a diameter of 1 mm and was also positioned carefully to have a length of 15 mm into the acid bath. They were then cleaned with 600 grit silicon carbide gridding papers from Buehler-Met® to remove any oxide layers on the surface then wiped down with ethanol followed by ample rinsing with deionised water.

Computing the exposed surface area would equate to or approximately 0.94 cm<sup>2</sup> for both wires hence the silver wires would require 9.4 mA current source. Finally, the silver wires were coated using a 0.1 M HCl bath. Following the coating process, the electrodes were tested for their reliability by measuring the potential difference across them. This was accomplished by immersing the two electrodes in a 3 M solution of KCl for 5 minutes while voltage measurements taken place to allow the potential to stabilised. The test demonstrated an averaged potential bias of 187  $\mu$ V with a deviation of  $\pm 1 \mu$ V.

Although the 187  $\mu$ V bias might contribute to some discrepancies with the final result; nevertheless the measured voltage deviations suggest it is within a stable and acceptable range according to of Ives and co-worker (Ives & Janz, 1961). Additional tests were also conducted where the Ag/AgCl electrode were compared with a Standard Calomel electrode. A saturated KCl solution was used for this comparative test with the Calomel electrode as the cathode. The measure potential bias for this test was found to be -46.5 mV bias with a deviation of  $\pm 0.3$  mV which was in agreement with previous works (Sawyer, Sobkowiak, & J. L. Roberts, 1995).

#### 8.1.2.6. LabVIEW™ Programming

This section describes programming prepared for the 2400 SourceMeter from KEITHLEY Instruments employed for the characterisation technique discussed in Section 8.1. The program was written to manage the source meter to conduct potential sweeps across a predetermined range. A sweep is described as a periodic application of one parameter (either voltage or current) whilst reading the other. This meant, should one conduct a voltage sweep, the applied potential periodically increased in a circuit while the device measures the current response from that particular system or vice-versa. The in-house drivers and examples only offer the user to do a single sweep with minimal control over the device that is not conducive

to conduct a cyclic sweep. As a result a custom-made control and measurement system was made for the device. The program written offers the user to modify seven parameters involved in a sweeping process. These parameters included:

- A. Source Mode: Choosing the parameter to sweep which in this case was either voltage or current.
- B. Cycle Count: Cycle count allows the user to control the amount of cycles. One cycle encompasses one ascending sweep and one descending sweep.
- C. Compliance Level: The maximum current or voltage applied to the electrode
- D. Minimum Amplitude: The start point of a ascending sweep which is also the end point of a descending sweep.
- E. Maximum Amplitude: The start point of a descending sweep which is also the end point of a ascending sweep.
- F. Number of Points: The number of points to be measured for a single sweep.
- G. Trigger Delay: The delay between measurement points.
- H. File Path: Path of the measurement information to be saved.

Additionally the program offers three bespoke cyclic sweeping modes:

- A. Mode 1: The device performs a simple cyclic scan with the origin point of the sweep, maximum amplitude. Figure 8.1.i demonstrates the sweeping function.

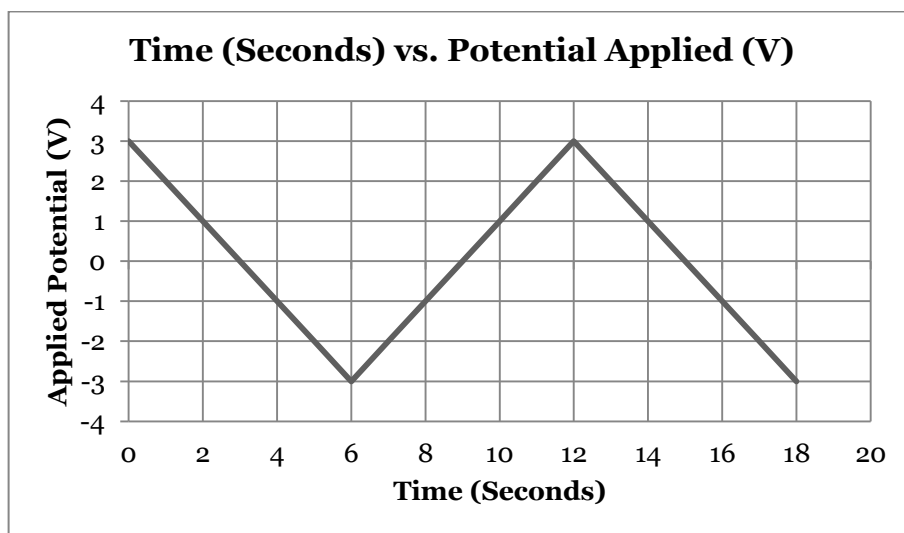


**Figure 8.1.i: Example of described sweep function relevant to Mode 1**

B. Mode 2: The origin is middle point between the minimum amplitude and the maximum amplitude. An ascending sweep is performed then cyclic scan is performed (similar to mode one). Once the cyclic scan is complete, a descending sweep to the origin point is performed. Figure 8.1.j demonstrates the sweeping function.

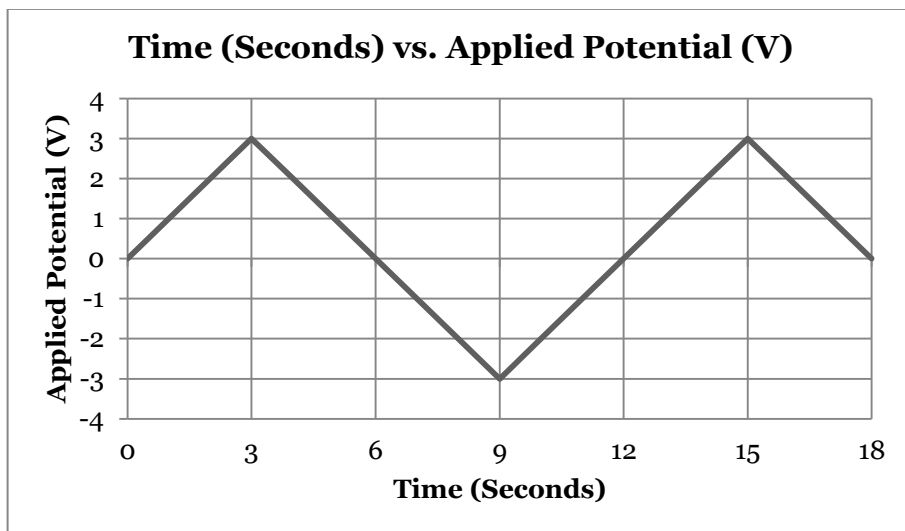


**Figure 8.1.j: Described sweep function relevant to Mode 2**

C. Mode 3: A repetitive linear ascending sweep is performed where the origin point is the minimum amplitude. Figure 8.1.k describes the sweeping function.

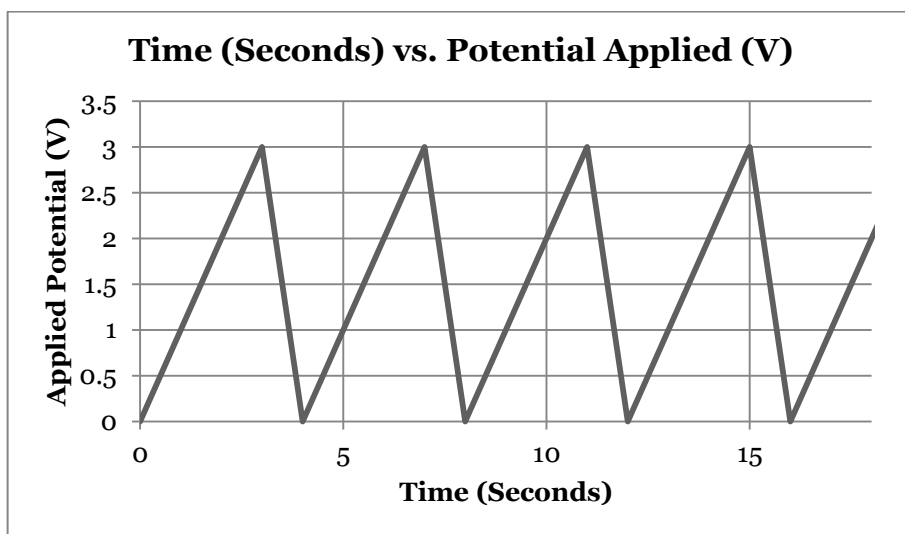


**Figure 8.1.k: Described sweep function relevant to Mode 3**

Cyclic sweep modes 1 and 3 were written to simulate the test conditions of past works relevant to nano-channel ionic conductivity characterisation experiments (Apel, Blonskaya, Levkovich, & Orelovich, 2011),(Siwy, et al., 2003) & (Honda, Rao, Fujishima, Watanabe, Yasul, & Masuda, 2000) and was used for initial testing purposes. Consequently mode 2 was created as an amalgamation of the two test conditions.

The rationale behind mode 2 was to determine the optimal potential range to operate which must be below the redox potential and solely focus on the of ionic transport dynamics through the membrane channels. Starting the sweep from a neutral position (zero point) or the middle point between the minimum and maximum amplitude was an intuitive step to determine the point before the redox reactions take place. Therefore once the maximum potential of the redox reaction was identified, the subsequent tests operated below the redox potential which was found to be  $-0.1 \text{ V} \leq x \leq +0.1 \text{ V}$ . This initial testing was demonstrated below in Sections 8.3 and 8.4. This concludes the complete design aspects relevant to the experimentation procedures and requirements. Following sections will cover the preliminary tests and results obtained and subsequent computations.

## 8.2. Preliminary Calibrations: The Open Circuit Test

Prior to any form of ionic conductivity characterisation, initial tests were conducted to examine the integrity of the seals around the flow cell and membrane diaphragm to ensure any unwanted leakages were present. Additionally, these tests were setup up to investigate the I-V characteristics of an open circuit system. This meant that the specimen secured to the diaphragm must not allow ionic transport effectively isolating the system. These results will stand as baseline measurements and evidence of an open circuit system which can then be compared to the actual porous samples later.

The operating amplitude range for this test was in the  $-0.1 \text{ V}$  to  $+0.1 \text{ V}$  range, the programming voltage sweep function was set to Mode 2 at  $2 \text{ mV/s}$  sample rate.

Furthermore, the specimen secured to the diaphragm was a commercial grade low LDPE and the actual material used to membrane fabrication; HDDA at various ranges of KCl immersion electrolyte concentrations (0.001 M, 0.01 M, 0.1 M and 1 M). Figure 8.2.a is presented below to exemplify the results obtained.

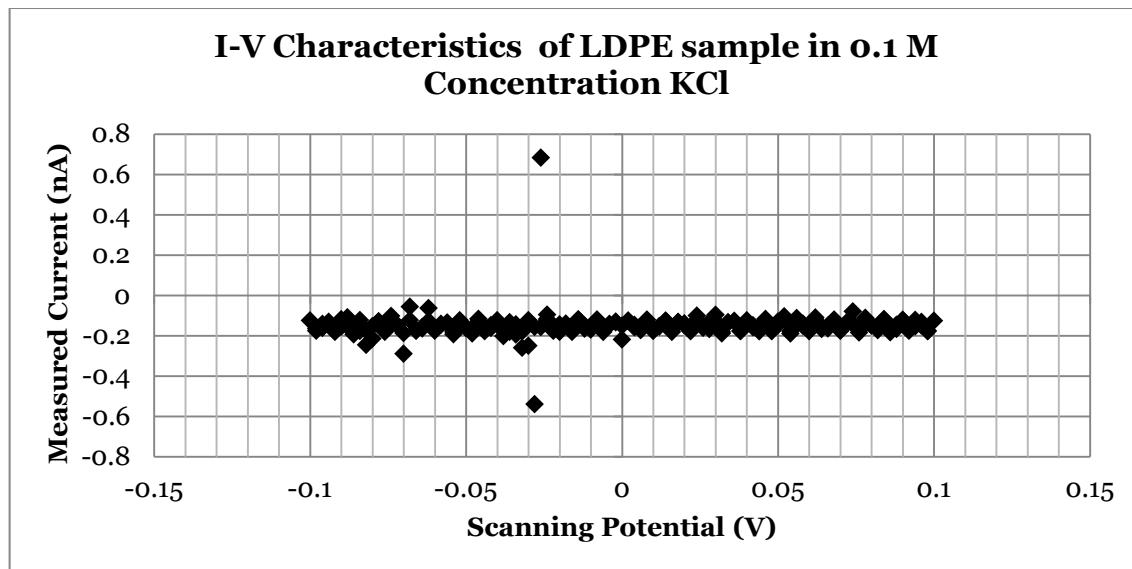


**Figure 8.2.a: I-V characteristic plot of LDPE specimen at 0.1 M KCl concentration**

The plot presented above is an I-V characteristic investigation of an LDPE film as a test sample; it is clear that the measurements were rather sporadic and does not resemble a smooth continuous curve. Furthermore, tests results from the different KCl immersion electrolyte concentrations did not exhibit any changes to the system.

Conversely, the photo-polymerised HDDA test membrane exhibited current responses demonstrated in Figure 8.2.b which was consistent to the existing premonition.

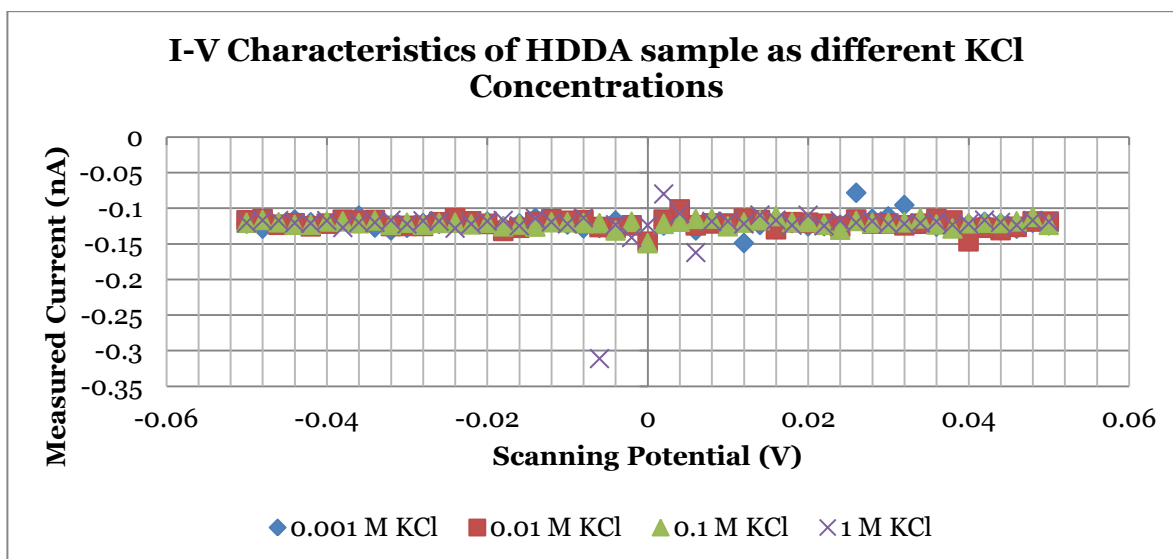


Figure 8.2.b: I-V plot of a blank HDDA sample at various KCl concentrations

As an additional note, the silicone RTV 630 gaskets in the aforementioned Flow Cell Design construction were also included for this test to check the sealing performance in Figure 8.2.c.

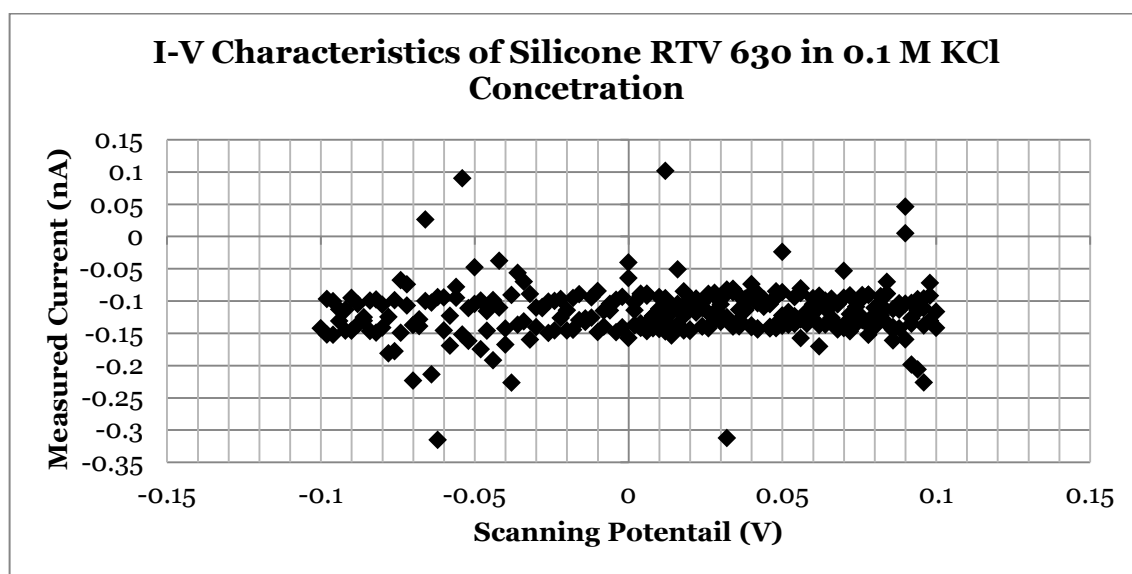


Figure 8.2.c: I-V characteristic plot of Silicone RTV 630 at 0.1 M KCl concentration

Once again the results demonstrate the similar characteristics to the previous test in Figure 8.2.a in the sporadic nature of the response. To conclude this section, the measurements obtained from these tests can be used to identify the expected measurements should the system was properly sealed and future samples that

exhibited similar sporadic measurements were considered not to have a sufficient amount of pores to contribute to any meaningful results. Therefore it can be concluded here that the fabricated electrochemical flow cell along with its silicone RTV gaskets demonstrate good electrical isolation properties thus subsequent measurements will be consistent.

### 8.3. Preliminary Calibrations: Cyclic Sweep Range Identification

Initial testing conducted prior to the actual experimentation was carried out to determine minimum and maximum amplitude range before the redox reaction takes place. The initial operating range selected for initial testing takes place in the  $-0.5$  V to  $+0.5$  V regions which is below the electrolysis threshold.

The electrolysis threshold is where the electrical energy is sufficient to sever the chemical bonds of molecules therefore causing the chemical reaction to be irreversible. This reaction is unwanted as it will exhaust the AgCl layer causing the electrode to shed its AgCl layer and thus skewing the conductance measurements.

The membrane platform chosen for this preliminary test was the 8  $\mu\text{m}$  diameter commercially available track-etched pores from Whatman<sup>TM</sup>. Immersion electrolyte used was a 0.1 M concentration KCl solution. It is important to note that these tests used the programming Mode 2 programming structure. For convenience sake, the experiment parameter characteristics for the commercial grade track-etched pore types are listed below.

Test Number	Parameter(s)					
	Max. Amplitude (V)	Min. Amplitude (V)	Cycle Count	No. of data Points per scan	Trigger Delay (Second)	Step Size (mV/Step)
1	-0.1	0.1	1 Cycle	100	0.1	2 mV/ Step
2	-0.2	0.2		200	0.1	
3	-0.3	0.3		300	0.1	
4	-0.4	0.4		400	0.1	
5	-0.5	0.5		500	0.1	

**Table 8.3.a: Parameters used for initial redox reaction limit identification**

The table depicted above features five tests accomplished to identify the redox potential. The rationale behind this was to subject a minimal wear to the electrode, testing range was increased gradually in 0.1 V steps till the maximum range of 0.5 V was achieved. This method enabled the experimenter to identify an accurate cyclic sweep window to perform the characterisation. To demonstrate the occurrence of redox potential the test number 5 (-0.5 V to +0.5 V) was illustrated in Figure 8.3.a to validate these queries.

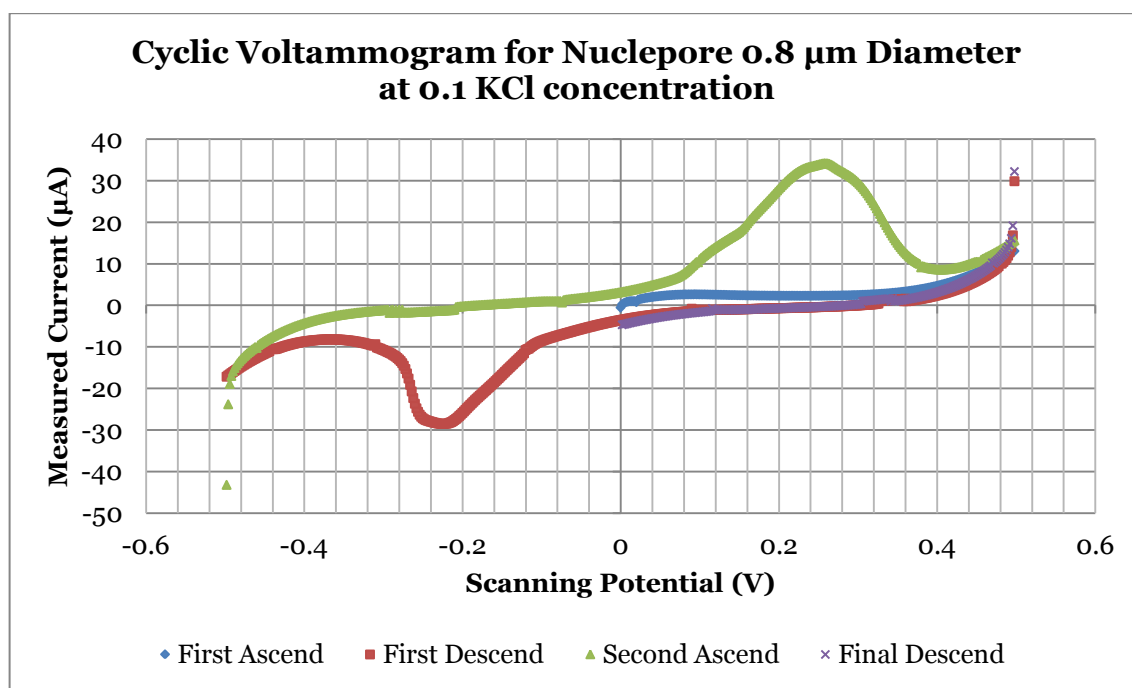


**Figure 8.3.a: Recorded cyclic voltammogram for 8 μm (0.1 Second scan delay)**

The voltammogram exhibited above is the full -0.5 V to 0.5 V scan range. The plot registers the entire cyclic voltammetric scan. This full scale test was important as it enabled one to identify the optimum scanning potential window to operate at. The dual peaks from the first descending and second ascending sweep are indicators that the both the reduction and oxidation reaction has taken place and thus the returning scanning potential will be slightly skewed and will not feature the same slope skewing the conductance measurement. Further details on interpreting a voltammogram can be found in Appendix: Chapter 8.

As a result this test determines the redox reaction would take place at a potential bias of  $\leq -0.2$  V and  $\geq +0.2$  V observable by the peaks in Figure 8.3.a. Consequently the -0.1 V to 0.1 V potential range was chosen as it demonstrated a stable linear pattern. To confirm this query, the voltammogram Figure 8.3.b demonstrates a scan window of -0.1 V to +0.1 to highlight this trend.

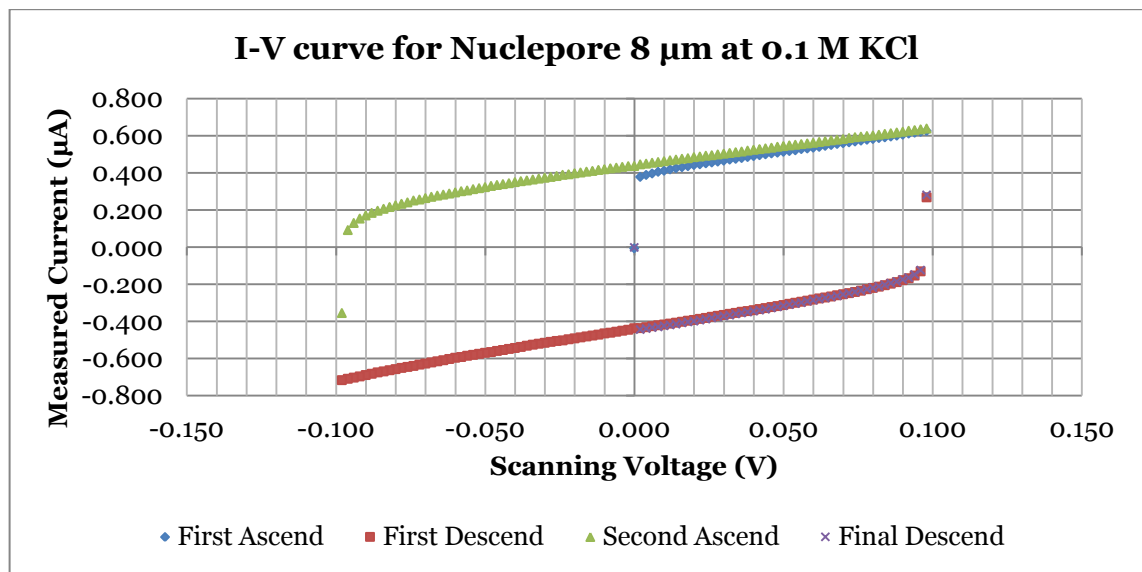


**Figure 8.3.b:** Plot of current response of the Nuclepore 8  $\mu\text{m}$  diameter pores at  $-0.1\text{ V}$  to  $+0.1\text{ V}$  range

The measurements indicate that an optimum operating sweep range between  $-0.1\text{ V}$  to  $+0.1\text{ V}$  provided a stable working range with no risk of redox reaction taking place and as such the measurements drawn from the tests are strictly the ohmic response from membrane contributing to the conductance of the system. However in accordance to the ohmic law, the I-V linear relationship must intersect its point of origin which understandably the results do not demonstrate. However it must be noted that the cause for this was due to the default measurement device offset.

As a result, all subsequent tests in this report were conducted within this range. Finally the result obtained here concludes the query to identify the accurate operational window for the membrane channel characterisation step.

## 8.4. Preliminary Calibrations: Shifting Current Response to Different Scan Delays

The current response was found to shift when subjected to different scan delays reflecting the built-in capacitance of the system. This meant that only the charging current was measured instead of the ohmic current. Therefore this section attempts to demonstrate the shifting gradient as it indicates the measurement of the

capacitive current. The aim of this test was to identify an appropriate scan delay to identify the ohmic current and thus verifying the consistency of measurement.

For this test, the operating ranges was set to the -0.1 V to +0.1 V range from the concluded tests from the previous sections and attempt to run scans at different scan delays. To approach this test systematically, the scans relevant to mode 2 was again divided into 4 sweeping scans i.e. the first ascending, first descending, second ascending and final descending sweeps. However the results presented here are only for the first descending and second ascending sweeps as these sweep scans have a wider range of measurements in comparison to the first ascending and final descending sweeps. This in turn provided better resolution when observing the linear trend of their corresponding plots and therefore all subsequent analysis will be done only on the first descending and second ascending scanning potential. The membrane platform chosen for analysis was the 8  $\mu\text{m}$  diameter track-etched pore. The immersion solution was a 0.1 M concentration of KCl solution. Again for convenience sake, parameters for this investigation are listed below.

<b>Test Number</b>	<b>Scan Delay (Second)</b>
<b>1</b>	No Delay
<b>2</b>	0.001
<b>3</b>	0.01
<b>4</b>	0.1
<b>5</b>	0.5
<b>6</b>	2
<b>7</b>	5
<b>8</b>	10

**Table 8.4.a: Test parameters initial test for change in current response under different scan rate**

It should be noted that Test Number 1 with no delay was accomplished using the device's (Keithley 2400 SourceMeter) internal clock and scanning was perform as quick as the clock will operate. Results from experimentation verified a gradual decrease of the gradient value on increasing the scan delay. Figure 8.4.a and Figure 8.4.b below exhibits the gradual changing gradient as the system was subjected increasing scan delay.

## Scan Gradient Comparison (First Descend)

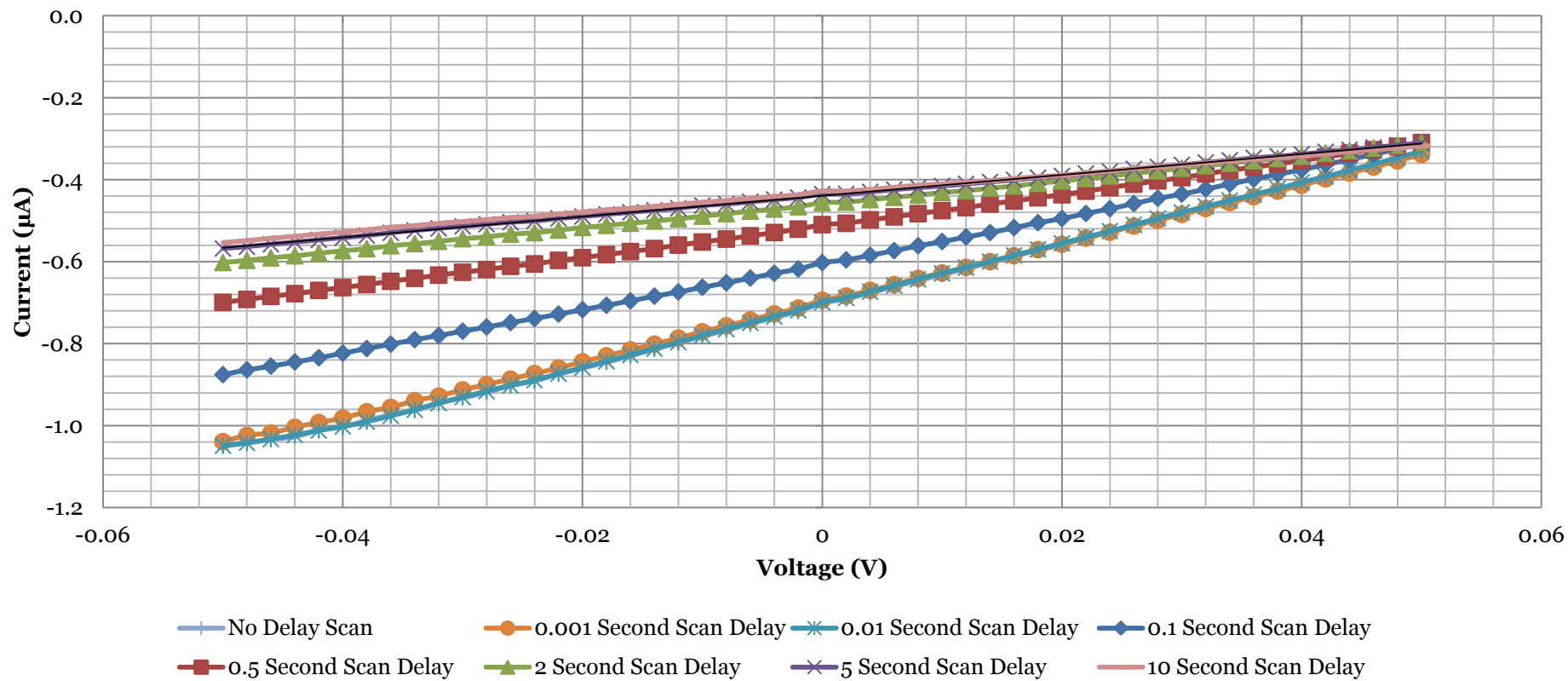


Figure 8.4.a : A plot of descending scan gradients comparison. Parameters of scan listed in Table 8.4.a

## Scan Gradient Comparison (Second Ascend)

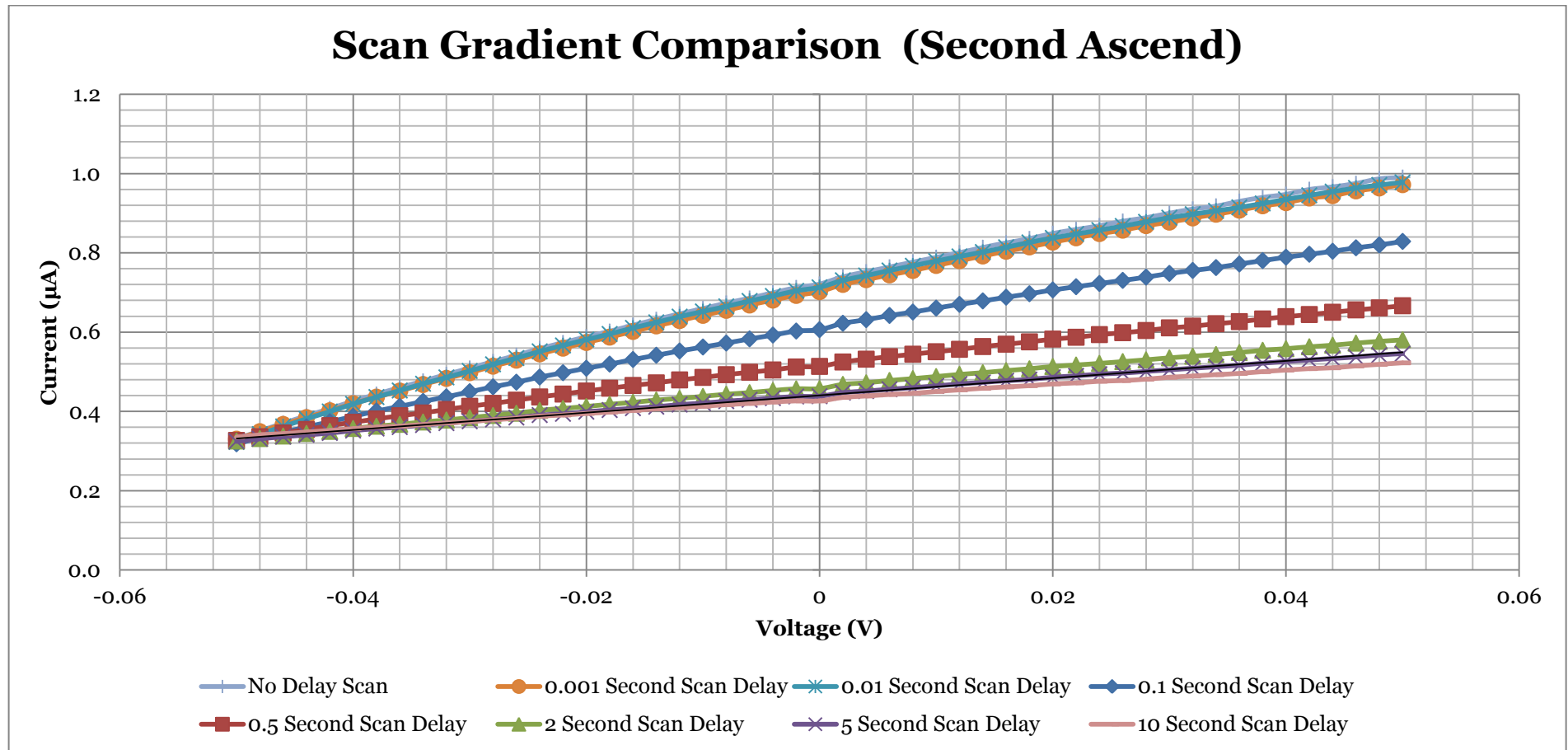


Figure 8.4.b: A plot of ascending scan gradients comparison. Parameters of scan listed in Table 8.4.a

Exhibited above, the gradient for both plots converge in the 2, 5 and 10 second scan delay designated as Test Number 6, 7, and 8 respectively. Diagram in Figure 8.4.a demonstrates the first descending scan from + 0.05 V to -0.05 V. Gradient values from test number 6, 7 and 8 shown little to no change and began to converge in the -0.4  $\mu$ A to -0.6  $\mu$ A region. Inversely the diagram in Figure 8.4.b, the plots were observed to converge in the +0.6  $\mu$ A to +0.4  $\mu$ A region. This suggests that scanning sweep in these time delays should yield more consistent measurements enabling to build a clearer picture towards the characterisation process. To verify this statement, a linear fit used to compute the gradient of these corresponding plots tabulated in Table 8.4.b.

Scan delay (seconds)	Computed gradient value	
	First Descending Sweep	Second Ascending Sweep
No Delay	7.39	6.55
<b>0.001</b>	7.09	6.36
<b>0.01</b>	7.40	6.47
<b>0.1</b>	5.60	5.01
<b>0.5</b>	3.88	3.33
<b>2</b>	2.90	2.53
<b>5</b>	2.54	2.18
<b>10</b>	2.32	1.85

**Table 8.4.b: Tabulated gradient values for both first descending and second ascending sweep at different scan delays.**

The tabulated results above demonstrate that the slope for 2, 5, and 10 second delay exhibit small deviations of  $\pm 0.36$  relative to shorter scan delays tested. The average from the three test regimes was found to be 2.39. From this, it can be concluded that subsequent measurements from the following scan delay between 5 to 10 seconds will yield consistent results.

This concludes the preliminary calibration tests required for actual experimentation. As a summary from the previous sections, an accurate measurement range of -0.1 V to +0.1 V and at the end the 5 second scan delay was chosen which was used in all proceeding experiments as to complete the experiments in a reasonable time span. Consequently this ensures that subsequent measurements detail recording the ohmic current of the system and not the charging current.

## 8.5. Experimentation: Ionic Conductance Characterisation

This characterisation method serves as supporting evidence to demonstrate the arrays formed using the self assembly technique indeed do propagate through the entirety of the thickness of the film. Thus exonerating the doubt of the presence of the nano-channels as a result of HCl etching but also provide a supplementary size and pore density approximations via computations based from past works (Lee, Joly, Siria, Biane, & Bocquet, 2012) & (Apel, Blonskaya, Levkovich, & Orelovich, 2011).

The experimentation was accomplished by observing the I-V response from the setup extensively covered previously and based on these evidence, only then one is able to build accounts to incentivise prove of concept and the applicability of this technology.

As such, preliminary tests to characterise a commercially available porous polymeric specimen was explored. The test provides initial confirmation that the entire measurement system and electrode pair are working accordingly. Only then, the actual fabricated membranes will be subsequently characterised.

### 8.5.1. Benchmark Characterisation: Track-Etched Membranes

Commercially available track-etched membranes were selected for initial ionic characterisation which was used as benchmark measurements. Therefore, any subsequent ionic measurements taken from the fabricated membrane platforms series can be then referenced and analysed for reliability later. For this characterisation process, the 8  $\mu\text{m}$  and 0.1  $\mu\text{m}$  diameter membrane type track-etched membranes were analysed. The rationale behind this choice was that physical data regarding these membranes can be easily obtained from the manufacturer<sup>13</sup>. A summary of the test parameters is as follows:

---

<sup>13</sup> Physical data can be found in Appendix: Chapter 8 which was reference from SPI Supplies product line

Parameter(s)					
Max. Amplitude (V)	Min. Amplitude (V)	Cycle Count	No. of data Points per scan	Trigger Delay (Second)	Step Size (mV/Step)
-0.1	0.1	1	100	5	2

**Table 8.5.a: Programming parameters conducted for benchmark tests measurements**

For consistency, the membrane type was characterised and immersed in four electrolyte concentrations which were 0.001 M, 0.01 M, 0.1 M and 1 M. Measurements were obtained using a Keithley 2400 SourceMeter controlled via LabVIEW™ programmed control system. The measurements recorded then the slope or gradient of the I-V curve is determined. This is because the slope of the I-V curve is a direct measure of the system conductance and as such it is possible to derive physical characteristics from the empirical data.

### 8.5.2. Analysis of Results: Track-Etched Membranes

To complete the ionic conductivity characterisation of the aforementioned track-etched membranes, one has to be familiar with the physical properties and mechanics of these membrane liquid junctions prior to extracting useful data from the series of plots.

Consider a single cylindrical pore embedded within a membrane with geometric dimensions length  $L$  and diameter  $D$ . Should the corresponding pore be filled with an electrolyte of a particular electrolyte of bulk conductivity,  $\sigma$  and subsequently subjected to an electromotive force; the system would register a potential difference through the conductive pass. Analogously, this system can be considered as a solid wire with the exact geometric characteristics and with it corresponding material conductivity. Hence the conductance of the channel  $G_{channel}$  can be equated as:

$$G_{channel} = \sigma \frac{\pi D^2}{4L}$$

**Equation 8.5.1: Equation to compute the conductivity of a single embedded pore within a membrane**

In practise, the membranes analysed feature a numerous embedded pores and also conveniently conductance is the reciprocal of resistivity. Conversely, past efforts from experimenters (Kowalczyk, Grosberg, Rabin, & Dekker, 2011) have noted a discrepancy revealing a poor data fit when discounting the access resistance of the system. Access resistance is an effect first observed by past works (Hille, 1978) where the effect of ions confined to traverse through a pore effectively contributes to the total resistivity of the system. Figure 8.5.a depicted by Vodyanoy and co-worker (Vodyanoy & Bezrukov, 1992) demonstrates an excellent representation of the access resistance theory.

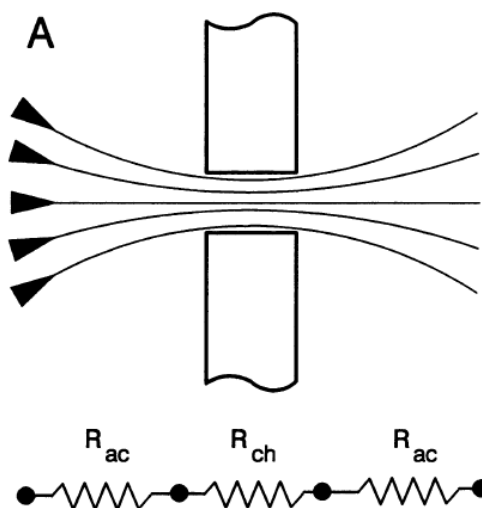


**Figure 8.5.a: Image representation of the access resistance theory and corresponding sum of resistance at both sides of the channel. Image taken from (Vodyanoy & Bezrukov, 1992)**

Later rectified by Hall (Hall, 1975), the access resistance,  $R_{access}$  can be denoted as  $R_{acc} = \rho/2D$  where  $\rho$  is the effective bulk resistivity of the electrolyte solution. Obtaining this variable, the total resistance of entire system can then be equated as:

$$R_{total} = R_{channel} + 2R_{access}$$

**Equation 8.5.2: Equation of the total resistance of a single embedded pore with access resistance taken into account**

Consequently, resistivity and conductance are reciprocals hence converting Equation 8.5.2 in to conductance will lead to:

$$G_{total} = \sigma \left[ \frac{4L}{\pi D^2} + \frac{1}{D} \right]^{-1}$$

**Equation 8.5.3: Equation of the total conductance for a single embedded pore complete with access resistance consideration**

Based on the computations of Equation 8.5.3, one is able to ascertain geometric approximations based on the I-V slopes obtained for a singular pore. Realistically this is not the case as the system features an array of pores which contributes to the entire system. Hence the pore density had to be taken into account, which encompasses a simple multiplication of the number of operational pores<sup>14</sup> to Equation 8.5.3 will compute total conductance embedded pores inside the membrane. For clarity sake we term this variable  $N_{pore}$ . The variable  $N_{pore}$  for the track-etch membranes was calculated based on the data provided by the manufacturer by multiplying the rated pore density (rated pores/m<sup>2</sup>) respectively with the sample area which is the exposed regions of the membrane that contribute to conductivity. This would equate to:

$$G_{total} = \left[ \sigma \left[ \frac{4L}{\pi D^2} + \frac{1}{D} \right]^{-1} \right] N_{pore}$$

**Equation 8.5.4: Theoretical model to obtain pore geometry estimates ascertained for multi pore systems**

The slopes of the I-V curves ascertained empirically were compared with a theoretical model from Equation 8.5.4 to obtain pore geometry estimates using the four KCl concentrations. Variable  $\sigma$  was computed using the formulae provided by Mckee (McKee, 2009) at the specific temperature which was measured to be 16 °C.

---

<sup>14</sup> The term operational pores refer to the number of pores which are exposed to the electrolyte at both openings allowing ionic transport through them and thus contributing to the conductance of the entire system.

The results from the ionic conductance test for track-etch membranes are presented below as a tabulated summary and an example plots demonstrating the I-V curves at different KCl concentrations of 8  $\mu\text{m}$  diameter track-etched pores demonstrated in Figure 8.5.b through Figure 8.5.e. It should be noted that a sufficient amount of time was allowed for the Ag/AgCl electrode pair potential to stabilise in the ranges of  $\pm 1 \mu\text{V}$  before any measurements were taken.

Pore Diameter ( $\mu\text{m}$ )	Averaged I-V Slope at KCl concentration ( $\mu\text{S}$ )			
	0.001 M	0.01 M	0.1 M	1 M
0.1	12.93	20.78	67.68	1458.00
8	28.83	33.08	141.50	1532.50

**Table 8.5.b: Tabulate summary of gradient values for two track-etch membrane using four KCl concentration values**

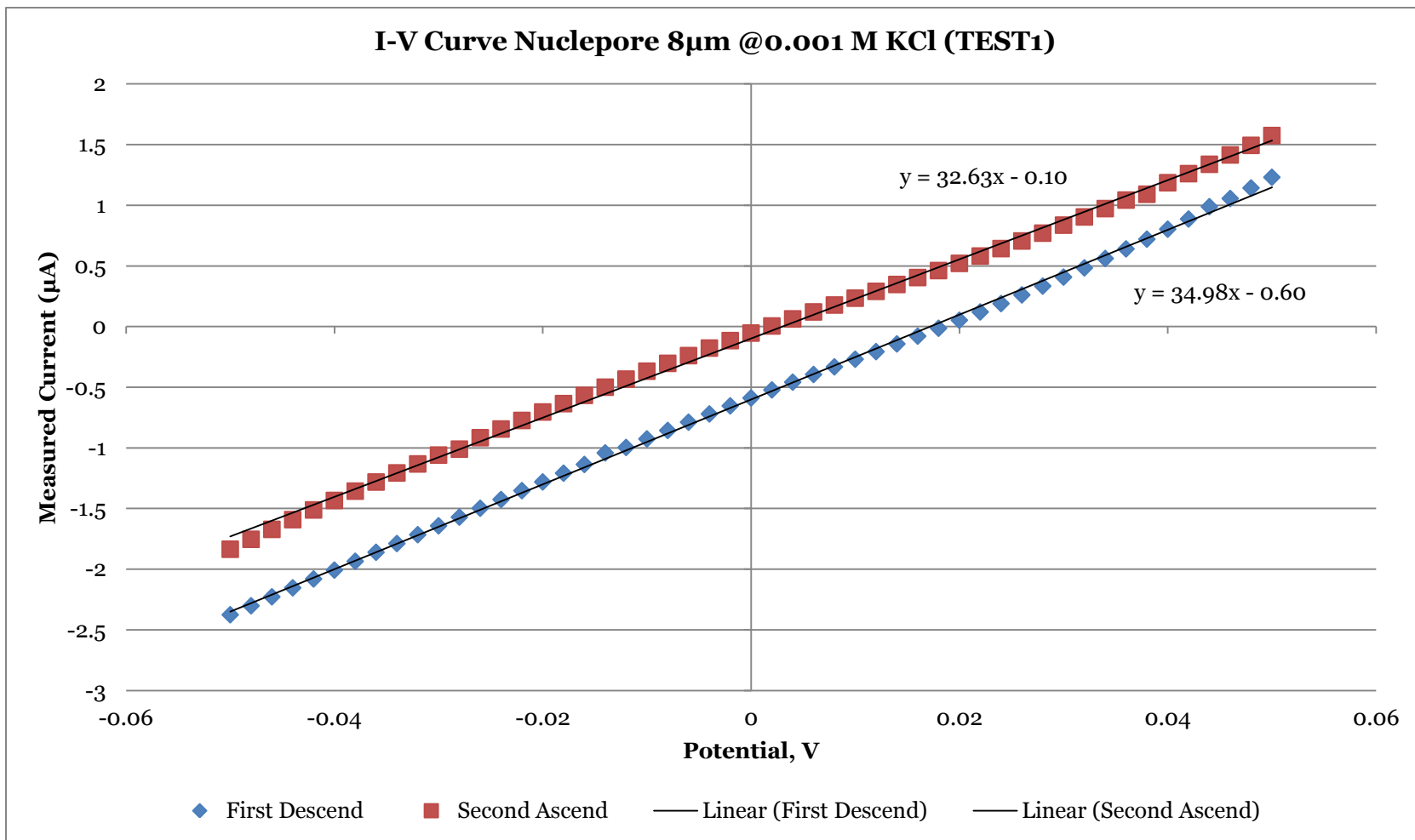
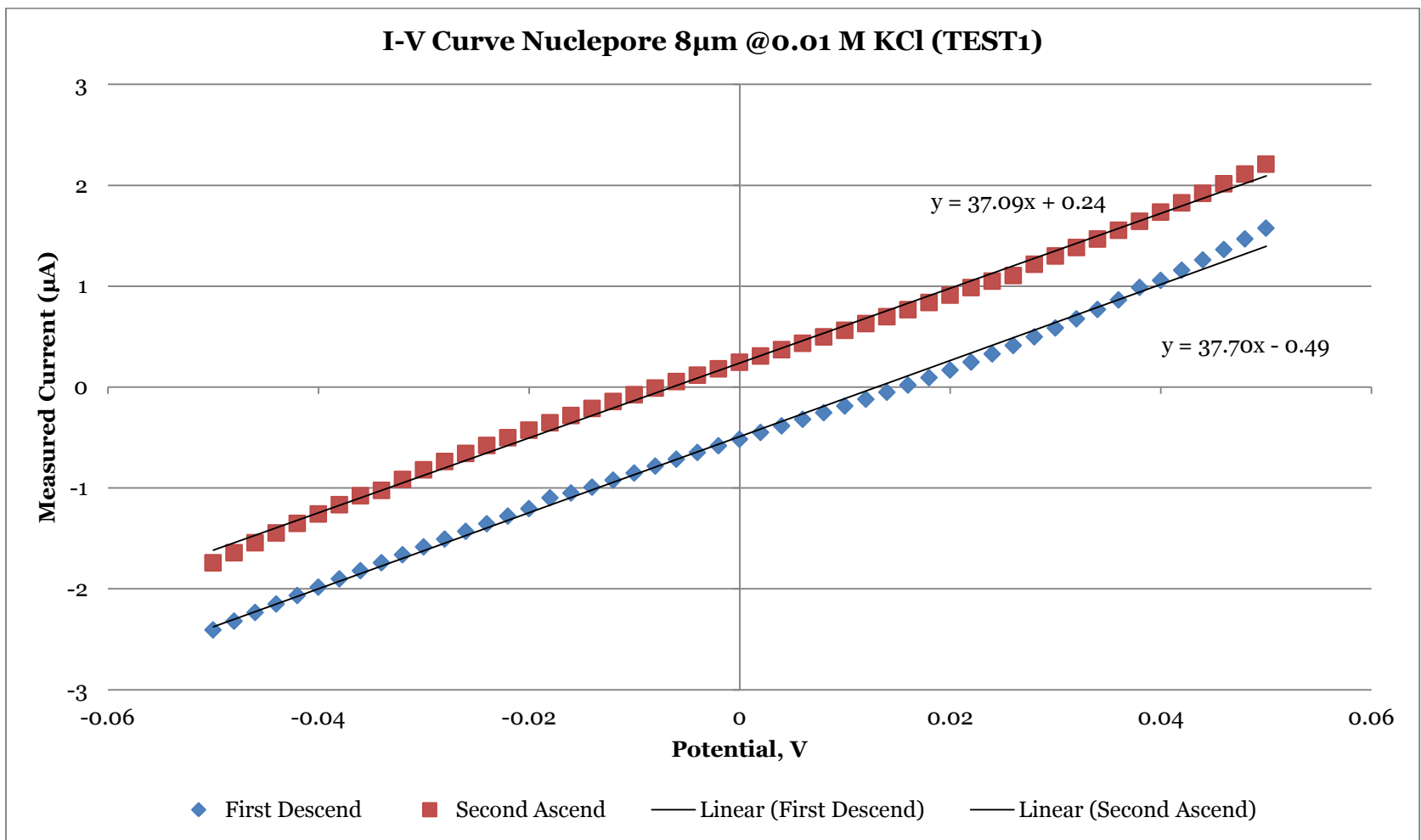


Figure 8.5.b: Exemplar plot of an 8 µm diameter pore using 0.001 M KCl concentration



**Figure 8.5.c: Exemplar plot of an 8 µm diameter pore using 0.01 M KCl concentration**

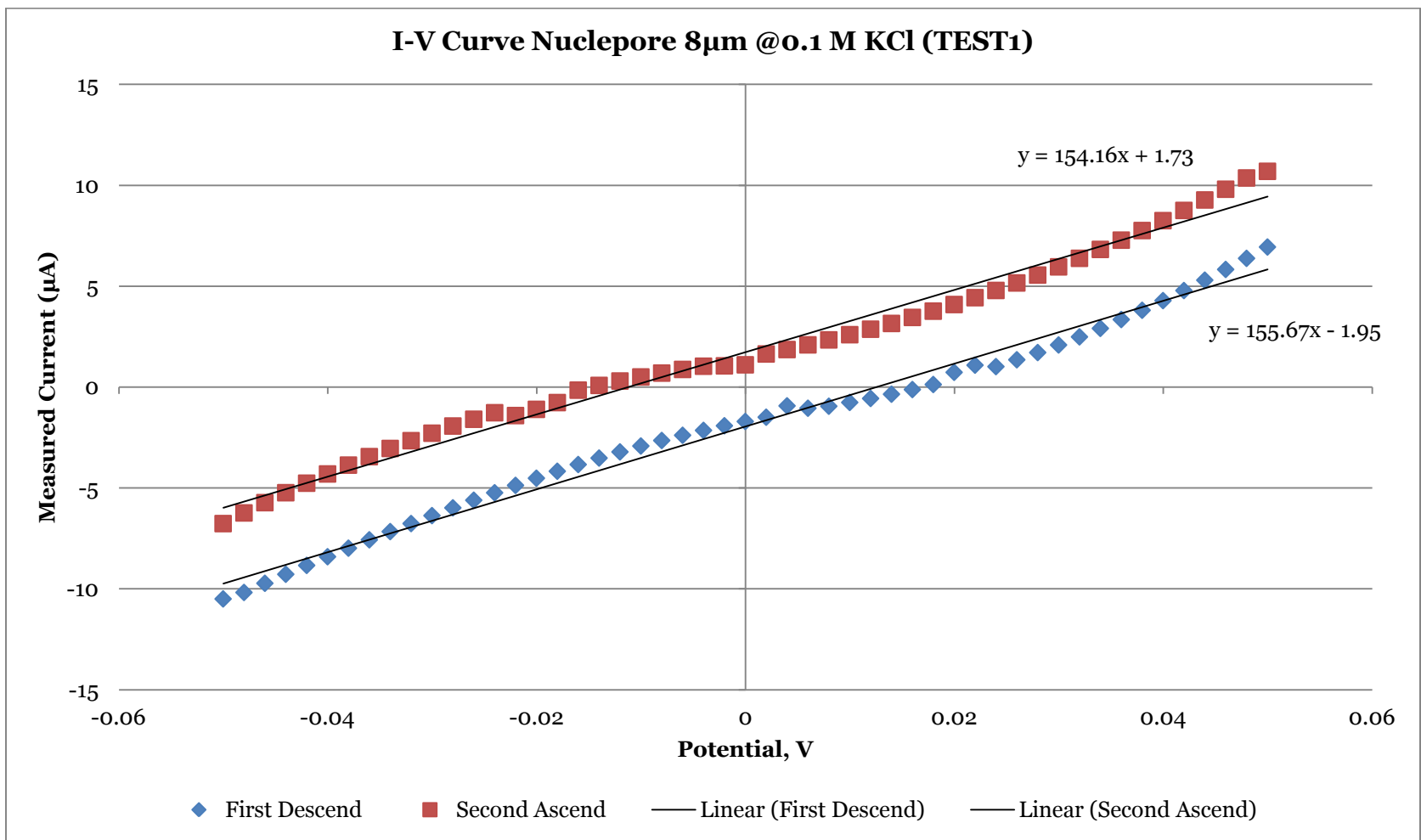
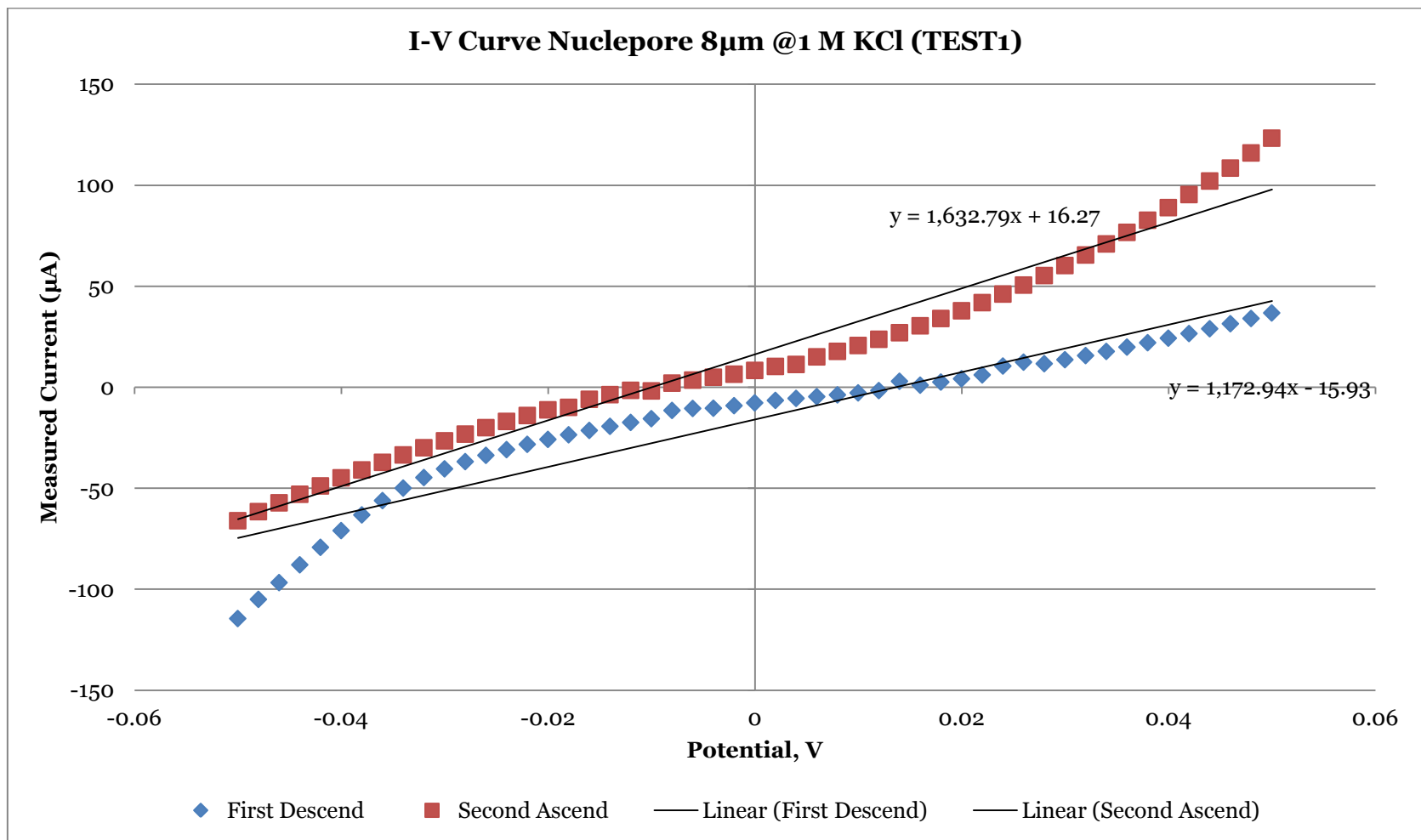


Figure 8.5.d: Exemplar plot of an 8 μm diameter pore using 0.1 M KCl concentration



**Figure 8.5.e: Exemplar plot of an 8 µm diameter pore using 1 M KCl concentration**

Figure 8.5.b through to Figure 8.5.e was presented for demonstrative purposes to provide the reader with a view of the current response obtained from the I-V curves. With regards to the lower concentration series (0.001M and 0.01M) it was regarded as to have registered erratic measurements because the computed slope does not scale appropriately as the tests involving higher KCl concentrations. It was concurred that the cause was the depletion of halide ions traversing due to the low concentration of KCl present in the test. Therefore the 1 M concentration KCl will receive more analytical focus.

Additionally, 0.1  $\mu\text{m}$  track-etched membranes were also tested and too demonstrated similar conductance though they have dissimilar pore diameter values. The causation for this can be explained by the ratio of pore size to pore density of these samples; while the 0.1  $\mu\text{m}$  diameter membranes featured smaller pore diameter sizes, however they also feature very high pore densities. Additionally the situation was the inverse for the 8  $\mu\text{m}$  diameter pores as they have a low pore density. Since these membranes were manufactured for filtering purposes, it is common practice that they feature this ratio effect.

Subsequently, the tabulated results were compared with their theoretical counterparts using Equation 8.5.4 the corresponding theoretical calculations. The physical parameters used for the calculations can be found in Appendix: Chapter 8 and the bulk conductivity of the electrolyte were calculated based on the formulas provided by McKee (McKee, 2009). The resultant the theoretical computations are presented below:

Pore Diameter ( $\mu\text{m}$ )	Computed electrolytic conductance at various KCl concentration ( $\mu\text{S}$ )			
	0.001 M	0.01 M	0.1 M	1 M
0.1	59.63	572.9	5230	45355
8	44.03	423.0	3862	33487

**Table 8.5.c: Tabulated summary of theoretical conductance values for two track-etched membranes using four KCl concentrations**

Initial comparison between the theoretical calculations demonstrated a higher conductance. To solve this discrepancy, the flow cell resistance was investigated to determine its contributing resistance to the entire system as a whole. Since

resistance and conductance are reciprocal values, the conductance measurements were converted into resistance values then cell resistance was subtracted from the total giving the pure conductance values. Through experimentation, the flow cell resistance was found to be  $600 \Omega \pm 100 \Omega$  at a KCl concentration of 1 M. It was also found that higher KCl concentrations offered more consistent flow cell resistance measurements and the subsequent resistance rectification was conducted accordingly using strong electrolytes (1 M). This was because the Ag/AgCl electrodes submerged in weak electrolytes (0.001 M) require a long period of time to reach an equilibrium potential. The results for both 0.1  $\mu\text{m}$  and 8  $\mu\text{m}$  diameter membranes were rectified accordingly.

Membrane type	Conductance at	Resistance		
	1 M KCl (results taken from Table 8.5.b)	Conversion into resistance (1/conductance)	Rectification (subtracting the cell resistance $600 \Omega$ )	Rectified Conductance Measurements
0.1 $\mu\text{m}$	1458 $\mu\text{S}$	685.9 $\Omega$	85.87 $\Omega$	11645.37 $\mu\text{S}$
8 $\mu\text{m}$	1533 $\mu\text{S}$	652.5 $\Omega$	52.53 $\Omega$	19037.27 $\mu\text{S}$

**Table 8.5.d: Table of results detailing the resistance rectification of actual measurements**

Table 8.5.d details the conversion of the reciprocals values which was accompanied with the resistance rectification. The conversion of measured conductance demonstrates that the effect of the cell resistance was relatively significant. However the rectified conductance values now demonstrate a better agreement with the theoretical results as they were now in the same order of magnitude.

With regards to lower concentration of KCl; intuitively these values should scale up accordingly by a factor of 10 should the concentration decreased by that same factor. Therefore when factoring the cell resistance back in to the actual measurements, the result should demonstrate a significant increase. However experimentation was not repeated for lower electrolyte concentrations.

Additionally it is also important to note that these Ag/AgCl electrodes systems are highly sensitive to the effects of temperature as a result of an unavoidable temperature gradient through the system (Sawyer, Sobkowiak, & J. L. Roberts, 1995). To conclude this section, the results obtained has demonstrated an

agreeable outcome to a certain extent and the theorems employed can be validated via actual experimentation therefore making it suitable as benchmark measurements for subsequent tests.

### 8.5.3. Ionic Characterisation: Fabricated Membrane Platforms

This section attempts to electrochemically characterise the fabricated membrane platforms using aforementioned experimentation methods. Several membrane samples were characterised in a range of electrolyte concentrations. Similarly, measurements were obtained using a Keithley 2400 SourceMeter controlled via LabVIEW™ programmable control system. Furthermore the regime of observing the current response first descending and second ascending scan was implemented. Results obtained from experimentation was then tabulated and summarised in Table 8.5.e demonstrating their respective I-V slopes which aids subsequent examination.

Sample Name	Membrane conductance at specific KCl concentration (nS)			
	0.001 M	0.01 M	0.1 M	1 M
<b>Mramptest 2 (06102013)</b>	5.021	85.73	584.6	3849
<b>Mramptest 4 (06102013)</b>	0.722	49.70	139.0	572.2
<b>Mramptest 3 (12092013)</b>	3.601	33.10	176.3	574.5
<b>Mramptest 5 (12092013)</b>	9.877	79.34	162.1	574.4

**Table 8.5.e: Summarised conductance measurements from fabricated membranes at various KCl concentration**

The subsequent measurements demonstrated were relatively consistent in terms of scaling upwards by a factor of ten at each KCl concentration step for KCl concentrations of 0.001 M through to 0.1 M. However this statement cannot hold true for the highest KCl concentration of 1 M. The causation for this is not fully understood. Nevertheless it should be noted that the experimental data obtained from the track-etch membranes cannot be taken as a direct comparison to with the data presented in Table 8.5.e as there may be other factors that may contribute to

the measurements (membrane material, pore shape, internal structure of the pore itself).

Nevertheless, previous works (Dekker, Smeets, Keyser, Krapf, Wu, & Dekker, 2006) & (Lee, Joly, Siria, Biane, & Bocquet, 2012) have demonstrated a deviation between their experimental and empirical data when considering becoming more apparent at lower KCl concentrations. Therefore the conductance measurements with the highest KCl concentration will be taken into account subsequent post-processing analysis.

Moving onwards, it can be observed that the samples series Mrampstest 2 (06102013) registered higher conductance at 0.1 M and 1 M KCl measurements as compared to the rest. It was hypothesised that the corresponding membrane had a higher concentration of larger assembled columnar array as compared to the others.

Additionally as mentioned before the effect of the flow cell resistance here was found to be a negligible as the conductance measurements obtained from our samples were many times bigger in order of magnitude ( $M\Omega$  vs.  $600\ \Omega \pm 100\ \Omega$ ).

### 8.5.3.1. Investigating Discrepancy: Mrampstest 2 (06102013)

To solve this discrepancy, a quick OM investigation was conducted across the four corresponding samples. The analysis was based on comparing the average apparent array size across the four samples. The rationale behind this was arrays with a bigger apparent pore size would register a higher conductance. Results of the analysis are presented below.

Sample Name	Average apparent array size (pixel <sup>2</sup> )
Mrampstest 2 (06102013)	7.54
Mrampstest4 (12112013)	4.21
Mrampstest3 (06102013)	6.06
Mrampstest5 (12112013)	4.40

**Table 8.5.f: Averaged apparent pore sizes for all samples**

Observing Table 8.5.f, it is evident that sample Mrampstest 2 (06102013) would register a higher conductance measurement in comparison to the other three since

it exhibits larger average. As an additional note, sample Mramptest3 (12092013) also registered some pores which were bigger than the average apparent pore size in size but at a very low frequency as compared to the Mramptest2 (06102113) and it too also registered slightly conductance value which was demonstrates some correlation between the apparent sizes and with the measurements detailed in Table 8.5.f. This quick analysis demonstrates a correspondence to the apparent size of the arrays with the resultant conductance measurement.

#### 8.5.4. Analysis of Results: Fabricated Membrane Platforms

Again, analytical techniques were employed to provide substantial evidence with regards to the approximations of the pore size. Analyses from the previous chapter were brought in as supporting data to formulate a summary. Theoretical models from Equation 8.5.4 were used to establish comparative element with the measured results. Evidently, three theoretical modes have incorporated in attempt to best model the pores.

Theoretical computations were conducted in three modes:

- Observing the effective pore opening diameter assuming the nanopores were perfectly cylindrical in shape. The temperature of the electrolyte was measured to be 16 °C.
- Observing the effective pore opening diameter assuming the nanopores were tapered columnar structures with the incorporation of realistic constraints observed from previous chapters.
- Observing the pore structure as a network of inter-connected nanoparticles along the membrane thickness. Model was based on SEM microscopy analysis discussed in previous chapters.

The first mode begins by addressing new values such as the rectified bulk electrolytic conductivity  $\sigma$  rating and a new  $N_{pore}$  was ascertained from the pore density analysis from the previous Chapter 7 Section 7.2.1. The pore density analysis was computed in the range of a minimum, average and maximum pore density of  $1.71 \times 10^9$  Pores/m<sup>2</sup>  $9.48 \times 10^9$  Pores/m<sup>2</sup> and  $1.64 \times 10^{10}$  Pores/m<sup>2</sup>

respectively. Therefore a simple multiplication of the pore densities with the exposed area of  $7.86 \times 10^{-7} \text{ m}^2$  should equate to the new value of  $N_{pore}$  which is tabulated in Table 8.5.g. The membrane thickness  $L$  was taken as  $6.7 \text{ }\mu\text{m}$  from Helmholtz coil pair specimens from Chapter 7 Section 7.2.2.

<b>Number of Pores, <math>N_{pore}</math></b>		
Minimum	Average	Maximum
1343	7451	12890

**Table 8.5.g: Tabulated values of  $N_{pore}$**

With all the new values assembled, the tabulated limits are summarised in Table 8.5.h, Table 8.5.i and Table 8.5.j for clarity and convenience. This mode utilises to aid our analysis. This analysis represents the first mode of the analysis where the pores are assumed to be perfect cylindrical columns.

<b>Theoretical conductance of membrane (Parameters: Minimum limit of pores at 1 M concentration KCl)</b>					
Pore Diameter Range (nm)	$N_{pore}$	Bulk conductivity of electrolyte (S/m)	Membrane thickness ( $\mu\text{m}$ )	Conductance of single pore (nS)	Total conductance (nS)
5	1343	8.66	6.7	0.025	34.06
15				0.228	306.22
20				0.405	544.07
25				0.633	849.61
30				0.910	1222.72
35				1.238	1663.29
40				1.617	2171.19
45				2.045	2746.31
50				2.523	3388.53
55				3.051	4097.73

**Table 8.5.h: Computed theoretical conductance of membrane at the minimum limit of pores using 1 M KCl concentration**

<b>Theoretical conductance of membrane (Parameters: Average limit of pores at 1 M concentration KCl)</b>					
Pore Diameter Range (nm)	$N_{\text{pore}}$	Bulk conductivity of electrolyte (S/m)	Membrane thickness ( $\mu\text{m}$ )	Conductance of single pore (nS)	Total conductance (nS)
5	7451	8.66	6.7	0.018	188.99
15				0.160	1698.90
20				0.285	3018.50
25				0.445	4713.64
30				0.640	6783.68
35				0.871	9227.95
40				1.137	12045.81
45				1.439	15236.59
50				1.776	18799.64
55				2.148	22734.32

**Table 8.5.i: Computed theoretical conductance of membrane at the average limit of pores using 1 M KCl concentration**

<b>Theoretical conductance of membrane (Parameters: Maximum limit of pores at 1 M concentration KCl)</b>					
Pore Diameter Range (nm)	$N_{\text{pore}}$	Bulk conductivity of electrolyte (S/m)	Membrane thickness ( $\mu\text{m}$ )	Conductance of single pore (nS)	Total conductance (nS)
5	12890	8.66	6.7	0.018	326.94
15				0.160	2939.04
20				0.285	5221.90
25				0.445	8154.46
30				0.640	11735.56
35				0.871	15964.08
40				1.137	20838.87
45				1.439	26358.82
50				1.776	32522.79
55				2.148	39329.66

**Table 8.5.j: Computed theoretical conductance of membrane at the maximum limit of pores using 1 M KCl concentration**

The pore range of 5 nm to 55 nm range was pre-selected to accommodate all 4 conductance measurements onto a single concurrent table. As a result the theoretical conductance was plotted as a function of pore diameter. Demonstrated in Figure 8.5.f:

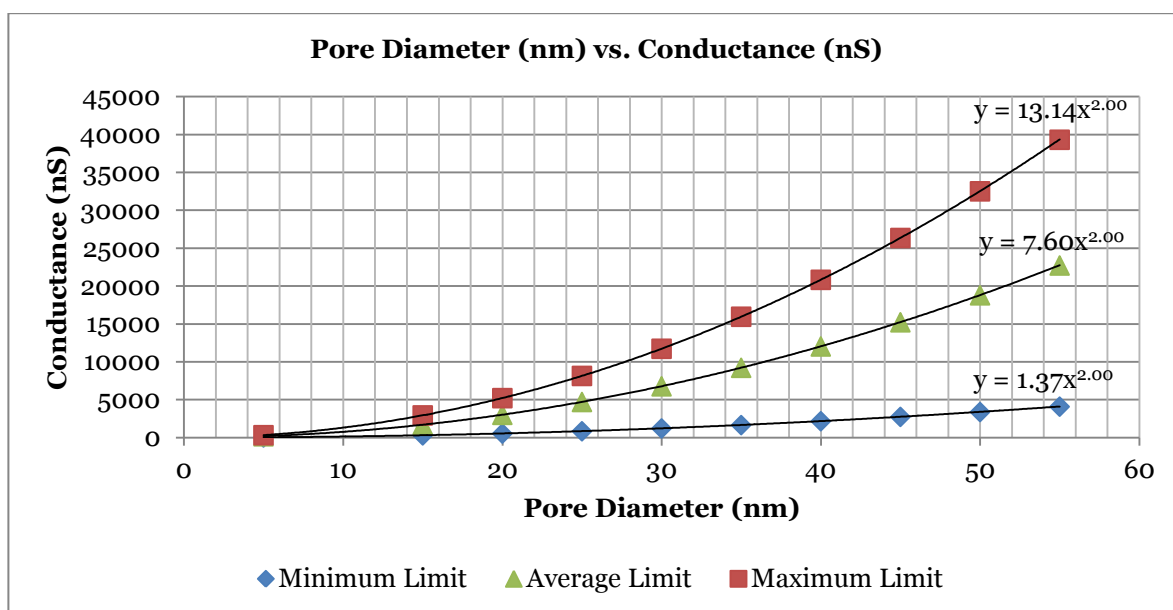


**Figure 8.5.f: Plot depicting the change in theoretical conductance versus pore diameter at 0.1 M KCl concentration**

Based on the ionic conductance measurements obtained from Table 8.5.e, the measured conductance values were substituted back into the curve fit obtained from Figure 8.5.f to ascertain the approximated pore sizes. The results have been tabulated in Table 8.5.k illustrated below. For clarity sake the curve trend lines are as follows:

- Minimum Limit:  $y = 1.37x^{2.00}$
- Average Limit:  $y = 7.60x^{2.00}$
- Maximum Limit  $y = 13.14x^{2.00}$

<b>Approximated Pore Diameter based on experimental measurement (nm)</b>			
<b>Sample Name</b>	<b>Minimum Limit</b>	<b>Average Limit</b>	<b>Maximum Limit</b>
<b>Mramtest 2 (06102013)</b>	53.01	22.50	17.11
<b>Mramptest 4 (06102013)</b>	20.44	8.68	6.60
<b>Mramptest 3 (12092013)</b>	20.48	8.69	6.61
<b>Mramptest 5 (12092013)</b>	20.48	8.69	6.61

**Table 8.5.k: Tabulated summary of pore size approximation based on measurement obtained**

Table 8.5.k exhibits the approximated pore opening size analysis based on the results obtained, the approximated largest pore size was found to be 53.01 nm and the smallest was 6.61 nm. Conversely, it is important to note that these approximations assume the geometry of pores contributing to conductance were cylindrical in shape and the mathematical model assumes the said shape accordingly. However this cannot be entirely true as the discussion in Chapter 3 Section 3.3 presented three expected forms of the Fe<sub>3</sub>O<sub>4</sub> columnar structure that templates the polymeric matrix; which was a cylindrical column with tapered ends. Furthermore the TEM analysis in Chapter 4: Section 4.1.3 has demonstrated an effective singular nanoparticle size to be at  $\approx 12$  nm therefore, measurements detailing sizes below this actual size of the particle become invalid. However the measurement above this range was acceptable of 17 nm – 53 nm.

Additionally, the analyses completed thus far were accomplished based on ideal scenarios such as the pore density values ascertained were assumed that all visible arrays in the OM analysis represented are completely opened pore and contributed to the conductance of the system. Realistically this cannot be the case as described in Chapter 7 Section 7.2.3 as only a certain percentage of visible arrays have been identified as pores that have fully propagated through both surfaces facilitating a conductive pass which allow ions to traverse through them.

Therefore, an alternative theoretical model was incorporated into the analysis whereby it takes into account the realistic pore openings which was designated to be at a minimum of 60.4 % and the effective shape of the tapered ends. Since the effective theoretical model shape is assumed to have tapered ends; hence they must feature smaller pore opening with respect to the central body on both ends of the column. As a result a larger access resistance  $R_{access}$  will be achieved. Reviewing, Equation 8.5.4 the equation can be modified into:

$$G_{total} = \sigma \left[ \frac{4L}{\pi D_{central}^2} + \frac{1}{D_{access}} \right]^{-1} \times N_{pore (60.4\%)}$$

**Equation 8.5.5: Modified equation for second theoretical pore model**

$D_{central}$  now is the central diameter which can be estimated from the apparent size of the arrays based of the Helmholtz coil pair samples,  $D_{access}$  is the pore opening

across the surface of the membrane which now we consider to be a singular particle that and  $N_{pore (60.4\%)}$  is now 60.4 % out of the total number of observable pores which are considered to be fully propagated pores spanning the entirety of the thickness of the membrane.

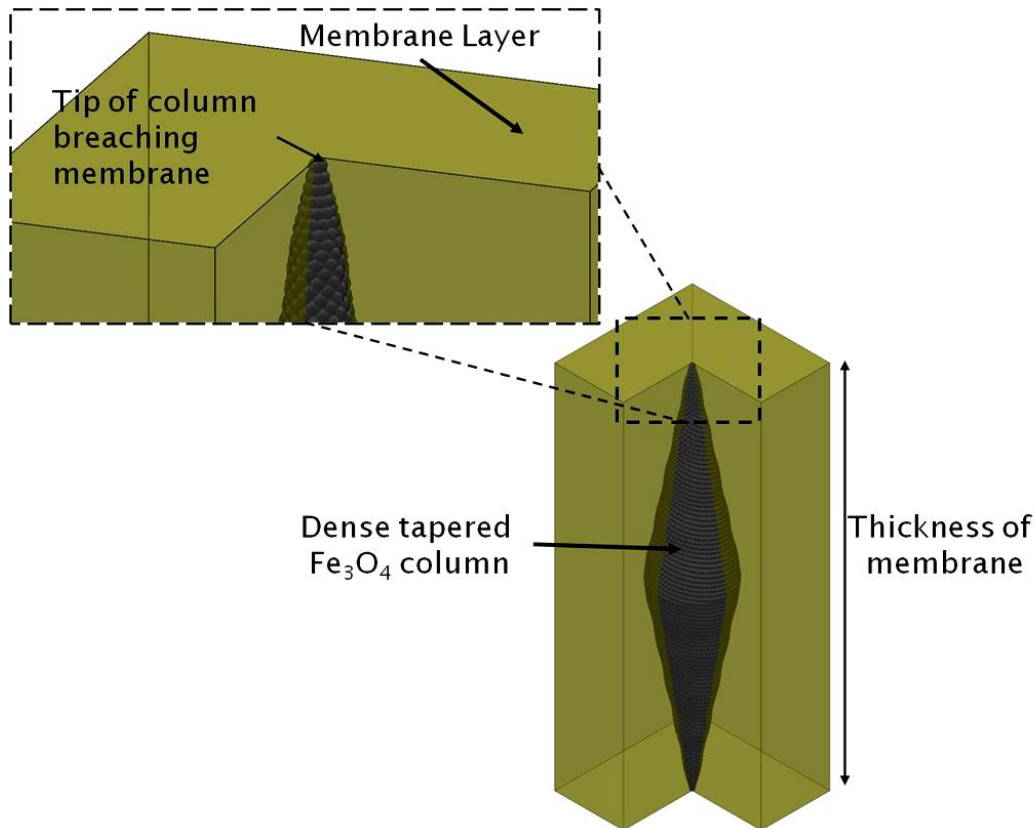


**Figure 8.5.g: Illustration demonstrating a cut-out view of dense tapered column as a template embedded in a membrane**

Figure 8.5.g is an illustration of a cut-out view of a single dense  $\text{Fe}_3\text{O}_4$  column embedded in a membrane layer. For this theoretical model we assume that only a singular particle breaches the membrane layer to form the pore openings by a height of 10% of the radius of a singular particle. The values of  $D_{access}$  can be determined by simple geometry based on a single particle breaching the membrane surface Figure 8.5.h is demonstrated below to aid the discussion.

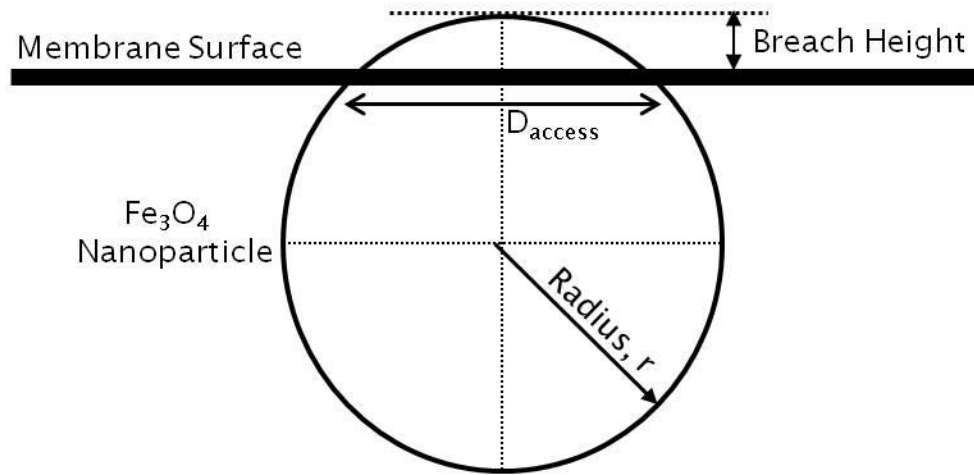


**Figure 8.5.h: Image illustrating the geometry of a single particle breaching the membrane surface**

Figure 8.5.h demonstrates geometry of a single nanoparticle breaching the surface of the membrane. The diameter of the pore opening  $D_{access}$  can be computed using

$$D_{access} = 2\sqrt{r^2 - (0.9r)^2}$$

**Equation 8.5.6: Geometric equation to determine the  $D_{access}$  of Figure 8.5.h**

Note we have applied conservative estimates to the model that the breach height of the particle across the membrane surface to be 10% of its radius. Through the TEM analysis the nominal diameter of a singular particle was determined to be  $\approx 12$  nm hence the  $D_{access}$  can be approximated to be at 5.23 nm.

Additionally the  $D_{central}$  of the columnar model now cannot be less than the nominal diameter of the singular particle hence to determine the  $D_{central}$ , iterative calculations were made to find the best data fit that corresponds to the measured conductance values within the aforementioned maximum, average and minimum limits. As a result, Figure 8.5.i demonstrates the plot detailing the theoretical conductance as a function  $D_{central}$  with respect to  $D_{access}$ .

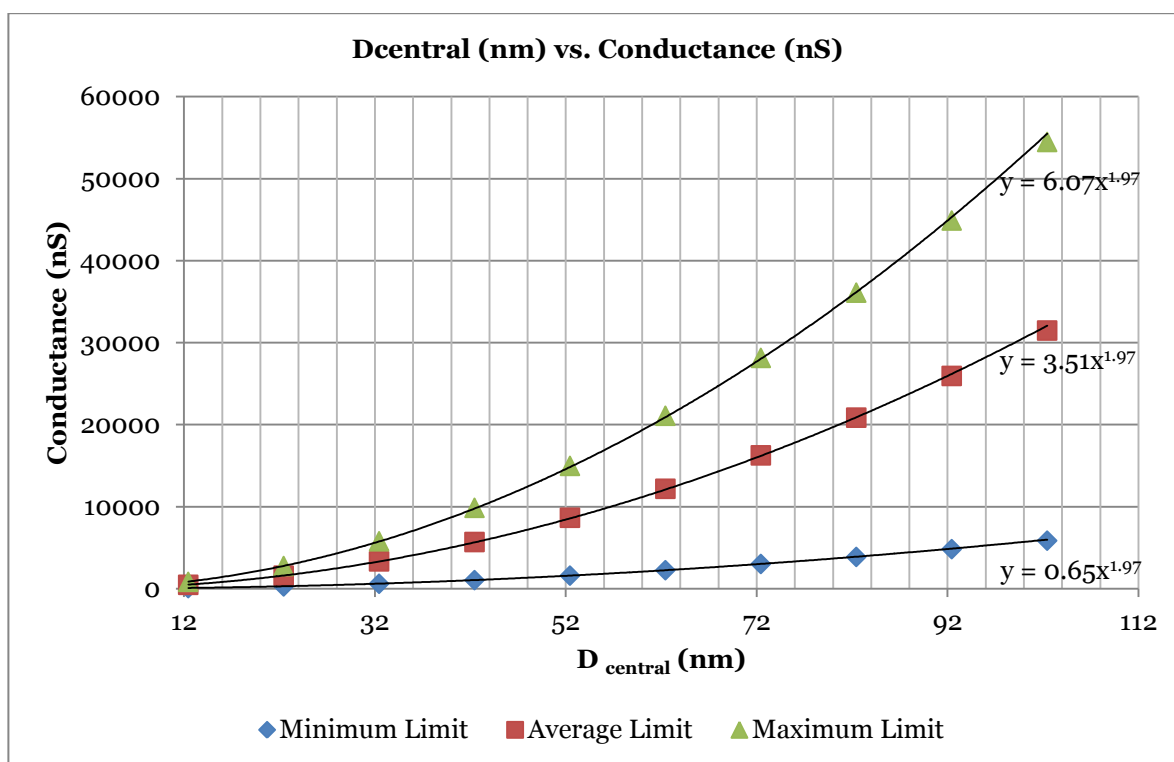


Figure 8.5.i: Plot depicting the  $D_{central}$  as a function of Conductance

Again based of the curve trend lines available on the plot, the exact  $D_{central}$  could be computed. It is important to note that the  $D_{access}$  was set to 1.25 nm as it offered the best fit corresponding to our measured data:

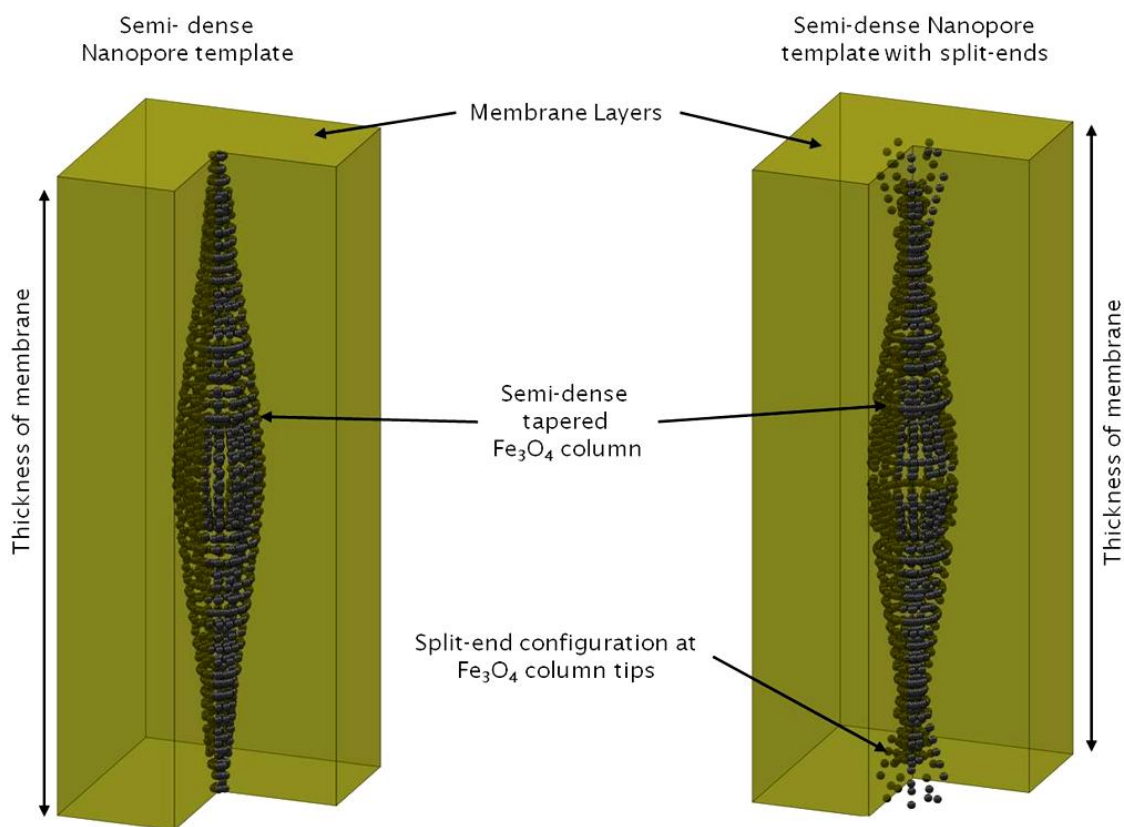
Approximated Pore Diameter based on experimental measurement (nm)			
Sample Name	Minimum Limit	Average Limit	Maximum Limit
<b>Mramtest 2 (06102013)</b>	69.80	29.38	22.27
<b>Mramptest 4 (06102013)</b>	26.66	11.22	8.50
<b>Mramptest 3 (12092013)</b>	26.71	11.24	8.52
<b>Mramptest 5 (12092013)</b>	26.71	11.24	8.52

Table 8.5.l: Tabulated results based on the theoretical model discussed

Based on the results tabulated in Table 8.5.l, the largest  $D_{central}$  was found to be 69.80 nm. However there is a discrepancy when observing smallest  $D_{central}$  as the pre-determined conditions of  $D_{central} \geq 12.45$  nm was not satisfied by the maximum limit. This indicates that either the  $N_{pore}$  was significantly smaller than it

was estimated from the experimental trials or the self-assembled column configuration does not match the proposed theoretical model and a more complex structure was present in the nanopore templates. Nevertheless the  $D_{access}$  values which were larger than the effective diameter of a single particle demonstrate an agreeable range of 22 nm – 70 nm with a 5.2 nm surface opening.

Based on the visual evidence obtained from our SEM microscopy analysis (Chapter 7) it was observed that membrane surface featured smaller clusters of pores which were inter-connected with each other forming a network that spans across the membrane thickness. Additionally past observations from preceding works have been reported by Liu (Liu, et al., 1995) & (Ivey, Liu, Zhu, & Cutillas, 2000) and modelled by Ricardi (Ricardi & Weis, 2011) where the ends of the columnar structures feature smaller more complex assemblies at the tips of the column similarly termed as split-ends. Therefore two possible scenarios of the pore templates were introduced.



**Figure 8.5.j: An exemplar illustration of a cut-out view of pore templates detailing a semi-dense structure with and without split-ends**

Figure 8.5.j illustrated above exemplifies two cut-out views of semi-dense structures with and without split-ends. As mentioned before, though they are less dense as compared to the previous model; they should be inter-connected with each other. To represent this structural configuration into a theoretical model, several assumptions were formulated; first since the pores now comprise of a network of inter-connected spherical openings. Thus the computation for a solid empty cylinder cannot hold true. The causation for this is due to the presence of intertwined material which occupies the physical volume of the cylinder. As such, this occupancy affects the conductance since the traversing ions must compete to go through every inter-connected particle template which now has a new  $R_{access}$  every time it attempts to cross-over into a new template. Figure 8.5.k below is a visual representation of the discussed scenario.

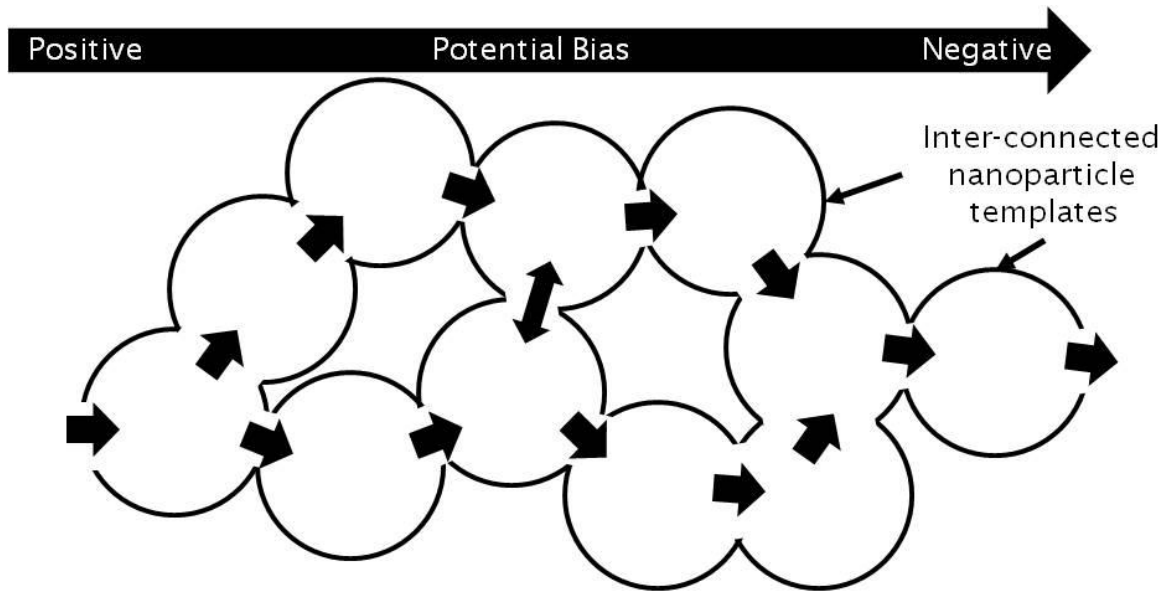
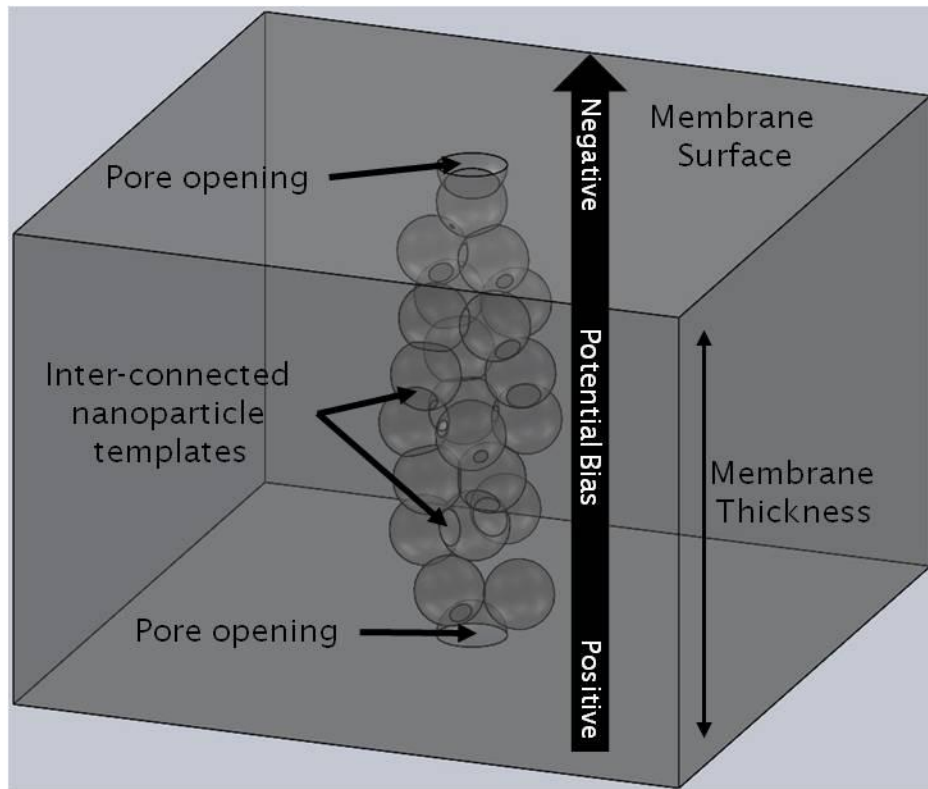


**Figure 8.5.k: A 3D and 2D visual interpretation of the discussion regarding the third theoretical model**

Figure 8.5.k is a visual interpretation of the inter-connected nanoparticle templates across its polymer matrix. The cluster of arrows pointing inwards into the inter-connected nanoparticle templates details the ionic track that the ionic species

must traverse through to reach the electro-negative electrode. Each arrow can also be seen as sites where access resistance  $R_{access}$  becomes dominant. The basis of this theoretical model was from the SEM findings in Chapter 7 Figure 7.4.ff where the cross-sectional view of the membrane revealed a pore structure which comprised of a network of spherical openings spanning the thickness of the membrane. To provide an accurate theoretical model of the structure would require a huge amount of computations with the aid of FEA software. However a simplified model was provided to obtain initial estimates. Figure 8.5.1 demonstrated below is a simplified circuit diagram detailing the pore structure.

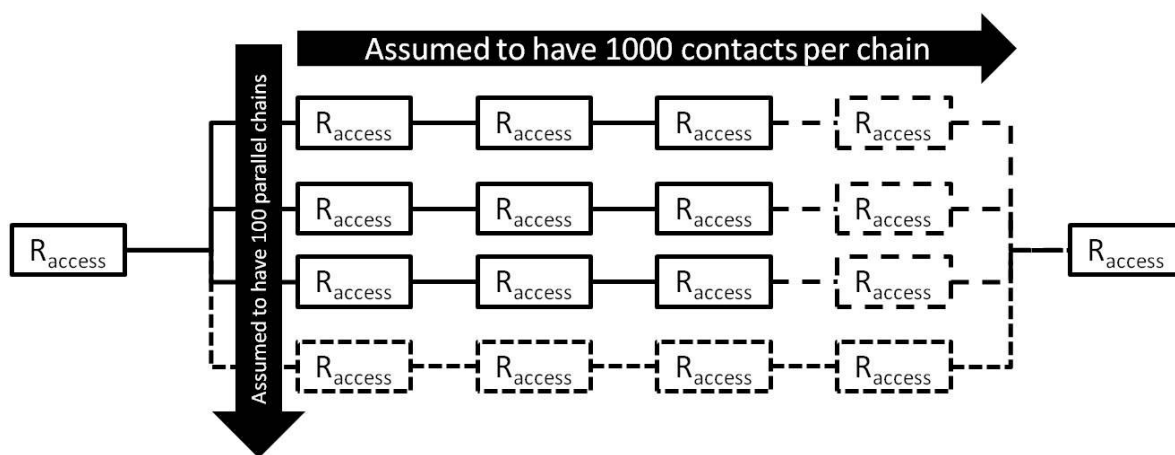


**Figure 8.5.1: A representative circuit diagram detailing a singular nanopore structure**

Figure 8.5.1 is a representative circuit diagram which details a simplified singular pore structure. The box with the inscription  $R_{access}$  describes the representative resistance of access resistance. The two  $R_{access}$  at both ends represent tapered tips of the column where only a single particle has breached the membrane layer assembly whereas the 1000 contact long branches represent a singular segregated network of pores. This 1000 contact figure was estimated from the membrane thickness being roughly  $10\ \mu\text{m}$  thick that accommodates 1000 particles ( $10\ \mu\text{m}$  was chosen for this task to simplify calculation) assembled into a long chain. Additionally the thickness of a singular pore structure was defined as 100 parallel chains thick due to observation made in the SEM analysis (Figure 7.4.ff) where the average thickness was estimated to be  $1\ \mu\text{m}$  wide. Therefore, a summation of the entire circuit diagram would equate to:

$$\sum R_{pore} = 10R_{access1} + 2R_{access2}$$

**Equation 8.5.7: Equation of the summation of  $R_{access}$  for a singular pore**

The terms  $10R_{access1}$  are the 100 parallel chains of each containing 1000 contacts and the term  $2R_{access2}$  signifies the two ends of the particle breaching the membrane surface respectively.  $R_{pore}$  is the total resistance of a singular pore. Therefore to determine the total resistance of the entire system is just the multiplication of the total number of pores contributing to the system  $N_{pore}$  with  $R_{pore}$ . Since resistance and conductance are reciprocal terms, the term  $R_{total}$  can be converted into total conductance of the system:

$$G_{total} = N_{pore} \times \sigma \left[ \frac{5}{D_{access1}} + \frac{1}{D_{access2}} \right]^{-1}$$

**Equation 8.5.8: Equation detailing the total conductance of the membrane**

The variables  $D_{access1}$  and  $D_{access2}$  are the effective diameter that contributes to the access resistance  $R_{access1}$  and  $R_{access2}$  respectively. The discussion of converting  $R_{access}$  into  $G_{pore}$  can be found in Section 8.5.2 and  $\sigma$  is the bulk conductivity of the electrolyte (calculated using McKee equation (McKee, 2009) at temperature 16 °C). To apply realistic values to Equation 8.5.8 we first assume that the individual particle contact each chain 10% of the total radius hence  $D_{access1}$  will equate to 5.23 nm since not all particle chains are fully conductive.

Unfortunately using the three pore density limits (minimum, average and maximum) could not accommodate the ranges for all actual measurements therefore we have introduced a new value of  $N_{pore}$  of 3000 which was slightly below the average limit of  $N_{pore(60.4\%)}$ . Additionally this new  $N_{pore}$  compensation was unable to accommodate the irregular measurements obtained from sample Mrampst2 (06102013) therefore only the other three samples were considered. A tabulated summary of the computations are presented in Table 8.5.m and corresponding plot of conductance as a function of  $D_{access2}$  in Figure 8.5.m.

Theoretical conductance computations based on Equation 8.5.8 determine  $D_{access2}$

% particle diameter	$D_{access2}$ (nm)	$N_{pore}$	Bulk Conductivity of Electrolyte for 1 M KCl (S/m)	Conductance (nS)
1	0.12	3000	8.66	540.938
2	0.25			590.114
3	0.37			608.555
4	0.500			618.214
5	0.625			624.159
6	0.750			628.185
7	0.875			631.094
8	1.000			633.293
9	1.125			635.014
10	1.250			636.397

Table 8.5.m: Tabulated computations based on Equation 8.5.8 to determine  $D_{access2}$

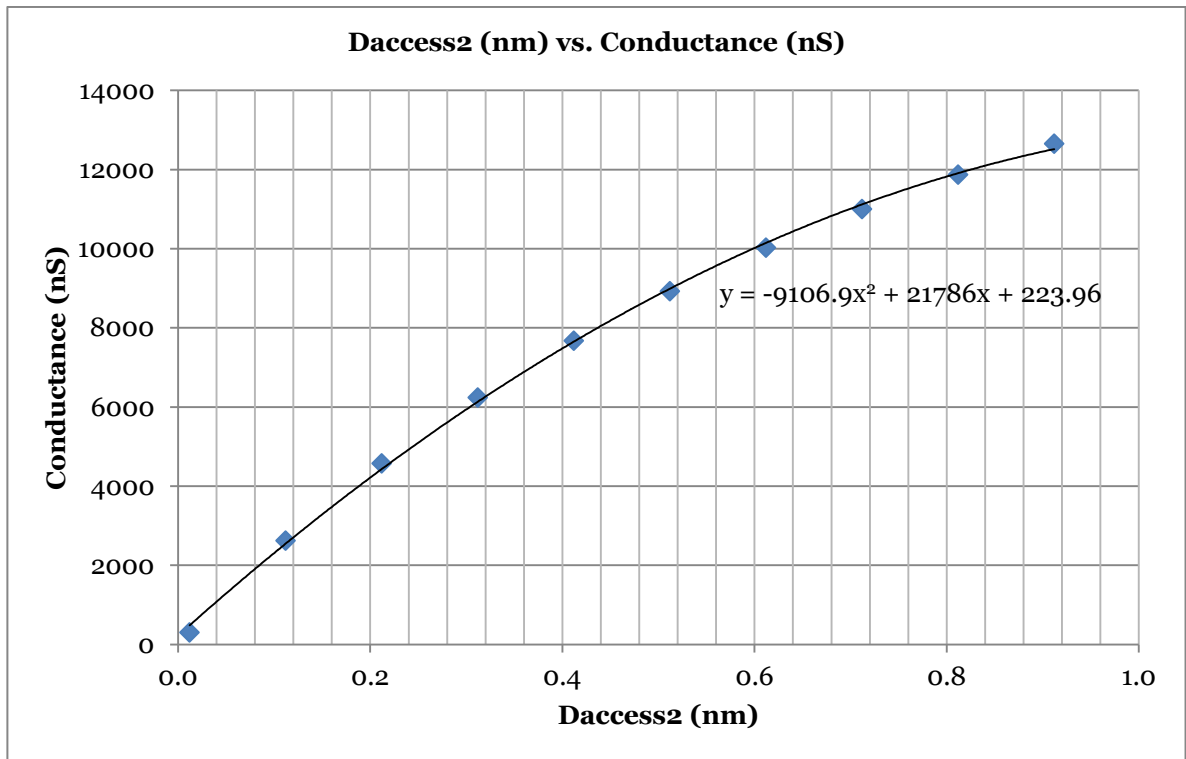


Figure 8.5.m: Plot of conductance as a function of  $D_{access2}$

Based on curve trend line obtained from Figure 8.5.m, the effective  $D_{access2}$  for each sample was found by substituting the actual conductance measurements to obtain a value of 2.4 nm. Nevertheless, the result obtained here still was not entirely convincing due to the  $N_{pore}$  compensation that took place. It was concurred that the model was over simplified and may have disregarded several

unknown important factors. Considering the split-end model would require adding more  $D_{access2}$  at both ends of the representative circuit which was found not to fit any of the actual measurement at all.

Nevertheless, the data obtained from the other two models suggests that pore-openings across the surface were within the nanometer range which demonstrates positive results and provides an explanation towards the low density of visible pore openings encountered during the SEM analysis. Since the gold coating was set to a minimum 15 nm, there was a possibility that the coating may have covered the entire pore itself. Unfortunately it was found that any gold coating thickness below 15 nm in thickness would result in charging inhibiting any useful image resolution. An additional factor that may contribute to this quandary was also the collapsed of the pore opening after selective etching discussed in Chapter 7

- Based on the first theoretical model, the pore diameters ranges were found to be at best 17 nm – 53 nm range.
- The second theoretical model, the best fit was 5.2 nm pore opening that tappers out to a central column of ranges 22 nm – 70 nm.
- The third model with a 5.23 nm internal contacts computed to have a 2.3 nm opening across the surface.

## 8.6. Chapter Summary

The chapter has demonstrated an electrochemical characterisation of the fabricated membranes. Utilising design elements from previous works was discussed in Section 8.1 detailing the required apparatuses for the corresponding characterisation.

Next, initial steps to devise an experimental setup using a pair of Ag/AgCl electrodes was discussed in Section 8.1.2 detailing the electroplating of silver, comparative potential test against pre-defined electrodes and the programming infrastructure to conduct potential sweeps were discussed. It was found that the electrode was sufficiently stable and exhibited good potential voltages against a standard calomel electrode. Next, we have conducted important preliminary

calibrations of the experimental setup in order to determine the optimum cyclic voltage sweep range, open circuit voltage range and the effect of shifting slope as a function of scan rate.

Subsequently, two commercially available track-etched pores with known pore diameters were characterised and the results have shown to be in an agreeable range with theoretical calculations. These initial tests have demonstrated that the both the measurement instrumentation and experimental setup have been manufactured to ascertain consistent and reliable results.

Finally the fabricated membranes were characterised using 3 theoretical models only 2 of which were conclusive. However the computations suggest that the pore diameters fabricated were found to be 17 nm – 53 nm range when using the cylindrical model and when considering the second theoretical model, the best fit was 5.23 nm pore opening that tappers out to a central column diameter of 22 nm - 70 nm. It was concluded that the third theoretical model may experience some mathematical over simplifications. Nevertheless the computations yielded a pore opening of 2.3 nm in diameter with a 5.2 nm diameter of inter-particle contact region with only 3000 pores.

To summarise, the results obtained from the prescribed characterisation technique has clearly demonstrated that the porous membranes procured from the fabrication process were indeed within the nanoscale ranges which provides some initial verification of this technology.

## Chapter 9: Summary and Conclusions

---

This chapter details and concludes the entire work completed during the course of the research. Additionally, possibilities of future work were also highlighted.

### 9.1. Final Summary

Efforts to develop a low cost novel method of fabricating polymeric nanoporous membranes have been explored. This was accomplished by first addressing established methods of fabrication previously employed by other scientist by identifying key design merits and limitations.

The limitations identified entailed the requirement of specialised equipment and materials in the micro-fabrication of solid-state membranes, the low size tuneable ranges of polymeric membrane fabrication and the limited operating conditions exemplified by organic nanopores.

Whereas the design merits highlighted were the low-cost fabrication method from track-etched membrane technology, thermoplastic nano-imprint lithography has demonstrated a fabrication method to template ordered uniformly shape nanopores and finally the size tuning capability from ion beam milling technology.

Understanding these specific requirements that encompass this technology, a manufacturing approach was established to implement important steps to procure our goals. The fabrication technique employed was relatively low in cost as only economically costed materials were ascertained membrane fabrication facilitating mass-production. Additionally, the technology also has the potential to control the effective size of the nanopore.

Several milestones can be identified in this project based on the involved challenges and their technical significance of the overall process. First, the surfactant coated superparamagnetic  $\text{Fe}_3\text{O}_4$  nanoparticles were synthesised adopting the standard methods to the project requirements. The particles were subsequently dispersed in a dispersed in a 1,6-Hexanediol Diacrylate (HDDA) monomer. At this step, a separate experimentation regime was conducted to determine the best surfactant coating conditions to ascertain a stable colloidal suspension of the nanoparticles in HDDA monomer. The latter was critical for obtaining high quality membranes.

Two different techniques of producing thin polymer layers were explored. One was based on the formation of a supported bubble membrane layer of the colloidal solution with subsequent polymerisation. Second approach involved the constraining the colloidal solution between two substrates with subsequent polymerisation under nitrogen atmosphere. The conducted research revealed the first method was prone to instabilities, therefore advocating the choice of the second method which was more robust. Where the experimental setup required for membrane production was designed and manufactured. This allowed forming and polymerising thin films with embedded nano-arrays under a controlled magnetic field and oxygen-free atmosphere.

The principle method of fabrication was based on the previous research findings in the field of magnetic field induced self-organisation of superparamagnetic

nanoparticles in colloidal solutions. With the help of the relevant theory this physical phenomena was exploited to create columnar arrays which were used to create embedded nano-templates in the polymeric material. The arrays then were subsequently removed by selective chemical etching leaving the system of parallel nanochannels in the polymeric film i.e. nanoporous membranes were created.

Completing the fabrication process, these membranes were systematically characterised using optical, scanning electron (SEM) and transmission electron microscopy (TEM). Our optical microscopy images results have shown that the etchant has successfully removed all embedded  $\text{Fe}_3\text{O}_4$  constituents which implies that the nanopores were procured. Additionally the resultant pore density was found to be in the average of  $2.66 \times 10^{10}$  pores/ $\text{m}^2$  for permanent magnet samples and  $9.48 \times 10^9$  pores/ $\text{m}^2$  for Helmholtz coil pair samples.

Revealing the exact morphology of the individual nanopore has proved to be a significant experimental challenge. Nevertheless special sample preparation methods were employed such as the ion milling technique (on polymers) that revealed a cross-sectional view in SEM imaging detailing the physical morphology of the pores which was consistent with the expected initial inference discussed in the previous chapter. The combination of all microscopy data allowed us to make a conclusion regarding most probable nanopore geometry.

In addition, ionic conductivity studies were employed to provide independent verification of the propagation of nanopores through the entirety of the thickness of the membrane. This required the fabrication of a specialised electrochemical cell to accommodate the membranes of interest equipped with a pair of silver-silver chloride (Ag/AgCl) electrodes. Next, current-voltage (I-V) measurements were taken through experimentation to ascertain the effective conductance of the system. The slope of the I-V curve was directly related to the conductance of the system. Measurements obtained were then compared with theoretical models as to obtain size approximations of channel openings. Our results have demonstrated that pores produced using this fabrication technique was indeed nano sized channels using the specific characterisation method. Which is was concurrent with the final aims and objectives with of the project.

## 9.2. Future work

Some revisions can be made to the fabrication methods employed in this research which might improve the resultant product.

- The exploring the option of annealing the structures while in its columnar state. This was attempted by Islam and co-workers (Islam, Lin, Lacoaste, Lubensky, & Yodh, 2003). They have reported to have induced equilibrium or steady-state structures by slowly cycling the field once maximum field was achieved. This cycling effect might have positive effect in terms of acquiring a denser packing of particles.
- A factor not investigated was the tuning of the size of the pores. This can be accomplished by further manipulation of the control factors that dictate the outcome of the size of the pores or the actual inherent size of the particles itself.
- With regards to the electrochemical characterisation, an alternative method can be used where the film is etched whilst being characterised. This meant that the ionic solution used was also the etchant. This method probably requires additional features to the flow cell such as electrode material which must be inert to the etchant. This method is advantageous as it can offer a better understanding towards percentage array propagation if the etchant only affect the sample for a single surface.
- A very useful tool for electrochemical characterisation is an electrical conductivity meter. It important to obtain the exact conductivity of the test electrolytes as it was the main contributing factor that determined the size of the nano-channels.

## 9.3. Conclusions

The following work has presented clear aims and objectives in the attempts to develop nanoporous polymeric membranes using self-assembled magnetic nanoparticles as templates. This was accomplished through the brief review of the current fabrication techniques then extracting their design merits and limitations and incorporating these elements into our design.

The fabrication methods employed here were cost effective with respect to other more established commercial methods which highlight the viability of this technology.

Our preliminary analyses have indicated that pores produced were indeed in the nanoscale range which encompasses the microscopy techniques coupled with image post processing methods and finally involving electrochemical characterization methods which has base knowledge of the developed technology.

# Appendix: Chapter 5

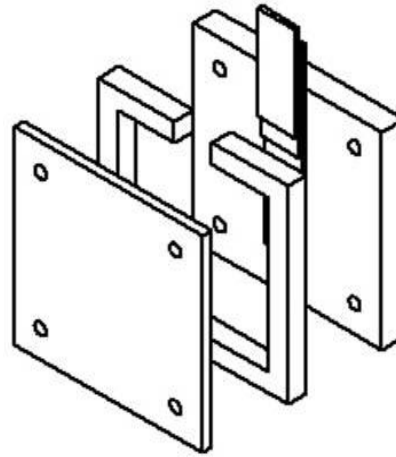
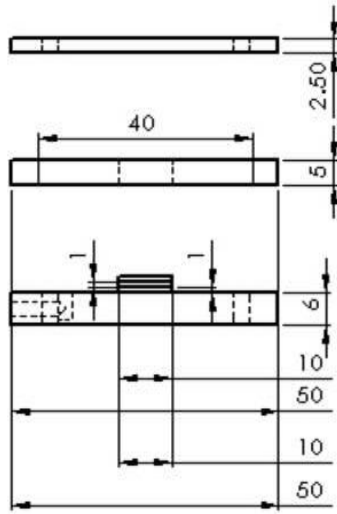
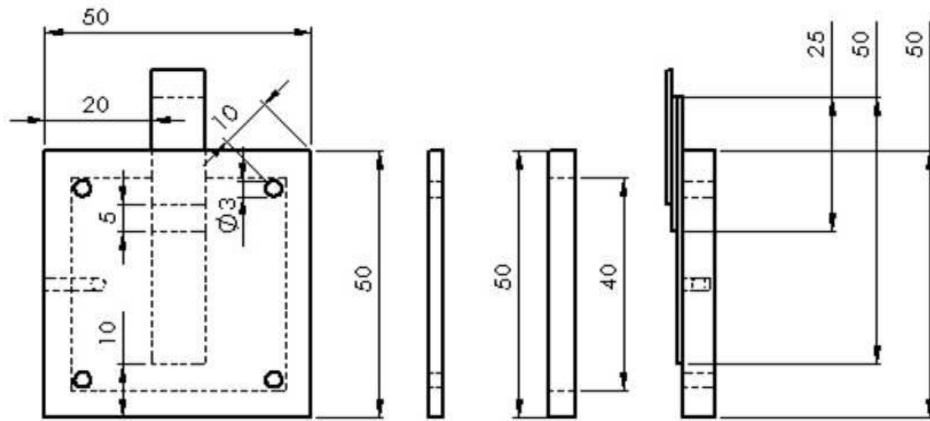
---

## **Specimen Containment Unit**

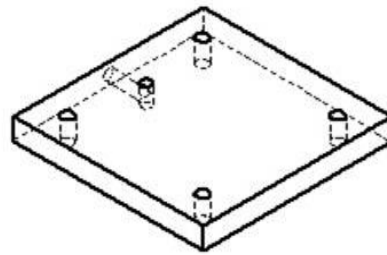
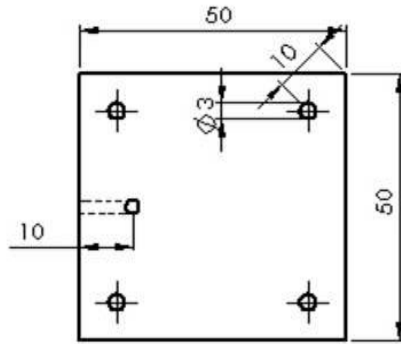
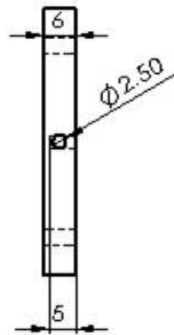
The specimen housing unit was constructed using these materials

- Two 50 mm × 50 mm × 6 mm polycarbonate pieces forming the base
- Two 26 mm × 10 mm × 1 mm glass pieces
- One 26 mm × 40 mm × 1mm glass piece forming the glass receptacle
- 1 mm diameter silicone tubing (50 mm long) for the nitrogen gas inlet
- 10 mm thick silicone RTV 360 pieces forming the walls of the housing

All relevant drawing of the housing are presented below:

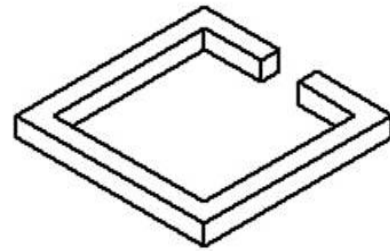
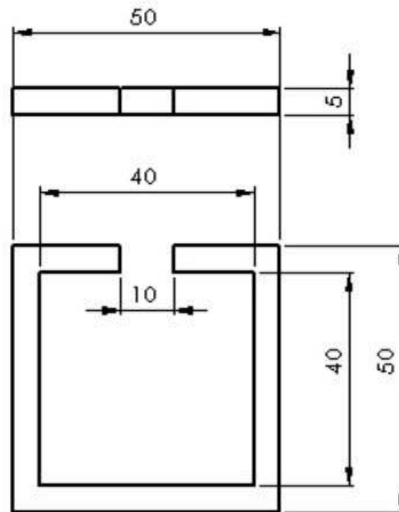


UNITS OF TENSORS SPECIFIED:				TENS-		DIPLO AND		DO NOT SCALE DRAWING		RTVSDP	
DIMENSIONS ARE IN MILLIMETERS						SCALE AND					
SURFACE FINISH:						EDGE SHARP					
FOR FINISH:						EDGES					
TYPICAL:											
ANGULAR:											
NAME		SIGNATURE		DATE		TITL		<h1>Housing Assembly</h1>		<span style="font-size: 2em;">A4</span>	
DRAWN											
CHECKED											
APPROVED											
DATE											
MATERIAL				DWG NO		SCALE: 1:1		SHEET 1 OF 1			
WEIGHT											



UNITS OF MEASURE SPECIFIED: DIMENSIONS ARE IN MILLIMETERS				FINISH:		DIPED AND EDGE SHARP EDGES		DO NOT SCALE DRAWING		REVISION	
SURFACE FINISH: TEXTURE: ANGLE:											
NAME		SIGNATURE		DATE						TITLE	
DRAWN										<h1 style="text-align: center;">Housing Base</h1> <h2 style="text-align: center;">Part1</h2>	
CHECKED											
APPROVED											
MFG											
Q.A.						MATERIAL: Polycarbonate		DWG NO		A4	
						WEIGHT:		SCALE: 1:1		SHEET 1 OF 1	





UNITS OF MEASURE SPECIFIED:				FINISH:		DRESS AND BEVEL SHARP EDGES		DO NOT SCALE DRAWING		FITTED	
DIMENSIONS ARE IN MILLIMETERS											
SURFACE FINISH:											
CORNER RADIUS:											
TOLERANCE:											
ANGULAR:											
DRAWN		NAME	SIGNATURE	DATE		TITLE					
CHECKED						Housing Wall Seals					
APPROVED											
MFG						MATERIAL		DWG NO		A4	
						Silicone RTV 630		Part3			
						WEIGHT		SCALE 1:1		SHEET 1 OF 1	

## Theoretical Computations

The equations for the Helmholtz pair were duly sourced from equations derived by Dennison (E.Dennison, 2005). The rationale behind this was to formulate a simple and elegant solution in order to provide a close estimation to the magnetic field strength without the use of complex commercially available FEA software. The equation begins with the formulation of an on-axis field caused by a single loop interpreted from the Biot-Savart law derived in Equation 5A Note that the equation only holds true if a constant current supply is present within the wire loop. To provide a clearer picture of the Figure 5A was provided to present the reader a clearer description. The direction of current flow is dictated by the • symbol which indicates the current flowing outwards and subsequently the × symbol denotes the inverse. Additionally the resultant polarity of the system is determined using the Right-hand rule. The following equations and diagrams are referenced from E. Dennison (E.Dennison, 2005) with supporting notes from D.B. Montgomery et al. (D.B. Montgomery, 1961).

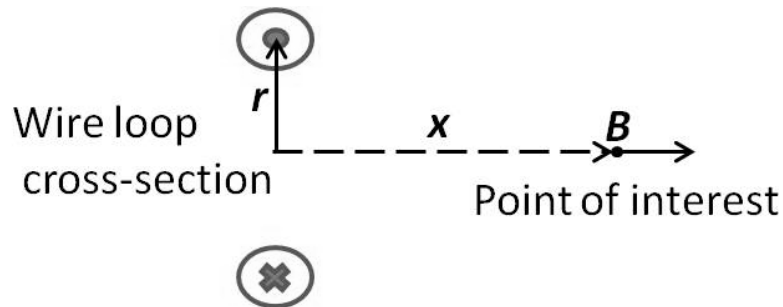


**Figure 5A: Cross-sectional view of a single wire loop**

$$B = \frac{\mu_0 i r^2}{2(r^2 + x^2)^{3/2}}$$

**Equation 5A: Equation for an on-axis field caused by a single wire loop**

The variables:  $B$  is the magnetic field strength from the wire loop along the axis perpendicular to the loop measured in T,  $\mu_0$  is the relative permeability constant valued at  $4\pi \times 10^{-7}$  Tm/A,  $i$  is the current supplied in the circuit,  $r$  is the radius of the wire loop and  $x$  is the on-axis distance measured from the middle plane of the wire loop to the point of interest. Note that variables  $\mu_0$ ,  $r$  and  $x$  must be in the

same units of a measurement (SI units). Progressing on, if one should include additional known amount of loops or windings then the system is considered a finite thin shell solenoid. Figure 5B and Equation 5B illustrated below exemplifies this.

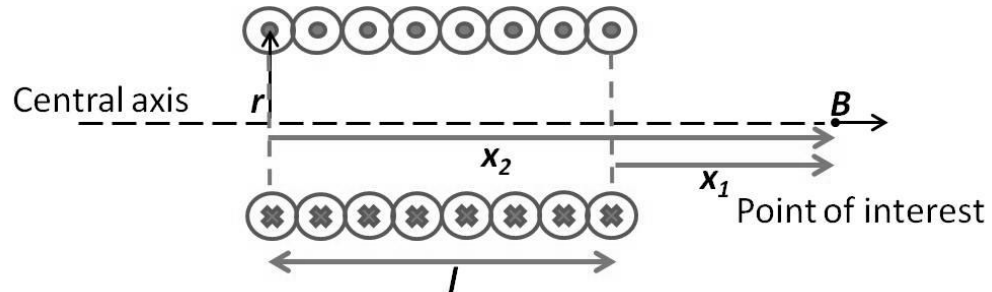


**Figure 5B: Cross-sectional view of a finite thin shell solenoid**

$$B = \frac{\mu_0 i N}{2l} \left( \frac{x_2}{\sqrt{x_2^2 + r^2}} - \frac{x_1}{\sqrt{x_1^2 - r^2}} \right)$$

**Equation 5B: Equation for an on-axis field for a finite thin shell solenoid**

The variables:  $N$  is the number of windings within the solenoid,  $l$  is the total length of the solenoid,  $x_1$  is the distance measured from the nearest end of the solenoid to the point of interest,  $B$  and  $x_2$  is the distance measured from the furthest end of the solenoid to the point of interest,  $B$ . Now, let's consider when more loops are added to form a thicker solenoid.

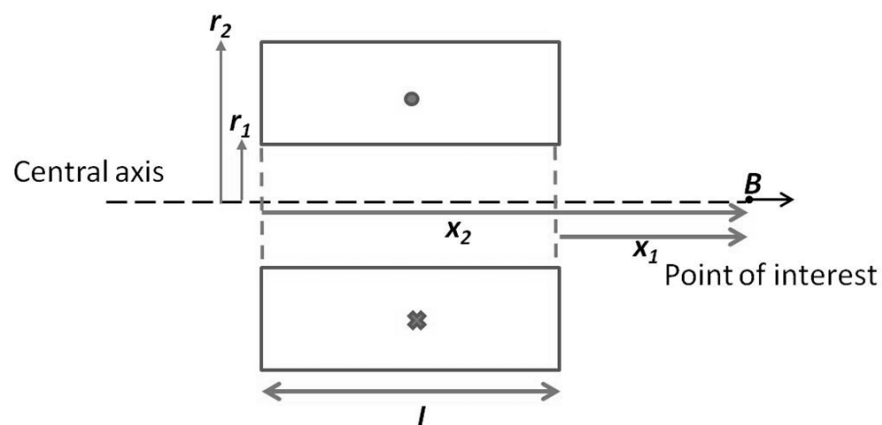


**Figure C: Cross-sectional view of a finite thick solenoid**

$$B = \frac{\mu_0 i n}{2(r_2 - r_1)} \left( x_2 \ln \frac{\sqrt{r_2^2 + x_2^2} + r_2}{\sqrt{r_1^2 + x_2^2} + r_1} - x_1 \ln \frac{\sqrt{r_2^2 + x_1^2} + r_2}{\sqrt{r_1^2 + x_1^2} + r_1} \right)$$

**Equation C: Equation for an on-axis field caused by a finite thick solenoid**

The variables:  $r_1$  and  $r_2$  respectively are the radius measured from the central axis of the solenoid to the inner- and outer-most coil winding and  $n$  number of turns or wire per unit length within the solenoid. Progressing on, let's consider the Helmholtz coil pair system simplified into two equal radii connected in series and separated from each other at a distance equal to its respective radius illustrated in Figure 5D.

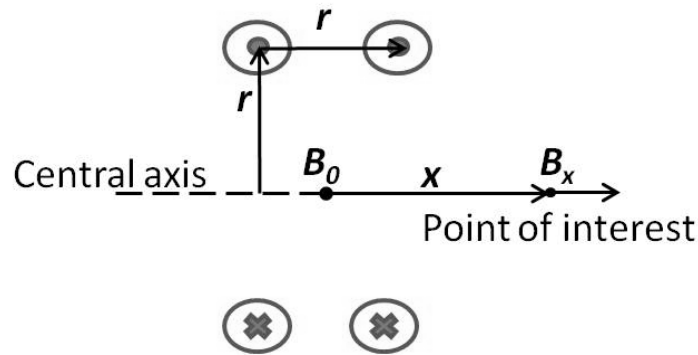


**Figure 5D: Cross-sectional view of a simplified Helmholtz coil pair system**

The variables:  $B_0$  is the magnetic field strength from geometric centre between the two coil windings (usually the area of interest) and  $B_x$  is the on-axis field magnetic field strength at that specific to that individual point. The equation for this system can derived from Equation 5D where the system if viewed as two single wire loops separated at distance  $r$ . Since there are two single wire loops in the system the magnetic field strength subjected in point  $B_0$  is twice as strong. Additionally, it is possible to change the point of interests for analysis;  $B_x$  is now situated in between the two loops and hence can be termed as  $r/2$  derived below.

$$B_0 = \frac{2\mu_0 i r^2}{2 \left( r^2 + \left( \frac{r}{2} \right)^2 \right)^{3/2}}$$

**Equation 5D: Equation derived for a simplified Helmholtz coil pair system**

The derivation of Equation 5D is the on-axis field strength for an equivalent single wire loop Helmholtz coil pair system. However to realistically a Helmholtz pair

usually comprises of more than a single wire loop as higher field strengths are usually required. Therefore, the variable  $n$  should be added to the equation taking to account the number of turns within a wire loop demonstrated in Equation E with its equation simplification.

$$B_0 = \frac{2\mu_0 n i r^2}{2 \left( r^2 + \left( \frac{r}{2} \right)^2 \right)^{3/2}}$$

$$\therefore B_0 = \left( \frac{4}{5} \right)^{3/2} \left[ \frac{\mu_0 n i}{r} \right]$$

**Equation E: Equation for the on-axis field strength at the geometric centre of an ideal Helmholtz coil pair system**

Now, to derive the on-axis field strength of the system at any point along the axis, some geometric considerations are needed. To demonstrate the derived equation for the on-axis field strength of any point along the central axis, Equation 5F is presented below.

$$B_x = \frac{\mu_0 i n}{2r} \left[ \frac{1}{\left( \gamma^2 + \gamma + \frac{5}{4} \right)^{3/2}} + \frac{1}{\left( \gamma^2 - \gamma + \frac{5}{4} \right)^{3/2}} \right]$$

**Equation F: Equation for the on-axis field strength of any point along the central axis of an ideal Helmholtz coil pair system**

The variables:  $\gamma$  is the ratio between the distance measured between the geometric centre of the two coils and the radius of the coils. Equation 5E and Equation 5F demonstrates the equation for an ideal Helmholtz coil system. The term ideal is used because the equation is an over-simplification of the system without taking into consideration the size and geometry of the coils itself. However to further expand the equations similarly derived in Equation 5B and Equation 5C would require more complex equations and thus increasing the probability of errors that may occur during computation. For this, another equation is derived from the supporting notes of D.B. Montgomery (D.B. Montgomery, 1961) and simplified by E. Dennison (E.Dennison, 2005) where it introduces additional variable of power and the unit-less geometric factor, G-factor (E.Dennison, 2005). This solution is advantageous as the system is derived as a finite Helmholtz coil system with the

coil size and relevant physical variables taken into consideration. The solution is derived as Equation 5G.

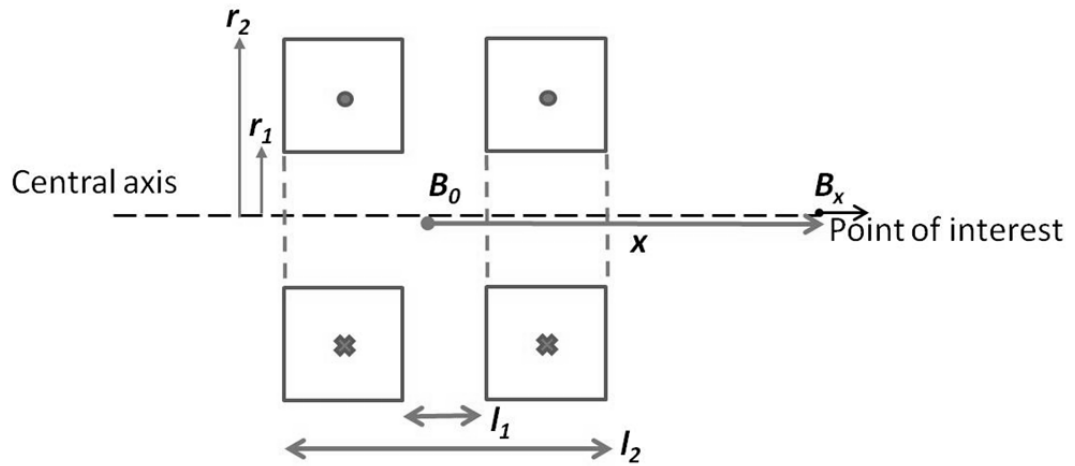


Figure 5E: Cross-sectional view of finite Helmholtz coil pair system

$$B_x = \mu_0 \sqrt{\frac{P\lambda}{r_1\rho}} G$$

Equation 5G: Derived solution for on-axis field strength at any point along the concentric axis for a finite Helmholtz coil pair system (E.Dennison, 2005) & (D.B. Montgomery, 1961)

The variables:  $l_1$  and  $l_2$  respectively are the distances between the inner- and outer-most coil winding of the system,  $P$  is the total power consumed,  $\rho$  is the conductor resistivity,  $\lambda$  is the ratio between the total conductor cross-section area and the total coil cross-section area and finally  $G$  is the unit-less geometric factor of the system. The  $G$ -factor is determined by shape and size of the coils. The  $G$ -factor equations were derived and compiled by D.B. Montgomery et al. (D.B. Montgomery, 1961) and can be found their work. In his work, E. Dennison (E.Dennison, 2005) has simplified and derived the equation for a dual coil system with square ends illustrated above.

$$G = \sqrt{\frac{1}{8\pi(\alpha^2 - 1)(\beta_2 - \beta_1)}} \left[ \begin{array}{l} +(\gamma + \beta_2) \ln \frac{\alpha + \sqrt{\alpha^2 + (\gamma + \beta_2)^2}}{1 + \sqrt{1 + (\gamma + \beta_2)^2}} \\ -(\gamma + \beta_1) \ln \frac{\alpha + \sqrt{\alpha^2 + (\gamma + \beta_1)^2}}{1 + \sqrt{1 + (\gamma + \beta_1)^2}} \\ +(\gamma - \beta_1) \ln \frac{\alpha + \sqrt{\alpha^2 + (\gamma - \beta_1)^2}}{1 + \sqrt{1 + (\gamma - \beta_1)^2}} \\ -(\gamma - \beta_2) \ln \frac{\alpha + \sqrt{\alpha^2 + (\gamma - \beta_2)^2}}{1 + \sqrt{1 + (\gamma - \beta_2)^2}} \end{array} \right]$$

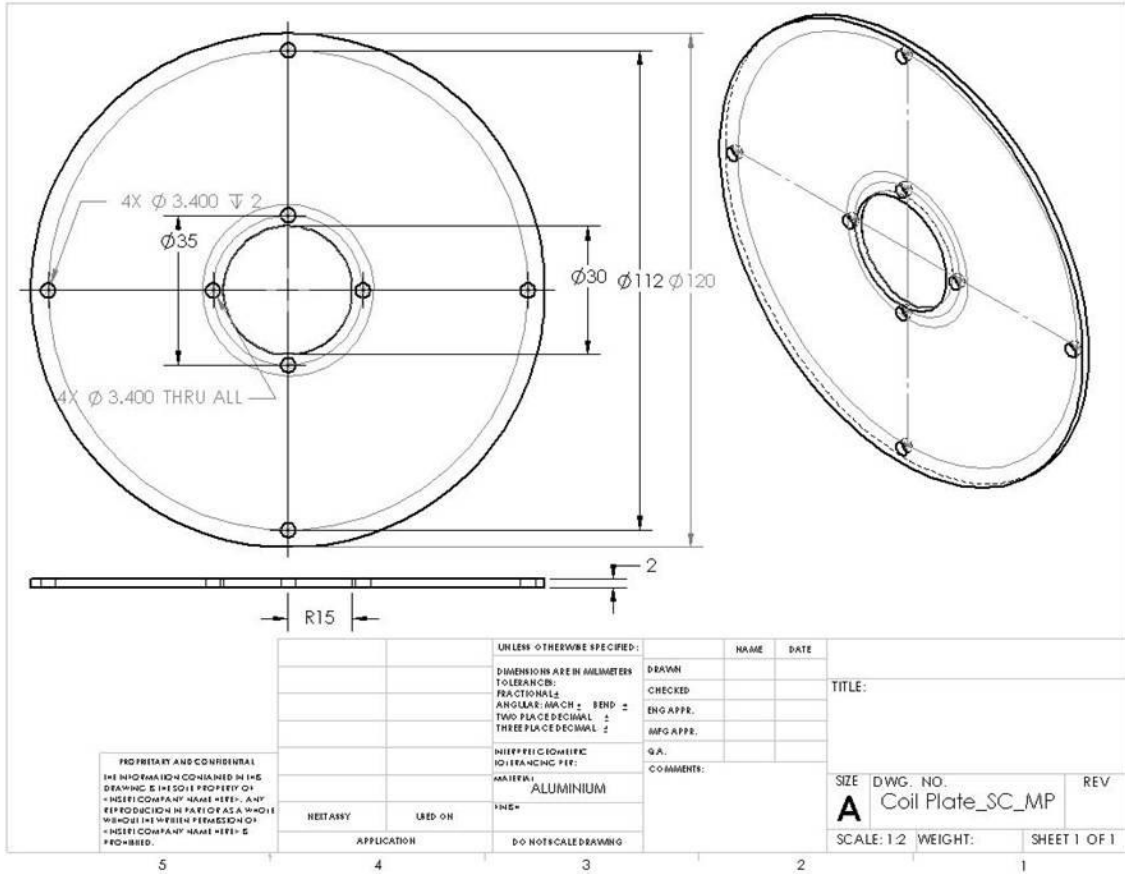
The variables:  $\gamma = \frac{x}{r_1}$   $\alpha = \frac{r_2}{r_1}$   $\beta_1 = \frac{l_1}{2r_1}$   $\beta_2 = \frac{l_2}{2r_1}$

**Equation 5H: Equation to determine the G-factor of a square-ended Helmholtz coil pair system**

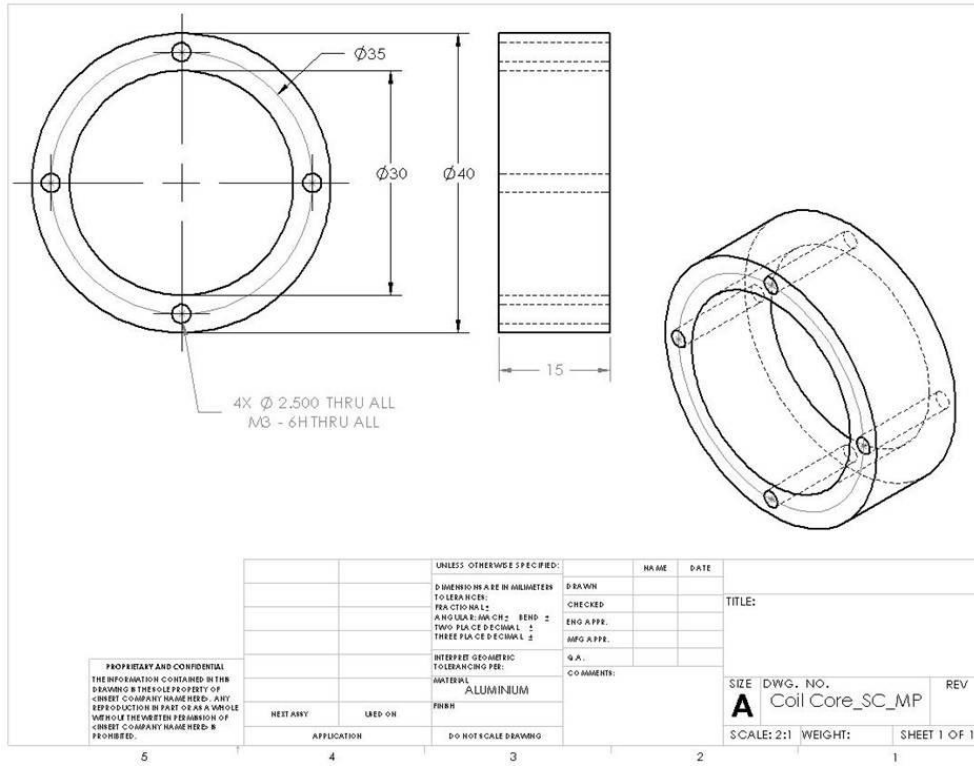
## **Multi-piece Design of Helmholtz Coil Pair system**

Presented below are the parts from the multi-piece coil assembly used for experimentation. The coil consists of:

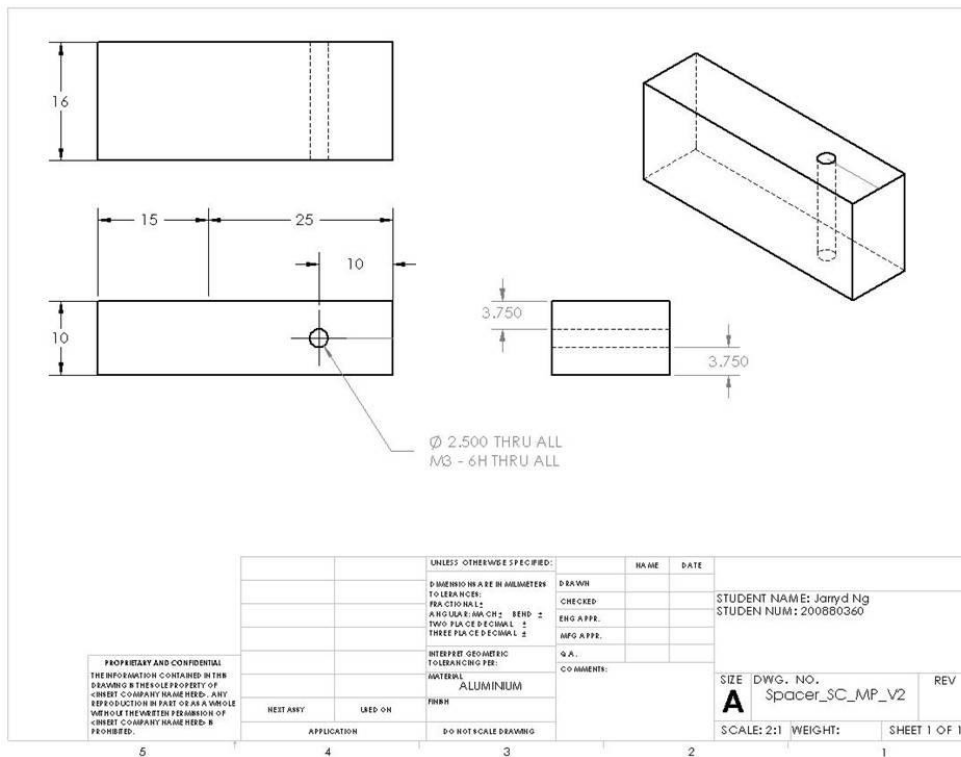
# 4 coil plates



## 2 coil cores



## 4 coil spacers



# LabVIEW Programming Infrastructure

Illustrated below is a flow diagram that describes control system design for the Helmholtz coil pair system.

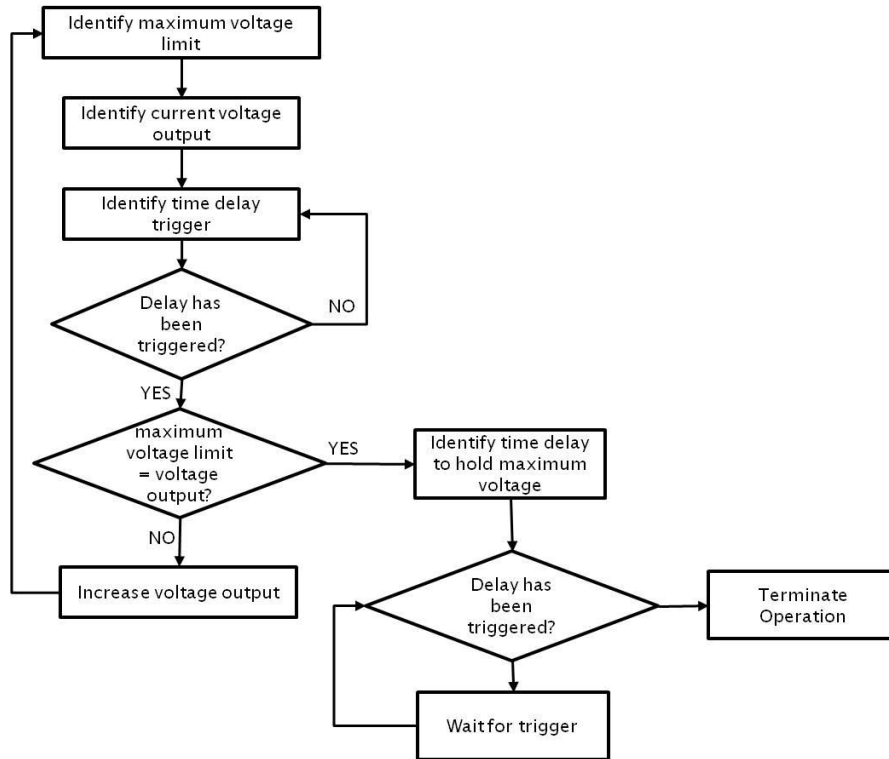
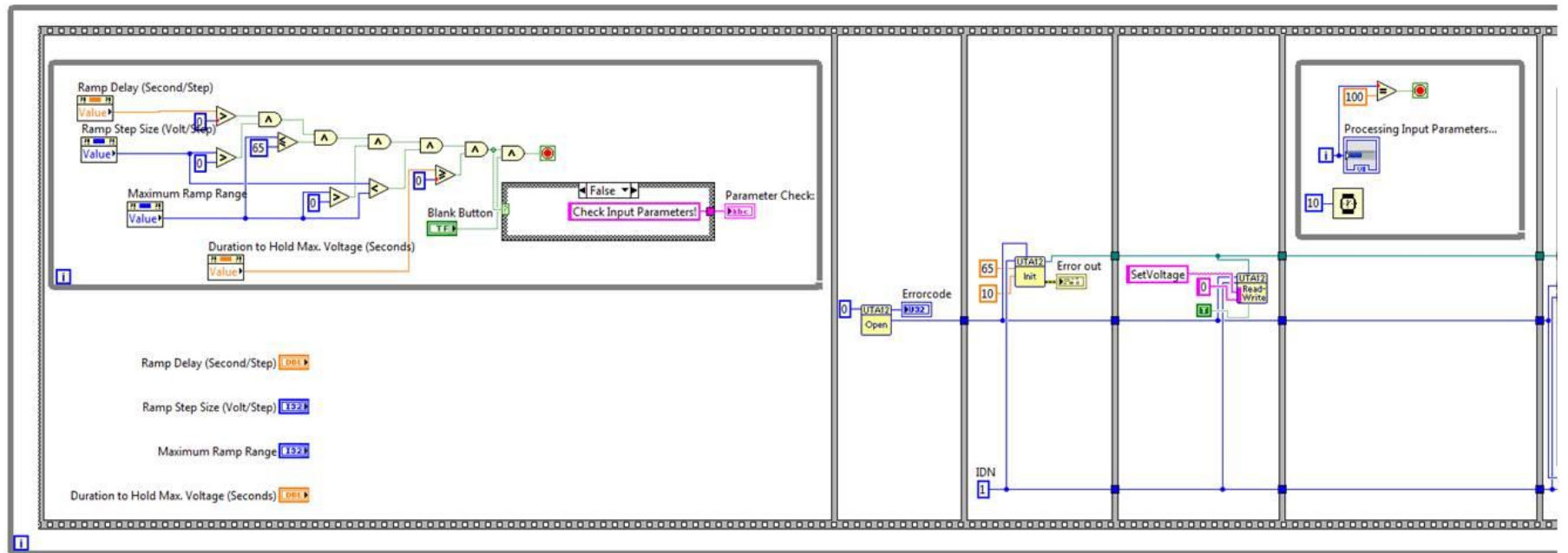


**Figure 5F: Flow diagram based on the control system designed for the programmable DC power supply**

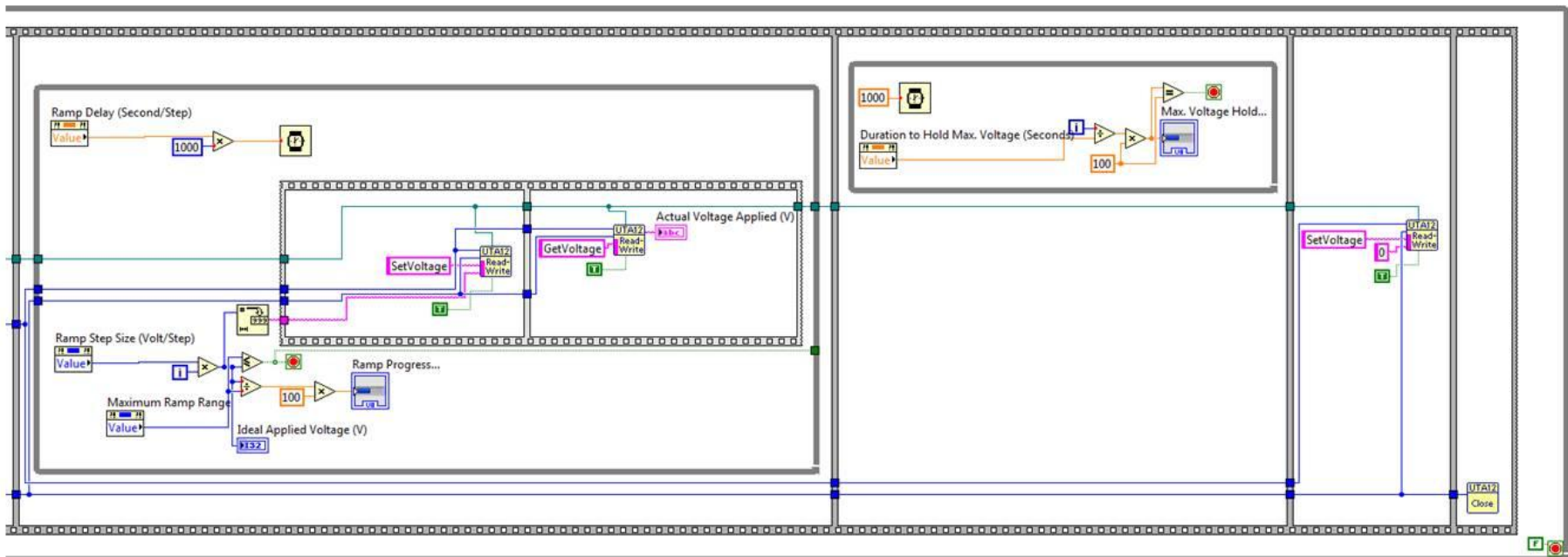
The control system begins with identifying parameters such as the maximum voltage limit, the voltage increment and time delay for each increment. It then increases the voltage output according to the increment size, starts the delay countdown, checks the countdown is over then changes the voltage output again. The minimum step size is 1 V and can only go by 1 V increments. As soon as the voltage output reaches the maximum voltage limit, it then checks the time delay to hold the maximum voltage and waits for the trigger. As the second time delay triggers the program will terminate the operation.

# LabVIEW Control System for the Helmholtz Coil System



Continued

Continued

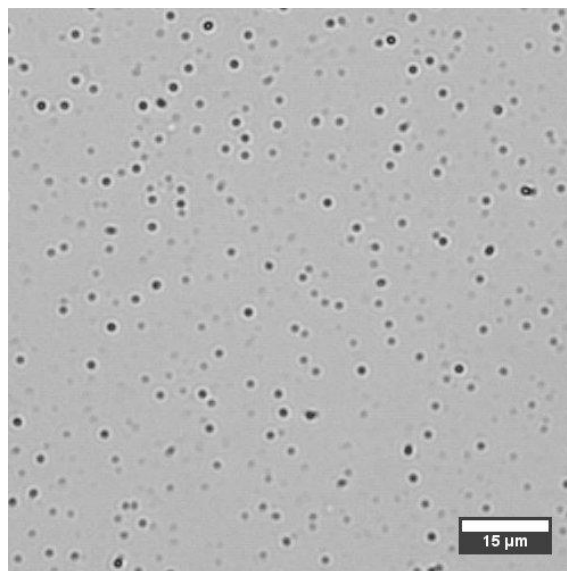


# Appendix: Chapter 7

---

## Optical Microscopy Analysis: Image Thresholding

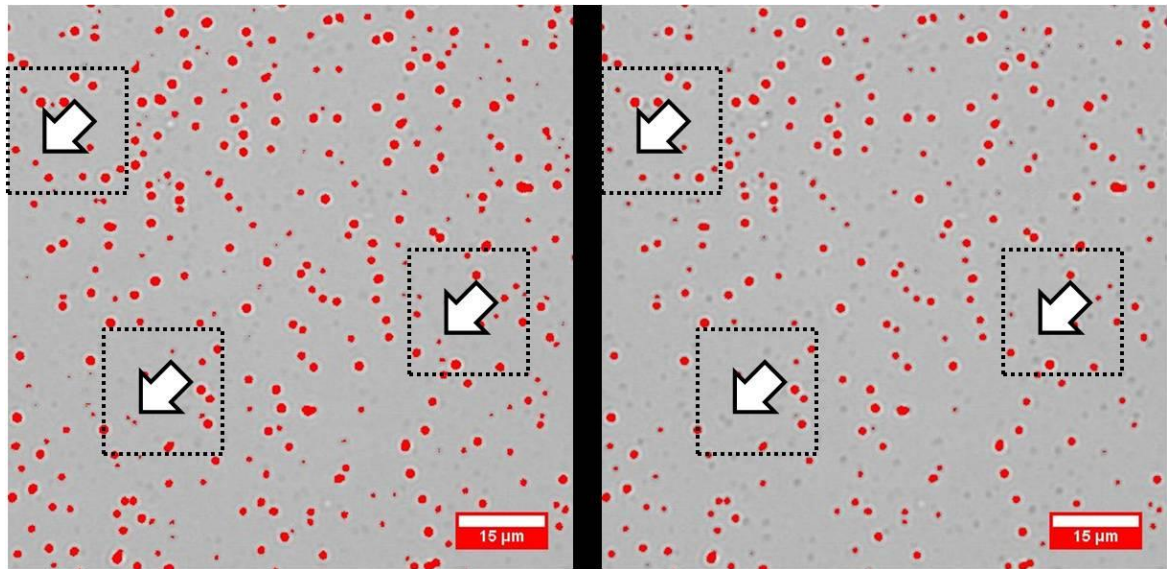
The thresholding technique was accomplished using the threshold image feature provided by ImageJ. The entirety of the samples analysed via OM were initially put through the conversion process prior to operating any macro functions. However, there were some discrepancies found by using this technique. One such quandary was the accuracy of the thresholding function itself due to some of the array featured in the cropped regions tend to have a lower contrast than others. Differences in contrast between arrays are an indication of dissimilar propagation conditions of the respective arrays during application of the external magnetic field hence causing the arrays to be immobilised at different depths subsequent to the monomer solution curing. Therefore arrays that appear darker in comparison to the background are better propagated through the film thickness and vice versa. As a result, less prominent and lesser propagated arrays tend not to be detected by the function Figure 7A demonstrated below is an example of the description above.



**Figure 7A: Original 500 x 500 square pixel image prior to thresholding**

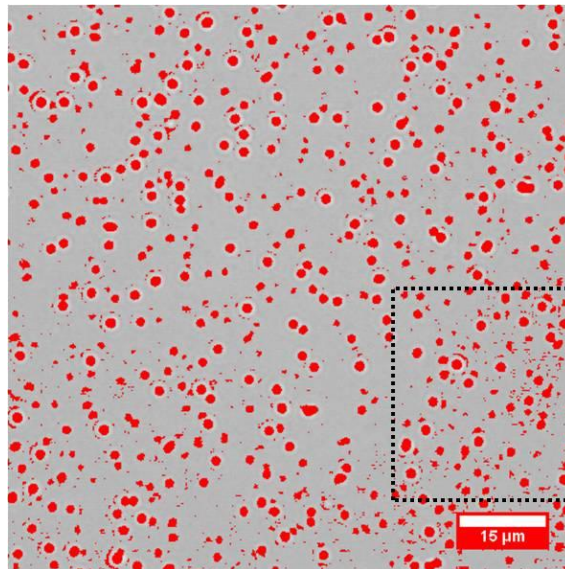
Conversely, it is understood that there are different intensities of contrast and classifying the state of array propagation from these form of discrimination will in

effect cause errors. The solution for this was to manipulate the threshold limits via increasing the detection sensitivity. This meant that a wider range of contrast intensities should be detected illustrated in Figure 7B.



**Figure 7B: (Left) Threshold limit rectified image (Right) Default setting of threshold limit**

Figure 7B above illustrated in red to provide the reader a clearer differentiation between the background and arrays present in the material. The final image generated from the thresholding process can be found in Figure 7C. This method however is a double edge sword because as the increase in detection sensitivity has a higher probability to pick up image noise and thus skewing the true number of arrays being counted and analysed.



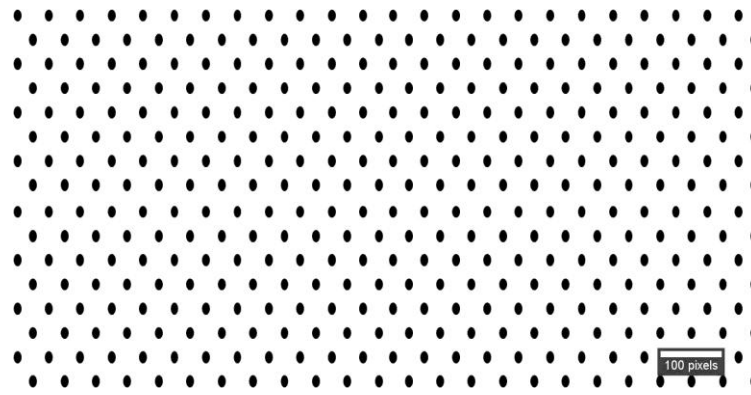
**Figure 7C: Signs of image noise occurring due to high sensitivity of detection**

Figure 7C presented above is an exemplar of the effects of an over sensitive array detection. The image noise generated here causes the macro used in later sections to produced falls results. This is due to the additional entities on the image that the macro has to analyse. However this problem can be rectified by strict scrutiny of over the image during the thresholding process to find the perfect balance between actual arrays to be represented and noise to be avoided in efforts not to skew the results.

## **ImageJ Image Analysis Tool: Radial Average**

### **Autocorrelation Function**

This is followed by the radial averaged autocorrelation macro analysis using ImageJ. Prior to the actual analysis a calibration sample was made for result validation purposes. For this, the calibration sample was made using a simple design that resembled a polka dot design of known inter-dot distances. Figure 7D below demonstrates the aforementioned calibration sample.



**Figure 7D: Polka dot design of calibration sample at a 50 pixel distance from each dot**

An initial trial of the radial averaged autocorrelation macro was conducted which yielded the plot Figure 7E To make sense of the obtained plots, one must refer to the description provided by the ImageJ Information and Documentation Portal provided via the main website (Ferreira & Rasband, 1997). For simplicity sake, the description can be condensed to the information regarding the inter-element distances which can be found as the first side maximum of the plot.

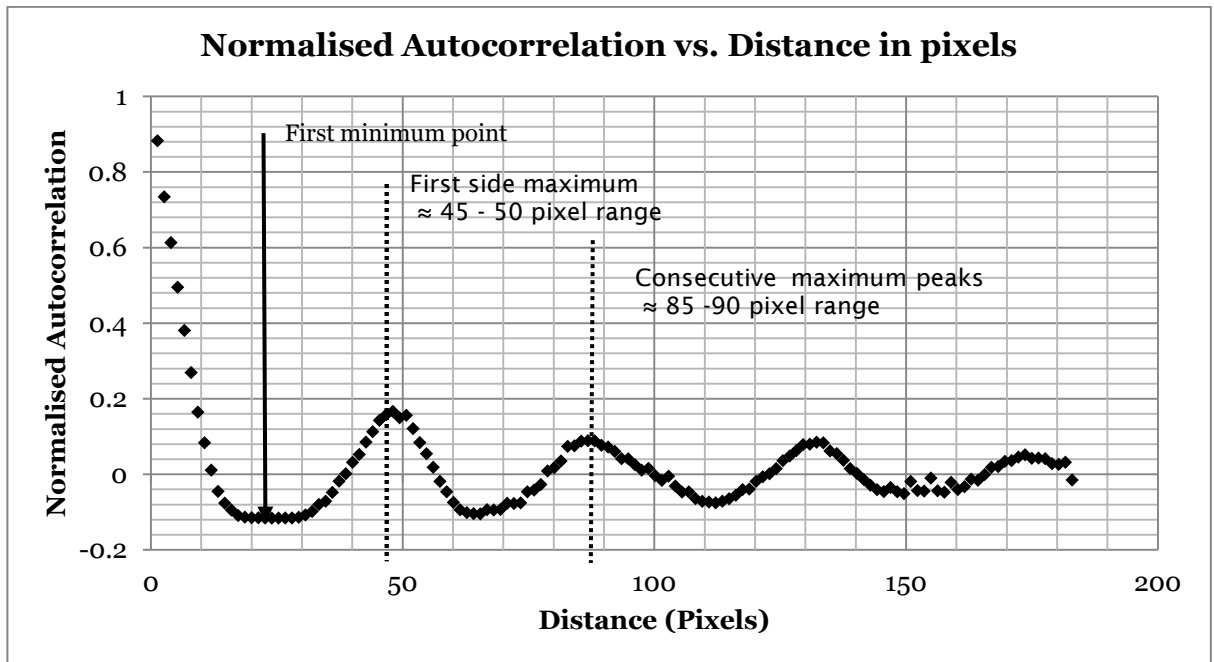


**Figure 7E: A radial average autocorrelation plot produced by the aforementioned ImageJ macro function**

The first side maximum of the plot can be explained as the first positive peak subsequent to the first negative minimum point. The location of the first side maximum along the X-axis provides information regarding the inter-element

distances. Hence reviewing the plot in Figure 7E it is clear that the first side maximum resides on the 45- 50 pixel range along X-axis. Additionally the subsequent peaks in the plot represent the second closest dot to each other which on closer inspection was found accurate. To summarise, the radial averaged autocorrelation macro function was proved suitable for the investigation.

# Appendix: Chapter 8

---

## **Cyclic Voltammetry: An Introduction**

Cyclic voltammetry is defined as a technique to analyse and characterise electrochemical reactions in the study of electro-active species. This chemical analysis has proven to be highly versatile whilst providing ease of measurement has paved its way into various fields of chemistry (Kissinger & Heineman, 1983) whilst demonstrating its robustness of design and potential applications in other various fields (Mabbott, 1983). One important feature of the technique is the capability to enable the experimenter to quickly observe the redox behaviour over a predetermined potential range. The redox is an abbreviation derived from the chemical reactions of reduction and oxidation. The term describes the chemical reaction of a molecule either losing or gaining electrons. Oxidation is the act of a molecule losing an electron charge hence its oxidation number increases whilst reduction is the act of a molecule gaining an electron charge, decreasing its oxidation number. Returning to the initial definition of cyclic voltammetry, it is made clear now that the electro-active species in a chemical reaction undergoes the aforementioned redox reaction.

## **The Cyclic Voltammetry Fundamentals**

The basic concept of the experimentation comprises of providing a cyclic voltage excitation across two silver/silver chloride (Ag/AgCl) electrodes immersed in an electrolyte. The resultant reaction of the redox species can then be analysed by measuring the resultant current obtained from the experiment. The excitation signal is a linear sweeping scan relative to the allocated time frame. This sweeping scan can also be defined as the switching potential (Kissinger & Heineman, 1983) demonstrated below.

Time (Seconds)	Applied Potential (Volt)
0	0.1
10	0.05
20	0
30	-0.05
40	-0.1
50	-0.05
60	0
70	0.05
80	0.1
90	0.05
100	0
110	-0.05
120	-0.1
130	-0.05
140	0
150	0.05
160	0.1

Figure 8A: Example of excitation voltage in a cyclic voltametry experiment

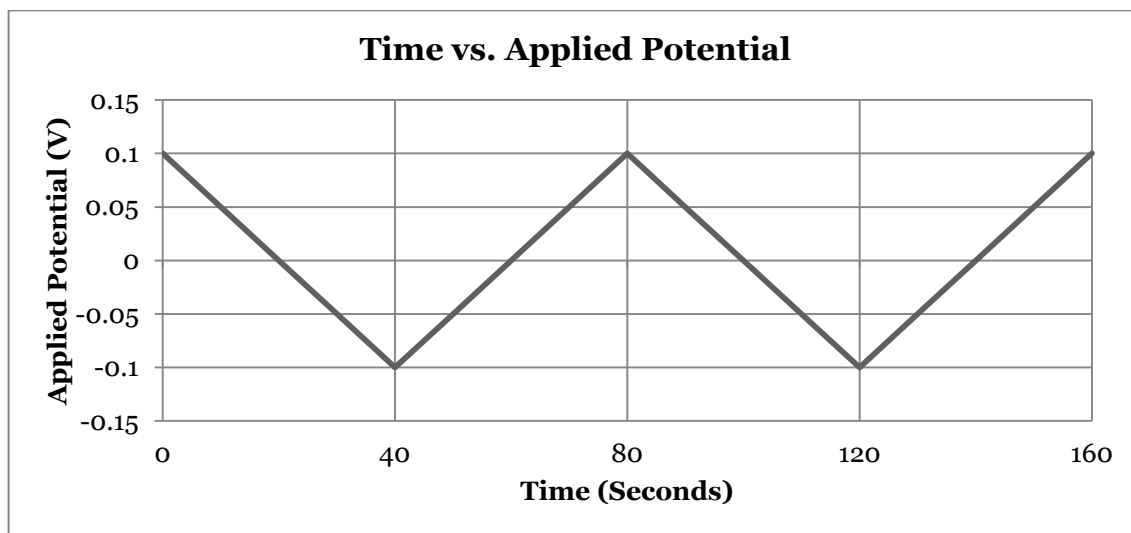
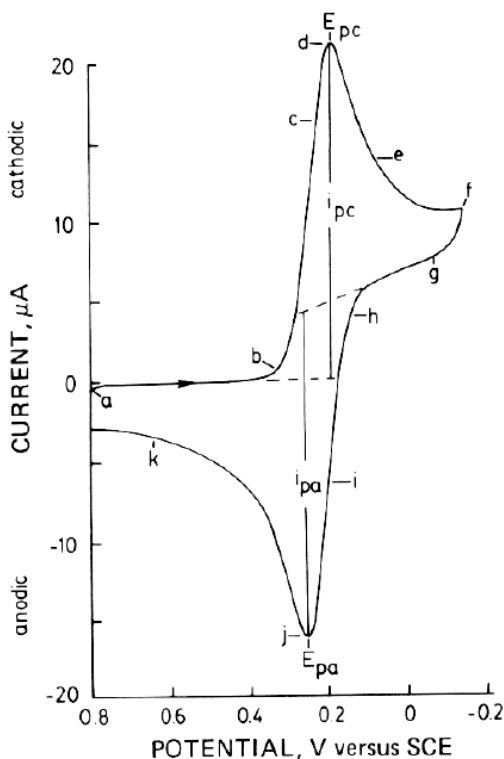


Figure 8B: Plot of excitation potential relevant to Figure 8A

From Figure 8B the excitation potential can be described as a negative forward scan. Consequently, a cyclic voltammogram can be obtained by measuring the current response from the scan at the electrode. The voltammogram is typically illustrated in a current versus situated on the vertical axis and scanning potential which is situated on the horizontal axis. Figure 8C is an example of a typical cyclic

voltammogram from the past works of Kissinger & Heineman (Kissinger & Heineman, 1983) which details the various parts of a cyclic voltammogram.



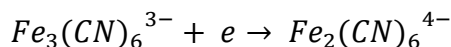
**Figure 8C: Cyclic voltammogram of 5nM  $K_3Fe(CN)_6$  in 1M  $KNO_3$ . Scan initiated at 0.8 V versus SCE (Saturated Calomel Electrode) in negative direction at 50mV/s. Platinum electrode, area=2.54 mm<sup>2</sup> (Kissinger & Heineman, 1983)**

Depicted Figure 8C, the cyclic voltammogram consist of ten elements each signifying the electrochemical causation of reduction and oxidation cycles and its corresponding current response from the system. It is important to note the potential scale of the plot whereby it is a descending scale rather than an ascending one. This is done to highlight the initial <sup>15</sup>*negatively, forward scan* scheme conducted during experimentation which explains the process chronologically. Since the excitation potential progresses in accordance with time, only then this can be seen as a logical step to present this data. Consequently, the current response signal indicates the redox reactions taking place.

The analysis would begin at point (a), the predetermined maximum amplitude which is below the electrolysis threshold. Moving along the potential axis (X-axis),

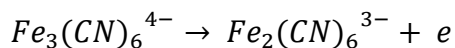
<sup>15</sup> A scanning regime thusly termed from the Kissinger and Hieneman (Kissinger & Heineman, 1983). The term implicates performing a descending potential sweep from its predetermined maximum amplitude whilst recording the current responses from the system.

it is apparent that the excitation potential drops causing the system attain a higher negative charge affinity. This affinity eventually builds up to allow the reduction process to take place designated at point (b). This is the designated threshold point whereby the reduction of the  $Fe_3(CN)_6^{3-}$  to  $Fe_2(CN)_6^{4-}$  demonstrated in Equation 8A.



**Equation 8A: Reduction equation for Ferricyanide species**

From here, the current response registers a noticeable steep increase from points (b) through (d) causing the drop of ferricyanide or  $Fe_3(CN)_6^{3-}$  concentration along the electrode surface. The peak at point (d) signifies the depletion of  $Fe_3(CN)_6^{3-}$  this causes the current to decay elements (d) to (f). At this point of time, the system scanning potential is alternated to an ascending sweep. The initial ascending scan indicates can be considered the inverse of elements (a) through (f) whereby the oxidation reaction of  $Fe_2(CN)_6^{4-}$  to  $Fe_3(CN)_6^{3-}$  takes place. Equation demonstrated below.



**Equation 8B: Oxidation reaction process which is the inverse of Equation 8A**

Again, the initial excitation potential gradually builds up a positive affinity elements (g) through (h). Then the system becomes sufficiently strong allowing the oxidation process to take place dropping the  $Fe_2(CN)_6^{4-}$  concentration along the electrode surface. This is depicted in the sharp decrease for the current response in elements (h) through (j). The eventual depletion point of  $Fe_2(CN)_6^{4-}$  at point (j) followed by its corresponding current decay in elements (j) through (k).

The information that can be gathered here is the approximated +0.4 V needed for the reduction of  $Fe_3(CN)_6^{3-}$  to  $Fe_2(CN)_6^{4-}$ . Inversely the reaction will also require the similar excitation potential to oxidise the  $Fe_2(CN)_6^{4-}$  back to  $Fe_3(CN)_6^{3-}$ . For the experimentation work at hand, it is imperative to define this range where the depletion of the redox reaction of ions is not wanted. The main focus is to solely observe and measure the passing ions through the membrane platforms.

## **LabVIEW™ Programming Architecture**

The in-house LabVIEW™ drivers and program examples for the Keithley 2400 source meter offers were found to be too simplistic for the requirements of the experimentation. Nevertheless these sources provided were still found useful as a foundation to build upon. Initially a programming flow chart was mapped out to ensure all requirements from the programming were met. To offer the readers a clearer picture, a <sup>16</sup>flow chart was devised for Mode 1, 2, 3 in Figure D, Figure E and Figure F respectively.

---

<sup>16</sup> The designed flow chart for all three figures was too big to fit in one page. Therefore it was it was systematically divided into 3 main compartments; Modes 1, 2 and 3.

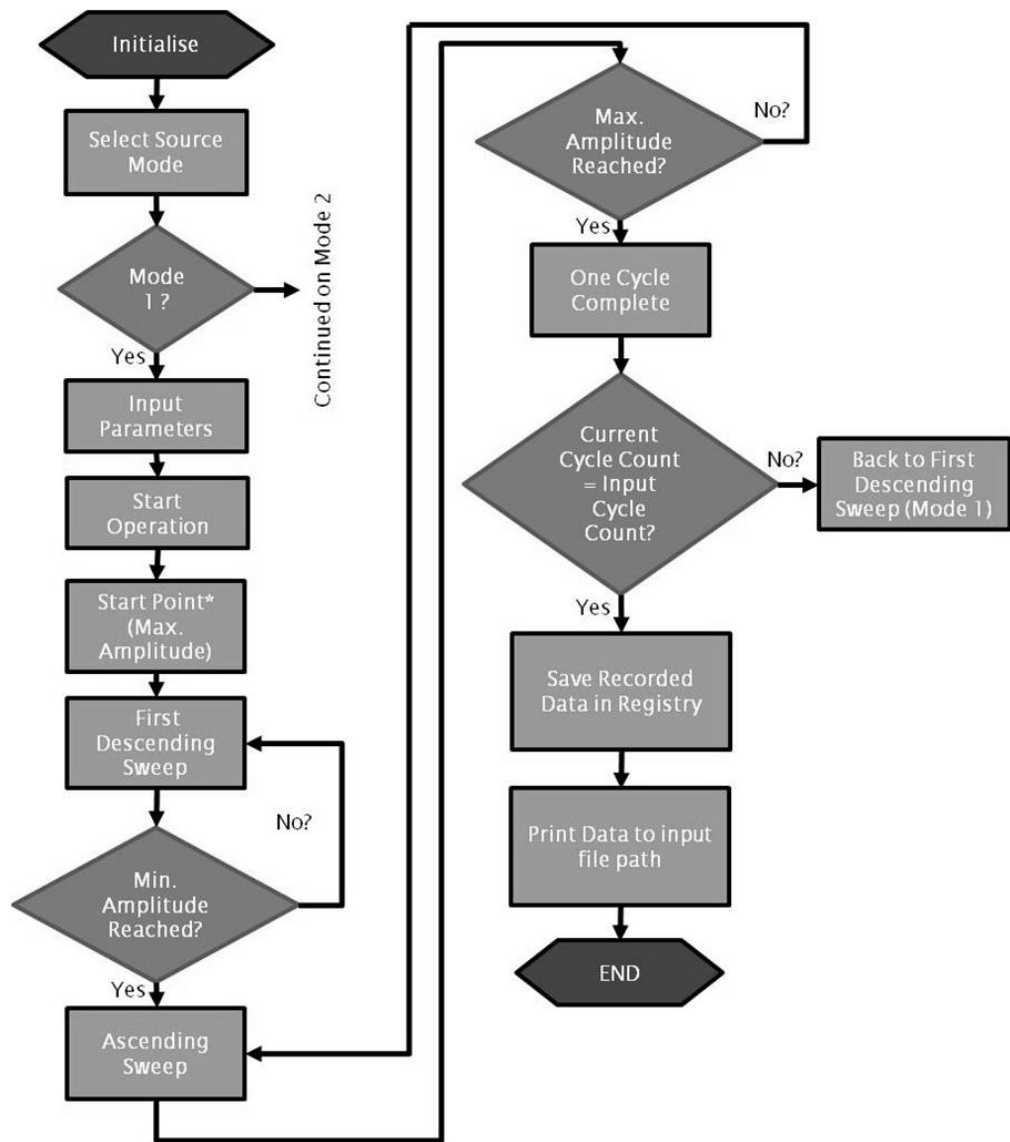


**Figure 8D: Programming flow diagram design for Mode 1**

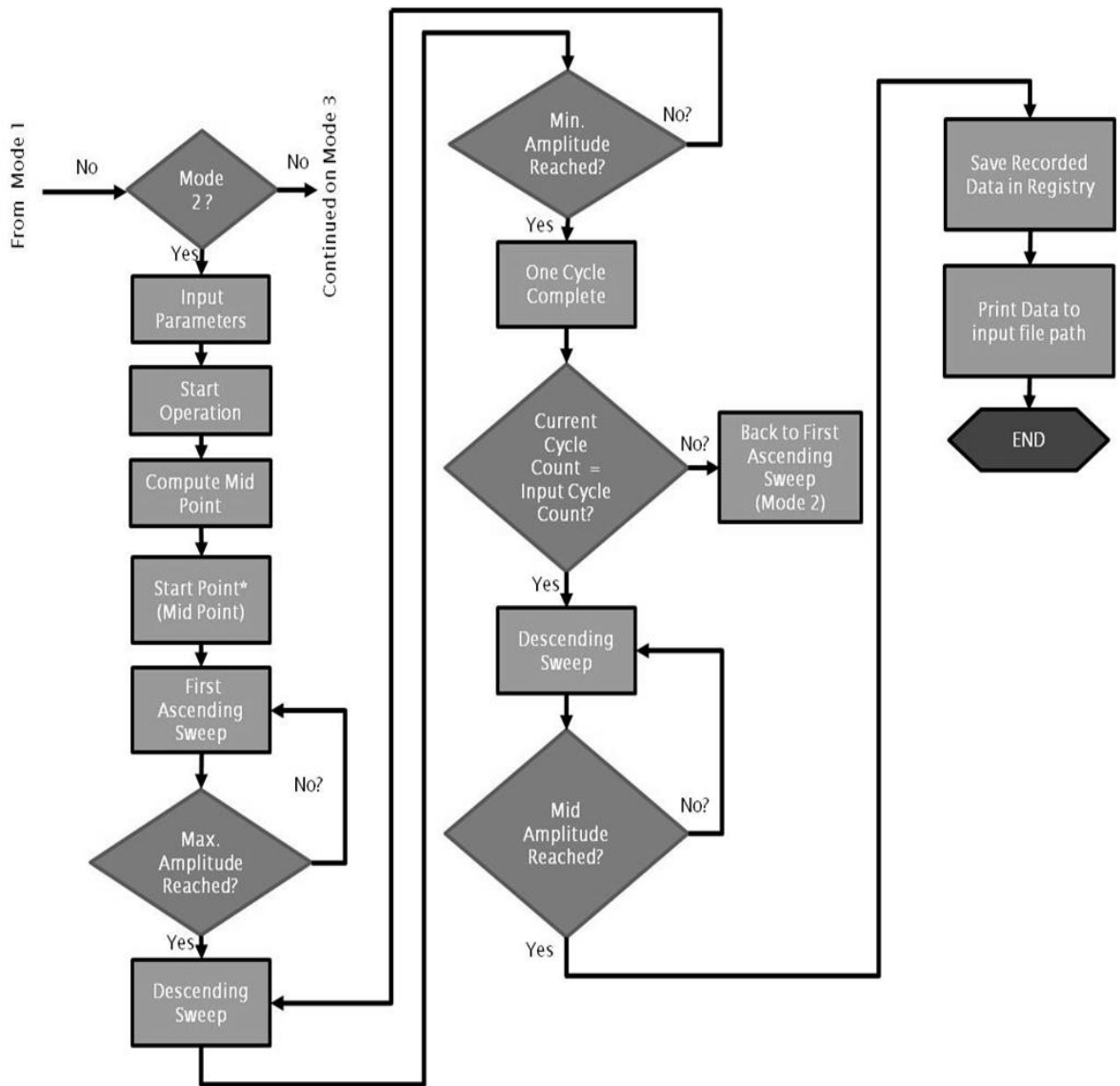


**Figure 8E: Continued programming flow diagram for Mode 2**

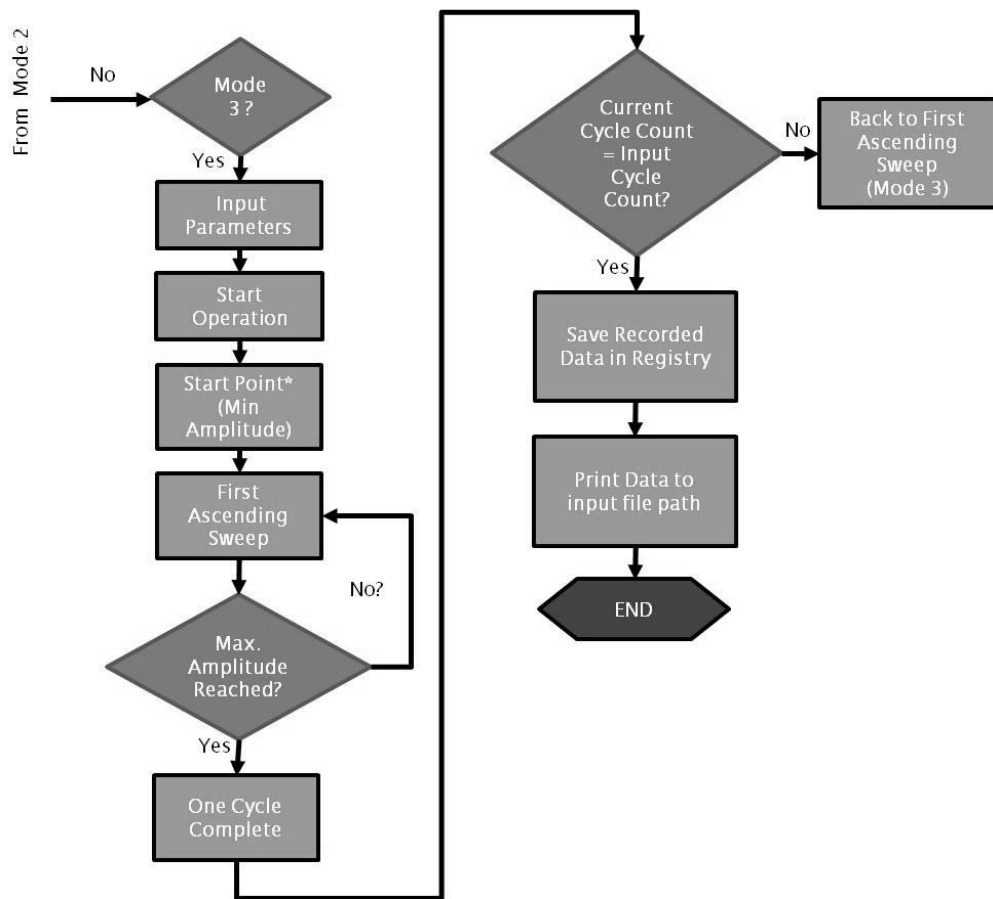


**Figure 8F: Continued programming flow diagram for Mode 3**

Keithley instrument drivers for the device had greatly simplified the task as there was no need for the user to send individual lines of code to the device to read. However should one require learning these lines of code the list can be found in the Keithley 2400 SourceMeter located in the company website; this manual was found useful to alter very specific lines which were crucial for the assigned program to work.

The program was written to manage the source meter to conduct sweeps across a predetermined range. A sweep is described as a periodic application of one parameter (either voltage of amperes) whilst reading the other. Meaning, should one conduct a voltage sweep, the applied potential periodically increased in a circuit while the devices measures the current response from that particular system or vice-versa. As mentioned above, the in-house driver and examples only offer the user to do a single sweep with minimal control over the device. Furthermore, they do not offer the user to conduct a cyclic sweep. This meant the sweep could only

either start from the minimum amplitude and progress to the maximum (ascending sweep) or the other way around (descending sweep). Illustrated in Figure G is the front panel of the Keithley 2400 SourceMeter cyclic sweep control system used for the work.

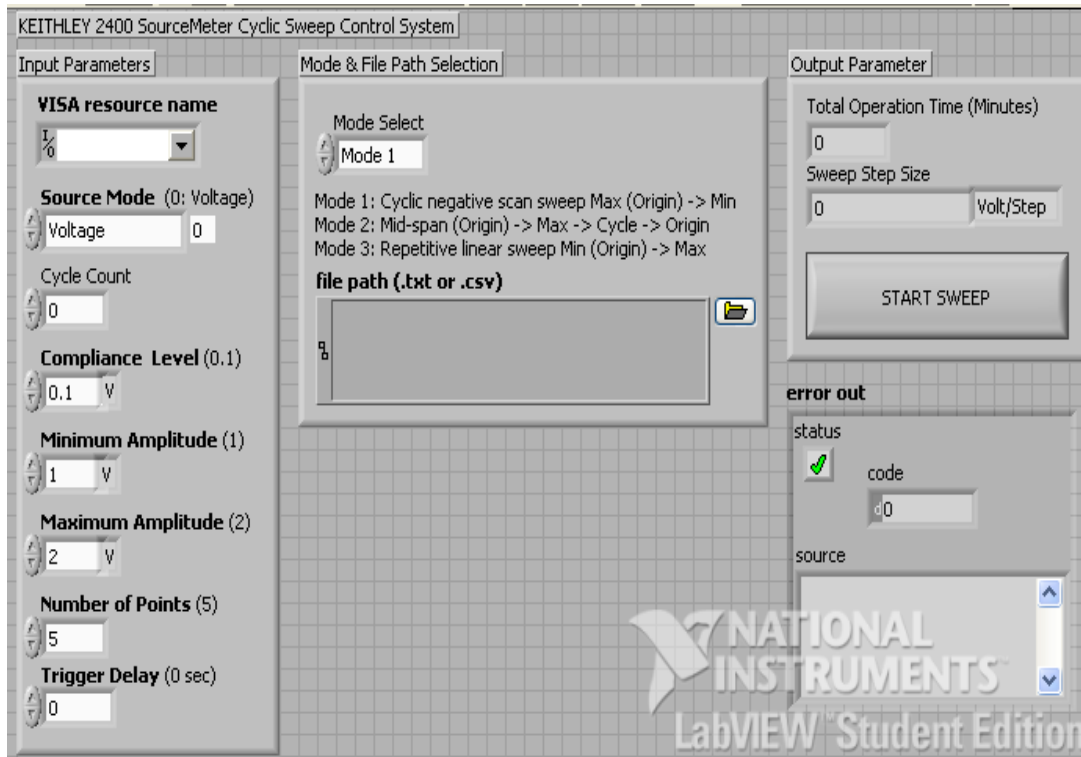
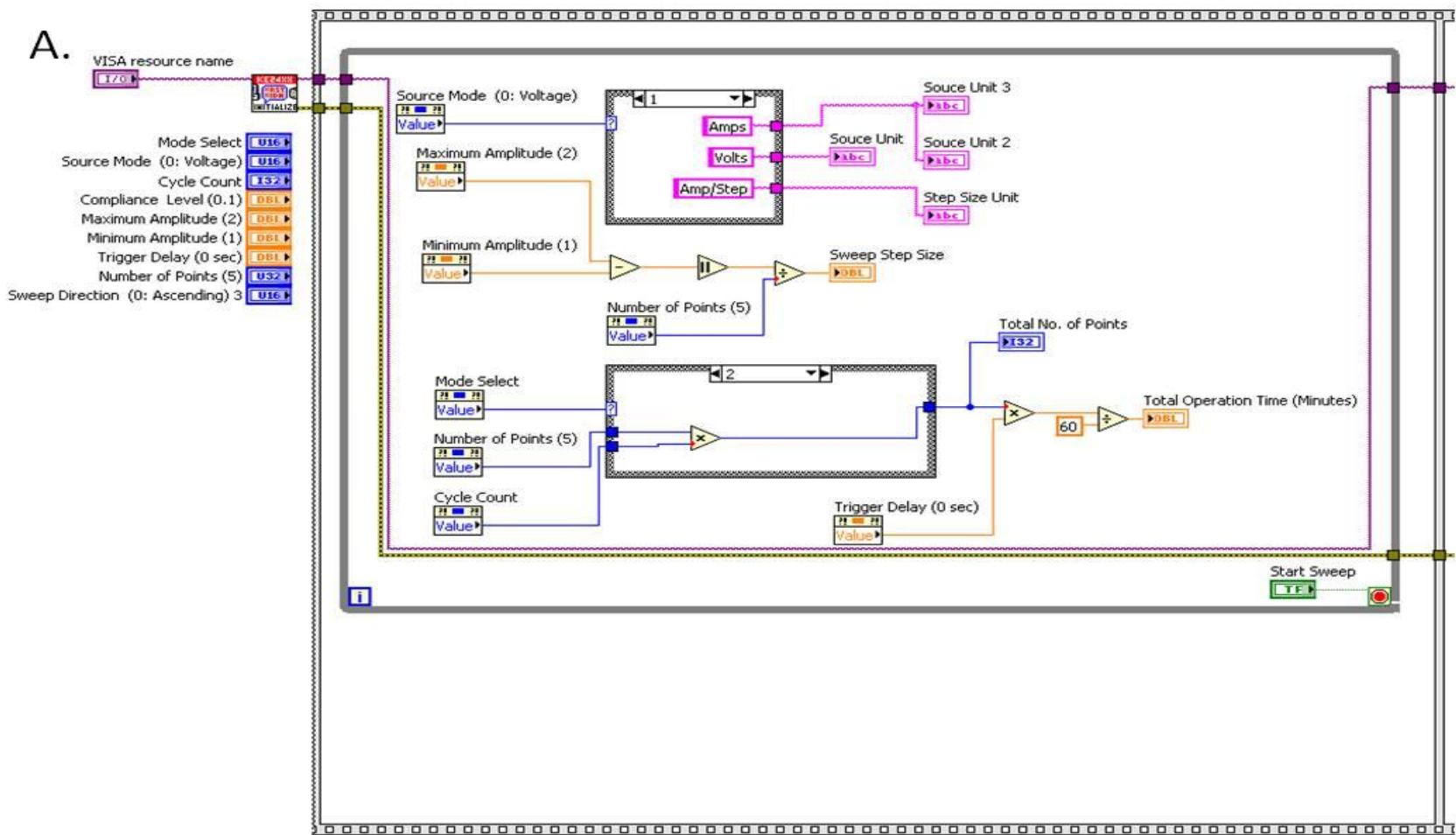


**Figure 8G: Front panel of the source meter control system.**

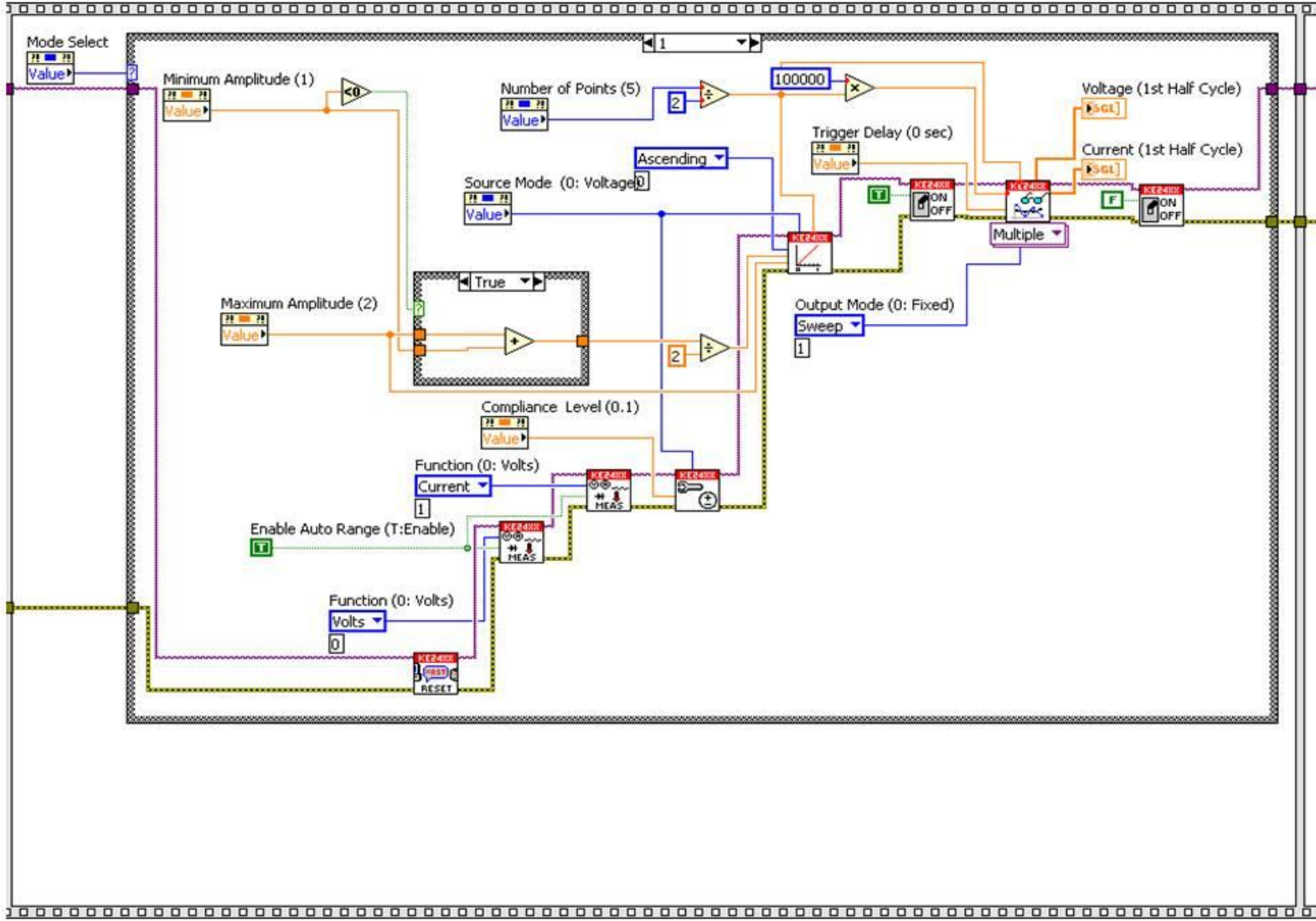
# LabVIEW Program Structure



Continued Next..

B.

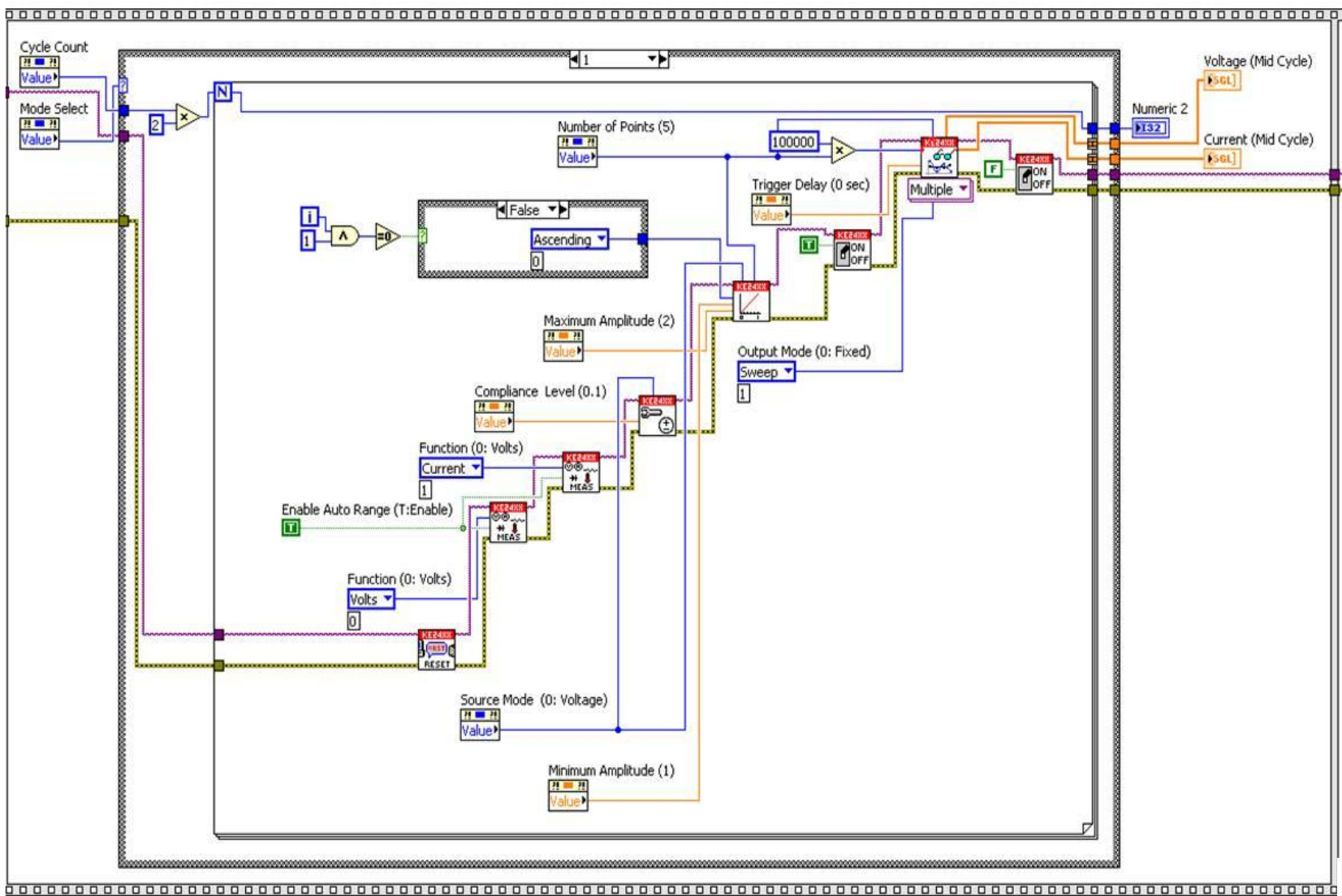
Start.



Continued Next..

C.

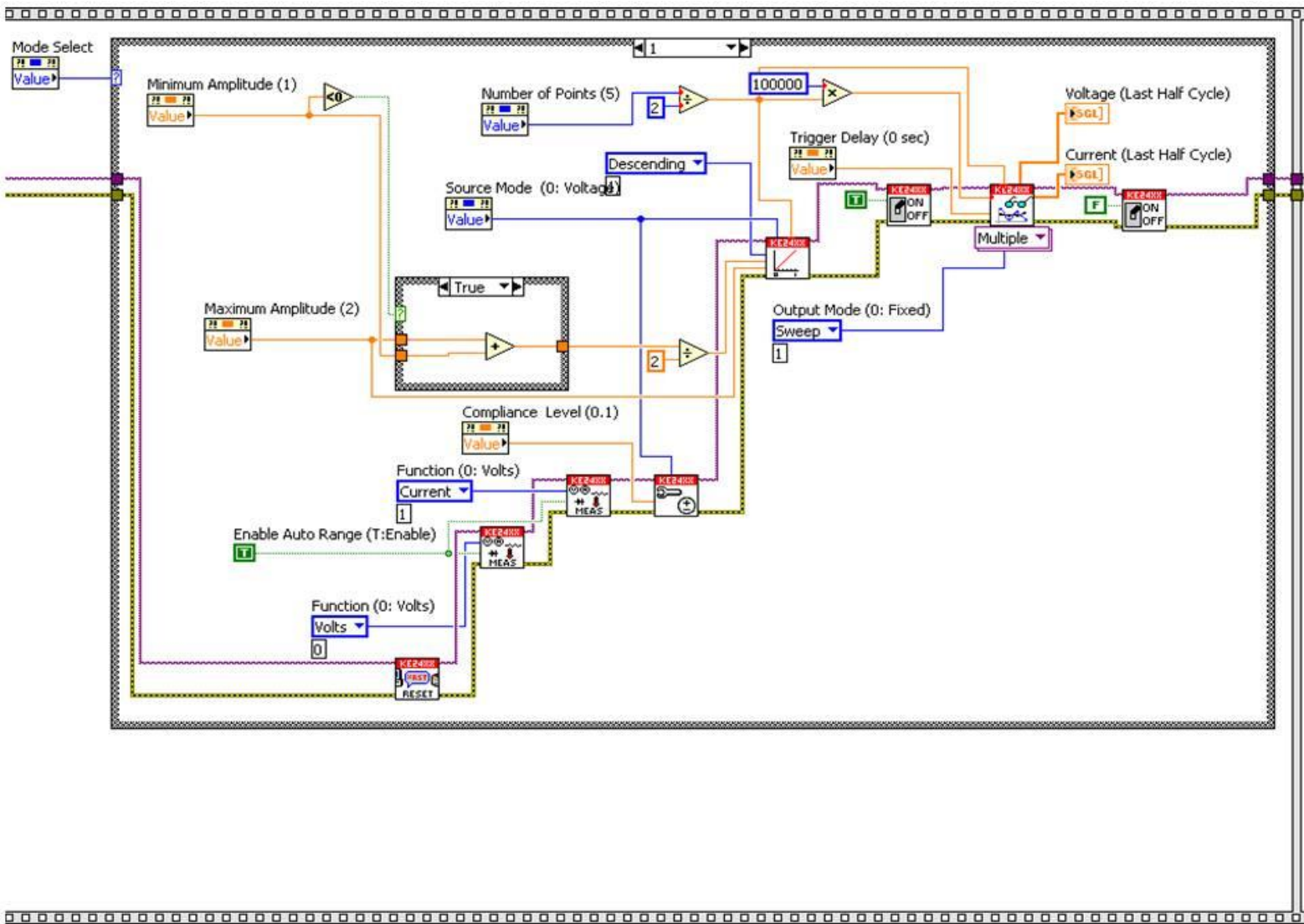
Start.



Continued Next..

D.

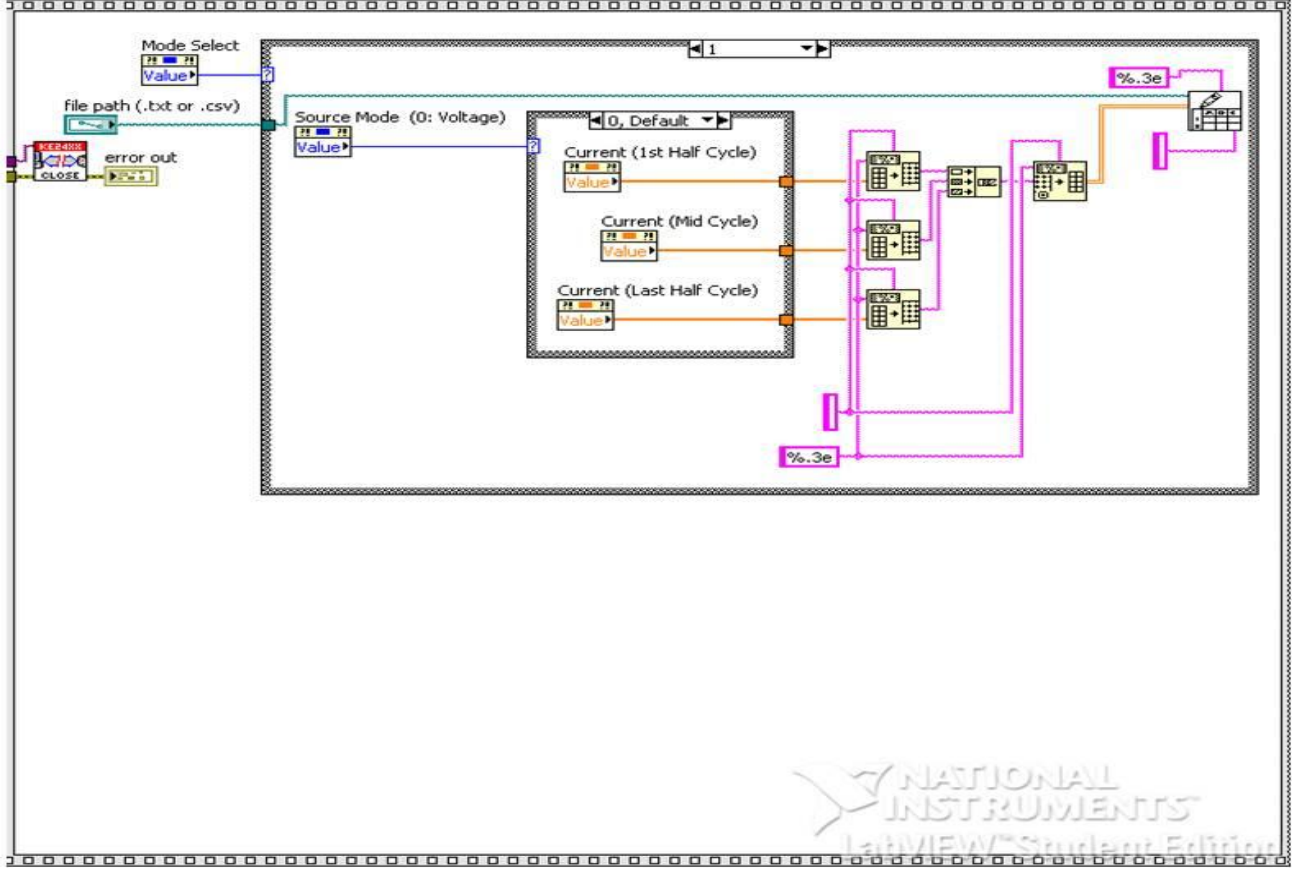
Start.



Continued Next..

E.

Start.



End



## Physical Data of Track-Etched Membranes

The table below is a tabulated physical attributes of the track-etch pores sourced from (SPI Supplies).

Pore Size	Pore Density	Nominal Weight	Nominal Thickness	Bubble Point <sup>2</sup>	Typical Water <sup>a</sup>	Flow Rates Air <sup>b</sup>
( $\mu\text{m}$ )	(pores/cm <sup>2</sup> )	(mg/cm <sup>2</sup> )	( $\mu\text{m}$ )	(psi)	(ml/min/cm <sup>2</sup> )	(l/min/cm <sup>2</sup> )
20	4x10 <sup>4</sup>	0.1	3	< 1	1100	80 <sup>3</sup>
14	5x10 <sup>4</sup>	0.6	6	< 1	2000	85 <sup>3</sup>
12	1x10 <sup>5</sup>	0.9	8	< 2	3000	85 <sup>3</sup>
10	1x10 <sup>5</sup>	1.1	10	< 2	1400	40 <sup>3</sup>
8	1x10 <sup>5</sup>	0.8	7	< 2	1300	40 <sup>3</sup>
5	4x10 <sup>5</sup>	1.1	10	3	650	40 <sup>3</sup>
3	2x10 <sup>6</sup>	0.9	9	5	600	50 <sup>3</sup>
2	2x10 <sup>6</sup>	1.1	10	7	170	22
1	2x10 <sup>7</sup>	1.1	11	14	170	25
0.8	3x10 <sup>7</sup>	0.9	9	18	120	20
0.6	3x10 <sup>7</sup>	1	9	24	83	10
0.4	1x10 <sup>8</sup>	1	10	36	41	10
0.2 <sup>1</sup>	3x10 <sup>8</sup>	1.1	10	72	17	4
0.1	4x10 <sup>8</sup>	0.7	6	> 100	2	2
0.08	4x10 <sup>8</sup>	0.7	6	> 100	1	1
0.05	6x10 <sup>8</sup>	0.7	6	> 100	0.4	0.5
0.03	6x10 <sup>8</sup>	0.7	6	> 100	0.2	0.1
0.01	6x10 <sup>8</sup>	0.7	6	> 100	< 0.1	0.01

a Initial flow rates in mL/min/cm<sup>2</sup> using prefiltered water at 10 psid (0.7 kg/cm<sup>2</sup>),  $\pm$  35% depending on test methodology

b Initial flow rates in L/min/cm<sup>2</sup> using prefiltered air at 10 psid (0.7 kg/cm<sup>2</sup>)

1 "Regular" flow grade. Low pore density grade available on special order and requiring order minimums

2 Calculated water bubble point, typical values (assuming 55° contact angle)

3 Differential pressure, 5 psi (0.35 kg/cm<sup>2</sup>)

**Figure 8H: Specifications of a wide selection of track-etched membranes (Source taken from:(SPI Supplies))**

# References

---

- Abetz, V., Clodt, J., Filiz, V., Rangou, S., Buhr, K., Abetz, C., et al. (2013). Double stimuli-responsive isoporous membranes via post-modification of pH-sensitive self-assembled diblock copolymer membranes. *Journal of Advanced Functional Materials* , 23, 731-738.
- Adiga, s., Jin, C., Curtiss, L., Monteiro-Riviere, N., & Narayan, R. (2009). Nanoporous membranes for medical and biological applications. *WIREs Nanomedical Nanobiotechnology* , 1, 568-581.
- Apel, P. Y., Blonskaya, I., Levkovich, N. V., & Orelovich, O. L. (2011). Asymmetric track membranes: Relationship between nanopore geometry and ionic conductivity. *Petroleum Chemistry* , 51 (7), 555 - 567.
- Argawal, D. C., & Maity, D. (2006). Synthesis of iron oxide nanoparticles under oxidizing environment and their stabilization in aqueous and non-aqueous media. *Journal of Magnetism and Magnetic Materials* , 308, 46-55.
- Axon Instruments, Inc. (1993). *The Axon guide for electrophysiology and biophysics laboratory techniques* (1 ed.). Foster City: Axon Instruments, Inc.
- Bates, R. G. (1954). Chapter 9: Cells , electrodes and techniques. In *Determination of pH: Theory and Practice* (pp. 281 - 286). New York: John Wiley & Sons.
- Bloemen, M., Brulot, W., Luong, T. T., Geukens, N., Gils, A., & Verbiest, T. (2012). Improved functionalization of oleic acid-coated iron oxide nanoparticles for biomedical applications. *Journal of Nanoparticle Research* , 14, 1100-1005.
- Branton, D., Chen, P., Gu, J., Brandin, E., Kim, Y.-R., & Wang, Q. (2004). Probing single DNA moldecule transport using fabricatied nanopores. *Nano Letters* , 4 (11), 2293-2298.
- Chen, C.-C., Derlyo, M. A., & Baker, L. A. (2009). Measurement of ion currents through porous membranes with scanning ion conductance microscopy. *Analytical Chemistry* , 81 (12), 4742 - 4751.

- Chou, S., Krauss, P., & Renstrom, P. (1996). Imprint lithography with 25 nanometer resolution. *Science* , 272, 85-87.
- Collins, S. D., Gierhart, B. C., Howitt, D. G., Chen, S. J., Zhu, Z., Kotecki, D. E., et al. (2008). Nanopore with traverse nanoelectrodes for electrical characterisation and sequencing of DNA. *Sensor and Actuators B* , 132, 593-600.
- Cosen, C. R. (1937). Rational wire tables. *Journal of Scientifi Instruments* , 12, 122-126.
- Crawford, G. .., Steele, L., Ondris-Crawford, R., & Iannacchione, G. G. (1992). Characterization of the cylindrical cavities of Anopore and Nuclepore membranes. *Journal of Chemical Physics* , 96 (10), 7788 - 7796.
- D.B. Montgomery, J. T. (1961). Some Useful Information for the Design or Air-Core Soleniods.
- Dekker, C., Smeets, R., Keyser, U., Krapf, D., Wu, M.-Y., & Dekker, N. (2006). Salt dependence of ion transport and DNA traslocation through solid-state nanopores. *Nano Letter* , 6 (1), 89-95.
- Desai, T., Chu, W., Tu, J., Beattie, G., Hayek, A., & Ferrari, M. (1998). Micofabricated Immunoisolating Biocapsules. *Biotechnology Bioengineering* , 57(1), 118-120.
- Dinesh, D., & Pradeep, P. (2011). Development of nanoporous polymer membranes by swift heavy ion irradiation. *Optics: Phenomena, Materials, Devices, and Characterisation AIP Conference Proceeding* , 1391, 796-798.
- Duan, C., Wang, W., & Xie, Q. (2013). Review Article: Fabrication of nanofluidci devices. *Biomicrofluidics* , 7, 026501-41.
- Dyab, A. K., Ozmen, M., Ersoz, M., & Paunov, V. (2009). Fabrication of novel anisotropic magnetic microparticles. *Journal of Materials Chemistry* , 19, 3475 - 3481.
- E.Dennison. (2005). *Magnet Formulas web site*. Retrieved 10 08, 2011, from <http://www.netdenizen.com/emagnet/index.htm>

Elektro-Automatik. (2000). *Elektro-Automatik*. Retrieved November 2013, from <http://www.elektroautomatik.de/en.html>

Ferreira, T., & Rasband, W. (1997). *ImageJ, image processing and analysis in Java*. Retrieved November 2013, from <http://rsb.info.nih.gov/ij/>

Fissell, W., Humes, H., Fleischman, A., & Roy, S. (2007). Dialysis and nanotechnology: Now, 10 years, or never? *Blood Purification* , 25, 12-17.

G.Flores, J.Liu, Mohebi, M., & Jamasbi, N. (1999). Magnetic-field-induced nonequilibrium structures in a ferrofluid emulsion. *Physical Review E* , 59 (1), 751 - 762.

Gaborski, T., Snyder, J., Striemer, C., Fang, D., Hoffman, M., Fauchet, P., et al. (2010). High-performance separation of nanoparticles with ultrathin porous nanocrystalline silicone membranes. *American Chemical Society Nano* , 4 (11), 6973-6981.

Guan, X., Liu, A., & Zhao, Q. (2010). Stochastic nanopore sensors for the detection of terrorist agents: Current status and challenges. *Analytica Chimica Acta* , 675, 106-115.

Gupta, A., & Gupta, M. (2005). Synthesis and surface engineering of iron oxide nanoparticles for biomedical applications. *Biomaterials* , 26, 3995-4021.

Hall, J. E. (1975). Access resistance of a small circular pore. *Journal of General Physiology* , 66, 531 - 532.

Hille, B. (1978). Ionic channels in excitable membranes: Current problems and biophysical approaches. *Biophysical Journal* , 22, 283 -294.

Honda, K., Rao, T. N., Fujishima, A., Watanabe, M., Yasul, K., & Masuda, H. (2000). Electrochemical characterization of the nanoporous honeycomb diamond electrode as an electrical double-layer capacitor. *Journal of the Electrochemical Society* , 147 (2), 659 - 664.

Hong, C.-Y., Jang, I. J., Horng, H. E., Hsu, C. J., Yao, Y. D., & Yang, H. C. (1997). Ordered structures in Fe<sub>3</sub>O<sub>4</sub> kerosene-based ferrofluids. *Journal of Applied Physics* , 81, 4275-4277.

- Isenberg, C. (1992). Draining and thinning of soap films. In *The science of soap films and soap bubbles* (pp. 31-49). New York: Dover Publications.
- Islam, M., Lin, K., Lacoaste, D., Lubensky, T., & Yodh, A. (2003). Field-induced structures in miscible ferrofluid suspensions with and without latex spheres. *Physical Review E* , 67, 021402-8.
- Ives, D. J., & Janz, g. J. (1961). Chapter 4: Silver-silver halide electrodes. In *Reference Electrodes: Theory and Practice* (pp. 179 -226). New York: Academic Presses.
- Ivey, M., J.Liu, Zhu, Y., & Cutillas, S. (2000). Magnetic-field-induced transitions in a ferrofluid emulsion. *Physical Review E* , 63, 011403.
- Ivey, M., Liu, J., Zhu, Y., & Cutillas, S. (2000). Magnetic-field-induced transitions in a ferrofluid emulsion. *Physical Review E* , 63, 011403.
- Jessensky, O., Muller, F., & Gosele, U. (1998). Self-organised formaton of hexgonal pore arrays in anodic alumina. *Applied Physics Letters* , 72 (10), 1173-1175.
- Jiang, C., & Tsukruk, V. (2006). Freestanding nanostructures via layer-by-layer assembly. *Advanced Materials* , 18, 829-840.
- John, W., Hering, S., Reischl, G., Sasaki, G., & Goren, S. (1983). Chracterization of Nuclepore filter with large pore size - I. Physical properties. *Atmospheric Environment* , 17 (1), 115 - 119.
- Kasianowicz, J., Robertson, J., Chan, E., Reiner, J., & Stanford, V. (2008). Nanoscoic Porous Sensors. *Annual Review of Analytical Chemistry* , 1, 737-766.
- Kim, D., Y.Zhang, Voit, W., Rao, K. V., & Muhammed, M. (2001). Synthesis and characterisation of surfactant-coated superparamagnetic monodispersed iron oxide nanoparticles. *Journal of Magnetism and Magnetic Materials* , 225, 30-36.
- Kissinger, P. T., & Heineman, W. (1983). Cyclic voltametry. *Journal of Chemical Education* , 60 (9), 702 - 706.

Kowalczyk, S. W., Grosberg, A. Y., Rabin, Y., & Dekker, C. (2011). Modelling the conductance and DNA blockade of solid-state nanopores. *Nanotechnology* , 22, 1 - 5.

Lee, C., Joly, L., Siria, A., Biane, A.-L., & Bocquet, R. &. (2012). Large apparent electric size of solid-state nanopores due to spatially extended surface conduction. *Nano Letters* , 12, 4037 - 4044.

Lee, J., Isobe, T., & Senna, M. (1996). Preparation of ultrafine Fe<sub>3</sub>O<sub>4</sub> particles by precipitation in the presence of PVA at high pH. *Journal of Colloid and Interface Science* , 177 (62), 490-494.

Li, J., Stein, D., McMullan, C., Branton, D., Aziz, M., & Golovchenko, J. (2001). Ion-beam sculpting at nanometer length scales. *Nature* , 412, 166-169.

Li, L., Szewczykowski, P., Clausen, L., Hansen, K., Jonsson, G., & Ndoni, S. (2011). Ultrafiltration by gyroid nanoporous polymer membranes. *Journal of Membrane Science* , 384, 126-135.

Lira, H., & Paterson, R. (2002). New an modified anodic alumina membranes part 3.: Preparation and characterisation by gas diffusion of 5 nm poreside anodic alumina membranes. *Journal of Membrane Science* , 206, 375-387.

Liu, J., Lawrence, E., Wu, A., Ivey, M., Flores, G., Javier, K., et al. (1995). Field-induced structures in ferrofluid emulsions. *Physical Review Letters* , 74 (14), 2828 - 2831.

Mabbott, G. (1983). An introduction to cyclic voltmetry. *Journal of Chemical Education* , 60 (9), 697 - 701.

McKee, C. (2009). An accurate equation for the electrolytic conductivity of potassium chloride solutions. *Journal of Solution Chemistry* , 38, 115-1172.

Meller, A., Kim, M., Wanunu, M., & Bell, D. (2006). Rapid fabrication of uniformly sized nanoporous and nanopore arrays for parallel DNA analysis. *Advanced Materials* , 18, 3149-3153.

Mo, Y., & Fei, T. (2012). Nanoporous membrane for biosensing applications. *Nano LIFE* , 2 (1), 1230003-16.

- Mohebi, M., & Jamasbi, N. (1996). Simulation of the formation of nonequilibrium structures in magnetorheological fluids subject to an external field. *Physical Review E* , 54 (5), 5407 - 5413.
- Park, Y., Ko, D., Yi, K., Petrov, I., & Kim, Y. (2007). Measurement and estimation of temperature rise in TEM sample during ion milling. *Ultramicroscopy* , 107, 663 - 668.
- Polarz, S., & Smarsly, B. (2002). Nanoporous Materials. *Journal of Nanoscience and Nanotechnology* 2 , 2 (6), 581-612.
- Quilter, R. E., & Surwillo, W. W. (1966). A simple method of preparing silver-silver chloride electrodes for recording of skin-potential. *The American Journal of Psychology* , 79 (2), 309 - 313.
- Raczkowska, J., Bernasik, A., Budkowski, A., Rysz, J., Kowalski, K., Lekka, M., et al. (2005). Pattern replication examine with integral geometry approach: Application to ion milling of polymer blend films. *Thin Solid Films* , 476, 358 - 365.
- Rhee, M., & Burns, M. (2007). Nanopore sequencing technology: nanopore preparations. *Trends in Biotechnology* , 24 (4), 174-181.
- Rhee, M., & Burns, M. (2006). Nanopore sequencing technology: Research trends and applications. *Trends in Biotechnology* , 24 (12), 580-586.
- Ricardi, J., & Weis, J.-J. (2011). Low density mesostructures of confined dipolar particles in an external field. *Journal of Chemical Physics* , 135, 124502.
- Rybchenko, S., Dyab, A. K., Haywood, S. K., Itskevich, I. E., & Paunov, V. N. (2009). Strained arrays of colloidal nanoparticles: conductance and magnetoresistance enhancements. *Nanotechnology* , 20, 1 - 7.
- Sawyer, D. T., Sobkowiak, A., & J. L. Roberts, J. (1995). Indicator Electrodes . In *Electrochemistry for chemists* (pp. 170 - 248). New York: John Wiley & Sons, Incorporated.
- Schüth, F., Lui, A.-H., & Salabas, E. (2007). Magnetic Nanoparticles: synthesis, protection functionalization and application. *Angew. Chem. Int* , 46, 1222-1244.

- Shong, C., Haur, S., & Wee, A. T. (2010). *Science at the nanoscale: An introductory textbook*. Singapore: Pan Stanford Publishing Pte. Ltd.
- Siwy, Z., Apel, P., Baur, D., Dobrev, D. D., Korchev, Y. E., Neumann, R., et al. (2003). Preparation of synthetic nanopores with transport properties analogous to biological channels. *Surface Science* , 1061 - 1066.
- Soref, R. (1974). *Patent No. US 3834794 A*. Chesnut Hill, USA.
- SPI Supplies. (n.d.). *SPI-Pore™ Standard White Polycarbonate "Track Etch" Screen Membrane Filters*. Retrieved July 1, 2013, from [http://www.2spi.com/catalog/spec\\_prep/spi-pore.html](http://www.2spi.com/catalog/spec_prep/spi-pore.html)
- Sun, J., S.Zhou, Hou, P., Yang, Y., Weng, J., Li, X., et al. (2006). Synthesis and characterisation of biocompatible Fe<sub>3</sub>O<sub>4</sub> nanoparticles. *Journal of Biomedical Materials Research Part A* , 333-341.
- Ulbricht, M. (2006). Advanced functional polymer membranes. *Polymer* , 47, 2217-2262.
- Vodyanoy, I., & Bezrukov, S. M. (1992). Sizing of an ion pore by access resistance measurements. *Biophysical Journal* , 62, 10 - 11 .
- Wang, C., J.Xu, Chen, H., & Xia, X. (2012). Mass transport in nanofluidic devices. *Science China Chemistry* , 55 (4), 453-468.
- Ward, K., Chun, M., Queenan, C., Calabro, A., Morales, J., & Becker, D. (2010). A novel method of resin-embedded thin, flexible polymer films for TEM sectioning. *Microscopy and Microanalysis* , 16, 712-713.
- Warner Instruments. (2002). Chloriding Ag/AgCl Electrodes. Hamden: Warner Instruments Inc.
- Ytreberg, F. M., & McKay, S. (2000). Calculated properties of field-induced aggregates in ferrofluids. *Physical Review E* , 61 (4), 4107 - 4110.
- Zhang, F., Liu, X., Pan, C., & Zhu, J. (2007). Nano-porous anodic aluminium oxide membranes with 6-19 nm pore diameters formed by low-potential anodising process. *Nanotechnology* , 17, 345302-345306.

Zhou, J., Ren, K., Zheng, Y., Su, J., Zao, Y., Ryan, D., et al. (2010). Fabrication of a microfluidic Ag/AgCl reference electrode and its application for portable and disposable electrochemical microchips. *Electrophoresis*, 31, 3083 - 3089.